Development of Noble Gases as Tracers of Subsurface Fluids – from Conventional and Unconventional Hydrocarbon to Geothermal Systems

by

Guolei Han

A dissertation submitted in partial fulfillment
of the requirements for the degree of
Doctor of Philosophy
(Earth and Environmental Sciences)
in the University of Michigan
2022

Doctoral Committee:

Professor Maria Clara Cruz Da Silva Castro, Chair
Associate Professor Brian R. Ellis
Emeritus Associate Research Scientist Chris M. Hall
Professor Kyger C. Lohmann
Professor Daniele L. Pinti, Université du Québec à Montréal

Guolei Han

hanguole@umich.edu

ORCID iD: 0000-0002-9685-8938

DEDICATION

To my family and friends.

ACKNOWLEDGEMENTS

I would like to express my sincere gratitude to my advisor, Dr. Clara Castro, for her continuous guidance and endless patience during this journey. This dissertation would not have been possible without her generous help and invaluable advice. I would like to thank Dr. Chris Hall, for his willingness to share his insightful suggestions, and patience to pick up my panic calls from the lab. I am also deeply indebted to Dr. Daniele Pinti, who offered me tremendous help and encouragement when they were greatly needed. I would like to thank Dr. Brian Ellis, for his thoughtful suggestions and inspiring classes. Special thanks go to Dr. Kyger Lohmann for his priceless and constructive advice. Finally, my thanks extend to Dr. Jean-Philippe Nicot and Dr. Toti Larson from the University of Texas in Austin, Dr. Juske Horita from the Texas Tech University, Dr. Aída López-Hernández' from the Universidad Michoacana de San Nicolás de Hidalgo for sharing their data and valuable knowledge in petroleum geology and geothermal systems. I thank Dr. Chris Ballentine from the University of Oxford for sharing the sample locations from his work in the Panhandle and Hugoton Field.

I would like to thank past lab members: Tao Wen, Julien Amalberti and Yi Niu, for their help and accompany.

Faculties and staff members make this department feels like home. To name a few: Dr. Naomi Levin, Dr. Jeroen Ritsema, Anne Hudon, Craig Delap, Chrissy Zigulis and Dale Austin.

I'm a lucky person who is surrounded by great friends. To name a few: Yi Wang, Xiaojing Du, Sooyeon Kim, Elizabeth Crowther, Prithvi Thakur, Lora Wingate, Meichen Liu, Xue Su,

Jingcheng Xiao, Mingjie Gao and many more. I am also grateful to friends in the University of Michigan kendo club, and Dr. Huan-Hsiang Ueng from CAPS.

Thanks to my parents, my sister, and my girlfriend Yang Xu for their unconditional love.

TABLE OF CONTENTS

DEDICATION ..... **ii**

ACKNOWLEDGEMENTS ..... **iii**

LIST OF TABLES ..... **ix**

LIST OF FIGURES ..... **xi**

LIST OF APPENDICES ..... **xv**

ABSTRACT ..... **xvi**

CHAPTER 1 Introduction **1**

1.1. Noble Gas Systematics **3**

1.2. Application of Noble Gases in Conventional and Unconventional Hydrocarbon Systems. **5**

1.3. Application of Noble Gases in Geothermal Systems **7**

1.4. Dissertation Structure **8**

1.5. References **11**

CHAPTER 2 Tracing the Origin, Migration and Mixing of Noble Gases and Methane in the Panhandle-Hugoton Field, Texas, United States **19**

Abstract **19**

2.1. Introduction **21**

2.2. Regional Settings **24**

2.2.1. Geological Background 24

2.2.2. Hydrogeological Setting 30

2.3. Methods **31**

2.3.1. Sample Collection 31

2.3.2. Analytical Techniques 32

2.4. Results 34

2.4.1. Major Gases 34

2.4.2. Noble Gases 35

2.5. Discussion 41

2.5.1. Western and Eastern Hydrocarbon and Noble Gas Sources in the Panhandle Field... 41

2.5.2. Mantle Noble Gas Sources in the Panhandle Field 47

2.5.3. In-situ Production versus an External Origin for Noble Gases 56

2.5.4. Relative Ages and Spatial Distribution Pattern of Natural Gas 63

2.5.5. Impact of Groundwater Flow as Revealed by Water/Gas Volume Ratio Estimation . 68

2.6. Conclusions 74

2.7. References 77

CHAPTER 3 MORB and Solar-OIB like Noble Gas Signatures in the Eagle Ford Shale, Southwest Texas – Implications for the Earth's Geological Evolution and Framework 88

Abstract 88

3.1. Introduction 90

3.2. Geological Background 94

3.3. Methods 99

3.3.1. Sample Collection 99

3.3.2. Analytical Techniques 100

3.4. Results 101

3.4.1. Major Gases 101

3.4.2. Noble Gases 103

3.5. Discussion 110

3.5.1. Resolving He and Ne Mantle Sources 111

3.5.2. Geological and Tectonic Evolution 119

3.2.5.1. MORB Endmember – Origin and Implications 119
3.2.5.2. Solar-Like Endmember – Origin and Implications 123
3.5.3. Hydrocarbon Reservoir Relative Ages and Origin - A compartmentalized Eagle Ford Shale 127
3.6. Conclusions 133
3.7. References 137
CHAPTER 4 Heat, Noble Gases and CO_2 Sources in Geothermal Fields of Mexico 149
Abstract 149
4.1. Introduction 151
4.2. Geological Setting 154
4.3. Sampling and Analytic Methods 159
4.4. Results 162
4.5. Discussion 165
4.5.1. Heterogeneous Helium Sources 165
4.5.2. Heat Transfer into Mexican Geothermal Systems 171
4.5.3. Source of Fluids and Heat Distribution 175
4.5.4. Mixing of Geothermal Fluids and Heat as Revealed by CO_2, Noble gases and Heat Data 178
4.5.5. Fractionation Between Heat and Volatile Species: Dependence on Magma Degassing? 185
4.6. Conclusions 188
4.7. Acknowledgments 191
4.8. References 192
CHAPTER 5 Summary and Conclusions 201
5.1. Summary of Major Results 201
5.2. Overall Conclusions 204
APPENDICES 206

Appendix A Supplementary Materials for Chapter 2 207

Appendix A1. Mass Fractionation..... 207

Appendix A2. Atmospheric Ne Removal and Optimized Crust-Solar Mixing Line 209

References 212

Appendix B Supplementary Materials for Chapter 3..... 213

Appendix B1. Nucleogenic Production of ^{20}Ne..... 213

Appendix B2. Mass Fractionation..... 214

Appendix B3. Atmospheric Ne Removal and Optimized Crust-Solar Mixing Line..... 215

Appendix B4. Ar Isochrons and ^{40}Ar Relative Ages..... 216

Appendix B5. Calculation of Noble Gases in-Situ Production 217

References 219

Appendix C Supplementary Materials for Chapter 4 220

LIST OF TABLES

CHAPTER 2

Table 2.1 Sample depths and major gas compositions of the Texas Panhandle gas samples**.**..... 34

Table 2.2 Noble gas volume fractions (cm^3/cm^3) and terrigenic noble gas volume fractions for production gas samples from the Panhandle Field**.** 39

Table 2.3 Noble gas isotopic ratios and air-correction helium isotopic ratios for gas samples from the Panhandle field..... 40

Table 2.4 Endmember isotopic and elemental ratios of distinct earth reservoirs 54

Table 2.5 Ne isotopic compositions after correction of atmospheric component..... 55

Table 2.6 Parameters used in the estimation of in-situ production of $^4He^*$ and $^{40}Ar^*$ 62

Table 2.7 Estimated percentages of in-situ production of $^4He^*$ and $^{40}Ar^*$..... 62

Table 2.8 Reverse of x-intercept values from modified Ar isochron method and water/gas ratios of the PHF samples in this study and from Ballentine and Lollar [2002]. 73

CHAPTER 3

Table 3.1 Major gas compositions of the Eagle Ford gas samples. 102

Table 3.2 Well names, depths, CH_4 contents, noble gas volume fractions (cm^3/cm^3) and crustal noble gas volume fractions for production gas samples from the Eagle Ford Shale. 108

Table 3.3 Noble gas isotopic ratios for production gas samples from the Eagle Ford Shale..... 109

Table 3.4 Endmember isotopic and elemental ratios of distinct earth reservoirs 117

Table 3.5 He and Ne isotopic compositions after correction of atmospheric component 118

APPENDICES

Table C1 Geothermal fields, sample ID, sampling year, CO_2 volume fractions, the $\delta^{13}C$ ratios of CO_2, R/Ra ratios, noble gas volume fractions (cm^3/cm^3) and crustal noble gas volume fractions in Mexican geothermal samples. ……220

Table C2 Temperature, enthalpy, measured $^{4}He/^{20}Ne$ ratios, air-corrected R/Ra ratios and estimated heat/^{3}He ratios in the Mexican geothermal… …….230

Table C3 Estimated percentages of various carbon sources in Mexican geothermal samples...234

LIST OF FIGURES

CHAPTER 2

Figure 2.1 Geological map of the Panhandle-Hugoton Field. Production blocks of the Panhandle and Hugoton Field are indicated by colored shaded areas. The Amarillo Uplift is indicated in grey while other uplifts are labeled in red. Major basins are labeled in blue. The Wichita Igneous Province (WIP) is indicated by orange grid. Sample locations in this study (circles and triangles) and those in Ballentine and Lollar [2002] (squares) are indicated as well. 26

Figure 2.2 Stratigraphy of the PHF and adjacent geological units [adapted from Brown, 2019]. Fine-grained clastic formations (e.g., shales and siltstones) are labeled in grey; carbonates are labeled in blue; coarse-grained clastic rocks (e.g., sandstones and "granite wash") are labeled in yellow; evaporites are labeled in green and igneous rocks are shown in red. 28

Figure 2.3 Methane volume percentages plotted as a function of the volume fractions of (a) total ^{4}He, (b) terrigenic $^{4}He^{*}$, (c) R/Ra, (d) terrigenic $^{21}Ne^{*}$, (e) terrigenic $^{40}Ar^{*}$ and (f) terrigenic $^{136}Xe^{*}$ for the Panhandle samples. 43

Figure 2.4 Sample depths plotted as a function of (a) terrigenic $^{4}He^{*}$, (b) terrigenic $^{21}Ne^{*}$, (c) terrigenic $^{40}Ar^{*}$ and (d) air-corrected $(R/Ra)_{c}$ of Panhandle samples. 46

Figure 2.5 Measured $^{20}Ne/^{22}Ne$ ratios plotted as function of $^{21}Ne/^{22}Ne$ ratios for Panhandle gas samples. Three components are presented in this diagram: Air, Mantle (MORB, OIBs, Solar), and Crust. Mixing lines between Air–Solar, Air–MORB and Air–OIB endmembers for Iceland, Hawaii, Reunion, and Kerguelen are indicated. Air–Crust mixing lines with $^{21}Ne/^{22}Ne$ ratios of 0.1, 0.47 and 0.33 (Table 2.4) are also shown. Triangular grey areas, from lighter to darker indicate the Air–Solar–MORB, Air–MORB–Crust, and Air Crust domains, respectively. All endmember values are listed in Table 2.4. 48

Figure 2.6 Two-component mixing plots for $(R/Ra)_{c}$ vs. (a) $(^{20}Ne/^{22}Ne)_{crust+mantle}$ and (b) $(^{21}Ne/^{22}Ne)_{crust+mantle}$ for Panhandle gas samples in this study. Theoretical crust-MORB, crust-OIB and crust-solar mixing lines are shown. Modified crust-solar [Castro et al., 2009] mixing line is also shown (cf., Appendix A2). 50

Figure 2.7 $^{21}Ne^{*}/^{40}Ar^{*}$ ratios plotted as a function of $^{4}He^{*}/^{40}Ar^{*}$ ratios of the Panhandle samples in this study and those from Ballentine and Lollar [2002]. The solid straight line represents solubility-controlled elemental fractionation from in-situ production of the reservoir rock [$^{4}He^{*}/^{40}Ar^{*}=2\times10\text{-}7$, $^{21}Ne^{*}/^{40}Ar^{*}=10$, Pierce, 1964]. The dashed straight line represents the solubility-controlled elemental fractionation from average crust [$^{4}He^{*}/^{40}Ar^{*}=2.15\times10\text{-}7$, $^{21}Ne^{*}/^{40}Ar^{*}=5$, Ballentine and Burnard, 2002], with the composition of average crust represented by black star. The dotted straight line represents the solubility-controlled elemental fractionation

from lower crust [$^{4}He^{*}/^{40}Ar^{*}$=2.15×10-7, $^{21}Ne^{*}/^{40}Ar^{*}$=3, Ballentine and Burnard, 2002]. The dotted curve passing through average crust point represents the diffusion-controlled fractionation line..... 56

Figure 2.8 (a) $^{36}Ar/^{40}Ar$ ratios as a function of the reverse of ^{40}Ar volume fractions for all gas samples in this study. (b) $^{36}Ar/^{40}Ar$ ratios as a function of the reverse of ^{40}Ar volume fractions for samples in this study and those of Ballentine and Lollar [2002]. Age groups are indicated by different color..... 64

Figure 2.9 Relative age groups based on modified Ar isochron method in Panhandle samples and samples from Ballentine and Lollar [2002]. Relative ages increase from group 1 to group 3. Red arrows indicate the hydrocarbon migration pathways concluded by Sorenson [2005]. Major geological units and state boundaries are also shown..... 67

Figure 2.10 Estimated water/gas ratios plotted as a function of the reverse of x-intercept in the modified Ar isochron method for samples in this study and from Ballentine and Lollar [2002]. 71

CHAPTER 3

Figure 3.1 Map of the Eagle Ford Shale play within Texas, showing sampled well locations (this study), oil, wet and dry gas windows, subsurface volcanic mounds and major structural features [adapted from Gherabati et al., 2016]. Byrne et al. [2018] well locations (red and blue open squares) and approximate Harrington et al. [2015] sampled area (dotted square area) are also indicated. Location and extent of the Llano uplift and fault zones follow Condon and Dayman [2006]..... 95

Figure 3.2 Jurassic, Cretaceous and Tertiary geological units in southern Texas [adapted from Condon and Dyman, 2006 and Kosters et al., 1989]. 98

Figure 3.3 (a) Total ^{4}He volume fractions, (b) Crustal $^{4}He^{*}$ volume fractions, (c) R/Ra ratios, (d) $^{21}Ne/^{22}Ne$ ratios, (e) $^{40}Ar/^{36}Ar$ and (f) Crustal $^{40}Ar^{*}$ volume fractions as a function of methane volume percentages..... 105

Figure 3.4 Measured $^{20}Ne/^{22}Ne$ ratios plotted as function of $^{21}Ne/^{22}Ne$ ratios for Eagle Ford gas samples. Three components are presented in this diagram: Air, Mantle (MORB, OIBs, Solar), and Crust. Mixing lines between Air–Solar, Air–MORB and Air–OIB endmembers for Iceland, Hawaii, Reunion, and Kerguelen are indicated. Air–Crust mixing lines with $^{21}Ne/^{22}Ne$ ratios of 0.1, 0.47 and 0.33 (Table 3.4) are also shown. Triangular grey areas, from lighter to darker indicate the Air–Solar–MORB, Air–MORB–Crust, and Air Crust domains, respectively. Endmember values are provided in Table 3.4. Blue dashed lines along the Air–Solar line provide uncertainty associated with measurements. Pink area represents the area in which Harrington et al. [2015] fall based on their reported $^{20}Ne/^{22}Ne$ values (10.2 - 11.1)..... 112

Figure 3.5 Two-component mixing plots for $(R/Ra)_c$ vs. (a) $(^{20}Ne/^{22}Ne)_{crust+mantle}$ and (b) $(^{21}Ne/^{22}Ne)_{crust+mantle}$ for Eagle Ford gas samples in this study and Michigan Basin brines [Castro et al.,2009]. Theoretical crust-MORB, crust-OIB and crust-solar mixing lines are shown. Modified crust-solar [Castro et al., 2009] mixing line is also shown (cf., Appendix B3)..... 114

Figure 3.6 Map showing the location of all sampled wells, i.e., this study, Byrne et al. [2018] and Harrington et al. [2015] as well as the oil, wet and dry gas windows and major tectonic features. Boundaries between pure crustal, MORB and solar-like/OIB noble gas signatures are shown (red dashed lines). Suggested rotations of the originally palinplastic reconstructed Ouachita Rift and Texas transform [Thomas, 1991] are shown. The rotated Ouachita rift coincides with the crust-MORB boundary (red dashed line). ^{40}Ar relative age compartments are indicated (see text). Boundaries between compartments are indicated with blue dashed lines, which correspond to possible small transform faults..... 122

Figure 3.7 (a) ^{36}Ar/^{40}Ar ratios as a function of the reverse of ^{40}Ar volume fractions for all gas samples (this study, Appendix B4). (b) ^{36}Ar/^{40}Ar ratios as a function of the reverse of ^{40}Ar volume fractions for samples in this study and those of Byrne et al. [2018]. Dashed lines represent different age groups. Intercept values of each isochron line on the X-axis are labeled in red 129

CHAPTER 4

Figure 4.1 Location of Mexican geothermal areas discussed in this study. Major tectonic structures are shown. Heat flow distribution in Mexico is displayed in different colors (simplified and redrawn from Prol-Ledesma, 2019). Batista Cruz et al. [2019] data are from the Baja California Peninsula and the Gulf of California. 152

Figure 4.2 $(R/Ra)_c$ of fluids in Mexican geothermal areas. Reference values: depleted mantle or DMM [8±1; Allègre et al., 1995]; DMM under Gulf of California [7.84±0.4; Lupton, 1979]; mantle wedge under the TMVB [7.3±0.3; Straub et al., 2011]; subcontinental lithospheric mantle or SCLM [6.1±0.9; Gautheron and Moreira, 2002]; SCLM beneath Mexico [7.39±0.14; Sandoval-Velasquez et al., 2021]; continental crust [Oxburgh et al., 1986]. 166

Figure 4.3 (a) Theoretical model of ^{3}He/^{40}Ar vs ^{4}He/^{40}Ar; (b) Total ^{3}He/^{40}Ar vs total ^{4}He/^{40}Ar measured in Mexican geothermal fluids; (c) Zoom in of b) with the extent shown as red dashed box. Hydrothermal and magmatic samples from Batista-Cruz et al. [2019] in the Baja California area are shown as green circles and squares, respectively. Regression lines for each geothermal field are shown with their slopes representing the R/Ra ratios of each field. LA: Los Azufres; LH: Los Humeros; A: Acoculco; CC: Cerritos Colorados; LTV: Las Tres Vírgenes; BCH: Baja California magmatic samples..... 168

Figure 4.4 The Q/^{3}He versus ^{4}He/^{36}Ar ratios in the Mexican geothermal fluids. Samples from the southern production zone of Los Azufres are shown as circles, while those from the northern production zone are shown as squares. The Q/^{3}He values of DMM are from Lupton et al. [1989] and ^{4}He/^{36}Ar values are from Burnard and Polya [2004]. Continental melts Q/^{3}He value is from Burnard and Polya [2004]. The ^{4}He/^{36}Ar value range of ASW calculated for MAAT of 12-22℃ is indicated as a grey surface. The dotted line represents the linear correlation between Q/^{3}He versus ^{4}He/^{36}Ar ratios among the samples. Symbols as in fig. 4.3..... 172

Figure 4.5 (a) The ^{4}He/^{3}He vs Q/^{3}He ratios of the Mexican geothermal fluids. Typical values for the crust, depleted mantle (DMM) and ASW endmembers are shown (see section 4.5.3 for endmember values); (**b**) zoom in to the vicinity of the DMM endmember. Theoretical mixing

lines between DMM, the crust and meteoric water are shown as dashed lines, with the percentages of crustal contribution in the mixture indicated in yellow. The orange dotted line represents a binary mixing trend between the DMM and a mixture of ASW and crust with ~75%. crustal contribution. The binary mixing trend between the ASW endmember and the residual liquid phase after boiling is also shown as black dotted line. The extent of b) is indicated by the red dashed box in a). Symbols as in fig. 4.3. 176

Figure 4.6 The $CO_2/^3He$ ratios of Mexican geothermal fluids vs the $\delta^{13}C$-CO_2. Endmember values of depleted mantle (DMM), the limestone and the organic-rich sediment endmembers from Sano and Marty [1995] are shown in red, blue and orange, respectively. Blue dashed lines represent fractionation caused by carbonate precipitation under 50℃ and 110℃ following Barry et al. [2020]. Symbols as in fig. 4.3. 178

Figure 4.7 The $Q/^3He$ vs $CO_2/^3He$ ratios of Mexican geothermal fluids. The average compositions of depleted mantle (DMM), crust and ASW at 22˚C are shown, while black dashed lines indicate binary mixing between these three endmembers. Orange shaded area indicate the extent of mixing between magma and the upper/lower limits of the crustal component, with $CO_2/^3He$ ratios equal to 1×10^{12} and 1×10^{14} [Sano and Marty, 1995], respectively. Symbols as in fig. 4.3. 182

Figure 4.8 (a) $CO_2/^3He$ and (**b**) $CO_2/^4He$ ratios plotted as a function of R/Ra ratios measured in Mexican geothermal fluids. The average compositions of depleted mantle (DMM); crust and meteoric water at 22℃ are shown. Black dashed lines indicate binary mixing between these three endmembers. Orange shaded area indicate the extent of mixing between magma and the upper/lower limits of the crustal component. Symbols as in Fig. 4.3..... 184

Figure 4.9 $CO_2/^3He$ ratios plotted as a function of air-corrected (terrigenic) $^{40}Ar^*/^4He^*$ ratios of the Mexican geothermal fluids. The depleted mantle endmember (DMM) and crust endmembers are shown. The extent of area affected by calcite precipitation is indicated by the blue arrow. 186

APPENDICES

Figure A1 Measured $^{20}Ne/^{22}Ne$ ratios plotted as a function of $^{38}Ar/^{36}Ar$ ratios. Mass-dependent fraction lines from an atmospheric component following Kaneoka [1980] and Marty [1984] are shown. 208

Figure A2 Measured $^{21}Ne/^{22}Ne$ ratios plotted as a function of $^{38}Ar/^{36}Ar$ ratios. Mass-dependent fraction lines from an atmospheric component following Kaneoka [1980] and Marty [1984] are shown 209

Figure B1 Measured $^{20}Ne/^{22}Ne$ ratios plotted as a function of $^{38}Ar/^{36}Ar$ ratios. Mass-dependent fraction lines from an atmospheric component following Kaneoka [1980] and Marty [1984] are shown..…….215

LIST OF APPENDICES

APPENDIX A 207

A1 Mass Fractionation 207

A2 Atmospheric Ne Removal and Optimized Crust-Solar Mixing Line 209

APPENDIX B 213

B1 Nucleogenic Production of ^{20}Ne 213

B2 Mass Fractionation 214

B3 Atmospheric Ne Removal and Optimized Crust-Solar Mixing Line 215

B4 Ar Isochrons and ^{40}Ar Relative Ages 216

B5 Calculation of Noble Gases in-Situ Production 217

APPENDIX C 220

ABSTRACT

In order to counteract the ongoing global warming and to cope with the increasing demand for clean energy, advancements in our understanding of subsurface energy systems are required to guide future exploration and management strategies. Noble gases (He, Ne, Ar, Kr, Xe) are stable and chemically inert, making them excellent tracers to fingerprint various crustal fluids, e.g., groundwater, natural gas and oil. This dissertation includes a study in the conventional Panhandle and Hugoton Field (PHF) in Texas, Oklahoma and Kansas, a study in the unconventional reservoir of the Eagle Ford Shale in Texas, and a study in Mexican geothermal fields. In hydrocarbon systems, noble gases are analyzed together with major gas components (e.g., CH_4, CO_2) to trace the sources, migration and mixing of subsurface fluids, and to clarify the tectonic and magmatic evolution of these regions. In the geothermal systems, noble gases are analyzed together with heat, CO_2, and stable isotopes ($\delta^{13}C$-CO_2) to evaluate their sources and fractionation mechanisms.

PHF gas samples show enrichment in terrigenic noble gases ($^{4}He^*$, $^{21}Ne^*$, $^{40}Ar^*$). A positive correlation between terrigenic noble gases and methane in west Panhandle suggests a common origin for both gases from adjacent basins. In east Panhandle, a positive correlation between terrigenic noble gases and depth points to a dominant upward noble gas flux from underlying rocks. The presence of a primordial mantle He-Ne component in east Panhandle and a mantle helium component of undetermined origin in west Panhandle suggest the presence of an open system. The primordial mantle component is likely associated with the presence of a mantle plume in the Wichita Igneous Province. The combined analysis of relative ^{40}Ar ages and estimated

water/gas volume ratios suggests that groundwater plays a major role in the accumulation and distribution of terrigenic noble gases.

Gas samples in the Eagle Ford Shale show a positive correlation between methane and crustal noble gases, suggesting a common origin for both. The noble gas dataset suggests also the presence of different hydrocarbon sources. Two distinct mantle components are observed: a primordial, solar-like component corresponding to an Ocean Island Basalts (OIBs) signature, and a component corresponding to a Mid-Ocean Ridge Basalt (MORB) signature. The MORB signature is likely representative of the Ouachita Rift during the breakup of Rodinia, while the OIB-like signature is consistent with an origin in the subcontinental lithospheric mantle, possibly from the shallow refractory reservoir beneath the Balcones Igneous Province. Relative ^{40}Ar ages display significant variations in the Eagle Ford samples, suggesting a highly developed compartmentalization within the shale reservoir and the presence of different hydrocarbon sources.

Fluid samples from Mexican geothermal fields display distinct R/Ra ratios (where R is the measured $^{3}He/^{4}He$ ratio and Ra is the atmospheric ratio) in the Trans-Mexican Volcanic Belt (TMVB) and Baja California. High R/Ra ratios in the TMVB correspond to active magmatic heat sources while low R/Ra ratios in Baja California point to crustal contributions from the subducted Farallon plate. A combined analysis of heat/helium ratios ($Q/^{3}He$) with $^{4}He/^{36}Ar$ ratios shows that convection is the main mechanism controlling the transport of heat and magmatic volatiles during magma degassing. Fractionation between heat and volatiles is caused by boiling and meteoric water dilution. The absence of significant fractionation in $CO_2/^{3}He$ ratios suggests that helium degassing is controlled by the CO_2 content in parental magma rather than helium diffusivity.

CHAPTER 1

Introduction

Without significant effort to reduce greenhouse gas emissions, global warming is projected to cause a temperature increase of more than 2℃ during the 21st century [IPCC, 2021]. In order to reduce greenhouse gas emissions and limit the global temperature increase to 2℃, preferably to 1.5℃, by the end of the 21st century [COP-21, 2015], the transition from fossil fuels to renewable, carbon neutral energy is needed. In the U.S., renewable energy is projected to account for 60% of the cumulative increase of electricity capacity from 2020 to 2050 [EIA, 2021]. Among the renewable energy resources, geothermal energy is gaining increasing interest due to the advancement in exploitation technologies such as hydraulic fracturing [van der Zwaan and Longa, 2019]. The hydraulic fracturing technique allows for the exploitation of (ultra) deep geothermal resources [e.g., Zhao et al. 2015; AbuAisha et al., 2016], which greatly increases the global potential of geothermal energy [van der Zwaan and Longa, 2019]. The utilization of geothermal resources is traditionally classified as being direct and indirect [Dickson and Fanelli, 2003], with direct application referring to using, e.g., heated fluid for space heating, and indirect application commonly referring to as electricity generation. The global installed capacity of indirect geothermal energy reached ~12.7GW in 2016 [IRENA, 2017], and is predicted to greatly exceed 100GW in 2050, accounting for 2-3% of the global electricity production [van der Zwaan and Longa, 2019]. However, although the long-term goal of reducing global carbon emissions can only

be achieved by replacing fossil fuels with renewable energy options, switching between different fossil fuels, e.g., from coal to natural gas, can also reduce carbon emissions in the short-term [e.g., Smil, 2015]. The carbon intensity of natural gas in electricity generation is about half that of coal, and the cumulative upstream carbon emission of natural gas is around 40% that of coal [Staffell, 2017]. A reduction of about 3% of global emissions can be achieved by replacing coal with natural gas in electricity power plants of 30 major countries worldwide [Wilson and Staffell, 2018]. In the U.S., natural gas is projected to account for ~40% of the cumulative electricity capacity addition between 2020 and 2050 [EIA, 2021]. The increasing demand of natural gas in our society calls for enhanced reservoir characterization, and improved understanding of hydrocarbon migration history and interaction between hydrocarbon phases and other subsurface fluids in natural gas systems [Pinti and Marty, 2000; Hunt et al., 2012; Prinzhofer, 2013]. Characterizing these systems with the aid of noble gas geochemistry is the goal of this dissertation.

Stable noble gases (Helium – He, Neon – Ne, Argon – Ar, Krypton – Kr, Xenon - Xe) are located on the rightmost side of the periodic table. Their outer shells are filled with electrons and are chemically inert. These five noble gases are also not radioactive and thus are mostly sensitive to physical processes (e.g., migration of crustal fluids and multi-phase interaction), making them excellent tracers in geological processes [e.g., Ozima and Posodek, 2002; Burnard, 2013]. Noble gas geochemistry has been used to trace hydrocarbons in conventional natural gas fields [e.g., Zartman et al., 1961; Bosch and Mazor, 1988; Ballentine et al., 1991; Pinti and Marty, 1995], unconventional fields [e.g., Osborn et al., 2011; Hunt et al., 2012; Darrah et al., 2014; Wen et al. 2015] and geothermal fields [e.g., Mazor and Truesdell, 1984; Kennedy and Truesdell, 1996; Kennedy and van Soest, 2006]. In this chapter, a brief introduction of the systematics of noble gas

geochemistry in subsurface fluids is followed by a review of the applications of noble gases as natural tracers in conventional and unconventional hydrocarbon systems and geothermal systems.

1.1. Noble Gas Systematics

Noble gases are stable and chemically inert, making them excellent tracers to fingerprint physical processes affecting geological systems [Andrews and Lee, 1979; Ballentine and O'Nions, 1994; Castro et al., 1998a; 1998b; Ozima and Podosek, 2002]. Noble gases in subsurface fluids are commonly derived from three major natural reservoirs: atmosphere, crust, and mantle.

Atmospheric noble gases enter subsurface systems through recharge water, which interacts and reaches equilibrium with the atmosphere at the water table. The air-saturated recharge water is commonly referred to as air saturated water (ASW). ASW enters the aquifer systems in the recharge area and is subsequently incorporated into the groundwater system. The noble gas composition in ASW is dependent mostly on the temperature and atmospheric pressure (altitude) of the recharge area [Weiss, 1970; 1971; Weiss and Kyser, 1978; Ozima and Podosek, 2002]. Atmospheric noble gases can also enter groundwater systems as excess air when the local water table experiences significant fluctuations [Weiss and Kyser, 1978; Heaton and Vogel, 1981]. Noble gases have been widely used in the reconstruction of paleo-temperatures based on atmospheric noble gas concentrations and assumptions on the altitude of the recharge area [e.g., Andrews and Lee, 1979; Stute and Schlosser, 1993; Aeschbach-Hertig et al., 2002; Castro and Goblet, 2003; Ma et al., 2004; Castro et al., 2007; 2012]. Interaction between ASW and other fluid phases (e.g., oil and natural gas) in subsurface environments leads to the redistribution of atmospheric noble gases [Zartman et al., 1961; Bosch and Mazor, 1988]. Because the solubilities of light noble gases (e.g., Ne) in water are lower than those of heavy noble gases (e.g., Kr and Xe),

light noble gases will preferentially go into the gas phase during a gas-water partition, while heavy noble gases tend to stay more in the liquid phase [Bosh and Mazor, 1988; Ballentine and O'Nions' 1994; Wen et al., 2017]. By contrast, heavy noble gases are more soluble in the oil phase compared to ASW, leading to enrichment of heavy noble gases in oil which is in equilibrium with ASW [Bosch and Mazor, 1988]. Thus, the analysis of atmospheric noble gas compositions in subsurface fluids allows for the identification of various types of subsurface fluids in geological systems.

Crustally produced noble gas isotopes, including $^{4}He^{*}$, $^{21}Ne^{*}$, $^{40}Ar^{*}$, $^{86}Kr^{*}$ and $^{136}Xe^{*}$ ("*" notation indicates crustal noble gases), are also commonly found in subsurface systems. The production of $^{4}He^{*}$ in crustal rocks is controlled by the radioactive decay of $^{235,238}U$ and ^{232}Th, while the production of $^{40}Ar^{*}$ is dominated by the electron capture decay of ^{40}K [Ballentine and Burnard, 2002]. Unlike $^{4}He^{*}$ and $^{40}Ar^{*}$, the production of $^{21}Ne^{*}$ is mostly from reactions between α particles from U-Th decay and O and Mg atoms in the crust [Wetherill, 1954]. Spontaneous fission of ^{238}U is the dominant mechanism that leads to production of $^{86}Kr^{*}$ and $^{136}Xe^{*}$ in crustal fluids [Ozima and Podosek, 2002]. ^{3}He in the crust is produced mostly through the thermal neutron capture of ^{6}Li [Ballentine and Burnard, 2002]. In aquifer systems, the concentration of crustal noble gases like $^{4}He^{*}$ is applied to reconstruct groundwater residence times [Torgersen and Ivey, 1985; Torgersen and Clarke, 1985; Stute et al., 1992; Castro et al., 2000; Phillips and Castro, 2003]. The elemental ratios between different crustal noble gas isotopes, e.g., $^{4}He^{*}/^{40}Ar^{*}$ and $^{21}Ne^{*}/^{40}Ar^{*}$, are direct reflections of multiple processes, including: (1) the abundance of parent elements (e.g., U, Th and K) in the reservoir/host rocks; (2) the preferential release of light noble gases (e.g., He and Ne) compared to heavy noble gases (e.g., Ar, Kr and Xe) and; (3) the elemental fractionation caused by solubility or diffusivity differences [Zartman et al., 1961; Torgersen et al., 1989;

Ballentine et al., 1994; Ballentine and O'Nions, 1994; Pinti and Marty, 1995; Solomon et al., 1996; Castro et al., 1998a; 1998b; Pinti and Marty, 2000].

A mantle component can also be present in sedimentary systems [e.g., Oxburgh et al., 1986; O'nions et al., 1993; Ballentine and O'Nions, 1992; Ma et al., 2009; Warrier et al., 2013]. Distinct He and Ne isotopic signatures (high $^{3}He/^{4}He$ and $^{20}Ne/^{22}Ne$ ratios) signal the presence of a mantle component [Ballentine, 1997; Castro et al., 2009]. A combined analysis of He and Ne isotopic ratios allows for the distinction between a primordial, solar-like signature commonly found in Ocean Island Basalts (OIBs), traditionally believed to originate deeper in the mantle and that of a Mid-Ocean Ridge Basalt (MORB) type, representative of a degassed upper-mantle [O'Nions and Oxburgh, 1983; Porcelli and Wasserburg, 1995; Moreira and Allegre, 1998; Moreira et al., 2001]. More recently, Castro et al. [2009] identified a solar-like component in deep brines in the Michigan Basin, which can be accounted for by a shallow refractory reservoir in the Archean subcontinental lithospheric mantle (SCLM).

1.2. Application of Noble Gases in Conventional and Unconventional Hydrocarbon Systems.

Conventional hydrocarbon systems are characterized by relatively high porosity and permeability in the reservoir rocks permitting the movement of hydrocarbons, and a caprock trapping hydrocarbons in the reservoir [Spencer, 1989; Schmoker, 1996]. Noble gas studies conducted in hydrocarbons systems have largely focused on conventional reservoirs, where atmospheric, crustal and mantle noble gases are transported to oil and gas reservoirs through various mechanisms [Zartman et al., 1961; Bosch and Mazor, 1988; Ballentine et al., 1991; Hiyagon and Kennedy, 1992; Pinti and Marty, 1995; Ballentine et al., 1996]. In these systems,

noble gas chemistry has been used to constrain mixing and migration of crustal fluids, as well as to quantify relative volumes and the extent of interactions between hydrocarbons and groundwater [Ballentine et al., 1991, 1996; Elliot et al., 1993; Xu et al., 1995; Ballentine and Lollar, 2002; Zhou et al., 2005].

Unlike conventional hydrocarbon systems, which act solely as a storage facility, unconventional systems (e.g., shale) act as a combination of reservoir, source and caprock simultaneously [Condon and Dyman, 2006]. Due to the absence of secondary migration (from source rock to reservoir rock), noble gas signatures in unconventional systems are less affected by external components from surrounding sedimentary basins, and likely reflect the original composition in the hydrocarbon phases. Heavy noble gases, i.e., Kr and Xe, can be absorbed by organic matter (kerogen) and therefore become enriched in shale formations [e.g., Podosek et al., 1981; Torgersen and Kennedy, 1999; Zhou et al., 2005]. Noble gas geochemistry has been applied in unconventional fields to identify genetic groups of natural gases with different sources, and the post-genetic thermal conditions of the source rock [Hunt et al., 2012]. Noble gases have also been applied to identify the sources of hydrocarbon contamination in groundwater in the vicinity of unconventional production wells in shale gas exploration areas, e.g., the Marcellus Shale and Barnett Shale [Osborn et al., 2011; Jackson et al., 2013; Darrah et al., 2014; Moritz et al., 2015; Siegel et al., 2015; Sherwood et al., 2016; Wen et al., 2016; 2017]. Although unconventional fields are traditionally considered to be closed systems, a certain level of openness has been observed in the Antrim Shale in the Michigan Basin, as evidenced by the presence of mantle noble gas signatures and thermogenic methane from greater depths than the source rock [Wen et al., 2015]. More recently, Byrne et al. [2018] and Han et al. [2020] reported external ^{4}He in the Eagle Ford shale in Texas, which further points to the open behavior of shale reservoirs.

1.3. Application of Noble Gases in Geothermal Systems

Geothermal systems are commonly associated with magmatic heat sources, which contribute to both heat and mantle noble gases [Kennedy et al., 2000]. The radioactive decay of $^{235,238}U$ and ^{232}Th is the dominating mechanism to produce both ^{4}He and heat in the earth's interior and therefore, a positive correlation between helium and heat is expected. This correlation has been observed in mid-ocean ridges, as evidenced by heat/helium ratios similar to predicted values [Lupton et al., 1999]. However, in most continental environments this theoretical correlation is absent, which was referred to as the 'heat-helium imbalance' by O'Nions and Oxburgh [1983] and Oxburgh and O'Nions [1987]. They concluded that the radioactivity associated with the ^{4}He flux in oceanic areas can only account for about 5% of the average oceanic heat flux, and thus a layered mantle model, in which the lower mantle would retain more helium than heat, was suggested to account for the imbalance between heat and helium. The ascending of mantle-derived helium and heat into the crust was suggested to be through silicate melt [Polyak and Tolstikhin, 1985], with heat being evacuated through conductive transfer and the original mantle helium composition being erased by crustal helium production [Polyak, 2005]. van Keken et al. [2001] confirmed the imbalance between heat and helium, and suggested that a radioelement-rich mantle domain, separated from the depleted mantle by a boundary layer, could be responsible for the observed imbalance, since heat would be released faster than helium from this domain. A gas-poor planet model was proposed by Anderson [1998], in which helium and other noble gases were trapped in shallow, refractory reservoirs in the upper mantle for a considerable amount of time, to explain the paradox between heat and helium. More recently, Castro et al. [2005] suggested that the heat-helium imbalance may result from the combined impact of ASW, advection, conduction and diffusion in the continental crust, rather than in the deep mantle. Mixing of fluid components from

different sources, including meteoric and ancient water, is also one of the processes behind the lack of observed correlation (e.g., Polyak, 2005; Kennedy et al, 2000).

Besides the theoretical correlation between heat and helium, noble gas geochemistry has also been applied to identify heat sources [e.g., Kennedy et al., 2000; Magro et al., 2003; Wen et al., 2018], evaluate the sources and circulation of hydrothermal fluids [e.g., Mazor and Truesdell, 1984; Kennedy and Truesdell, 1996; Kennedy and van Soest, 2006; Birkle et al., 2016; Pinti et al., 2021], and monitor the exploitation-related physical processes within reservoirs [e.g., Kennedy and Shuster, 2000; Pinti et al., 2013; 2019; Wen et al., 2018].

1.4. Dissertation Structure

In chapter 2, the first complete noble gas dataset collected from both the east and west sides of the Panhandle Field is presented. This new dataset combined with that of Ballentine and Lollar [2002] from the Hugoton Field, provides a more comprehensive overview of the composition, sources and migration of both hydrocarbons and noble gases in the conventional Panhandle-Hugoton Field (PHF) that has been previously available. PHF samples are generally enriched in terrigenic noble gases ($^{4}He^{*}$, $^{21}Ne^{*}$ and $^{40}Ar^{*}$). A strong positive correlation between terrigenic noble gases and methane in west Panhandle suggests a common origin for both gases from adjacent basins. In east Panhandle, a positive correlation between terrigenic noble gases and depth points to a dominant upward noble gas flux from underlying rocks. The presence of a primordial mantle He-Ne component in east Panhandle and mantle helium in west Panhandle suggest an open behavior of the system. A groundwater accumulation model is also suggested based on the combined analysis of Ar relative ages and estimated water/gas volume ratios to explain the enrichment of terrigenic noble gases in the PHF.

Chapter 3 presents a complete noble gas dataset collected in the oil zone of the Eagle Ford Shale. This dataset is combined with that of Byrne et al. [2018] and noble gas information from Harrington et al. [2015] to explore the tectonic and magmatic history of the region, as well as to characterize of the shale reservoir. Noble gas analyses reveal the presence of two distinct mantle components: a primordial, solar-like component corresponding to an OIBs-like signature, and a component corresponding to a MORB signature. A pure crustal component is also observed in the southern part of the shale play. The MORB signature is likely representative of the Ouachita Rift during the breakup of Rodinia, while the OIBs-like signature is consistent with an origin in the SCLM, possibly from the shallow refractory reservoir beneath the Balcones Igneous Province. Ar relative ages display significant variations in the Eagle Ford samples, suggesting a highly developed compartmentalization within the shale reservoir and the presence of different hydrocarbon sources.

Chapter 4 presents a combined dataset of published and newly collected data on heat and volatile species, primarily He, Ar but also CO_2, from six geothermal reservoirs in Mexico. This study focuses on the identification of heat and volatile sources, the evaluation of the heat distribution, and assessment of mixing among different fluid sources. The R/Ra ratios (where R is the measured $^3He/^4He$ ratio and Ra is the atmospheric ratio) in geothermal samples reflect characteristics of local tectonic settings, with high R/Ra ratios (7.14-7.27) in the Trans-Mexican Volcanic Belt corresponding to younger, active magmatic heat sources, while the low R/Ra ratios (1.21-6.62) in Baja California point to crustal contributions from the subducted Farallon plate. The analysis of heat/He and noble gas ratios reveal that the transfer of heat and helium are dominated by convection. Boiling and dilution by meteoric water led to further fractionation of heat and

volatiles. This study also discusses the mechanisms behind the absence of signification fractionation between CO_2 and ^3He in geothermal samples.

A summary of the major results and conclusions of this dissertation are provided in chapter 5. This dissertation is relevant to studies of hydrocarbon (conventional and unconventional) reservoirs and geothermal sysyems. Chapter 2 contributes to a better understanding of noble gas geochemistry in permeable reservoirs and the mechanisms behind the migration and accumulation of hydrocarbons and noble gases. Chapter 3 contributes to the characterization of low-permeability shale reservoirs that has been influenced from past tectonic and magmatic events. Results in chapter 4 contributes to a better understanding of the sources, mixing and evolution of heat and volatile species in geothermal systems. This dissertation has important implications to the fields of petroleum geology, hydrology, and geothermal research.

1.5. References

AbuAisha, M., Loret, B., and Eaton, D. (2016). Enhanced Geothermal Systems (EGS): Hydraulic fracturing in a thermo-poroelastic framework. *Journal of Petroleum Science and Engineering* 146. 1179–1191, doi:10.1016/j.petrol.2016.07.027

Aeschbach-Hertig, W., Stute, M., Clark, J. F., Reuter, R. F., and Schlosser, P. (2002). A paleotemperature record derived from dissolved noble gases in groundwater of the Aquia Aquifer (Maryland, USA). *Geochimica et Cosmochimica Acta* 66(5), 797–817.

Anderson, D.L. (1998). A model to explain the various paradoxes associated with mantle noble gas geochemistry. *Proceedings of the National Academy of Sciences* 95, 9087– 9092.

Andrews, J. N., and Lee, D. J. (1979). Inert gases in groundwater from the Bunter Sandstone of England as indicators of age and palaeoclimatic trends. *Journal of Hydrology* 41(3–4), 233–252, doi:10.1016/0022-1694(79)90064-7.

Ballentine, C. J., O'Nions, R. K., Oxburgh, E. R., Horvath, F., and Deak, J. (1991). Rare gas constraints on hydrocarbon accumulation, crustal degassing and groundwater flow in the Pannonian Basin. *Earth and Planetary Science Letters* 105, 229–246.

Ballentine, C. J., and O'Nions, R. K. (1992). The nature of mantle neon contributions to Vienna Basin hydrocarbon reservoirs. *Earth and Planetary Science Letters* 113, 553–567.

Ballentine, C. J., Mazurek, M., and Gautschi, A. (1994). Thermal constraints on crustal rare gas release and migration: Evidence from Alpine fluid inclusions. *Geochimica et Cosmochimica Acta* 58(20), 4333–4348.

Ballentine, C. J., and O'nions, R. K. (1994). The use of natural He, Ne and Ar isotopes to study hydrocarbon-related fluid provenance, migration and mass balance in sedimentary basins. *Geological Society, London, Special Publications* 78(1), 347–361, doi:10.1144/GSL.SP.1994.078.01.23.

Ballentine C. J., O'Nions R. K., and Coleman M. L. (1996). A Magnus opus: Helium, neon, and argon isotopes in a North Sea oilfield. *Geochimica et Cosmochimica Acta* 60, 831-849.

Ballentine, C. J. (1997). Resolving the mantle He/Ne and crustal 21Ne/22Ne in well gases. *Earth and Planetary Science Letters* 152, 233-249.

Ballentine, C. J., and Burnard, P. G. (2002). Production, release and transport of noble gases in the continental crust. *Reviews in Mineralogy and Geochemistry* 47, 481-538.

Ballentine, C.J., and Sherwood Lollar, B. (2002). Regional groundwater focusing of nitrogen and noble gases into the Hugoton-Panhandle giant gas field, USA. *Geochimica et Cosmochimica Acta* 66, 2483–2497. doi:10.1016/S0016-7037(02)00850-5.

Birkle, P., Portugal Marín, E., Pinti, D.L., and Castro, M.C. (2016). Origin and evolution of geothermal fluids fromLas Tres Vírgenes and Cerro Prieto fields, Mexico - Co-genetic volcanic activity and paleoclimatic constraints. *Applied Geochemistry* 65, 36–53.

Bosch, A., and Mazor, E. (1988). Natural gas association with water and oil as depicted by atmospheric noble gases: case studies from the southeastern Mediterranean Coastal Plain. *Earth Planetary Science Letters* 87, 338-346.

Burnard, P. ed. (2013). The Noble Gases as Geochemical Tracers. pp. 1-391, New York: Springer.

Byrne D. J., Barry P. H., Lawson M., and Ballentine C. J. (2018). Determining gas expulsion vs retention during hydrocarbon generation in the Eagle Ford Shale using noble gases. *Geochimica et Cosmochimica Acta* 241, 240-254.

Castro, M. C., Jambon, A., Marsily, G. d., and Schlosser, P. (1998a) Noble gases as natural tracers of water circulation in the Paris Basin. 1. Measurements and discussion of their origin and mechanisms of vertical transport in the basin. *Water Resource Research* 34, 2443-2466.

Castro, M. C., Goblet, P., Ledoux, E., Violette, S., and Marsily, G. d. (1998b). Noble gases as natural tracers of water circulation in the Paris Basin. 2. Calibration of a groundwater flow model using noble gas isotope data. *Water Resource Research* 34, 2467-2483.

Castro, M. C., Stute, M., and Schlosser, P. (2000). Comparison of ^{4}He ages and ^{14}C ages in simple aquifer systems: implications for groundwater flow and chronologies. *Applied Geochemistry* 15(8), 1137–1167, doi:10.1016/S0883-2927(99)00113-4.

Castro, M. C., and Goblet, P. (2003). Noble gas thermometry and hydrologic ages: evidence for late Holocene warming in Southwest Texas. *Geophysical Research Letters* 30(24), 2251, doi:10.1029/2003GL018875.

Castro, M. C., Patriarche, D., and Goblet, P. (2005). 2-D numerical simulations of groundwater flow, heat transfer and 4He transport—implications for the He terrestrial budget and the mantle helium–heat imbalance. *Earth and Planetary Science Letters* 237(3), 893–910. doi:10.1016/j.epsl.2005.06.037.

Castro, M. C., Hall, C. M., Patriarche, D., Goblet, P., and Ellis, B. R. (2007). A new noble gas paleoclimate record in Texas—Basic assumptions revisited. *Earth and Planetary Science Letters* 257(1), 170–187.

Castro, M. C., Ma, L., and Hall, C. M. (2009). A primordial, solar He-Ne signature in crustal fluids of a stable continental region. *Earth and Planetary Science* Letters 279, 174-184.

Castro, M. C., Warrier, R. B., Hall, C. M., and Lohmann, K. C. (2012). A late Pleistocene–Mid-Holocene noble gas and stable isotope climate and subglacial record in southern Michigan. *Geophysical Research Letters* 39, L19709. doi:10.1029/2012GL053098.

Condon, S. M., and Dyman, T. S. (2006). 2003 Geologic assessment of undiscovered conventional oil and gas resources in the upper Cretaceous Navarro and Taylor groups, Western Gulf Province, Texas. In Petroleum System and Geological Assessment of Undiscovered Oil

and Gas, Navarro and Taylor Groups, Western Gulf Province, Texas. U.S. Geological Survey.

COP-21 (2015). Paris agreement. United Nations Framework Convention on Climate Change, Conference of the Parties 21.

Darrah T. H., Vengosh A., Jackson R. B., Warner N. R., and Poreda R. J. (2014). Noble gases identify the mechanisms of fugitive gas contamination in drinking-water wells overlying the Marcellus and Barnett Shales. *Proceedings of the National Academy of Sciences*. 111, 14076-14081.

Dickson, M. H., and Fanelli, M. (2003). *Geothermal energy: utilization and technology*. pp. 1-225, Routledge.

EIA (2021). Annual Energy outlook 2021. US Energy Information Administration.

Elliot, T., Ballentine, C. J., O'nions, R. K., and Ricchiuto, T. (1993). Carbon, helium, neon and argon isotopes in a Po basin (northern Italy) natural gas field. *Chemical Geology*, 106(3-4), 429–440. doi:10.1016/0009-2541(93)90042-H.

Han, G., Castro, M.C., Hall, C.M., Larson, T.E., and Nicot, J.-P. (2021). MORB and solar-OIB like noble gas signatures in the Eagle Ford Shale, southwest Texas – Implications for the earth's geological evolution and framework. American Geophysical Union Fall Meeting, New Orleans, LA, USA. 13-17 December, 2021. American Geophysical Union.

Heaton, T. H. E., and Vogel, J. C. (1981). "Excess air" in groundwater. *Journal of Hydrology* 50(0), 201–216. doi:10.1016/0022-1694(81)90070-6.

Hiyagon, H., and Kennedy, B. M. (1992). Noble gases in CH4-rich gas fields, Alberta, Canada, *Geochimica et Cosmochimica Acta*, 56(4), 1569–1589. doi:10.1016/0016-7037(92)90226-9.

Hunt, A. G., Darrah, T. H., and Poreda, R. J. (2012). Determining the source and genetic fingerprint of natural gases using noble gas geochemistry: A northern Appalachian Basin case study. *AAPG Bulletin*, 96(10), 1785–1811, doi:10.1306/03161211093.

IPCC (2021). Climate Change 2021: the Physical Science Basis. Working Group I, Intergovernmental Panel on Climate Change.

IRENA (2017). Geothermal Power: Technology Brief. International Renewable Energy Agency, Abu Dhabi.

Jackson, R. B., Vengosh, A., Darrah, T. H., Warner, N. R., Down, A., Poreda, R. J., Osborn, S. G., Zhao, K., and Karr, J. D. (2013). Increased stray gas abundance in a subset of drinking water wells near Marcellus shale gas extraction. *Proceedings of the National Academy of Sciences* 110(28), 11250–11255. doi:10.1073/pnas.1221635110/-/DCSupplemental/pnas.201221635SI.pdf.

Kennedy, B. M., and Truesdell, A. H. (1996). The northwest geysers high-temperature reservoir: evidence for active magmatic degassing and implications for the origin of the Geysers geothermal field. *Geothermics* 25, 365–387.

Kennedy, B.M., Fischer, T.P., and Schuster, D.L. (2000). Heat and helium in geothermal systems. Twenty-Fifth Workshop on Geothermal Reservoir Engineering. SGP-TR-165. Stanford University, Stanford, California, p. 5.

Kennedy, B.M., and Shuster, D.L. (2000) Noble Gases: sensitive natural tracers for detection and monitoring lnjectate returns to geothermal reservoirs. *Geothermal Resources Council Transactions* 24, 247-252.

Kennedy, B. M., and van Soest, M.C. (2006). A helium isotope perspective on the Dixie Valley, Nevada, hydrothermal system. *Geothermics* 35, 26–43.

Lupton, J.E., Baker, E.T., and Massoth, G. J. (1999). Helium, heat, and the generation of hydrothermal event plumes at mid-ocean ridges. *Earth and Planetary Science Letters* 171, 343–350. DOI: 10.1016/S0012-821X(00)00150-3

Ma, L., Castro, M. C., and Hall, C. M. (2004). A late Pleistocene–Holocene noble gas paleotemperature record in southern Michigan. *Geophysical Research Letters* 31(23), L23204. doi:10.1029/2004GL021766.

Ma, L., Castro, M. C., and Hall, C. M. (2009). Atmospheric noble gas signatures in deep Michigan Basin brines as indicators of a past thermal event. *Earth and Planetary Science Letters* 277(1–2), 137–147. doi:10.1016/j.epsl.2008.10.015.

Magro, G., Ruggieri, G., Gianelli, G., Bellani, S., and Scandiffio, G. (2003). Helium isotopes in paleofluids and present-day fluids of the Larderello geothermal field: Constraints on the heat source. *Journal of Geophysical Research* 108, ECV 3-1 – 3-12. DOI:10.1029/2001JB001590

Mazor, E., and Truesdell, A. (1984). Dynamics of a geothermal field traced by noble gases: Cerro Prieto, Mexico. *Geothermics* 13, 91–102.

Moreira, M., and Allegre, C. J. (1998). Helium-neon systematics and the structure of the mantle. *Chemical Geology* 147, 53–59.

Moreira, M., Breddam, K., Curtice, J., and Kurz, M. D. (2001). Solar neon in the Icelandic mantle: new evidence for an undegassed lower mantle. *Earth and Planetary Science Letters* 185, 15–23. doi:10.1016/S0012-821X(00)00351-4

Moritz, A., Helie, J.-F., Pinti, D. L., Larocque, M., Barnetche, D., Retailleau, S., Lefebvre, R., and Gelinas, Y. (2015). Methane Baseline Concentrations and Sources in Shallow Aquifers from the Shale Gas-Prone Region of the St. Lawrence Lowlands (Quebec, Canada), *Environmental Science and Technology* 49(7), 4765–4771. doi:10.1021/acs.est.5b00443.

O'Nions, R. K., and Oxburgh, E. R. (1983) Heat and helium in the Earth. *Nature*. 306, 429-431.

O'nions, R. K., Ballentine, C. J., Halliday, A., McKenzie, D. P., and Coleman, M. L. (1993). Rare Gas Studies of Basin Scale Fluid Movement [and Discussion]. *Philosophical Transactions: Physical Sciences and Engineering* 344(1670), 141–156.

Osborn, S. G., Vengosh, A., Warner, N. R., and Jackson, R. B. (2011). Methane contamination of drinking water accompanying gas-well drilling and hydraulic fracturing. *Proceedings of the National Academy of Sciences* 108(20), 8172–8176. doi:10.1073/pnas.1100682108.

Oxburgh, E. R., O'nions, R. K., and Hill, R. I. (1986). Helium isotopes in sedimentary basins. *Nature* 324(6098), 632–635. doi:10.1038/324632a0.

Oxburgh, E.R., and O'Nions, R.K. (1987). Helium loss, tectonics, and terrestrial heat budget, Science 237, 1583-1588.

Ozima, M., and Podosek, F. A. (2002). *Noble gas geochemistry*. Cambridge University Press.

Phillips, F. M., and Castro, M. C. (2003). 5.15 - Groundwater Dating and Residence-time Measurements, in *Treatise on Geochemistry* (eds. H. D. Holland and K. K. Turekian). pp. 451–497, Pergamon, Oxford.

Pinti, D. L., and Marty B. (1995). Noble gases in crude oils from the Paris Basin, France: Implications for the origin of fluids and constraints on oil-water-gas interactions, *Geochimica et Cosmochimica Acta* 59(16), 3389–3404, doi:10.1016/0016-7037(95)00213-J.

Pinti, D. L., and Marty, B. (2000). Chapter 7. Noble Gases in Oil and Gas Fields: Origins and Processes, in *Fluids and Basin Evolution* 28, pp. 160–196.

Pinti, D.L., Castro, M.C., López-Hernández, A., Hernández-Hernández, M.A., Shouakar-Stash, O., Hall, C.M., Bahena-Romero, J., and Ramírez-Montes, M. (2021). Origin of volatile species and aqueous fluids in the Los Humeros Geothermal Field, Mexico. *Chemical Geology* 584, 120539. doi:10.1016/j.chemgeo.2021.120539.

Podosek, F. A., Bernatowicz, T. J., and Kramer, F. E. (1981). Adsorption of xenon and krypton on shales. *Geochimica et Cosmochimica Acta* 45(12), 2401–2415. doi:10.1016/0016-7037(81)90094-6.

Polyak, B.G., and Tolstikhin, I.N. (1985). Isotopic composition of the Earth's helium and the motive forces of tectogenesis. *Chemical Geology* 52, 9-33.

Polyak, B.G. (2005). Heat and mass transfer from the mantle: heat flow and He-isotope constraints. *Annals of Geophysics* 48, 9-17.

Porcelli, D., and Wasserburg, G. J. (1995). Mass transfer of helium, neon, argon, and xenon through a steady-state upper mantle. *Geochimica et Cosmochimica Acta* 59, 4921-4937.

Prinzhofer, A. (2013). Noble Gases in Oil and Gas Accumulations, in *The Noble Gases as Geochemical Tracers* (ed. Burnard, P.). 225–247, doi:10.1007/978-3-642-28836-4_9.

Schmoker, J. W. (1996). A Resource evaluation of the Bakken Formation (upper Devonian and lower Mississippian) continuous oil accumulation, Williston Basin, North Dakota and Montana. *The Mountain Geologists* 33, 1-10.

Sherwood, O. A., Rogers, J. D., Lackey, G., Burke, T. L., Osborn, S. G., and Ryan, J. N. (2016). Groundwater methane in relation to oil and gas development and shallow coal seams in the Denver-Julesburg Basin of Colorado. *Proceedings of the National Academy of Sciences* 113(30), 8391–8396.

Siegel, D. I., Azzolina, N. A., Smith, B. J., Perry, A. E., and Bothun, R. L. (2015). Methane Concentrations in Water Wells Unrelated to Proximity to Existing Oil and Gas Wells in Northeastern Pennsylvania. *Environmental Science and Technology* 49(7), 4106–4112, doi:10.1021/es505775c.

Smil, V. (2015). *Natural gas: fuel for the 21st century*. pp. 1-264, Wiley.

Solomon, D. K., Hunt, A., and Poreda, R. J. (1996). Source of radiogenic helium 4 in shallow aquifers: Implications for dating young groundwater. *Water Resources Research* 32(6), 1805–1813. doi:10.1029/96WR00600.

Spencer, C. W. (1989). Review of characteristics of low-permeability gas reservoirs in western United States. *AAPG Bulletin* 73, 613-629.

Staffell, I. (2017). Measuring the progress and impacts of decarbonizing British electricity. E*nergy Policy* 102. 463–475.

Stute, M., Sonntag, C., Déak, J., and Schlosser, P. (1992). Helium in deep circulating groundwater in the Great Hungarian Plain: flow dynamics and crustal and mantle helium fluxes. *Geochimica et Cosmochimica Acta* 56(5), 2051–2067.

Stute, M., and Schlosser, P. (1993). Principles and applications of the noble gas paleothermometer, in *Climate Change in Continental Isotopic Records* (eds. P. K. Swart et al.) 78, 89–100. AGU.

Torgersen, T., and Clarke, W. B. (1985). Helium accumulation in groundwater, I: An evaluation of sources and the continental flux of crustal 4He in the Great Artesian Basin, Australia, *Geochimica et Cosmochimica Acta* 49(5), 1211–1218, doi:10.1016/0016-7037(85)90011-0.

Torgersen, T., and Ivey, G. N. (1985). Helium accumulation in groundwater. II: A model for the accumulation of the crustal 4He degassing flux. *Geochimica et Cosmochimica Acta* 49(11), 2445–2452, doi:10.1016/0016-7037(85)90244-3.

Torgersen, T., Kennedy, B. M., Hiyagon, H., Chiou, K. Y., Reynolds, J. H., and Clarke, W. B. (1989). Argon accumulation and the crustal degassing flux of40Ar in the Great Artesian Basin, Australia. *Earth and Planetary Science Letters* 92(1), 43–56.

Torgersen, T., and Kennedy, B. M. (1999). Air-Xe enrichments in Elk Hills oil field gases: role of water in migration and storage. *Earth and Planetary Science Letters* 167(3–4), 239–253, doi:10.1016/S0012-821X(99)00021-7.

van der Zwaan, B., and Dalla Longa, F. (2019). Integrated assessment projections for global geothermal energy use. *Geothermics* 82, 203–211. doi:10.1016/j.geothermics.2019.06.008

van Keken, P.E., Ballentine, C.J., Porcelli, D. (2001). A dynamical investigation of the heat and helium imbalance. *Earth and Planetary Science Letters* 188, 421– 434.

Warrier, R. B., Castro, M. C., Hall, C. M., Lohmann, K. C. (2013). Large atmospheric noble gas excesses in a shallow aquifer in the Michigan Basin as indicators of a past mantle thermal event. *Earth and Planetary Science Letters* 375, 372-382.

Weiss, R. F. (1970). The solubility of nitrogen, oxygen and argon in water and seawater. *Deep Sea Research and Oceanographic Abstracts* 17(4), 721–735. doi:10.1016/0011-7471(70)90037-9.

Weiss, R. F. (1971). Solubility of helium and neon in water and seawater, *Journal of Chemical and Engeering Data* 16(2), 235–241. doi:10.1021/je60049a019.

Weiss, R. F., and Kyser, T. K. (1978). Solubility of krypton in water and sea water. *Journal of Chemical and Engeering Data* 23(1), 69–72.

Wen, T., Castro, M. C., Ellis, B. R., Hall, C. M., and Lohmann, K. C. (2015). Assessing compositional variability and migration of natural gas in the Antrim Shale in the Michigan Basin using noble gas geochemistry. *Chemical Geology* 417, 356-370.

Wen, T., Castro, M. C., Nicot, J. P., Hall, C. M., Larson, T., Mickler, P., and Darvari, R. (2016). Methane sources and migration mechanisms in shallow groundwaters in Parker and Hood counties, Texas - A Heavy Noble Gas Analysis. *Environmental Science and Technology* 50, 12012-12021.

Wen, T., Castro, M. C., Nicot, J. P., Hall, C. M., Pinti, D. L., Mickler P., Darvari R., and Larson T. (2017). Characterizing the noble gas isotopic composition of the Barnett Shale and Strawn Group and constraining the source of stray gas in the trinity aquifer, North-Central Texas. *Environmental Science and Technology* 51, 6533-6541.

Wen, T., Pinti, D.L., Castro, M.C., López-Hernández, A., Hall, C.M., Shouakar-Stash, O., and Sandoval-Medina, F. (2018). A noble gas and $^{87}Sr/^{86}Sr$ study in fluids of the Los Azufres geothermal field, Mexico – Assessing impact of exploitation and constraining heat sources. *Chemical Geology* 483, 426–441. doi:10.1016/j.chemgeo.2018.03.010.

Wetherill, G.W. (1954). Variations in the isotopic abundances of neon and argon extracted from radioactive minerals. *Physical Review* 96, 679-683.

Wilson, I. A. G., and Staffell, I. (2018). Rapid fuel switching from coal to natural gas through effective carbon pricing. *Nature Energy* 3, 365–372, doi:10.1038/s41560-018-0109-0

Xu, S., Nakai, S., Wakita, H., and Wang, X. (1995). Mantle-derived noble gases in natural gases from Songliao Basin, China. *Geochimica et Cosmochimica Acta* 59(22), 4675–4683. doi:10.1016/0016-7037(95)00301-0.

Zartman, R. E., Wasserburg, G. J., and Reynolds, J. H. (1961). Helium, argon, and carbon in some natural gases. *Journal of Geophysical Research* 66, 277-306.

Zhao, Y., Feng, Zijun, Feng, Zengchao, Yang, D., and Liang, W. (2015). THM (Thermo-hydro-mechanical) coupled mathematical model of fractured media and numerical simulation of a 3D enhanced geothermal system at 573 K and buried depth 6000–7000 M. *Energy* 82, 193–205. doi:10.1016/j.energy.2015.01.030

Zhou, Z., and Ballentine, C J. (2006). ^{4}He dating of groundwater associated with hydrocarbon reservoirs. *Chemical Geology* 226, 309–327. doi:10.1016/j.chemgeo.2005.09.030.

Zhou, Z., Ballentine, C. J., Kipfer, R., Schoell, M., and Thibodeaux, S. (2005). Noble gas tracing of groundwater/coalbed methane interaction in the San Juan Basin, USA. *Geochimica et Cosmochimica Acta* 69(23), 5413–5428. doi:10.1016/j.gca.2005.06.027.

CHAPTER 2

Tracing the Origin, Migration and Mixing of Noble Gases and Methane in the Panhandle-Hugoton Field, Texas, United States

Abstract

The Panhandle-Hugoton Field (PHF) is the largest conventional gas field in North America and a major helium producer. The PHF consists of two major production blocks: the Panhandle Field in Texas and the Hugoton Field spanning northwest Texas, Oklahoma, and Kansas. Despite its long-term exploitation, questions remain with respect its sources of helium and hydrocarbon as well as its hydrocarbon migration history. Here, we present the first complete dataset of stable noble gases for gas samples collected from twelve producing wells in both the east and west side of the Panhandle Field. The goal is to investigate the composition, sources and migration of both hydrocarbons and noble gases in the PHF. This new dataset combined with that of Ballentine and Lollar [2002] from the Hugoton Field, further north, provides a more comprehensive overview of this system.

PHF samples are generally enriched in terrigenic noble gases ($^{4}He^{*}$, $^{21}Ne^{*}$ and $^{40}Ar^{*}$). A strong positive correlation between terrigenic noble gases ($^{4}He^{*}$ and $^{21}Ne^{*}$) and methane in west Panhandle suggests a common origin for both gases. Both may have originated from adjacent basins to the west, i.e., the Palo Duro and Dalhart basins and been subsequently delivered by groundwater of the deep-basin brine aquifer to west Panhandle. In east Panhandle, a positive

correlation between terrigenic noble gases and depth is observed, and points to a dominant upward noble gas flux from underlying rocks. A combined He-Ne analysis reveals the presence of a primordial mantle component with an Ocean Island Basalts (OIBs)-like signature in east Panhandle. The latter has likely originated from a mantle plume related to the Wichita Igneous Province. However, an origin in the subcontinental lithospheric mantle (SCLM) cannot be ruled out. The west Panhandle samples display both air-corrected helium isotopic ratios higher (0.1008-0.1145) than typical crustal values and CO_2 contents higher than those in east Panhandle, suggesting contribution originates in the Bravo Dome field.

A positive correlation between $^{4}He^{*}/^{40}Ar^{*}$ and $^{21}Ne^{*}/^{40}Ar^{*}$ is observed and points to a solubility-controlled fractionation from the average and lower crustal components, suggesting an external input from crustal sources. A first-order estimation of in-situ $^{4}He^{*}$ and $^{40}Ar^{*}$ production suggests that in-situ production across the PHF accounts for a minor portion of the total crustal noble gases. In the west Panhandle and Hugoton Fields these contributions vary from 5.11% to 21.76% for $^{4}He^{*}$, and from 9.15% to 26.46% for $^{40}Ar^{*}$. These are higher in east Panhandle Field and vary from 28.53% to 65.46% for $^{4}He^{*}$, and from 21.22% to 78.79% for $^{40}Ar^{*}$. ^{40}Ar relative ages are increasingly older from east Panhandle to Kansas Hugoton to west Panhandle, Texas and Oklahoma Hugoton. More interaction with groundwater in West Panhandle, Texas and Oklahoma Hugoton gas results in higher Vw/Vg ratios and also higher concentrations of terrigenic noble gases, likely brought by groundwater from west adjacent areas, in particular, from the Dalhart and Palo Duro basins. The relatively low Vw/Vg ratios and terrigenic noble gas contents in east Panhandle samples are consistent with the shortest migration distance, youngest migration ages and absence of significant groundwater flow in this area.

2.1. Introduction

Discovered in 1918, the Panhandle-Hugoton Field (PHF) is the largest conventional natural gas field in North America, with a production area exceeding 20000 km^2 [Pippin, 1970; Ruppel and Garett, 1989; Dubois et al., 2007]. This reservoir sits on the Wolfcampian Stage carbonates and the Granite Wash, a liquid-rich tight sands play, and extends from north Texas, through Oklahoma and into southern Kansas. The field is also a global primary commercial helium producer due to the high helium concentration, which reaches 1.9-2.2 % [Pippin, 1970; Rice, 1988; Brown, 2010]. However, due to its complex tectonic setting and geological history, questions remain in relation to the sources of this major helium reservoir [Anderson and Hinson, 1951; Boone, 1958; Rice, 1988; Brown, 2019]. Early studies suggested that the overlying Permian uranium-rich evaporite formations provided the high helium amounts to the PHF [e.g., Pierce 1964]. These evaporite formations alone, however, are not sufficient to produce the amount of helium enrichment observed in the field [Ballentine and Lollar, 2002; Brown, 2019]. Ballentine and Lollar [2002] proposed a groundwater helium accumulation model in which the excess helium was assumed to have been collected by groundwater flow from adjacent sedimentary basins to account for the observed helium content (e.g., Dalhart Basin and Palo Duro Basin). More recently, Brown [2019] estimated that approximately 40% of the helium in the field is associated with groundwater flow, with the remaining 60% coming from formations underlying the PHF reservoirs. However, these studies did not focus on specific helium sources and their locations with respect to the PHF.

Hydrocarbon migration patterns and sources within the PHF are other aspects requiring clarification. Source rocks are absent from the PHF and the Anadarko Basin, to the east, has traditionally been assumed to be the hydrocarbon provider [Rice, 1988; Burrus and Hatch, 1989;

Ball et al., 1991; Sorenson, 2005]. However, the possibility that hydrocarbon phases originating in organic-rich rocks in adjacent basins such as the Palo Duro Basin are present, has not been the subject of an in-depth analysis [Dutton, 1980a, b; Rose, 1986]. This has exacerbated our lack of understanding of connectivity levels between local tectonic units, regional groundwater flow in the area and how these affect this petroleum system. To date, comprehensive noble gas studies have primarily focused on the Hugoton reservoir [Ballentine and Lollar, 2002]. No complete noble gas dataset has been collected in the Panhandle reservoir that might provide further constraints on some of the issues discussed above.

Noble gas geochemistry has long been used to trace groundwater, oil and gas in sedimentary systems [Zartman et al, 1961; Bosch and Mazor, 1988; Ballentine et al., 1991; Pinti and Marty, 1995; Castro et al., 1998a, b; Castro et al., 2005; Patriarche et al., 2004; Warrier et al., 2012; Prinzhofer, 2010]. Stable noble gases (He, Ne, Ar, Kr, Xe) are chemically inert and are thus transported by crustal fluids without being affected by chemical reactions [Ozima and Podosek, 2002]. Noble gases in subsurface fluids are derived from the atmosphere, the crust, and the mantle, all of which show distinct isotopic and elemental signatures [Castro et al., 1998a, b; Ballentine et al., 2002; Hilton and Porcelli, 2003]. In most subsurface fluids within sedimentary systems, noble gases are dominated by an atmospheric (Air Saturated Water or ASW) and/or a crustal component derived primarily from radioactive decay of $^{235,238}U$, ^{232}Th and ^{40}K [Torgersen et al., 1989; Ballentine and Burnard, 2002; Ma et al., 2009; Sun et al., 2010; Hall et al., 2012; Aeschbach-Hertig and Solomon, 2013]. Noble gases are thus source-specific and time-dependent rendering them ideal natural tracers for studying the origin and evolution of crustal fluids. Although less common and abundant in sedimentary systems, noble gases originating from the mantle can also be present [Ballentine and O'Nions, 1992; Ma et al., 2009; Warrier et al., 2013]. In particular, the

presence of excess ^{3}He compared to ^{4}He with respect to the atmosphere is a good indicator of mantle volatiles in crustal environments [e.g., Marty et al, 1992; Kennedy and van Soest, 2007]. Mantle neon can also be resolvable in crustal fluids as shown in natural gases in the Vienna Basin [e.g., Ballentine and O'Nions, 1992] and in groundwater in the Michigan Basin [e.g., Castro et al., 2009]. A combined analysis of He and Ne isotopic ratios allows for the distinction between a primordial, solar-like signature commonly found in Ocean Island Basalts (OIBs), believed to originate deeper in the mantle, and that of a Mid-Ocean Ridge Basalt (MORB) type, representative of a degassed upper-mantle [O'Nions and Oxburgh, 1983; Porcelli and Wasserburg, 1995; Moreira and Allegre, 1998; Moreira et al., 2001]. A shallow refractory reservoir in the subcontinental lithospheric mantle (SCLM) was also suggested to account for the presence of a primordial component [Castro et al., 2009].

Noble gas studies have been conducted in conventional oil and gas fields for many decades [Zartman et al., 1961; Bosch and Mazor, 1988; Ballentine et al., 1991; Hiyagon and Kennedy, 1992; Pinti and Marty, 1995; Ballentine et al., 1996; Barry et al., 2017; Byrne et al., 2020]. These studies have focused on fluid sources and their migration, estimation of residence times as well as identification of interconnectivity between different hydrocarbon reservoirs. In conventional systems, hydrocarbons undergo extensive interaction with groundwater, which ultimately affects their noble gas signatures. The use of noble gases to estimate the distance and pattern of secondary migration based on oil-gas-water interactions was proposed early on by Zartman et al. [1961] and Bosch and Mazor [1988], and later refined by Byrne et al. [2018; 2020]. However, studies focusing on understanding the sources of major natural helium reserves remain scarce [Ballentine and Lollar, 2002; Hilton et al., 2012; Kimani et al., 2021].

Because of their characteristics and physical properties, noble gases are also excellent tools to complement tectonic studies in complex and poorly understood tectonic settings [e.g., Hoke et al., 2000; Castro et al., 2009; Klemperer et al., 2013]. Noble gases can provide clarification on the tectonic and geological history of a region by identifying and constraining the location of major tectonic structures, including rifts, faults and fracture networks in addition to identifying past magmatic activity. Here, we present two complete noble gas data sets collected on the east and west side of the Panhandle reservoir in Texas. Significant differences in noble gases and major gas compositions are apparent between these two datasets and point to distinct sources of both noble gases, methane and CO_2 on either side of the field. The noble gas dataset on the eastern side of the Panhandle points to the presence of an OIB-type signature and provides further constraints on the tectonic history of this area. Our two noble gas datasets in the Panhandle together with that of Ballentine and Lollar [2002] collected in the Hugoton reservoir to the north of our sampling area, allow for a more general understanding of the sources, migration and impact of groundwater on the giant Panhandle – Hugoton Field (PHF).

2.2. Regional Settings

2.2.1. Geological Background

The Panhandle-Hugoton Field consists of two major production blocks: the Panhandle Field, along an east-west direction in northern Texas, and the Hugoton Field extending along a north-south direction, occupying parts of northern Texas, Oklahoma and Kansas (Fig. 2.1). The production area of the Panhandle Field generally coincides with the extent of the Amarillo Uplift, while the Hugoton Field extends further north (Fig. 2.1).

The PHF is located in a complex geological setting with a tectonic history since the Paleoproterozoic, and an age of at least 1.6 Ga. The basement rock underneath the PHF belongs to the Mazatzal and Southern Yavapai Provinces [1.7-1.6 Ga; Van Schmus et al., 1987]. During the Mesoproterozoic), subduction of Laurentia towards the northwest led to partial deformation of the crust and the formation of Rodinia [~1.3 – 1.0 Ga, Grenville orogeny; Thomas 2005; Chiarenzelli et al., 2010]. In late Proterozoic (~800 - 650 Myrs), Rodinia began to breakup leading to several failed rifts [Salvador, 1991; Adams, 1993; Dehler, 1998] and transform fault zones in the area [Thomas, 1991, 2005; Jacques and Clegg, 2002]. During the continental rifting event and the opening of the Iapetus Ocean, a series of igneous provinces formed in the southern Laurentia craton, including the ~540 Ma old Wichita Igneous Province (WIP) within the Southern Oklahoma Aulacogen (Fig. 2.1)

Following the breakup of the Rodinia, from late Cambrian to early Carboniferous, the majority of the current PHF was part of the Oklahoma Basin, an epicontinental sea [Pippin, 1970; Johnson et al., 1988a]. The current major geological units, including the Wichita and Amarillo Uplifts, the Anadarko, Dalhart and Palo Duro Basins and the Cimmaron Arch (Fig. 2.1), were all part of the ancient Oklahoma Basin and accumulated similar sedimentary deposits during this period [Pippin, 1970, Rice, 1988]. Extensive carbonates with shale and sandstone interbeds, including the organic-rich Woodford shale (Fig. 2.2), were widely distributed throughout the region, but later eroded in the PHF area by tectonic activity [Pippin, 1970; Johnson et al., 1988b].

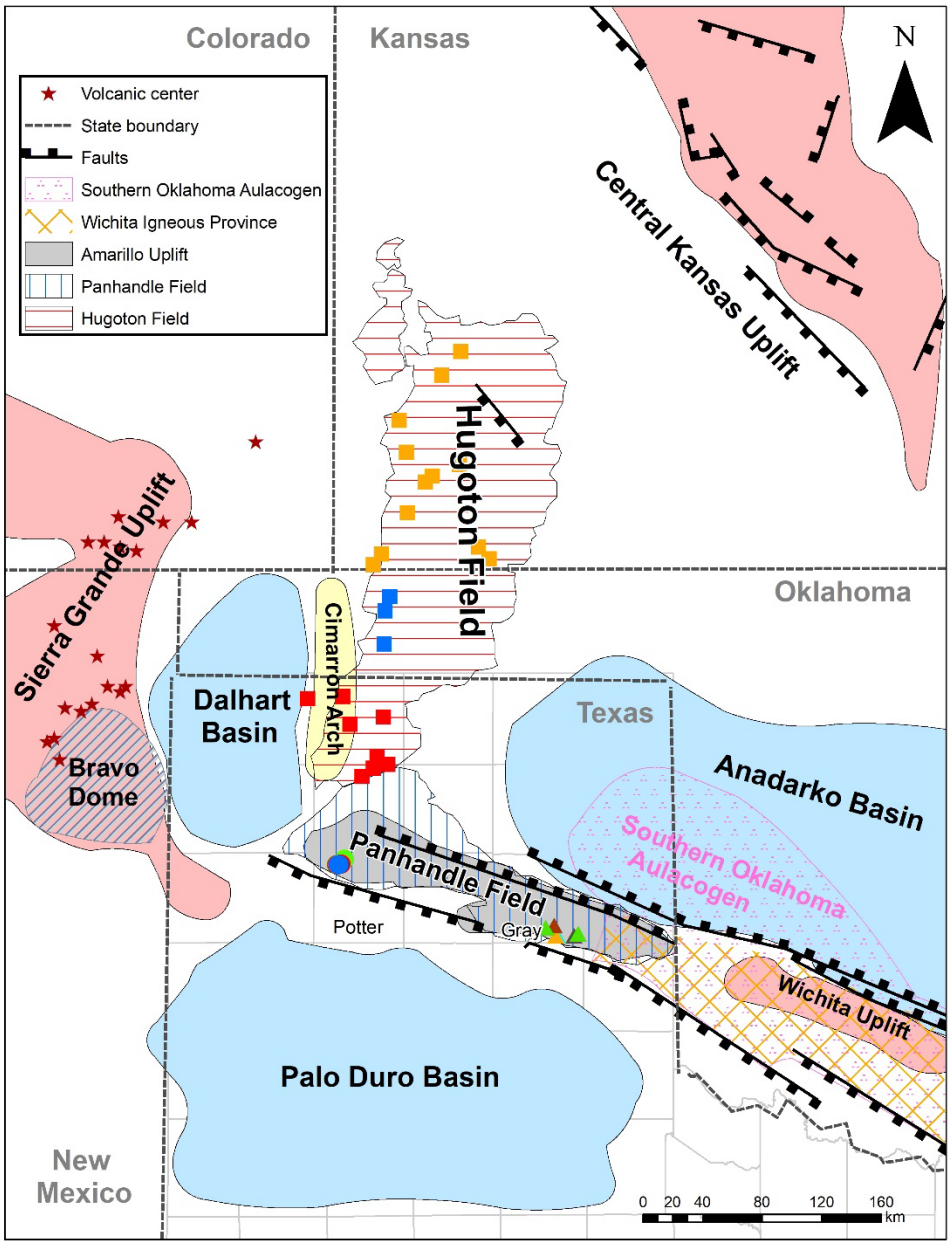

Figure 2.1 Geological map of the Panhandle-Hugoton Field. Production blocks of the Panhandle and Hugoton Field are indicated by colored shaded areas. The Amarillo Uplift is indicated in grey while other uplifts are labeled in red. Major basins are labeled in blue. The Wichita Igneous Province (WIP) is indicated by orange grid. Sample locations in this study (circles and triangles) and those in Ballentine and Lollar [2002] (squares) are indicated as well.

Most of the existing pre-Pennsylvanian strata are now located in the current Anadarko Basin [Fig. 2.1; Johnson et al., 1998b]. Among those late Cambrian to early Carboniferous strata, the late Devonian Woodford shale (~375-360 Ma; Fig. 2.2) is considered the most prominent source rock in the region due to its high organic content and maturity. Subsequently, in the Pennsylvanian (~323-298 Ma), the Ouachita orogeny reactivated existing discontinuities in the intra-cratonic area, causing regional uplift and dividing the ancestral Anadarko Basin into multiple uplifts and basins, including the current Anadarko Basin, the Cimarron Arch and the Wichita and Amarillo uplifts [Algeo 1992; Cambell 2007, Fig. 2.1]. The southern boundary of the Anadarko Basin consequently moved northward, where the current Amarillo uplift stands [Pippin 1970]. In the Panhandle Field, the igneous basement with Mesoproterozoic age [1350 Ma; Van Schmus and Bickford, 1993] was exposed and eroded between mid-Pennsylvanian and early Permian, and the erosion of the basement resulted in a coarse clastic formation, referred to as the Granite Wash (Fig. 2.2). In the Hugoton Field, late Cambrian to early Carboniferous strata contain thick sequences of carbonates and lesser amounts of shale [Johnson et al., 1988a]. These were also eroded during the Pennsylvanian orogenic movement [Johnson et al., 1988b]. Throughout the PHF, post-orogeny shales and sandstones unconformably overly the early Carboniferous limestone, and gradually changes to alternating limestone and clastic rocks at the end of the Carboniferous [Johnson et al., 1988a].

In the Permian (~295 -251 Ma), the Wichita and Amarillo uplifts gradually ceased and regional subsidence resumed, with a faster subsidence rate being observed in the Amarillo area [Pippin 1970; Johnson et al., 1988a; Johnson 1989]. Basin filling resumed at this time and the Amarillo uplift and Cimarron arch were both covered by Permian carbonates, red beds and evaporites [Pippin 1970; Johnson 1989]). An extensive layer of carbonates with early Permian age

directly overlies the Granite Wash, which first showed as interbeds and then transitioned into thick layers of dolomite (Fig. 2.2). These early Permian (Wolfcampian, ~295-280 Ma) carbonates and the Granite Wash are the major reservoirs of the Panhandle Field. The Wolfcampian reservoirs are overlain by the Panhandle Lime, an evaporite layer with early-mid Permian age [Fig. 2.2; Presley, 1987].

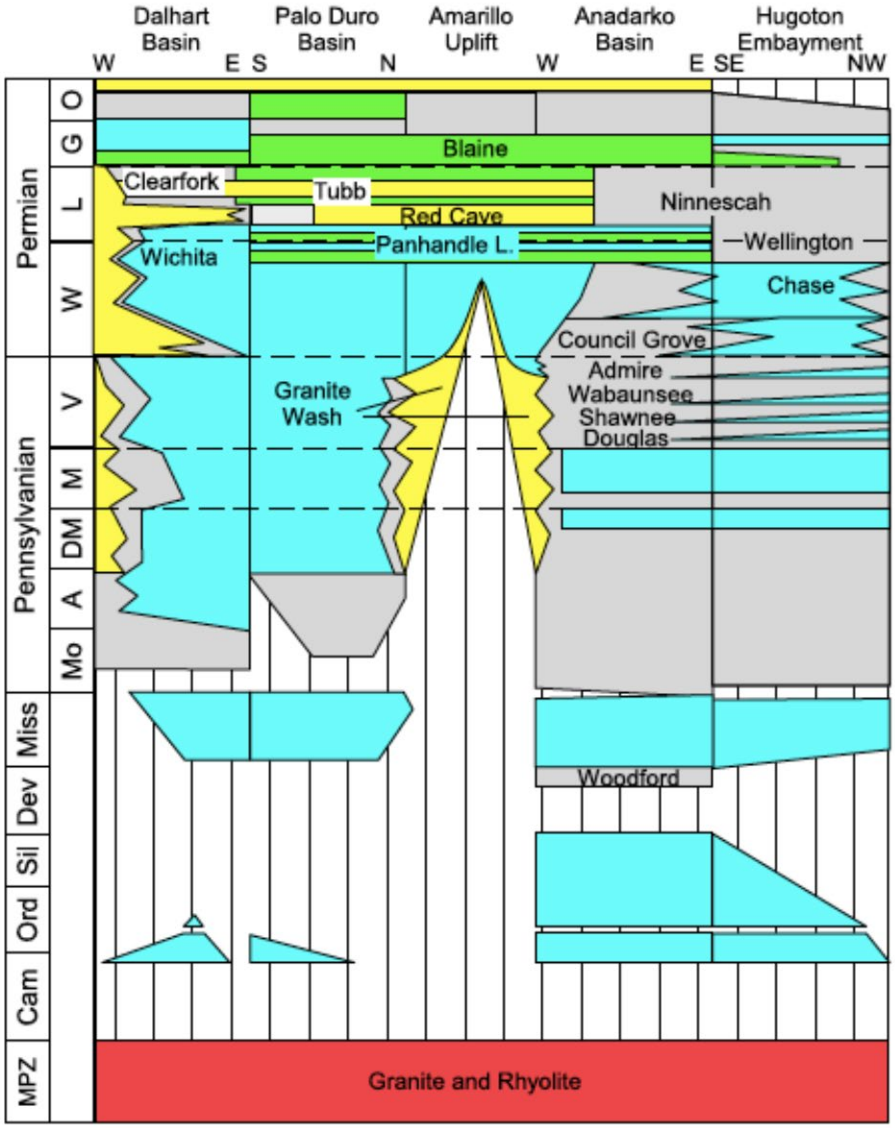

Figure 2.2 Stratigraphy of the PHF and adjacent geological units [adapted from Brown, 2019]. Fine-grained clastic formations (e.g., shales and siltstones) are labeled in grey; carbonates are labeled in blue; coarse-grained clastic rocks (e.g., sandstones and "granite wash") are labeled in yellow; evaporites are labeled in green and igneous rocks are shown in red.

The Panhandle Lime serves as the regional seal of the carbonate reservoirs, and separates them from overlying younger minor natural gas reservoirs [Jorgensen et al., 1993]. Above the Panhandle Lime there are two discontinuous mid-Permian sandstone units, the Red Cave Formation and the Tubb Sandstone Member [Hills and Kottlowski, 1983]. Both sandstone units are considered minor hydrocarbon reservoirs [Fig. 2.2; Pierce et al., 1964]. These clastic formations are overlain and sealed by evaporites from the Blaine Formation [Fig. 2.2; Pierce et al., 1964; Johnson 1989]. Permian stratigraphy in the Hugoton Field is similar to that of the Panhandle Field. On top of the interbedded Carboniferous limestones and shales are the early Permian Council Grove and Chase Groups (Fig. 2.2). These carbonate units were deposited in a shallow marine shelf environment during Wolfcampian time and are equivalent to the Wolfcampian carbonate reservoirs in the Panhandle Field [Fig. 2.2; Sorenson, 2005; Dubois et al., 2007]. During regression periods, continental clastics and evaporites formed the low-porosity Wellington Formation [Fig. 2.2; Jordan and Vosburg, 1963; Johnson 1989], which is considered as the top seal of the underlying carbonate reservoirs in the Hugoton Field.

Post-Permian sediments in the PHF, including Triassic, Jurassic, Cretaceous, Tertiary and Quaternary strata were mostly eroded during tectonic events, with only remnants distributed sparsely throughout the region [Gustavson et al., 1980; Johnson et al, 1988b]. The regional uplift caused the complete erosion of post-Wolfcampian rocks in the eastern Kansas area, where the Wolfcampian carbonate reservoir rocks outcrop [Schmoker, 1989; Hubert, 1995; Sorenson, 2005].

Rapid burial during Pennsylvanian and Permian in the Anadarko Basin moved the source rocks into the early stage of hydrocarbon generation window (~65°C), and oil and gas generated in the deep Anadarko Basin first migrated southward into the Granite Wash in Permian, which served as both local reservoir and as a migration conduit to the Panhandle Field [Pippin, 1970].

Most of the source rocks in the Anadarko Basin are overmature now, and current oil production window in the basin is at around 1.4-4 km depth [Schmoker, 1986, 1989; Cardott, 1989; Hester et al., 1990]. Oil accumulation in the Wichita Mountains suggests that early hydrocarbon migration into the Panhandle Field began in the Permian [Donovan et al., 1992]. Oil deposits exist mainly in the northern margin of the Amarillo Uplift indicating that contemporaneous gas migration may have also happened together with the oil migration [Sorenson 2005]. Pennsylvanian source rocks in the Anadarko Basin reached the gas window in the Mesozoic, which marked a major gas migration event from the Anadarko Basin to the Panhandle Field [Sorenson 2005]. The removal of post-Permian formations by the Tertiary Laramide tectonics in eastern Kansas [Gustavson et al., 1980; Johnson et al, 1988b] caused the exposure of the reservoir rock, and subsequent discharge of formation water. Discharging of formation water led to a dramatic decrease in the reservoir pressure, causing the gas in the Panhandle Field to expand and it eventually passed the spill point into the Hugoton Field [Sorenson, 2005]. Further pressure drop in the reservoirs was triggered by erosion caused by Quaternary glaciations [Beck, 1959; Sorenson 2005].

2.2.2. Hydrogeological Setting

Several aquifers exist in the PHF area, including the Ogallala, the Rita Blanca, and the Dockum Aquifers as well as the deep-basin brine aquifer [George et al., 2011]. The deepest aquifer unit in the PHF area is the deep-basin brine aquifer that resides in the lower Permian – upper Carboniferous carbonates and sandstones. Most groundwater studies in this area do not recognize it as an aquifer due to the high salinity and low accessibility of the water it contains. Existing groundwater research about this hydrological unit has been mostly done by oil companies. The brine aquifer itself coincides with the major hydrocarbon reservoirs of the PHF and the brine is

thus considered as the local formation water [e.g., Basset and Bentley, 1983; Fisher and Kreitler, 1987]. The extensive distribution of Carboniferous – Permian strata in this area leads to greater coverage of the brine aquifer, including parts of Texas, New Mexico, Oklahoma, Kansas, Colorado and Nebraska [Rascoe, 1968]. The general west to east, and southwest to northeast groundwater flow within the deep-basin brine aquifer, was initiated in Late Tertiary when Wolfcampian carbonates outcropped in eastern Kansas and Oklahoma due to the Laramide Orogeny [Basset and Bentley, 1983; Senger and Fogg, 1987; Sorenson, 2005; Dubois et al, 2007]. Although recharge of meteoric water into the brine aquifer appears to occur through sparsely distributed topographic highs further to the west, in New Mexico, a significant amount of groundwater within the aquifer is still from the concentrated seawater that was incorporated in the formation during deposition [Kreitler, 1989]. The extreme underpressure conditions present in the Wolfcampian reservoir [Orr and Kreitler, 1985; Senger and Fogg, 1987] indicates that vertical recharge from overlying aquifers has been severely inhibited by the overlying evaporite aquitard, otherwise downward recharge of freshwater would have compensated the pressure loss due to the discharge of formation water in the outcrop area [Kreitler, 1989]. However, there is evidence for interconnectivity between the major basins within and outside of the PHF, including the Palo Duro, Anadarko, Permian and Midland Basins, indicating that recharge of groundwater to the deep-basin brine aquifer may also occur through inter-basin flow [Wirojanagud et al., 1986; Fisher and Kreitler, 1987].

2.3. Methods

2.3.1. Sample Collection

Twelve gas samples were collected for analysis of volume fractions and isotopic ratios of He, Ne, Ar, Kr, and Xe from twelve producing wells in the Panhandle Field in Texas, with six

from Potter County on the west side of the field, and six from Gray County on the east side (Fig. 2.1). Samples for noble gas analysis were collected directly from wellheads in standard refrigeration grade 3/8" copper tubes, which were then sealed by steel pinch-off clamps [Weiss, 1968]. Atmospheric contamination during sampling was minimized by allowing the gas to flush through the system for approximately 5 minutes prior to sample collection. In addition, samples for hydrocarbon gas geochemistry analysis were collected by pre-evacuated commercial propane tanks, connected to the outlet valve of the wellhead through a stainless-steel flexible tube with a pressure gauge. The tube was flushed to remove air and possible liquid petroleum. A detailed description of the sampling process can be found in Liu et al., [2018].

2.3.2. Analytical Techniques

Noble gas analyses for the Panhandle gas samples were carried out in the Noble Gas Laboratory at the University of Michigan. Extraction, purification, and analysis procedures are described below.

Copper tubes containing the gas samples are connected to a vacuum extraction and purification system at a pressure of ~5 x 10^{-7} Torr. Once this pressure is achieved and the system isolated from its turbo-molecular vacuum pump, the lower clamp is opened to release the natural gas into a low He diffusion glass flask. Gas samples were then expanded in a known volume and gas pressure reduced by computer-controlled sequential pumping until reaching a value acceptable for analyses (typically 35 Torr). The gas sample was initially exposed to a Cu-CuO getter at 800°C in order to oxidize the hydrocarbons. The Cu-CuO getter was then allowed to cool to 450°C in order to reabsorb O_2. Subsequently, the gas sample was exposed to a 3Å molecular trap to reduce

water vapor pressure and reactive gases were removed using three Ti-getters at 600°C for three minutes each.

He, Ne, Ar, Kr, and Xe were quantitatively extracted using a dual chamber computer-controlled cryo-separator at temperatures of 49 K, 84 K, 210 K, 245 K, and 290 K respectively, and sequentially allowed to enter a Thermo® Helix SFT mass spectrometer for He and Ne isotope analyses, and a Thermo® ARGUS VI mass spectrometer for the Ar, Kr, and Xe isotope analyses. At the He release temperature, a small percentage of He is introduced into the SFT mass spectrometer and the signal intensity of ^{4}He is determined for use as the He concentration estimate. This estimate is then used by the automated system to optimize the amount of He that should be introduced for measurement of the $^{3}He/^{4}He$ ratio. All noble gas isotopes were measured using a Faraday detector, except for ^{3}He, which was measured using an electron multiplier in ion counting mode. Prior to each analysis, a blank run was conducted using the same procedure as the sample. Typical blanks are 0.3% - 0.9% of the measured sample values. Quantitative analyses were obtained by calibrating the two mass spectrometers with a known aliquot of standard air. Typical standard reproducibility for ^{4}He, ^{20}Ne and ^{36}Ar are 0.4%, 0.9% and 0.3% while for $^{20}Ne/^{22}Ne$ and $^{40}Ar/^{36}Ar$ ratios the reproducibilities are 0.08% and 0.04%, respectively. Calculated standard errors for concentrations range from 1.3 to 2.2% of the measured values. Analyses for hydrocarbon geochemistry were carried out at the Texas Tech University in Lubbock using a Bruker 400 MHz AVANCE III HD NMR spectrometer with a dual-channel BBFO probe. The abundances of methane (C_1), ethane (C_2), propane(C_3), butane(C_4) and pentane(C_5) are measured and the results are reported as volume fraction percentages. More details about the analysis procedures can be found in Liu et al., [2018].

2.4. Results

2.4.1. Major Gases

Sample ID, well depth and abundances of major gas species for all 12 samples are listed in Table 2.1. Methane (C_1) abundance ranges between 42.5% and 78.7%, with smaller contributions from heavier hydrocarbon molecules, i.e., ethane (C_2), propane (C_3) butane (C_4) and pentane (C_5) ranging between 5.3 - 9.9%, 4.7 – 13.4%, 2.5 - 11.9% and 0.8 - 5.3%, respectively (Table 2.1). Samples collected from the eastern side of the Panhandle Field have significantly higher methane abundances compared to those from the western side. Dryness ($C_1/(C_2+C_3+C_4+C_5)$) of Panhandle samples varies between 1.09 and 5.1 (Table 2.1). CO_2 is also present in small amounts, with the western samples displaying higher carbon dioxide contents (2.35-3.90%) compared to those in the east (0.02-0.11%, Table 2.1).

Table 2.1 Sample depths and major gas compositions of the Texas Panhandle gas samples.

		Chemical composition (%)						
Sample ID	Depth(m)	Methane (C_1)	Ethane (C_2)	Propane (C_3)	Butane (C_4)	Pentane (C_5)	CO_2	$C_1/(C_{2+})$
West								
Bivins-2R	668.7	53.02	8.84	12.02	11.16	4.52	3.14	1.45
Bivins-a-88	-	57.41	8.81	11.44	10.39	4.27	2.81	1.64
Bivins-a-96	951.6	42.54	9.14	13.41	11.92	4.43	3.90	1.09
Bivins-a-201	944.9	51.94	9.92	12.98	11.60	5.29	2.35	1.31
Bivins-a-217	914.7	55.58	9.09	12.26	10.99	4.29	3.29	1.52
Bivins-a-219	970.8	64.89	7.99	8.28	6.81	3.17	3.34	2.47
East								
Griffin-2	721.9	73.53	9.58	7.13	3.91	1.34	0.05	3.35
Hanner-No1-x	728.5	68.43	5.28	4.75	3.76	1.79	0.11	4.39
Johnson-3	772.5	71.02	8.92	6.57	2.97	0.88	0.03	3.67
Johnson-5	750.1	74.30	7.61	5.16	2.49	0.81	0.03	4.62
Tibbets-No1	750.1	78.74	6.40	4.90	3.09	1.33	0.07	5.01
Wilson-2	667.5	77.42	8.15	6.32	3.65	1.24	0.03	4.00

2.4.2. Noble Gases

Total ^{4}He, ^{22}Ne, ^{36}Ar, ^{84}Kr and ^{132}Xe volume fractions are provided in Table 2.2. Terrigenic noble gas components (^{4}He*, ^{21}Ne*, ^{40}Ar* and ^{136}Xe*) were also estimated and are shown in Table 2.2. The terrigenic component comprises both a crustal (radiogenic or nucleogenic) and a mantle component. Helium is treated as a mixture between a terrigenic and an atmospheric component. Using an atmospheric ^{4}He/^{22}Ne value of 3.12 [Ozima and Podosek, 2002], terrigenic He volume fractions were estimated as follow [Ballentine et al., 2002]:

$$^{4}\mathrm{He}^{*} = {}^{4}\mathrm{He}_{\mathrm{measured}} - \left(\frac{^{4}\mathrm{He}}{^{22}\mathrm{Ne}}\right)_{\mathrm{air}} \times {}^{22}\mathrm{Ne}_{\mathrm{measured}} \quad (2.1)$$

where the subscripts air and measured refer to the atmosphere and measured values.

Similarly, Ne, Ar and Xe are treated as a two-component mixture between an atmospheric and terrigenic endmember. Terrigenic ^{21}Ne, ^{40}Ar and ^{136}Xe contributions (^{21}Ne*, ^{40}Ar*, ^{136}Xe*) were estimated as follow [Ballentine et al., 2002]:

$$^{21}\mathrm{Ne}^{*} = \left(\left(\frac{^{21}\mathrm{Ne}}{^{22}\mathrm{Ne}}\right)_{\mathrm{measured}} - \left(\frac{^{21}\mathrm{Ne}}{^{22}\mathrm{Ne}}\right)_{\mathrm{air}}\right) \times {}^{22}\mathrm{Ne}_{\mathrm{measured}} \quad (2.2)$$

$$^{40}\mathrm{Ar}^{*} = \left(\left(\frac{^{40}\mathrm{Ar}}{^{36}\mathrm{Ar}}\right)_{\mathrm{measured}} - \left(\frac{^{40}\mathrm{Ar}}{^{36}\mathrm{Ar}}\right)_{\mathrm{air}}\right) \times {}^{36}\mathrm{Ar}_{\mathrm{measured}} \quad (2.3)$$

$$^{136}\mathrm{Xe}^{*} = \left(\left(\frac{^{136}\mathrm{Xe}}{^{130}\mathrm{Xe}}\right)_{\mathrm{measured}} - \left(\frac{^{136}\mathrm{Xe}}{^{130}\mathrm{Xe}}\right)_{\mathrm{air}}\right) \times {}^{130}\mathrm{Xe}_{\mathrm{measured}} \quad (2.4)$$

where $(^{21}\mathrm{Ne}/^{22}\mathrm{Ne})_{\mathrm{air}} = 0.029$, $(^{40}\mathrm{Ar}/^{36}\mathrm{Ar})_{\mathrm{air}} = 295.5$ and $(^{136}\mathrm{Xe}/^{130}\mathrm{Xe})_{\mathrm{air}} = 2.176$ [Ozima and Podosek, 2002].

Noble gas isotopic ratios are listed in Table 2.3. ^{3}He/^{4}He ratios (R) are normalized to the atmospheric ratio Ra, where Ra = (1.384±0.013) × 10^{-6} [Clarke et al., 1976].

Total ^{4}He volume fractions in the Panhandle samples range from 1.00×10^{-3} to 4.81×10^{-3}, with the samples from the western side displaying significantly higher helium contents than those

in the eastern side (Fig. 2.3a, Table 2.2). Terrigenic ^{4}He* is dominant in all samples and accounts for more than 99.9% of the total ^{4}He. Samples from the eastern side display R/Ra ratios between 0.0325 and 0.0428 (Table 2.3), consistent with typical crustal R/Ra ratios of 0.02-0.05 [Oxburgh et al., 1986]. Samples from the western side show R/Ra ratios between 0.1008-0.1145 (Table 2.3), consistently higher than the crustal value. The contribution of atmospheric helium and its influence on the measured R/Ra ratios can be removed using the ^{4}He/^{20}Ne ratios, following Craig et al. [1978]:

$$\left(\frac{R}{Ra}\right)_c = \frac{\left(\frac{R}{Ra} - r\right)}{(1-r)} \tag{2.5}$$

$$\text{with } r = \frac{\left(\frac{^{4}He}{^{22}Ne}\right)_{ASW}}{\left(\frac{^{4}He}{^{22}Ne}\right)} \tag{2.6}$$

where subscripts "c" and "ASW" represent the air-corrected value and the value in air-saturated water (ASW), respectively.

The ^{4}He/^{22}Ne ratio in air-saturated water is 2.531 and is calculated following Smith and Kennedy [1983] assuming the mean annual temperature of 13°C as the local recharge temperature. Measured ^{4}He and ^{22}Ne volume fractions of the Panhandle samples are reported in Table 2.2 and the calculated air-corrected R/Ra ratios ($(R/Ra)_c$) are reported in Table 2.3. Overall air-corrected $(R/Ra)_c$ ratios are indistinguishable from the measured ratios (Table 2.3), pointing to negligible amounts of atmospheric helium. R/Ra ratios higher than the crustal value range in the west Panhandle samples are thus likely the result of a mantle helium contribution. The presence of a potential mantle component is discussed below.

All ^{21}Ne/^{22}Ne ratios are above the atmospheric value of 0.029 [Ozima and Podosek, 2002], with values varying between 0.03043 and 0.04596 (Table 2.3). ^{21}Ne* volume fractions for the gas samples are highly variable and range from 0.45×10^{-10} to 2.45×10^{-10}, representing terrigenic

contributions varying between 4.71% and 36.83%, respectively, with respect to the total measured ^{21}Ne volume fractions (Fig. 2.3b, Table 2.2). The western side samples generally have higher ^{21}Ne* volume fractions compared to the eastern samples, and the highest ^{21}Ne* content is found in sample Bivins-a-219, on the western side (Fig. 2.1; Table 2.3). A significant correlation between ^{21}Ne* and methane is observed in the western side samples (Fig. 2.3b), but absent in the eastern samples. Most of the measured ^{20}Ne/^{22}Ne ratios in the eastern samples are higher than the atmospheric value of 9.80 [Ozima and Podosek, 2002; Table 2.3], while the western side samples have ^{20}Ne/^{22}Ne ratios varying between 9.4338 and 9.7226, consistently lower than the atmospheric value (Table 2.3).

All samples display ^{40}Ar/^{36}Ar ratios above the atmospheric value of 295.5 [Ozima and Podosek, 2002], varying between 394.47 and 1401.67 (Table 2.3), reflecting the addition of terrigenic ^{40}Ar*. The highest ^{40}Ar/^{36}Ar ratio is found in sample Bivins-a-219 on the western side, while the lowest value is found in sample Hanner-No1, to the east (Table 2.3). Radiogenic ^{40}Ar* volume fractions range from 0.96×10^{-4} to 6.42×10^{-4} (Fig. 2.3c, Table 2.2) and show no clear correlation with methane. Like ^{4}He and ^{21}Ne, samples from the western side generally have higher ^{40}Ar* contents compared to the eastern side samples.

The ^{86}Kr/^{84}Kr ratios are indistinguishable from the atmospheric value of 0.30524 [Table 2.3; Ozima and Podosek, 2002]. Most samples display ^{136}Xe/^{130}Xe ratios above the atmospheric value of 2.176 [Table 2.3; Ozima and Podosek, 2002]. Volume fractions of terrigenic ^{136}Xe* vary between 0.07×10^{-11} and 1.42×10^{-11} (Fig. 2.3d, Table 2.2), corresponding to a minor terrigenic contribution varying between 0.22% - 2.12%. An inverse correlation is observed between ^{136}Xe* and methane in all samples (Fig. 2.3d). The mechanism that causes the negative correlation is

unclear. A possible explanation is that in-situ produced $^{136}Xe^{*}$ is diluted by hydrocarbon gases, as suggested in the gas zone of the Eagle Ford Shale [Byrne et al., 2018].

Table 2.2 Noble gas volume fractions (cm^3/cm^3) and terrigenic noble gas volume fractions for production gas samples from the Panhandle Field**.**

Sample ID (NGL)	Total ^{4}He	Total ^{22}Ne	Total ^{36}Ar	Total ^{84}Kr	Total ^{132}Xe	$^{4}He^*$	$^{21}Ne^*$	$^{40}Ar^*$	$^{136}Xe^*$
	($x10^{-3}$)	($x10^{-7}$)	($x10^{-7}$)	($x10^{-8}$)	($x10^{-9}$)	($x10^{-3}$)	($x10^{-10}$)	($x10^{-4}$)	($x10^{-11}$)
West									
Bivins-2R	3.64	2.71	9.69	1.78	2.01	3.64±0.05	1.66±0.02	6.12±0.08	1.42±0.12
Bivins-a-88	3.95	2.65	7.15	1.84	1.75	3.95±0.06	1.83±0.03	4.86±0.06	0.62±0.08
Bivins-a-96	2.71	2.74	10.10	1.50	2.20	2.71±0.04	1.17±0.02	5.04±0.07	1.11±0.10
Bivins-a-201	3.31	0.82	3.24	1.12	1.43	3.31±0.05	1.20±0.02	3.58±0.05	0.92±0.09
Bivins-a-217	4.12	2.79	7.97	1.89	1.86	4.12±0.06	1.71±0.02	4.99±0.07	0.79±0.10
Bivins-a-219	4.81	1.44	5.41	1.59	1.54	4.81±0.07	2.45±0.03	6.42±0.08	0.79±0.07
East									
Griffin-2	0.97	0.71	1.87	0.54	0.80	0.97±0.01	0.45±0.02	1.05±0.01	0.32±0.04
Hanner-No1-x	1.17	6.61	10.45	1.91	1.12	1.17±0.02	0.95±0.02	1.03±0.01	-
Johnson-3	2.23	2.03	5.20	1.18	1.03	2.23±0.03	1.10±0.02	3.42±0.04	0.41±0.06
Johnson-5	1.77	0.59	2.41	0.82	0.79	1.77±0.03	0.77±0.01	2.06±0.03	0.32±0.04
Tibbets-No1	1.99	2.46	5.36	1.26	0.93	1.99±0.03	1.03±0.02	1.76±0.02	0.07±0.04
Wilson-2	1.00	1.33	2.54	0.63	0.74	1.00±0.01	0.52±0.01	0.96±0.01	0.23±0.05
Air[a]	0.005	16.78	314.2	64.98	23.39				

[a] Ozima and Podosek [2002].

Table 2.3 Noble gas isotopic ratios and air-correction helium isotopic ratios for gas samples from the Panhandle field

Sample ID (NGL)	R/Ra	$(R/Ra)_c$[a]	$^{20}Ne/^{22}Ne$	$^{21}Ne/^{22}Ne$	$^{38}Ar/^{36}Ar$	$^{40}Ar/^{36}Ar$	$^{86}Kr/^{84}Kr$	$^{136}Xe/^{130}Xe$
West								
Bivins-2R	0.1008±0.0014	0.1008±0.0014	9.6832±0.0028	0.03514±0.00003	0.1897±0.0005	927.26±0.59	0.3047±0.0004	2.2231±0.0040
Bivins-a-88	0.1076±0.0015	0.1076±0.0015	9.6605±0.0032	0.03592±0.00004	0.1903±0.0005	975.10±0.70	0.3056±0.0005	2.1996±0.0029
Bivins-a-96	0.1094±0.0013	0.1094±0.0013	9.7226±0.0019	0.03325±0.00002	0.1894±0.0002	794.39±0.51	0.3057±0.0005	2.2096±0.0031
Bivins-a-201	0.1145±0.0016	0.1145±0.0016	9.4801±0.0138	0.04363±0.00021	0.1905±0.0006	1401.67±1.20	0.3061±0.0005	2.2186±0.0040
Bivins-a-217	0.1084±0.0016	0.1084±0.0016	9.6730±0.0029	0.03511±0.00003	0.1903±0.0003	922.16±0.59	0.3057±0.0004	2.2042±0.0035
Bivins-a-219	0.1040±0.0010	0.1040±0.0010	9.4338±0.0071	0.04596±0.00009	0.1912±0.0008	1481.86±1.42	0.3065±0.0005	2.2101±0.0028
East								
Griffin-2	0.0423±0.0006	0.0423±0.0006	9.9882±0.0158	0.03534±0.00021	0.1896±0.0006	859.06±0.82	0.3065±0.0005	2.2023±0.0032
Hanner-No1-x	0.0417±0.0007	0.0416±0.0007	10.1544±0.0026	0.03043±0.00003	0.1858±0.0002	394.47±0.21	0.3039±0.0004	2.1745±0.0043
Johnson-3	0.0344±0.0005	0.0343±0.0005	10.0161±0.0044	0.03440±0.00008	0.1882±0.0002	953.28±0.59	0.3055±0.0004	2.2020±0.0035
Johnson-5	0.0375±0.0006	0.0375±0.0006	9.5982±0.0169	0.04208±0.00018	0.1905±0.0006	1151.88±0.95	0.3064±0.0005	2.2027±0.0035
Tibbets-No1	0.0325±0.0006	0.0324±0.0006	9.9991±0.0050	0.03319±0.00005	0.1884±0.0003	623.66±0.40	0.3054±0.0005	2.1809±0.0029
Wilson-2	0.0428±0.0006	0.0427±0.0006	10.0869±0.0089	0.03292±0.00010	0.1882±0.0007	672.28±0.57	0.3071±0.0005	2.1969±0.0040
Air[b]	1		9.80	0.029	0.188	295.5	0.305	2.176

[a]Estimated after removal of the atmospheric component using the atmosphere-derived ^{22}Ne concentrations following Craig et al. [1978]. $(R/Ra)_c$ ratios are indistinguishable from the measured $^{3}He/^{4}He$ ratios due to the extremely high measured $^{4}He/^{22}Ne$ ratios of the Eagle Ford natural gas samples (17640 - 403843), 5654–129436 times the atmospheric value [3.12,Ozima and Podosek, 2002].

[b] Ozima and Podosek, [2002]

2.5. Discussion

While displaying distinct signatures, it is clear that significant amounts of terrigenic components are present in the eastern and western sides of the Panhandle Field, as evidenced by the noble gas volume fractions and isotopic ratios. In particular, on the eastern side, the combined analysis of R/Ra, $^{20}Ne/^{22}Ne$ and $^{21}Ne/^{22}Ne$ ratios suggest the presence of a mantle signature, a component that appears to be absent in the western side. These variations point to multiple sources of noble gases and hydrocarbons within the Panhandle Field and thus, a complex and heterogeneous petroleum system. In the discussion that follows, the origin of the crustal and mantle noble gas components as well as that of hydrocarbons within the various locations of the PHF are analyzed.

2.5.1. Western and Eastern Hydrocarbon and Noble Gas Sources in the Panhandle Field

In conventional fields, hydrocarbons are produced in a source rock and subsequently transferred into the reservoir rock [Chapman, 2000]. The almost complete removal of Cambrian through Carboniferous strata in the PHF, in particular in the Panhandle Field [Johnson et al., 1988b], results in the absence of potential source rocks in this region, and therefore, points to an external origin to these hydrocarbons. The source rock of the Panhandle and the greater PHF is thought to be primarily the Woodford Shale, a late Cambrian to early Carboniferous organic-rich formation (Fig. 2.2) in the Anadarko Basin [Fig. 2.1; Pippin, 1970; Rice, 1988; Johnson, 1989; Sorenson, 2005]. Early oil and gas are thought to have first migrated into the east Panhandle during the Permian and gradually occupied the entire field [Sorenson, 2005]. In the Tertiary, natural gases in the Panhandle Field expanded due to a reservoir pressure drop, causing a northward migration

of Panhandle natural gas into the Hugoton Field [Sorenson, 2005]. However, while a direct correlation between hydrocarbons and terrigenic noble gases, in particular between $^{4}He^{*}$ and $^{21}Ne^{*}$, (Figs. 2.3b, d) is observed in the west Panhandle Field, such correlation is absent in the east Panhandle. The absence of correlation in the east Panhandle point to distinct sources of both, hydrocarbons and noble gases on both sides of the field. In the western side of the Panhandle Field (Figs. 2.3b, d), the positive correlation between terrigenic noble gases and methane is an indication that they may have originated from a common source, and subsequently mixed and migrated together before reaching the west Panhandle Field. This common source for hydrocarbons and noble gases on the western side of the Panhandle is unlikely to be the Woodford Shale in the Anadarko Basin, as most of the terrigenic noble gases would have been added to the gas samples during or after migration, not directly from the source rock. Indeed, the estimated terrigenic noble gas amounts (Table 2.2) require significantly longer production and accumulation time than the time period during which hydrocarbons remained in the Woodford Shale prior to migration (< 75Myrs). Instead, a more plausible explanation is that terrigenic noble gases and methane are both from adjacent basins on the western side of the Panhandle. Possible sources are the Palo Duro or Dalhart Basins (Fig. 2.1). Ballentine and Lollar [2002] and Brown [2019] argued that crustal noble gases produced in those basins are initially mixed and subsequently delivered by the general W-E groundwater flow in the deep-basin brine aquifer to the west of the Panhandle Field. If natural gas produced in those basins are also collected and carried by the regional groundwater flow to the west Panhandle, that could explain the observed positive correlation, which points to a common source for hydrocarbons and terrigenic noble gases. Petroleum exploration in the Palo Duro Basin indicates that Pennsylvanian to Permian organic-rich shales in those basins have the potential to generate hydrocarbons [Dutton, 1980a, b; Rose, 1986]. The lower methane content and thus, lower

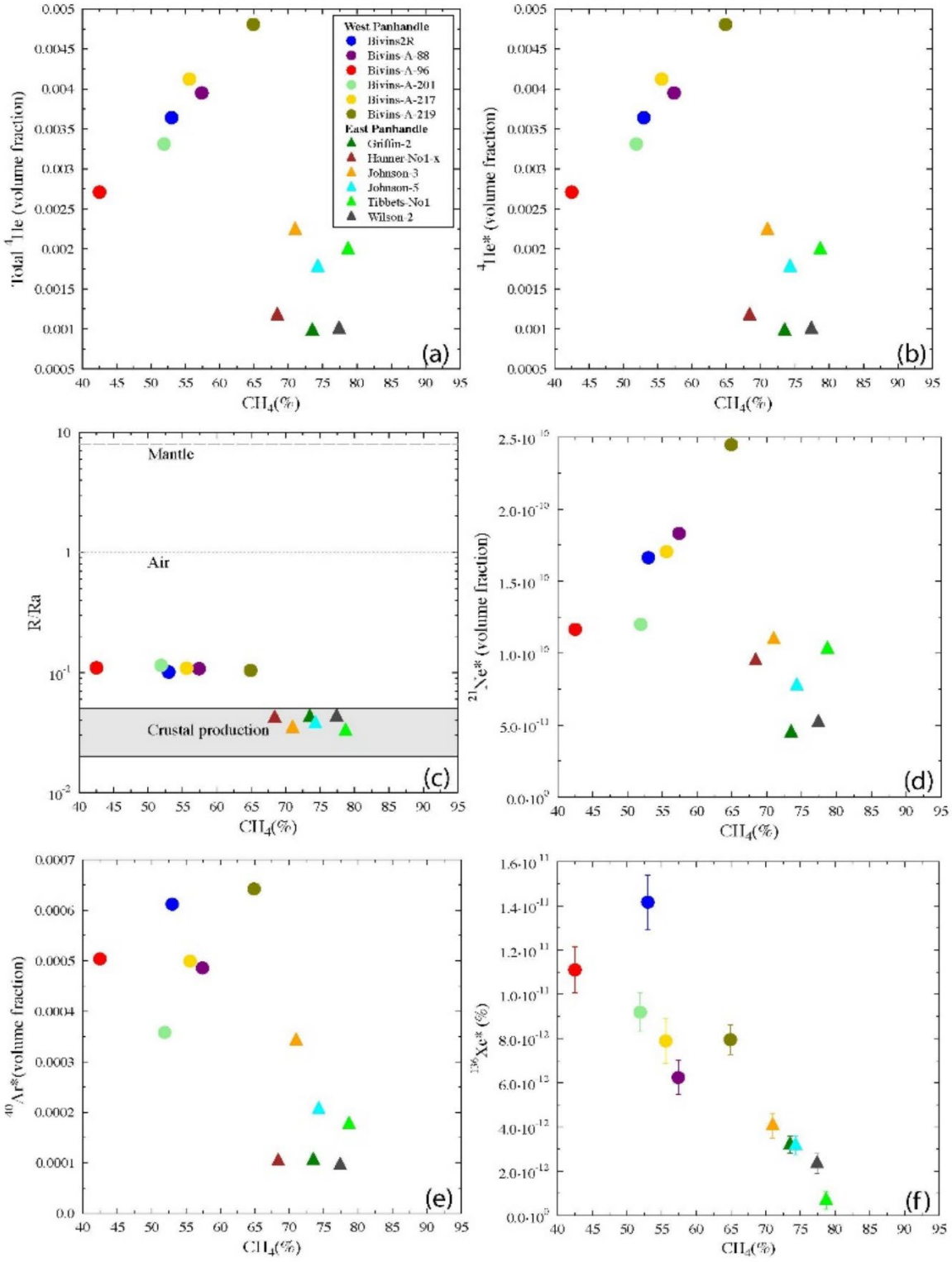

Figure 2.3 Methane volume percentages plotted as a function of the volume fractions of (a) total ^{4}He, (b) terrigenic ^{4}He*, (c) R/Ra, (d) terrigenic ^{21}Ne*, (e) terrigenic ^{40}Ar* and (f) terrigenic ^{136}Xe* for the Panhandle samples.

dryness in west Panhandle samples compared to those in the eastern side (Table 2.1) further supports this hypothesis. Indeed, Palo Duro Basin source rocks display lower maturity compared to that of the Woodford Shale due to the lower geothermal gradient and shallower burial depth at which they are exposed [Rose, 1986]. The higher CO_2 content in all samples from the west side compared to those in the east side (Table 2.1) further reinforces the connection between hydrocarbons and groundwater on the west side of the Panhandle. It is likely that the high CO_2 content has originated from the Bravo Dome CO_2 field on the west side of the Panhandle Field (Fig. 2.1) and subsequently carried to the field by regional W-E groundwater flow.

In contrast to the west Panhandle samples, no correlation is observed between methane and terrigenic noble gases in the east Panhandle samples (Fig. 2.3a, b). While previous studies suggest that hydrocarbons in the Panhandle Field are mainly sourced from the Anadarko Basin, other sources might be responsible for the presence of terrigenic noble gases (e.g., $^{4}He^{*}$ and $^{21}Ne^{*}$). These include in-situ production in the reservoir rock and external contributions, in particular, an upward flux of terrigenic noble gases, either from deeper levels in the crust or of mantle origin. Absence of direct correlation between methane and terrigenic noble gases suggests a different source for both hydrocarbons and terrigenic noble gases. Decoupling of methane and noble gases was previously reported in other hydrocarbon fields [e.g., Wen et al., 2015a, 2017; Byrne et al., 2018]. The decoupled methane and terrigenic noble gases suggest that hydrocarbons in the east Panhandle Field originated primarily from the Woodford Shale in the Anadarko Basin. The majority of the terrigenic noble gases in east Panhandle were likely added to hydrocarbons either during the migration stage or following the emplacement of hydrocarbon phases. As significant groundwater flow is absent in the east Panhandle area [Bassett and Bentley, 1983; Senger and

Fogg, 1987], in-situ production, an upward flux or a combination of both are likely the sources of terrigenic noble gases in this area.

The existence of an upward flux is also suggested by a positive correlation between sample depth and terrigenic $^{4}He^{*}$, $^{21}Ne^{*}$ and $^{40}Ar^{*}$ in the east Panhandle Field (Fig. 2.4a, b, c). Such a correlation points to an origin of terrigenic noble gases from the underlying strata, including deeper sedimentary formations and basement rock, similar to observations in many other sedimentary basins [e.g., Ballentine et al., 1991; Castro et al., 1998a, b; Wen et al., 2015a]. By contrast, the absence of such a correlation in the west Panhandle region points to an origin other than external contribution from underlying formations (Fig. 2.4a, b, c), and further reinforces the hypothesis that external inputs from adjacent basins, possibly via groundwater flow [e.g., Ballentine and Lollar, 2002], are responsible for both hydrocarbons and noble gases in that area. The impact of groundwater in the west Panhandle Field may also explain higher (R/Ra)c ratios compared to typical crustal values (Fig. 2.4d), as these samples are expected to carry mantle helium from the Bravo Dome [Ballentine et al., 2005].

Distinct correlations between crustal noble gases, methane and sample depth between the east and west Panhandle samples point to various sources of noble gases and hydrocarbons within the Panhandle Field. Such variations may also be reflected in the presence or absence of specific mantle noble gas signatures, as evidenced by a combined analysis of helium and neon isotopic signature. Below, the presence of a mantle signature in the Panhandle Field is discussed together with magmatic and tectonic implications.

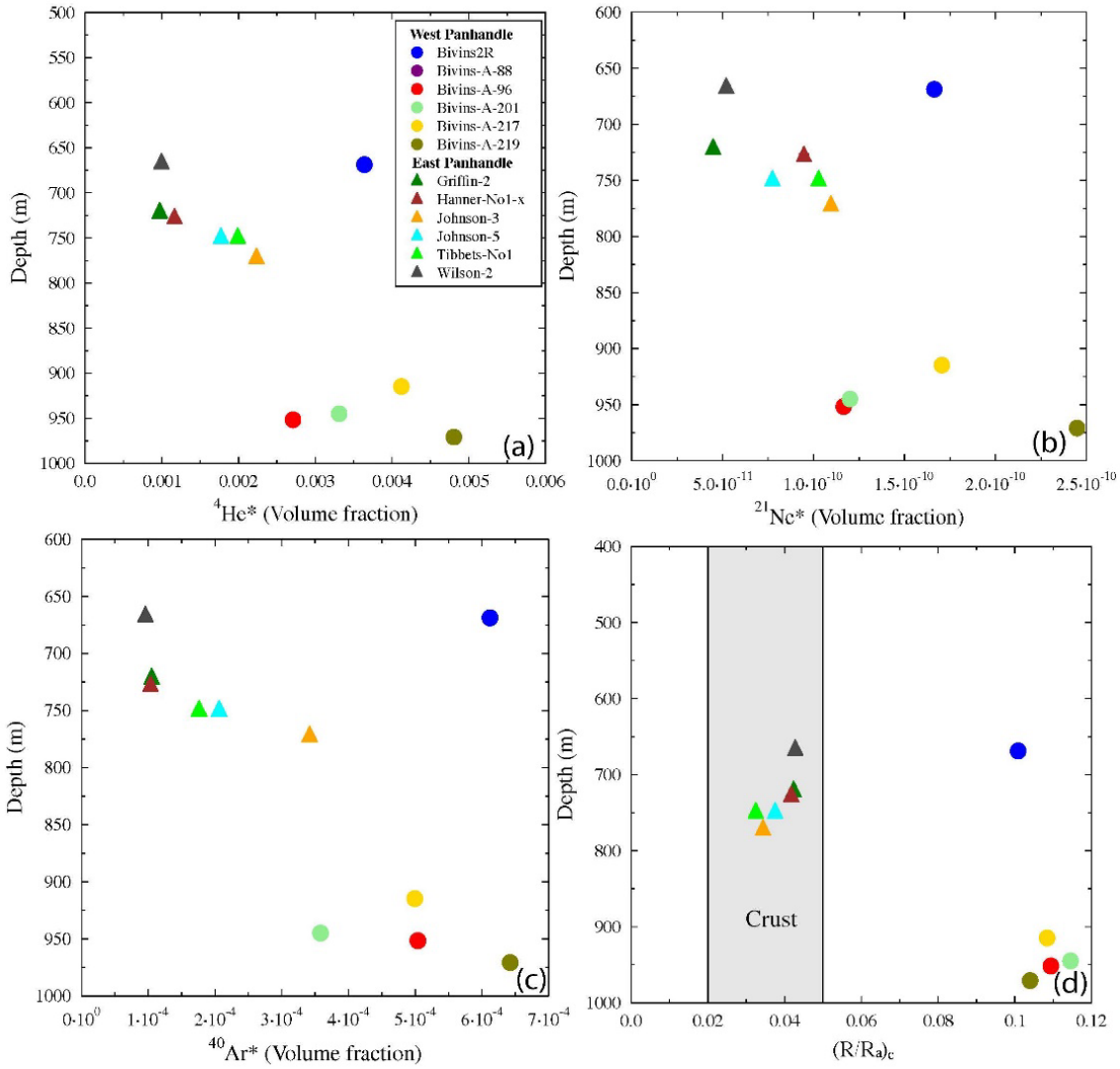

Figure 2.4 Sample depths plotted as a function of (a) terrigenic ^{4}He*, (b) terrigenic ^{21}Ne*, (c) terrigenic ^{40}Ar* and (d) air-corrected $(R/Ra)_c$ of Panhandle samples.

2.5.2. Mantle Noble Gas Sources in the Panhandle Field

Figure 2.5 shows $^{20}Ne/^{22}Ne$ versus $^{21}Ne/^{22}Ne$ ratios for both the east and west Panhandle Field samples. It is apparent that our samples reflect a three-component mixing between the atmosphere, the crust and the mantle, and provide further clarification on the nature of this mantle component, i.e., a MORB, OIB or solar-like source. All east Panhandle samples fall above the air-MORB line and plot within the mantle area with $^{20}Ne/^{22}Ne$ and $^{21}Ne/^{22}Ne$ ratios higher than that of the atmosphere (Fig. 2.5). Sample Hanner-No1-x falls in the OIB domain, while all other eastern samples fall within the MORB domain. Since mass dependent fractionation has been ruled out as a potential source of the elevated $^{20}Ne/^{22}Ne$ and $^{21}Ne/^{22}Ne$ ratios (Appendix A1) in the eastern samples and crustal production of ^{20}Ne is negligible, high $^{20}Ne/^{22}Ne$ and $^{21}Ne/^{22}Ne$ ratios largely reflect the addition of mantle Ne. Indeed, both upper and lower mantle are enriched in ^{20}Ne, with the $^{20}Ne/^{22}Ne$ reaching up to 13.8 for the solar component [Starkey et al., 2009]. $^{21}Ne/^{22}Ne$ ratios in east Panhandle samples are also consistently higher than the atmospheric value of 0.029 (Table 2.3), indicating the addition of crustally produced nucleogenic ^{21}Ne. By contrast, all samples from the west Panhandle Field fall along the typical air-crust line with a crustal $^{21}Ne/^{22}Ne$ ratio of 0.47 [Fig. 2.5; Kennedy et al., 1990]. This Ne isotopic composition pattern is that expected for crustal neon production, as ^{22}Ne is produced more rapidly than ^{20}Ne, but slower than ^{21}Ne in crustal rocks [Ballentine and Burnard, 2002]. However, the presence of mantle helium in west Panhandle, as evidenced by the higher $(R/Ra)_c$ ratios compared to typical crustal values, indicates that it is unlikely to have pure crustal neon signals in the west Panhandle Field. It is clear that west Panhandle samples underwent mass fractionation (Appendix A1) and thus it is not possible to pursue a combined He-Ne isotopic ratio analysis for the west Panhandle. Such analysis, which provides clarification on the nature of the mantle component present given below for the east

Panhandle samples.A primordial mantle component is commonly characterized by positively correlated $^{20}Ne/^{22}Ne$ and inversely correlated $^{21}Ne/^{22}Ne$ with R/Ra ratios, respectively [Moreira

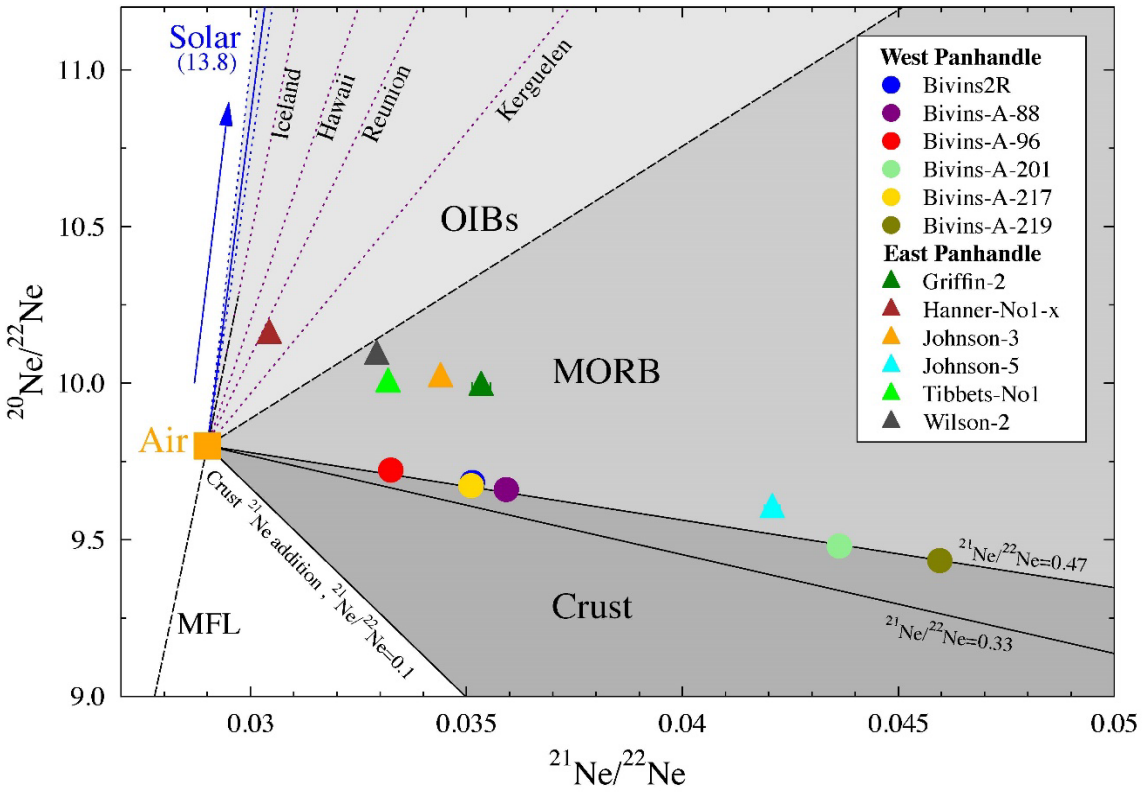

Figure 2.5 Measured $^{20}Ne/^{22}Ne$ ratios plotted as function of $^{21}Ne/^{22}Ne$ ratios for Panhandle gas samples. Three components are presented in this diagram: Air, Mantle (MORB, OIBs, Solar), and Crust. Mixing lines between Air–Solar, Air–MORB and Air–OIB endmembers for Iceland, Hawaii, Reunion, and Kerguelen are indicated. Air–Crust mixing lines with $^{21}Ne/^{22}Ne$ ratios of 0.1, 0.47 and 0.33 (Table 2.4) are also shown. Triangular grey areas, from lighter to darker indicate the Air–Solar–MORB, Air–MORB–Crust, and Air Crust domains, respectively. All endmember values are listed in Table 2.4.

and Allegre, 1998; Graham, 2002]. This combined analysis in our gas samples requires removal of the atmospheric He and Ne components so that He and Ne isotopic ratios will represent solely a binary mixture between the crust and mantle (MORB, OIB, or Solar) endmembers ($(^{20}Ne/^{22}Ne)_{crust+mantle}$ and $(^{21}Ne/^{22}Ne)_{crust+mantle}$). The removal of atmospheric He from measured R/Ra ratios is exercised following Craig et al. (1978) and the air-corrected R/Ra ratios are indistinguishable from the measured values (Table 2.3). Removal of atmospheric Ne from the measured $^{20}Ne/^{22}Ne$ and $^{21}Ne/^{22}Ne$ ratios is achieved through previously developed procedures

[Appendix A2, see also Ballentine and O'Nions, 1992; Ballentine, 1997 and Castro et al., 2009]. Results of air-corrected He and Ne isotopic ratios are shown in Table 2.5, and the east Panhandle samples are plotted in figure 2.6. The theoretical crust-MORB, crust-OIB and crust-solar mixing lines (Table 2.4) as well as the crust-solar mixing line estimated for the Michigan Basin brines [Castro et al., 2009] with a crustal $^{21}Ne/^{22}Ne$ endmember value of 0.047 are also shown. Mixing lines between the crust and mantle (MORB, OIB, and Solar, respectively) in these two-element isotope plots are defined by their respective isotopic ratio endmembers (Table 2.4) as well as by the curvature of each hyperbola defined by $K_{crust\text{-}mantle} = (^4He/^{22}Ne)_{crust}/(^4He/^{22}Ne)_{mantle}$, where $(^4He/^{22}Ne)_{crust}$ and $(^4He/^{22}Ne)_{mantle}$ are the crustal and mantle (MORB, OIB, Solar) $^4He/^{22}Ne$ elemental ratios, respectively (Table 2.4). If no uncertainty were to be associated with the crustal and mantle He and Ne endmembers, and if prior to mixing all endmembers had a constant crustal and mantle $^4He/^{22}Ne$ ratio, all samples would fall along a single mixing line within error. Most of the east Panhandle samples fall close to the crust-solar mixing line derived from the Michigan Basin brines [Castro et al., 2009], with sample Johnson-5 falling on the theoretical crust-solar line (Fig. 2.6). Considering that the $^{20}Ne/^{22}Ne$ ratio of Johnson-5 is possibly the result of mass fractionation (Appendix A1), it may be excluded from the discussion of a potential mantle signal. The origin of the primordial mantle signal for most of the east Panhandle samples is discussed below.The presence of a primordial combined He and Ne component (OIBs-type) has historically been associated with the presence of a lower, primordial, largely undegassed reservoir from which OIBs would originate via deep mantle plumes [O'Nions and Oxburgh, 1983; Porcelli and Wasserburg, 1995; Moreira et al., 1998]. In the study area, a large volume of mafic rocks has been identified in the WIP, which occupies the Southern Oklahoma Aulacogen and also extends into the east Panhandle Field (Fig. 2.1). Our east Panhandle samples are located close to the western

end of the igneous province (Fig. 2.1). The emplacement of the WIP happened during the breakup of Rodinia and the opening of the Iapetus Ocean in the Cambrian [Hanson et al., 2013; Wall. et al., 2020], under an extensional or transtensional environment. The U-Pb dating of mafic and felsic rocks in the WIP yield a narrow age range between 532.49 ± 0.12 Ma to 530.23 ± 0.14 Ma, indicating that the emplacement of the igneous province happened through a rapid thermal event,

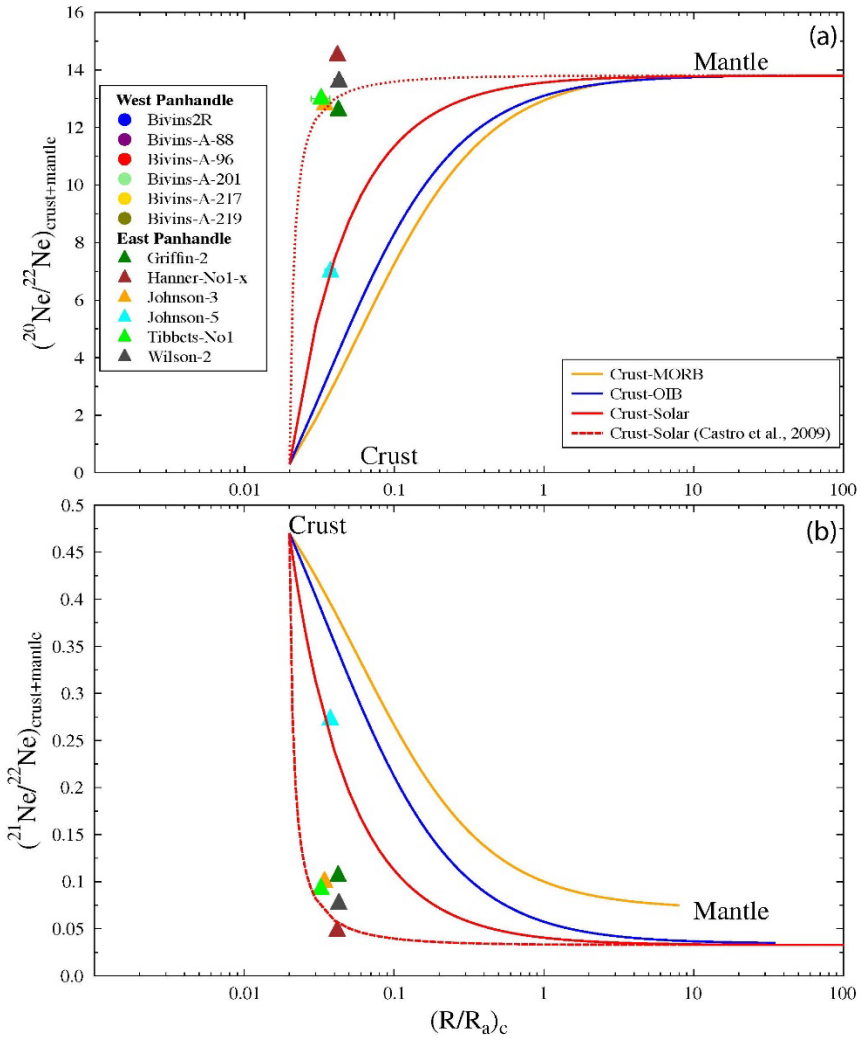

Figure 2.6 Two-component mixing plots for $(R/Ra)_c$ vs. (a) $(^{20}Ne/^{22}Ne)_{crust+mantle}$ and (b) $(^{21}Ne/^{22}Ne)_{crust+mantle}$ for Panhandle gas samples in this study. Theoretical crust-MORB, crust-OIB and crust-solar mixing lines are shown. Modified crust-solar [Castro et al., 2009] mixing line is also shown (cf., Appendix A2).

probably an upwelling mantle plume [Wall et al., 2020]. The presence of a mantle plume in the WIP aligns well with the formation mechanism of the Southern Oklahoma Aulacogen, where the

WIP is located [Hogan et al., 1995; Lidiak et al., 2014; Wall et al., 2020]. Two mechanisms were proposed to explain the formation of the Southern Oklahoma Aulacogen: 1) it developed as a transform fault system along the transform plate boundary during the continental rifting [Thomas, 2011, 2014], or; 2) it developed from a failed arm of a triple-junction point [Hoffman et al., 1974]. Both hypotheses may have active mantle plumes involved [Wall et al., 2020]. Thus, the primordial mantle component identified in the east Panhandle is likely representative of the remnants of this mantle plume activity during the emplacement of the WIP. On the other hand, the mantle helium identified in the west Panhandle Field is likely to have originated in the Bravo Dome, where solar-like He and Ne signatures were reported by Ballentine et al. [2005]. Because Ne isotopic ratios in the west Panhandle samples are likely affected by MDF, confirmation on the nature of this mantle component is not possible at this time.

Although previous studies have mostly favored the idea of a mantle plume to explain the formation of the WIP, evidence of magmatism linked to the subcontinental lithospheric mantle (SCLM) has also been reported. Specifically, trace elements and isotopic ratios, in particular Sr and Nd isotopic data from the mafic rocks in the WIP, display OIB-type signatures or signatures suggesting the presence of a depleted continental mantle [Hogan et al., 1995; Lidiak et al., 2014; Brueseke et al., 2016], opening up the possibility of having a SCLM component in the WIP. Although the zircon trace-element data of felsic rocks with relatively younger ages in the WIP suggest a partially melted asthenosphere source, similar zircon trace-element results in older rocks of the WIP suggest a modified continental lithosphere source [Wall et al., 2020]. Wall et al. [2020] concluded that the thermal anomaly first caused the melting of the SCLM and the subsequent formation of the older rocks in the WIP, followed by asthenosphere upwelling and intensified formation of the younger rocks. The potential existence of a SCLM component in the WIP provides

another possible source for the observed primordial He-Ne signature in east Panhandle. Castro et al. [2009] suggested that the solar-like component observed in the Michigan Basin can be accounted for by a shallow refractory reservoir in the Archean SCLM. Ancient SCLMs, in particular Archean SCLMs, are distinct from younger SCLMs both in chemical composition and evolution history [e.g., Dunai and Procelli, 2002; Gautheron and Moreira, 2002; Gautheron et al., 2005]. The latter are depleted, refractory, and buoyant relative to the asthenosphere, greatly limiting their potential for recycling, enhancing preservation over time [e.g., Menzies, 1990; Griffin et al., 1999; Young and Lee, 2009]. They tend to be rich in depleted lherzolites and harzburgites [Griffin et al., 2004], which suggests a highly depleted U-Th-K environment [Anderson, 1998; Rudnick and Nyblade, 1999]. Depleted U-Th environments together with a high concentration of depleted lherzolites and harzburgites suggests the presence of potential He and Ne reservoirs at relatively shallow depths, likely serving as reservoirs for primordial noble gas components [Graham et al., 1990; Anderson, 1998; Coltice and Ricard, 2002; Meibom et al., 2005]. Most of the PHF basement rocks belongs to the Mazatzal Province [~1.65Ga; Shaw and Karlstrom, 1999] and is likely to be comparable to the SCLM underneath the Michigan Basin and thus, replicate its depleted nature. The similarity of the solar-like He-Ne signatures found in both, Michigan Basin brines and the east Panhandle gas samples may suggest a common source for both solar-like components, possibly a shallow refractory reservoir within the depleted SCLM created by one of the mechanisms proposed by Anderson [1998].

At this stage, it is not possible to determine which of the two mechanisms discussed above is responsible for the observed mantle signature in the east Panhandle Field, i.e., a mantle plume versus the SCLM. Either way, the presence of a primordial mantle component in the east Panhandle Field, together with the upward flux of terrigenic noble gases strongly suggests a high

level of openness of the reservoir rock in this area. As for the west Panhandle Field, the presence of mantle helium and the possibility of receiving hydrocarbons and noble gases from regional groundwater flow is also an indication of a relatively open system. Below, the open versus close nature of the PHF reservoir rocks as well as in-situ production contributions are evaluated through a more in-depth crustal noble gases analysis. Noble gas data from natural gas samples from Ballentine and Lollar [2002], collected in Texas Hugoton, Oklahoma and Kansas (Fig. 2.1) are combined with data from this study to provide a more comprehensive view of the entire PHF.

Table 2.4 Endmember isotopic and elemental ratios of distinct earth reservoirs

	Isotopic ratios			Elemental ratios			$(^4He/^{22}Ne)_{crust}$ / $(^4He/^{22}Ne)_{mantle}$
	R/Ra	$^{20}Ne/^{22}Ne$	$^{21}Ne/^{22}Ne$	$^4He/^{20}Ne$	$^3He/^{22}Ne$	$^4He/^{22}Ne$	
Crust[a]	0.05	0.3	0.47			7.9×10^7	
			0.1				
Mantle							
Primordial (primitive solar nebula)[b]	120	13.8	0.0328	850		1.17×10^4	6735
OIB mantle (Iceland)[c]	35	13.8	0.035		6	1.24×10^5	636
OIB mantle (Hawaii)[c]		13.8	0.039				
OIB mantle (Reunion)[c]		13.8	0.043				
OIB mantle (Kerguelen)[c]		13.8	0.053				
MORB mantle[c]	8	13.8	0.075		8.8	7.50×10^5	105

[a] R/Ra ratio after Oxburgh et al. [1986]; $^{21}Ne/^{22}Ne$ after Kennedy et al. [1990]. $^4He/^{22}Ne$ ratio after Yatsevich and Honda [1997].

[b] R/Ra ratio after Starkey et al. [2009]; $^{20}Ne/^{22}Ne$ and $^{21}Ne/^{22}Ne$ ratios after Benkert et al. [1993]; $^4He/^{20}Ne$ ratio after Anders and Grevesse [1989]; $^4He/^{22}Ne$ ratio calculated from $^4He/^{20}Ne$ and $^{20}Ne/^{22}Ne$ ratios.

[c] Summarized by Graham (2002); Iceland - Dixon et al. (2000), Hawaii - Honda et al. (1991), Reunion - Hanyu et al. (2001), Kerguelen - Valbracht et al. (1996), MORB - Moreira et al. (1998). $^4He/^{22}Ne$ ratios calculated from $^3He/^{22}Ne$ and R/Ra ratios.

Table 2.5 Ne isotopic compositions after correction of atmospheric component

Sample ID	$(^{20}Ne/^{22}Ne)_{crust+mantle}$	$(^{21}Ne/^{22}Ne)_{crust+mantle}$
West		
Bivins-2R	3.645±0.006	0.3708±0.0002
Bivins-a-88	3.161±0.007	0.3851±0.0002
Bivins-a-96	4.308±0.005	0.3511±0.0001
Bivins-a-201	2.866±0.005	0.3938±0.0001
Bivins-a-217	2.403±0.007	0.4076±0.0002
Bivins-a-219	1.692±0.010	0.4287±0.0003
East		
Griffin-2	12.591±0.002	0.1055±0.0001
Hanner-No1-x	14.535±0.0143	0.0478±0.0004
Johnson-3	12.789±0.005	0.0996±0.0001
Johnson-5	6.989±0.003	0.2716±0.0001
Tibbets-No1	13.031±0.005	0.0925±0.0001
Wilson-2	13.570±0.003	0.0765±0.0001

2.5.3. In-situ Production versus an External Origin for Noble Gases

The elemental ratios between terrigenic $^{4}He^{*}$, $^{21}Ne^{*}$ and $^{40}Ar^{*}$ are a function of their parental nuclides (U, Th, K, O, F, Mg) in the rocks where they were produced [e.g., Ballentine and Burnard, 2002; Pinti and Marty, 1995, 1998]. These ratios can be also impacted by solubility or diffusive fractionation during migration between sedimentary strata [Kennedy et al., 2002]. Figure 2.7 shows $^{21}Ne^{*}/^{40}Ar^{*}$ ratios as a function of $^{4}He^{*}/^{40}Ar^{*}$ ratios for the Panhandle samples (this study) and those previously published for the Hugoton Field further north [Ballentine and Lollar, 2002]. In-situ production ratios between $^{4}He^{*}$, $^{21}Ne^{*}$ and $^{40}Ar^{*}$ are estimated from elemental concentration data of the reservoir rock in the PHF [Pierce, 1964], while average and lower crust

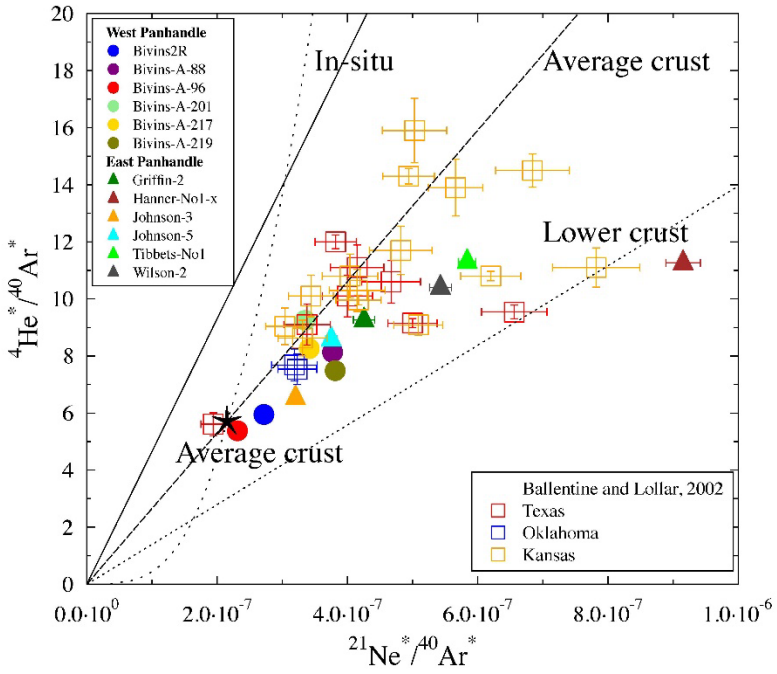

Figure 2.7 $^{21}Ne^{*}/^{40}Ar^{*}$ ratios plotted as a function of $^{4}He^{*}/^{40}Ar^{*}$ ratios of the Panhandle samples in this study and those from Ballentine and Lollar [2002]. The solid straight line represents solubility-controlled elemental fractionation from in-situ production of the reservoir rock [$^{4}He^{*}/^{40}Ar^{*}$=2×10-7, $^{21}Ne^{*}/^{40}Ar^{*}$=10, Pierce, 1964]. The dashed straight line represents the solubility-controlled elemental fractionation from average crust [$^{4}He^{*}/^{40}Ar^{*}$=2.15×10-7, $^{21}Ne^{*}/^{40}Ar^{*}$=5, Ballentine and Burnard, 2002], with the composition of average crust represented by black star. The dotted straight line represents the solubility-controlled elemental fractionation from lower crust [$^{4}He^{*}/^{40}Ar^{*}$=2.15×10-7, $^{21}Ne^{*}/^{40}Ar^{*}$=3, Ballentine and Burnard, 2002]. The dotted curve passing through average crust point represents the diffusion-controlled fractionation line.

production ratios are from Ballentine and Burnard [2002]. Solubility-dependent fractionation lines from in-situ production (solid), average crust (dashed) and lower crust (dotted) are straight lines since the solubility of He and Ne are similar in subsurface environments [Ballentine and Burnard, 2002; Fernandez-Prini et al., 2003]. Thus, the $^{4}He^{*}/^{21}Ne^{*}$ ratio in subsurface fluids should remain constant.

It is apparent that most of the samples, both from this study and those from Ballentine and Lollar [2002], do not follow the in-situ production line (Fig. 2.7). Rather, many of the samples plot close to the fractionation line for the average crust composition, suggesting the presence of an external flux of radiogenic/nucleogenic noble gases from a crust-like source outside of the reservoir rock. On the eastern side of Panhandle Field, the existence of external noble gases from underlying crustal formations is apparent as indicated by the correlation between depth and terrigenic noble gases (Fig. 2.4). In addition, the presence of a mantle signature in the east Panhandle Field as discussed above is also an indication of the involvement of noble gases from both, a mantle source and the lower crust. These findings are further supported by the fact that all samples from the east Panhandle Field fall between average crust and lower crust lines, with Wilson-2 falling close to the lower crust (Fig. 2.7). On the other hand, the presence of groundwater-delivered terrigenic noble gases from adjacent basins on the west Panhandle Field, is further supported by the proximity of these samples to the fractionated average crust line and non-fractionated crustal production value (Fig. 2.7). The Hugoton samples from Ballentine and Lollar [2002] display a wider range of values, with most samples falling near the average crust line, with a few samples closer to or on the fractionated lower crust line. Ballentine and Lollar [2002] suggest that externally produced noble gases in the Hugoton Field originate in western adjacent basins (e.g., the Dalhart Basin, Fig. 2.1), since regional W-E groundwater flow is also present in the deep

basin brine aquifer in that area [Dubois et al., 2007]. None of the samples follows the diffusivity-dependent fractionation pattern (dotted curve). It is also noteworthy that sample Hanner-No1-x plots close to the lower crust line (Fig. 2.7) while displaying the most OIB-like Ne isotopic signature (Fig. 2.5). This is consistent with the presence of noble gases from both the lower crust and OIB-type mantle in the east Panhandle, potentially through the basement faults bounding the Amarillo Uplift [Fig. 2.1, Hanson et al., 2013; Campbell, 2007]. From the discussion above, it is apparent that the PHF reservoir rocks exhibit a significant level of openness and thus, noble gases with an external origin could account for most of the total terrigenic noble gas content in all samples. To further test this hypothesis, an estimation of the contributions from both in-situ production and external inputs is needed.

The accumulation of radiogenic and nucleogenic noble gas isotopes in the crust depends on three main factors: 1) the production rate of the isotope of interest; 2) the time period during which production and accumulation took place, and; 3) the release efficiency of the produced isotope from the host rock to the pore space. The production rate of an isotope can be calculated using the concentration and decay rate of the corresponding parent element. For instance, ^{4}He is a product of the α-decay of U and Th and its production rate is given as [Craig and Lupton, 1976]:

$$J(^4\mathrm{He}) = 0.2355 \times 10^{-12} \times [\mathrm{U}]\left(1 + 0.123\left(\frac{[\mathrm{Th}]}{[\mathrm{U}]} - 4\right)\right) \tag{2.7}$$

where J(^{4}He) is the production rate of ^{4}He in units of cm^{3}STP·g^{-1}yr^{-1}, and [U], [Th] are the concentrations of U and Th in rock in ppm, respectively. The in-situ produced ^{4}He is calculated following [modified from Torgersen, 1980]:

$$[^4\mathrm{He}] = \frac{J(^4\mathrm{He})\rho t \Lambda R(1-\varphi)}{\varphi(1-S)} \tag{2.8}$$

where [^{4}He] is the volume fraction of ^{4}He in natural gas, ρ is the density of the rock in gcm^{-3}, t is the production time in years, φ is the rock porosity, S is the water saturation rate since part of the pore space is filled by water, and Λ is the release efficiency of the produced ^{4}He from the host rock to the pore space ($0 \leq \Lambda \leq 1$). R represents the expansion coefficient from the reservoir under standard surface conditions, i.e., an atmospheric pressure of 1 atm and local mean annual temperature (MAAT) of 13°C, and is expressed as:

$$R = \frac{T_{Rev} \times P_{STP}}{P_{Rev} \times T_{STP}} \tag{2.9}$$

where P stands for the pressure and T represents the temperature. Subscripts "Rev" and "STP" stand for reservoir and standard surface conditions.

Using a similar approach, the in-situ production of radiogenic ^{40}Ar* is calculated as follows [modified from Ballentine and Burnard, 2002]:

$$J[^{40}Ar] = \frac{102.2[K] \times V_{STP}}{NA} \tag{2.10}$$

where [K] is the concentration of potassium in the rock in ppm, V_{STP} is the molar volume of ideal gas in cm^3 and NA is the Avogadro number. The calculated production rate of ^{40}Ar can be applied to equation (2.2) for the expected volume fraction of ^{40}Ar*.

The in-situ production of ^{4}He* and ^{40}Ar* are calculated under two scenarios: 1) assuming that the reservoir rock contains pure granite to simulate the granite wash reservoir, and; 2) assuming a reservoir rock that matches the average composition of the Wolfcampian reservoir with carbonate and shale interbeds. These two scenarios represent the extreme conditions when ^{4}He* and ^{40}Ar* are produced solely in each of the two major types of reservoir rocks in the PHF, to help constrain the potential limits of in-situ noble gas production. The in-situ production of noble gases in potential source rocks in the Anadarko and Palo Duro basins is either minor or negligible, since a) the time period between hydrocarbon production and migration (< 75Myrs) in source rocks is

significantly shorter than the hydrocarbon emplacement time (< 295Myrs) in the PHF and; b) the concentrations of parental elements (U, Th and K) in the source rocks are not significantly higher than those of in the PHF reservoirs [e.g., Jolly, 1988]. The release efficiency (Λ) of both He and Ar is assumed to be 100%, which is reasonable for He due to its high diffusivity. However, the release of Ar from parent minerals is significantly more difficult to accurately assess compared to He and thus, our estimation should represent the upper limit for $^{40}Ar^*$ in-situ production. Parameters used in the estimation of in-situ production under both scenarios are listed in Table 2.6. The percentage of calculated $^{4}He^*$ and $^{40}Ar^*$ in-situ produced with respect to total measured volume fractions are provided in Table 2.7. This estimation assumes that all of the produced isotopes remain in the reservoir during its entire geological, which leads to an upper limit of in-situ production estimation.

Estimation of in-situ produced $^{4}He^*$ shows that, under the first scenario, about 28-65% of the total $^{4}He^*$ resulted from in-situ production in the east Panhandle Field. The percentages decrease to approximately 13.26%-23.52% in the west Panhandle Field and about 6.09-21.76% in the Hugoton Field. As for $^{40}Ar^*$, the estimated values account for around 21.22-75.74%, 11.29%-20.26% and 9.15%-25.47% in the east Panhandle, west Panhandle and Hugoton Fields, respectively. Under the second scenario, estimated in-situ produced $^{4}He^*$ accounts for about 23.99-55.02% of the total $^{4}He^*$ in east Panhandle Field. Like the first scenario, the percentages decrease in the west Panhandle and Hugoton Fields to approximately 11.15%-19.77% and 5.11%-18.29%, respectively. As for $^{40}Ar^*$, the estimated values account for about 22.07-78.79%, 11.75%-21.07% and 9.52%-26.46% in the east Panhandle, west Panhandle and Hugoton Fields, respectively. It is apparent that for all the samples, in-situ production cannot account for the observed amount of radiogenic noble gases, and external sources are required. This finding is consistent with previous

studies in other sedimentary basins, where external inputs of radiogenic noble gases are present [Castro and Goblet, 2003; Ma et al., 2005; Wen et al., 2015a, b; Zhou and Ballentine, 2006]. Because the estimation primarily assumes a closed-system scenario, which means all the in-situ produced noble gases since deposition (~295 Ma) remained in place, this estimation represents an upper-limit of the in-situ production percentage. Only two of the samples have in-situ $^{4}He^{*}$ production over 50%, while three samples display $^{40}Ar^{*}$ in-situ production over 50%. All these samples are from the east Panhandle Field. It is thus likely that in-situ production represents a minor contributor of terrigenic noble gases in most of the samples, in particular, those from the western PHF. In-situ production variations between the east and west Panhandle Field are present, with the east Panhandle samples displaying generally higher of in-situ production contributions compared to the western side (Table 2.7). Considering that the east Panhandle Field has potentially received influx from underlying sedimentary sequences and the basement rock, while the western side received most of the input from groundwater with some contribution from underlying strata, a lower percentage of in-situ production in the west Panhandle samples is expected. This would also be consistent with findings by Ballentine and Lollar [2002] and Brown [2019] which considered groundwater as an important factor of helium enrichment in the PHF.

Besides the variation between west and east Panhandle Field, a spatial distribution pattern can also be vaguely identified based on the estimation of in-situ production. Samples from the eastern side of PHF are relatively less abundant in external radiogenic noble gases with respect to the western side samples (west Panhandle and Hugoton Fields). Even though samples from the Hugoton Field have their in-situ production percentages close to those of the west Panhandle Field samples (Table 2.7), the lowest percentages exist in the Hugoton samples. Since the accumulation of radiogenic noble gases in crustal environments is a highly time-dependent process, the potential

distribution pattern of radiogenic noble gases likely reflects a spatial pattern of sample ages. In the next section, a more in-depth analysis of the relative chronological relationship between different locations of the PHF is carried out to test this hypothesis.

Table 2.6 Parameters used in the estimation of in-situ production of $^{4}He^{*}$ and $^{40}Ar^{*}$

Lithology	Thickness (m)	Pressure (psi)	Temperature (°C)	Saturation Rate	Porosity	Density (g/cm^3)	U (ppm)	Th (ppm)	K (ppm)
Granite wash[a]	121	360	32	1	0.05	2.6	2.8	10.7	20000
Wolfcampian reservoir[b]					0.08	2.7	4	14.4	33100

[a] Average thickness, pressure and temperature of the PHF reservoir is from Mason [1968]; Density and chemical composition of granite wash is approximated by average upper crust from Leventhal [1980].

[b] Porosity of carbonate reservoir is from Watney and French [1988]; Density and chemical composition of Wolfcampian reservoir is from Pierce [1964].

Table 2.7 Estimated percentages of in-situ production of $^{4}He^{*}$ and $^{40}Ar^{*}$

		Eastern Panhandle	Western Panhandle	Hugoton*
Scenario 1 (Granite wash)	$^{4}He^{*}$	28.53 – 65.46%	13.26 – 23.52%	6.09 – 21.76%
	$^{40}Ar^{*}$	21.22 – 75.74%	11.29 – 20.26%	9.15 – 25.47%
Scenario 2 (Carbonate)	$^{4}He^{*}$	23.99 – 55.02%	11.15 – 19.77%	5.11 – 18.29%
	$^{40}Ar^{*}$	22.07 – 78.79%	11.75 – 21.07%	9.52 – 26.46%

*Samples from Ballentine and Lollar (2002)

2.5.4. Relative Ages and Spatial Distribution Pattern of Natural Gas

The observed variation of radiogenic noble gases across the PHF points to a potential spatial distribution pattern of gas ages. One way to assess the relative ages of gas samples from different locations in a particular gas the field is via a modified Ar isochron method. In Ar-Ar dating, $^{36}Ar/^{40}Ar$ is commonly plotted as a function of $^{39}Ar/^{40}Ar$, where ^{39}Ar is an artificially produced proxy for potassium [McDougall and Harrison, 1999]. Because ^{40}Ar appears in the denominator of both the x and y values of such a plot, any mixture between two fixed end members, i.e., a single initial $^{36}Ar/^{40}Ar$ and a single $^{39}Ar/^{40}Ar$ ratio will plot along a line. Since the apparent age of a rock sample is a function of the $^{39}Ar/^{40}Ar^{*}$ ratio, where $^{40}Ar^{*}$ is the pure crustal (radiogenic) component, the x-intercept of an isochron line defines the argon age of the rock sample [McDougall and Harrison, 1999]. By analogy to the Ar-Ar dating isochron procedure, a similar graphical analysis can be used to provide a relative gas sample age. Instead of $^{39}Ar/^{40}Ar$ values, $1/^{40}Ar$ is plotted on the x-axis under the assumption that a universal potassium content is applied to all samples. A gas sample will consist of a mixture of the atmospheric $^{36}Ar/^{40}Ar$ ratio (y-intercept) and a fixed crustal volume fraction (x-intercept). In this plot, relative ages increase from right to left and samples that share the same K-content in their source and the same transport history should plot along a mixing line between air and a fixed x-intercept value of $1/^{40}Ar$.

Figure 2.8a shows $^{36}Ar/^{40}Ar$ ratios as a function of $1/^{40}Ar$ values in the Panhandle Field. Samples Wilson-2 and Hanner-No1-x from east Panhandle display the youngest relative age among the Panhandle samples, while sample Bivins-A-219 from west Panhandle displays the oldest age (Fig. 2.8a). It is apparent that most of the east Panhandle samples (light yellow area,

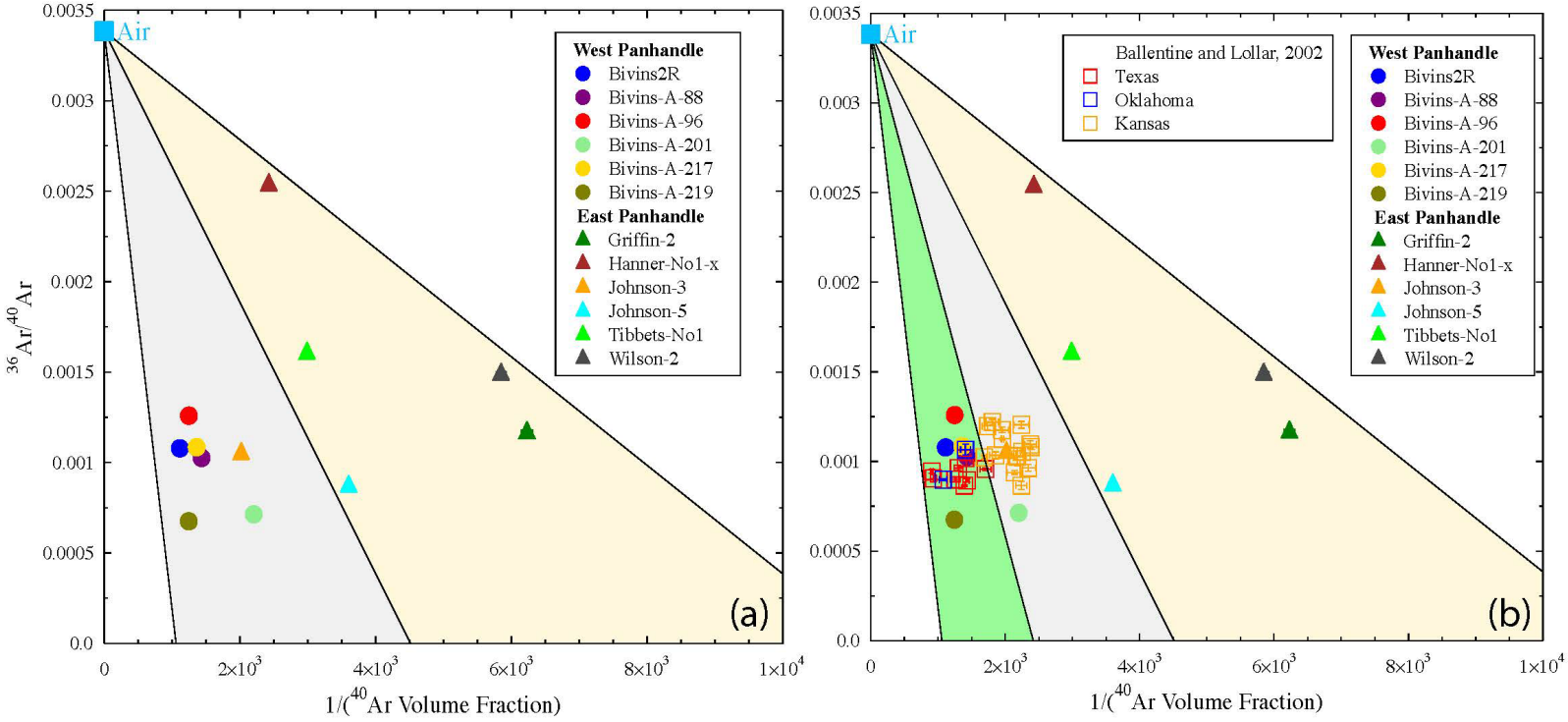

Figure 2.8 (a) $^{36}Ar/^{40}Ar$ ratios as a function of the reverse of ^{40}Ar volume fractions for all gas samples in this study. (b) $^{36}Ar/^{40}Ar$ ratios as a function of the reverse of ^{40}Ar volume fractions for samples in this study and those of Ballentine and Lollar [2002]. Age groups are indicated by different color.

Fig. 2.8a) display relative ages about 3-6 times younger than the west Panhandle samples (grey area, Fig. 2.8a). Figure 2.8b shows $^{36}Ar/^{40}Ar$ ratios versus $1/^{40}Ar$ values for the Hugoton samples [Ballentine and Lollar, 2002] plotted together with samples from the Panhandle Field (this study). From this plot, it is apparent that the variation in relative ages is also present within the Hugoton Field. The wider age variations are observed primarily between samples from Kansas Hugoton (orange boxes) and those from Texas/Oklahoma Hugoton (red and blue boxes). Samples from Kansas Hugoton are relatively younger compared to the samples from Texas and Oklahoma Hugoton. Some of Texas Hugoton samples display the oldest relative ages among all samples (Fig. 2.8). A spatial pattern of the relative ages appears to emerge with the two [this study, Ballentine and Lollar, 2002] combined datasets. Three age groups are apparent (Fig. 2.8b): 1) the youngest relative ages group represented by the east Panhandle samples (light yellow area); 2) intermediate relative ages represented by the Kansas Hugoton samples (grey area), and; 3) the oldest relative ages represented by most west Panhandle samples together with those from Texas and Oklahoma Hugoton (light green area). Relative ages increase from group 1 to group 3. The meaning of these relative ages and their potential implications in terms of sources and migrations of natural gases in the PHF is discussed below.

In conventional hydrocarbon fields, due to the existence of primary (within the source rock and from the source rock to the reservoir) and secondary migration (within the reservoir), the apparent ages of natural gas samples may not reflect their formation ages, since the different accumulation rates of radiogenic noble gases within the reservoir and the source rocks render the reconstruction of the actual ages of the gas samples difficult. In the absence of an external component, it is fair to assume that the apparent ages of natural gas samples in a conventional field reflect the timing of their migration from the source rock to the reservoir rock, especially when the

reservoir rocks contain low concentrations of parent elements and therefore, have negligible contribution from in-situ production. However, this assumption may not hold when natural gases experience long distance migration. A more recent study in the East Texas Basin proposes that the accumulation of radiogenic noble gases, particularly $^{40}Ar^*$, is highly dependent on migration distances of natural gas [Byrne et al., 2020]. Their model reveals that most radiogenic $^{40}Ar^*$ in these samples are accumulated along the migration pathway, with $^{40}Ar^*$ abundances being directly proportional to the migration distance. The well-established hydrocarbon charge history indicates that hydrocarbon phases generated in the Anadarko Basin first migrated southward into the Panhandle Field, and subsequently moved northward to the Hugoton Field due to gas expansion [Fig. 2.9; Sorenson, 2005; Brown, 2019]. If the same assumption is applied to all the PHF samples [this study; Ballentine and Lollar, 2002], one would expect the east Panhandle samples to display the youngest relative ages as they are the closest to the source rock area, and this is indeed the case. On the other hand, the Kansas Hugoton samples would be expected to display the oldest ages as they would have experienced the longest migration. However, except for the east Panhandle samples, the relative ages of the west Panhandle and Hugoton Field samples derived from the modified Ar isochron method do not align with the expected scenario, with the Kansas Hugoton samples being younger than samples in western Panhandle, Texas Hugoton and Oklahoma Hugoton (Fig. 2.8b, Fig. 2.9).

The apparent inconsistency might be explained by the impact of groundwater flow on noble gas concentrations. Five contributing factors should be considered when interpreting the relative ages of the PHF samples: 1) crustal contribution from the Anadarko Basin source rock; 2) accumulation along the migration pathway; 3) in-situ production within the reservoir rock; 4) upward noble gas flux from sedimentary sequences and basement rocks, and; 5) noble gas

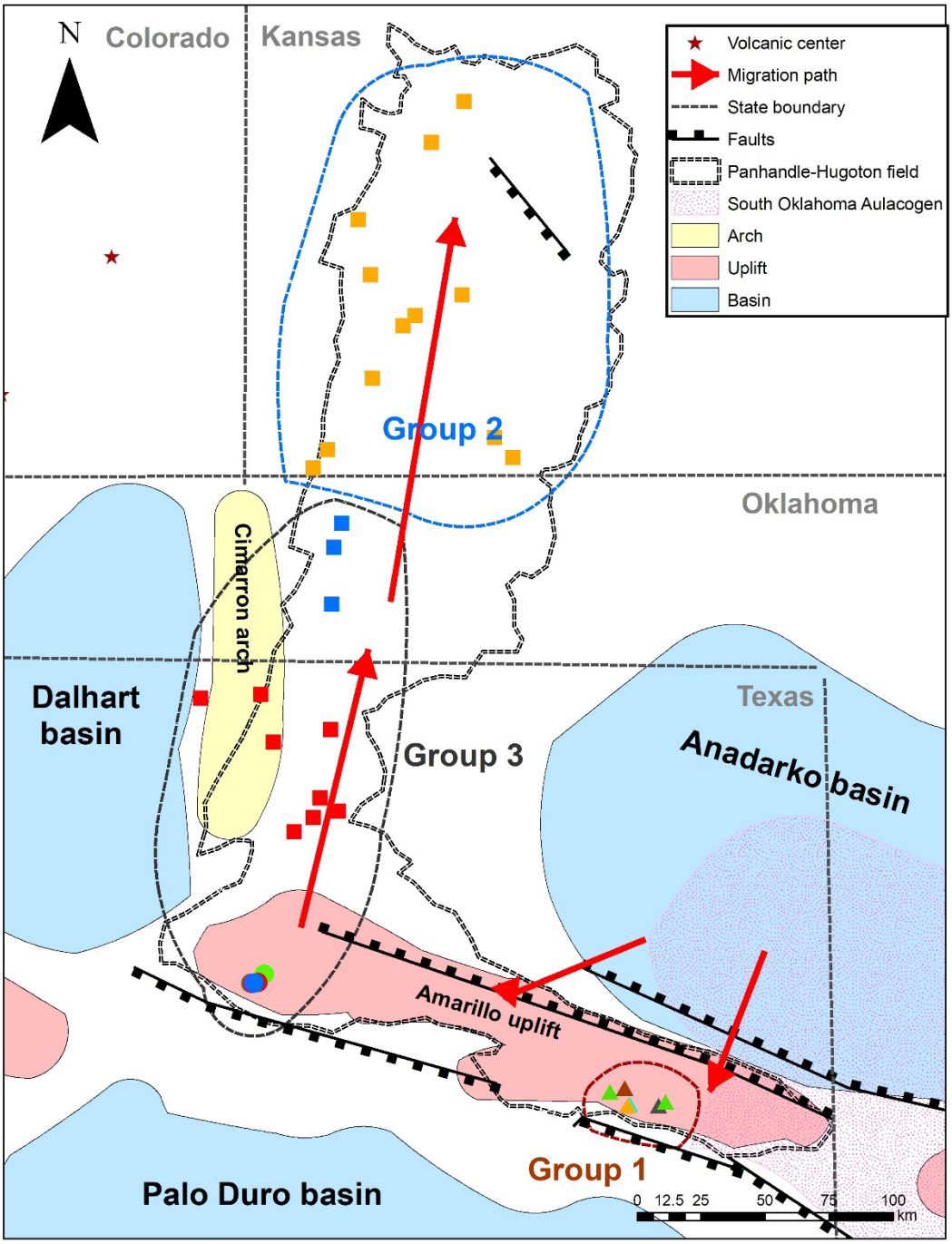

Figure 2.9 Relative age groups based on modified Ar isochron method in Panhandle samples and samples from Ballentine and Lollar [2002]. Relative ages increase from group 1 to group 3. Red arrows indicate the hydrocarbon migration pathways concluded by Sorenson [2005]. Major geological units and state boundaries are also shown.

contributions from adjacent basins transported by groundwater. Contributing factors 1) and 3) are either minor or negligible considering the insufficient time periods for in-situ production in both the source and reservoir rocks to account for the measured terrigenic noble gases. Among the remaining three sources, a depth versus terrigenic noble gases correlation suggesting a dominant upward flux is only observed in the east Panhandle samples. No sample depth is provided by Ballentine and Lollar [2002], and thus it is not possible to correlate noble gases with depth for samples in the Hugoton Field, but the lack of basement faults in the Hugoton area may have inhibited the input from deep formations in that region (Fig. 2.1). As for contributions along the migration pathway, natural gas sample ages from east Panhandle samples are consistent with this scenario, displaying both the youngest ages and shortest migration distance. Samples from west Panhandle, Texas Hugoton and Oklahoma Hugoton may have received more groundwater flow, or the groundwater they have interacted with is more enriched in radiogenic components. Below, a combined analysis of both terrigenic and atmospheric noble gases is carried out to quantitatively evaluate the potential impact of groundwater flow in the western PHF samples.

2.5.5. Impact of Groundwater Flow as Revealed by Water/Gas Volume Ratio Estimation

In the modified Ar isochron method, the inverse of the x-intercept values reflects the abundance of radiogenic ^{40}Ar* in the terrigenic endmember, with increasing inverse intercept values representing higher accumulation of radiogenic ^{40}Ar and thus, higher relative ages. Table 2.8 lists the ^{40}Ar* crustal endmember calculated for each sample in the Panhandle (this study) and Hugoton [Ballentine and Lollar, 2002] fields based on the x-intercept values obtained for each sample. It is apparent that the x-inverse intercept values display a spatial variation pattern, with the west Panhandle samples and samples from Oklahoma and Texas Hugoton showing the highest

intercept values, the east Panhandle samples showing the lowest values and Kansas Hugoton samples displaying intermediate values.

Regional groundwater flow was proposed to explain the discrepancy between relative ages and the well-established migration history, as an increased impact from groundwater may lead to greater accumulation of terrigenic isotope abundances in the Texas and Oklahoma Hugoton areas. To estimate the impact of groundwater on atmosphere-derived noble gases, ^{36}Ar is used to calculate the volume ratio between natural gas and groundwater. ^{36}Ar in sedimentary systems originates mostly from atmospheric sources, considering that the production of ^{36}Ar in sedimentary environment is negligible [Bosch and Mazor, 1988; Ballentine et al., 1996]. The atmospheric noble gases in subsurface reservoirs (ASW component) originates primarily from groundwater. Subsequent interactions between groundwater and natural gas results in the partition of atmospheric noble gases, as the latter move into the gas phase. Thus, under the assumption that the AWS noble gas component in natural gas samples, and ^{36}Ar in particular, are solely derived from groundwater, it is possible to estimate the volume ratio between groundwater and natural gas. Using such an approach, Byrne et al., [2020] estimated the volume ratio between water (V_w) and gas (V_g) as follows:

$$\frac{V_g}{V_w} = \frac{\rho_w C^{ASW}}{C^{meas}} - \frac{16T\rho_w}{195K_{Ar}^m} \tag{2.11}$$

where subscripts *ASW* and *meas* refer to air-saturated water at local standard surface conditions and total measured sample value, respectively. C refers to the concentrations of ^{36}Ar, T is the reservoir temperature (62°C, Table 2.6; Fisher, 1995), ρ_w is the water density, and K_{Ar}^m is the Henry's constant of Ar under reservoir conditions [calculated after Ballentine et al, 2002].

Calculated PHF water/gas ratios are shown in Table 2.8. The east Panhandle samples display generally the lowest water/gas volume ratios, except for Hanner-No1-x (Table 2.8). The

generally lower Vw/Vg ratios indicate a smaller impact from groundwater flow, and may explain why Ne mantle signals can be identified in this area. The abnormally high Vw/Vg ratio in Hanner-No1-x may be an indication that the assumed single-stage water-gas equilibrium scenario is not applicable to this sample. An alternative explanation is that instead of a simple water-gas interaction, sample Hanner-No1-x may have received influence from the oil phase within the reservoir itself. Considering that solubilities of all noble gases in oil are significantly higher than those in water [Kharaka and Specht, 1988], equilibration with large amounts of ASW may lead to significantly higher ^{36}Ar concentration in the oil phase with respect to ASW. If the oil phase interacts with natural gas, the oil-equilibrated gas phase may end up with a higher ^{36}Ar concentration compared to ASW-equilibrated gases, and thus, a higher Vw/Vg ratio. The highest Vw/Vg ratios are present in samples from the west Panhandle Field, Texas Hugoton and Oklahoma, while the Kansas Hugoton samples fall between these two groups.

In figure 2.10, the estimated PHF water/gas ratios are plotted as a function of estimated ^{40}Ar* crustal endmembers. It is apparent that water/gas ratios are positively correlated with their relative ages in most samples, except for sample Hanner-No1-x, which may not have undergone a water-gas interaction as discussed above. A similar positive correlation is also observed in Byrne et al. [2020], where increasing Vw/Vg ratios are accompanied by higher abundances of radiogenic ^{40}Ar*. Byrne et al. [2020] argued that longer migration distances allow for the gas phase to interact with more formation water along the pathway and also acquire more radiogenic isotopes. However, even though the east Panhandle samples can be explained by the migration distance theory as they are the closest to the source rock and also least enriched in ^{40}Ar*, Byrne et al. [2020] hypothesis cannot account for the observed pattern in the western side of the PHF. If the estimated Vw/Vg ratios were solely dependent on migration distances, higher Vw/Vg ratios and relative ages would

be expected in the Kansas Hugoton samples, as they have experienced the longest migration distance among all samples [Sorenson, 2005]. However, this is not observed. On the other hand, more interaction with groundwater in West Panhandle, Texas Hugoton and Oklahoma Hugoton samples results in higher Vw/Vg ratios and also higher concentrations of $^{40}Ar^*$, since groundwater flow may have collected crustal noble gases from adjacent basins (e.g., Dalhart and Palo Duro basins, Fig. 2.1). This hypothesis is also supported by the regional hydrogeological setting, as the deep brine aquifer within the Kansas Hugoton area displays a significantly lower hydraulic gradient compared to the West Panhandle, Texas Hugoton and Oklahoma Hugoton areas [Dubois

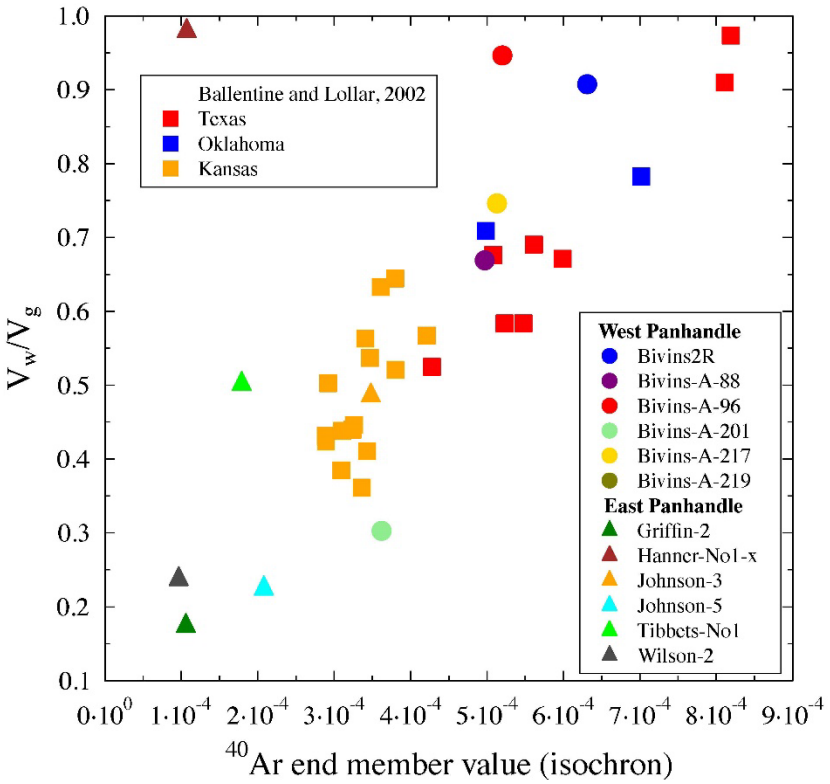

Figure 2.10 Estimated water/gas ratios plotted as a function of the reverse of x-intercept in the modified Ar isochron method for samples in this study and from Ballentine and Lollar [2002].

et al., 2007]. The W-E faults and fracture system distributed along the Amarillo uplift may have also facilitated the transport of groundwater into the west Panhandle area (Fig. 2.1). At this point, due to the complex origin of the radiogenic noble gases within the PHF, especially those from west

Panhandle and Hugoton Fields which may have received input from groundwater flow, Ar isochron relative ages, may be a more suitable parameter to represent radiogenic Ar present in the PHF. With this in mind, a more comprehensive view of factors affecting terrigenic noble gas abundances throughout the PHF emerges. Specifically, in the east Panhandle Field, the shortest migration distance, youngest migration ages and absence of significant groundwater flow results in the lowest Vw/Vg ratios and also the lowest abundance of terrigenic noble gases. Kansas Hugoton samples on the other hand display higher Vw/Vg ratios and terrigenic noble gas concentrations than the east Panhandle samples due to their longer migration and a W-E groundwater flow. Finally, in west Panhandle Field, Texas Hugoton and Oklahoma, the impact of groundwater is the most pronounced resulting in the highest water/gas ratios and terrigenic noble gas concentrations.

The observed pattern in the PHF clearly indicates that atmospheric noble gases in natural gas samples are a direct reflection of both, migration distance and groundwater flow. It is thus vital to consider both mechanisms when using water/gas volume ratios to assess potential migration patterns of natural gases.

Table 2.8 Reverse of x-intercept values from modified Ar isochron method and water/gas ratios of the PHF samples in this study and from Ballentine and Lollar [2002].

Sample ID	^{40}Ar endmember values	Vw/Vg	Sample ID	^{40}Ar endmember values	Vw/Vg
West Panhandle			Baughman H-2	$4.21*10^{-4}$	0.5670
Bivins-2R	$6.12*10^{-4}$	0.9074	Crayton A-1	$3.26*10^{-4}$	0.4459
Bivins-a-88	$4.86*10^{-4}$	0.6689	Mills C-1	$3.36*10^{-4}$	0.3611
Bivins-a-96	$5.04*10^{-4}$	0.9464	Parsley A-1	$2.89*10^{-4}$	0.4236
Bivins-a-201	$3.58*10^{-4}$	0.3026	Oberly A-1	$2.92*10^{-4}$	0.5027
Bivins-a-217	$4.99*10^{-4}$	0.7460	Tucker B-1	$3.80*10^{-4}$	0.5205
Bivins-a-219	$6.43*10^{-4}$	0.5064	Barnes A-1	$2.89*10^{-4}$	0.4313
East Panhandle			**Oklahoma Hugoton**[b]		
Griffin-2	$1.05*10^{-4}$	0.1744	Hill A-1	-	-
Hanner-No1-x	$1.03*10^{-4}$	0.9707	Buzzard D-1	$4.98*10^{-4}$	0.7087
Johnson-3	$3.42*10^{-4}$	0.4861	Stonberaker A-69	$7.02*10^{-4}$	0.7825
Johnson-5	$2.06*10^{-4}$	0.2250	**Texas Hugoton**[b]		
Tibbets-No1	$1.76*10^{-4}$	0.5018	Coffee-Estates#1	$5.48*10^{-4}$	0.5837
Wilson-2	$0.96*10^{-4}$	0.2375	Blake Trust Estates#2	$8.11*10^{-4}$	0.9098
Kansas Hugoton[b]			Mary A Long#1	$5.61*10^{-4}$	0.6901
Ratzlaff D "A" #1	$3.61*10^{-4}$		Donelson et al#1	-	-
Hefner Gas Unit #2	$3.41*10^{-4}$	0.6327	Sarah Claybaugh#1	-	-
Guldner Unit #1	$3.80*10^{-4}$	0.5629	Cameron Walls#1	$5.99*10^{-4}$	0.6709
Guldner Unit #2	$3.47*10^{-4}$	0.6445	Horner#1	$8.19*10^{-4}$	0.9735
Campbell, R.W. #1	-[a]	0.5367	Witherbee#2	$5.08*10^{-4}$	0.6761
Keller, Ernest #2	$3.43*10^{-4}$	-	Flores 23	$5.23*10^{-4}$	0.5834
Jarvis Unit #2	$3.09*10^{-4}$	0.4105	Nisbett#1	$4.28*10^{-4}$	0.5247
Ball, Clyde H. #2	$3.24*10^{-4}$	0.3846	McDade #2+#5	-	-
Wright "C" Unit #1	$3.10*10^{-4}$	0.4398	Brumley A#1	-	-

[a]Samples without Ar data are shown as "-".

[b]Samples from Kansas, Oklahoma and Texas Hugoton fields are from Ballentine and Lollar [2002].

2.6. Conclusions

Twelve gas samples were collected from twelve wells in the Panhandle Field in northern Texas, half in east Panhandle, half in west Panhandle, for the complete set of noble gas (He, Ne, Ar, Kr and Xe) analysis. A terrigenic component is present in all samples as revealed by noble gas data and a positive correlation between terrigenic noble gases ($^{4}He^{*}$ and $^{21}Ne^{*}$) and methane is observed in the west Panhandle Field. The latter suggests that both terrigenic noble gases and methane are produced and/or transported together. Hydrocarbons from adjacent basins to the west, e.g., Palo Duro and Dalhart basins, may have been primarily mixed with terrigenic noble gases and subsequently transported W-E by groundwater in the deep-basin brine aquifer to the west Panhandle Field. By contrast, no correlation is found between methane and terrigenic noble gases in east Panhandle. Instead, a positive correlation between terrigenic noble gases and depth is observed, suggesting a dominant upward flux from underlying strata and basement rocks in east Panhandle compared to other possible sources.

A combined analysis of the He and Ne isotopic composition reveals the presence of a primordial, OIB-type mantle component in the east Panhandle Field. This primordial component is likely associated with the presence of a mantle plume and emplacement of the Wichita Igneous Province (WIP) during the breakup of Rodinia. The WIP overlaps the westernmost area of the east Panhandle Field and extends further to the west. However, the possibility that the subcontinental lithospheric mantle (SCLM) is the source of this primordial component cannot be ruled out. West Panhandle samples display $(R/Ra)_c$ ratios higher (0.1008-0.1145) than typical crustal values and suggest the presence of a small mantle component. CO_2 contents are also higher than those in east Panhandle, suggesting that CO_2 and this mantle helium contribution originates in the Bravo Dome field.

The observed correlations between $^{4}He^{*}/^{40}Ar^{*}$ and $^{21}Ne^{*}/^{40}Ar^{*}$ in our dataset in the Panhandle Field together with that of Ballentine and Lollar [2002] in the Hugoton Field shows that all samples have solubility-controlled fractionation patterns similar to the average and lower crustal components, suggesting an external input from crustal sources. A first-order estimation of in-situ $^{4}He^{*}$ and $^{40}Ar^{*}$ production assuming a chemical composition of the granite wash reservoir or the Wolfcampian carbonate and shale reservoir suggests that in-situ production across the PHF accounts for a minor portion of the total crustal noble gases, in particular, in the west Panhandle and Hugoton Fields, with contributions varying from 5.11% to 21.76% for $^{4}He^{*}$, and from 9.15% to 26.46% for $^{40}Ar^{*}$. Contributions from in-situ production in the east Panhandle Field vary from 28.53% to 65.46% for $^{4}He^{*}$, and from 21.22% to 78.79% for $^{40}Ar^{*}$. The high percentages of external crustal noble gases in PHF samples also suggest a high level of openness of the reservoir, which is in agreement with the involvement of groundwater flow in west Panhandle and an upward flux in east Panhandle.

^{40}Ar elative ages determined through the modified Ar isochron method reveal the presence of three age groups with samples becoming increasingly older from east Panhandle to Kansas Hugoton to west Panhandle, Texas Hugoton and Oklahoma Hugoton. The volume ratio between groundwater (ASW) and gas can be estimated by the ^{36}Ar concentration in natural gas samples. More interaction with groundwater in West Panhandle, Texas Hugoton and Oklahoma Hugoton samples results in higher Vw/Vg ratios and also higher concentrations of terrigenic noble gases, since groundwater flow may have collected terrigenic noble gases from adjacent basins (e.g., Dalhart and Palo Duro basins) and transported them to these areas. The relatively low Vw/Vg ratios and terrigenic noble gas contents in east Panhandle are consistent with the shortest migration distance, youngest migration ages and absence of significant groundwater flow in this area.

This work highlights the potential of noble gases to trace the source and migration of hydrocarbons, while shedding light on understanding the impact of groundwater in hydrocarbon fields.

2.7. References

Adams, R. L. (1993). Effects of Inherited Pre-Jurassic Tectonics on the U. S. Gulf Coast. *GCAGS Transaction* 43, 1-9.

Aeschbach-Hertig, W., and Solomon, D. K. (2013). Noble Gas Thermometry in Groundwater Hydrology. In *The Noble Gases as Geochemical Tracers* (ed. P. Burnard). Springer Berlin Heidelberg. p. 81-122.

Algeo, T. J. (1992). Continent-scale wrenching of southwestern Laurussia during the Ouachita-Marathon orogeny and tectonic escape of the Llano block. In *Sequence stratigraphy applied to Permian basin reservoirs: outcrop analogs in the Caballo and Sacramento Mountains of New Mexico*. West Texas Geological Society, pp. 115-131.

Anders, E., and Grevesse, N., (1989). Abundance of the elements: meteoritic and solar. *Geochimica et Cosmochimica Acta* 53, 197–214.

Anderson, C. C., and Hinson, H. H. (1951). Helium-bearing natural gases of the United States: Analyses and analytical methods. *US Bureau of Mines Bulletin* 486, pp.141.

Anderson, D. L. (1998). A model to explain the various paradoxes associated with mantle noble gas geochemistry. *Proceedings of the National Academy of Sciences* 95, 9087–9092. doi:10.1073/pnas.95.16.9087

Ball, M. M., Henry, M. E., and Frezon, S. E. (1991). Petroleum Geology of the Anadarko Basin Region, Province (115), Kansas, Oklahoma, and Texas. US Geological Survey.

Ballentine, C. J., O'Nions, R. K., Oxburgh, E. R., Horvath, F., and Deak, J. (1991). Rare gas constraints on hydrocarbon accumulation, crustal degassing and groundwater flow in the Pannonian Basin. *Earth and Planetary Science Letters* 105, 229–246.

Ballentine, C. J., and O'Nions, R. K. (1992). The nature of mantle neon contributions to Vienna Basin hydrocarbon reservoirs. *Earth and Planetary Science Letters* 113, 553–567.

Ballentine, C. J., O'Nions, R. K., and Coleman, M. L. (1996). A Magnus opus: Helium, neon, and argon isotopes in a North Sea oilfield. *Geochimica et Cosmochimica Acta* 60, 831-849.

Ballentine, C. J. (1997). Resolving the mantle He/Ne and crustal 21Ne/22Ne in well gases. *Earth and Planetary Science Letters* 152, 233-249.

Ballentine, C. J., and Burnard, P. G. (2002). Production, release and transport of noble gases in the continental crust. *Review in Mineralogy and Geochemistry* 47, 481-538.

Ballentine, C. J., Burgess, R., and Marty, B. (2002). Tracing fluid origin, transport and interaction in the crust. *Review in Mineralogy and Geochemistry* 47, 539-614.

Ballentine, C. J., and Lollar, B. S. (2002). Regional groundwater focusing of nitrogen and noble gases into the Hugoton-Panhandle giant gas field, USA. *Geochimica et Cosmochimica Acta* 66, 2483–2497. doi:10.1016/S0016-7037(02)00850-5.

Ballentine, C. J., Marty, B., Lollar, B. S., and Cassidy, M. (2005). Neon isotopes constrain convection and volatile origin in the Earth's mantle. *Nature* 433, 33-38.

Barry, P. H., Lawson, M., Meurer, W. P., Danabalan, D., Byrne, D. J., Mabry, J. C., and Ballentine, C. J. (2017). Determining fluid migration and isolation times in multiphase crustal domains using noble gases. *Geology* 45, 775–778. doi:10.1130/G38900.1.

Bassett, R. L., and Bentley, M. E. (1983). Deep Brine Aquifers in the Palo Duro Basin: Regional Flow and Geochemical Constraints. Bureau of Economic Geology Report of Investigations No. 130. 59 p.

Beck, H. V. (1959). Geology and ground-water resources of Kansas River valley between Wamego and Topeka vicinity. State Geological Survey of Kansas Bulletin, 135, 88 p.

Benkert, J.-P., Baur, H., Signer, P., and Wieler, R. (1993). He, Ne, and Ar from the solar wind and solar energetic particles in Lunar ilmenties and pyroxenes. *Journal of Geophysical Research* 98, 13147-13162.

Boone, W. J. (1958). Helium-bearing natural gases of the United States: Analyses and analytical methods: Supplement to Bulletin 486. *US Bureau of Mines Bulletin* 576, pp.117.

Bosch, A., and Mazor, E. (1988) Natural gas association with water and oil as depicted by atmospheric noble gases: case studies from the southeastern Mediterranean Coastal Plain. *Earth and Planetary Science Letters* 87, 338-346.

Brown, A. A. (2010). Formation of high helium gases: A guide for explorationists. AAPG Search and Discovery article 80115, accessed July 27, 2018,

Brown, A. A. (2019). Origin of helium and nitrogen in the Panhandle–Hugoton field of Texas, Oklahoma, and Kansas, United States. *AAPG Bulletin* 103, 369–403. doi:10.1306/07111817343.

Brueseke, M. E., Hobbs, J. M., Bulen, C. L., Mertzman, S. A., Puckett, R. E., Walker, J. D., and Feldman, J. (2016). Cambrian intermediate-mafic magmatism along the Laurentian margin: Evidence for flood basalt volcanism from well cuttings in the Southern Oklahoma aulacogen (U.S.A.). *Lithos* 260, 164–177. doi:10.1016/ j.lithos.2016.05.016.

Burruss, R. C., and Hatch, J. R. (1989). Geochemistry of oils and hydrocarbon source rocks, greater Anadarko basin: Evidence for multiple sources of oils and long-distance oil migration, in *Anadarko basin Symposium* (ed. Johnson, K. S.). Oklahoma Geological Survey Circular 90, 53– 64.

Byrne, D. J., Barry, P. H., Lawson, M., and Ballentine, C. J. (2018). Determining gas expulsion vs retention during hydrocarbon generation in the Eagle Ford Shale using noble gases. *Geochimica et Cosmochimica Acta* 241, 240-254.

Byrne, D. J., Barry, P. H., Lawson, M., and Ballentine, C. J. (2020). The use of noble gas isotopes to constrain subsurface fluid flow and hydrocarbon migration in the East Texas Basin. *Geochimica et Cosmochimica Acta* 268, 186-208.

Campbell, J. A. (2007). Understanding the structure of the Wichita uplift, southern Oklahoma. *The Shale Shaker* 58 3, 87-97.

Cardott, B. J. (1989). Thermal maturation of the Woodford Shale in the Anadarko basin, in *Anadarko basin symposium* (ed. K. S. Johnson). Oklahoma Geological Survey Circular 90, pp. 32–46.

Castro, M. C., Jambon, A., Marsily, G. d., and Schlosser, P. (1998a). Noble gases as natural tracers of water circulation in the Paris Basin. 1. Measurements and discussion of their origin and mechanisms of vertical transport in the basin. *Water Resource Research* 34, 2443-2466.

Castro, M. C., Goblet, P., Ledoux, E., Violette, S., and Marsily, G. d. (1998b). Noble gases as natural tracers of water circulation in the Paris Basin. 2. Calibration of a groundwater flow model using noble gas isotope data. *Water Resource Research* 34, 2467-2483.

Castro, M. C., and Goblet, P. (2003). Calibration of regional groundwater flow models: Working toward a better understanding of site-specific systems: calibration of regional groundwater flow models. *Water Resource Research* 39, 1172. doi:10.1029/2002WR001653

Castro, M. C., Patriarche, D., and Goblet, P. (2005). 2-D numerical simulations of groundwater flow, heat transfer and 4He transport – implications for the He terrestrial budget and the mantle helium-heat imbalance. *Earth and Planetary Science Letters* 237, 893-910.

Castro, M. C., Ma, L., and Hall, C. M. (2009). A primordial, solar He-Ne signature in crustal fluids of a stable continental region. *Earth and Planetary Science Letters* 279, 174-184.

Chapman, R. E. (2000). *Petroleum geology*. Elsevier.

Chiarenzelli, J., Lupulescu, M., Cousens, B., Thern, E., Coffin, L., and Regan, S. (2010). Enriched Grenvillian lithospheric mantle as a consequence of long-lived subduction beneath Laurentia. *Geology* 38, 151–154. doi:10.1130/G30342.1.

Clarke, W. B., Jenkins, W. J., and Top, Z. (1976). Determination of tritium by mass spectrometric measurement of 3He. *The International Journal of Applied Radiation and Isotopes* 27, 515-522.

Coltice, N., and Ricard, Y. (2002). On the origin of noble gases in mantle plumes. *Philosophical Transactions of the Royal Society* 360, 2633–2648. doi:10.1098/rsta.2002.1084

Craig, H., and Lupton, J. E., (1976). Primordial neon, helium, and hydrogen in oceanic basalts. *Earth and Planetary Science Letters* 31, 369-385.

Craig, H., Lupton, J. E., and Horibe, Y. (1978). A mantle helium component in circum Pacific volcanic gases: Hakone, the Marianas, and Mt Lassen. In *Terrestrial Rare Gases* (eds. E.C Alexander, M. Ozima). Japan Sci Societies Press, Tokyo, 3–16.

Dehler, C. M. (1998). Facies analysis and environmental interpretation of the Middle Chuar Group (Proterozoic)—Implications for the timing of Rodinian breakup. AAPG Annual Convention and Exhibition, Salt Lake City, Utah. #90937 (abstr.)

Dixon, E. T., Honda, M., McDougall, I., Campbell, I. H., and Sigurdsson, I. (2000). Preservation of near-solar neon isotopic ratios in Icelandic basalts. *Earth and Planetary Science Letters* 180, 309-324.

Donovan, R. N., Busbey, A. B., Elmore, R. D., and Engel, M. H. (1992). Oil in Permian karst in the Slick Hills of southwestern Oklahoma, in *Source rocks in the southern mid-continent, 1990 symposium* (eds. K. S. Johnson and B. J. Cardott,). Oklahoma Geological Survey Circular 93, pp. 198– 209.

Dubois, M. K., Byrnes, A. P., Bhattacharya, S., Bohling, G. C., Doveton, J. H., and Barba, R. E. (2007). Hugoton Asset Management Project (HAMP): Hugoton geomodel final report: Lawrence, Kansas, Kansas Geological Survey, Open File Report 2007-060-1, 700 p.

Dunai, T. J., and Porcelli, D. (2002). Storage and Transport of Noble Gases in the Subcontinental Lithosphere. *Review in Mineralogy and Geochemistry* 47, 371–409.

Dutton, S. P. (1980a). Depositional Systems and Hydrocarbon resource Potential of the Pennsylvanian System, Palo Duro and Dalhart Basins, Texas Panhandle. Bureau of Economic Geology Geological Circular 80-8, pp.46.

Dutton, S. P. (1980b) Petroleum source rock potential and thermal maturity, Palo Duro basin, Texas. Bureau of Economic Geology Geological Circular 80-10, pp.48.

Fernandez-Prini, R., Alvarez, J. L., and Harvey, A. H. (2003). Henry's constants and vapor-liquid distribution constants for gaseous solutes in H_2O and D_2O at high temperatures. *Journal of Physical and Chemical Reference Data* 32, 903–916.

Fisher, R. S., and Kreitler, C. W. (1987). Geochemistry and hydrodynamics of deep-basin brines, Palo Duro Basin, Texas, U.S.A. *Applied Geochemistry* 2, 459–476. doi:10.1016/0883-2927(87)90002-3

Fisher, R. S. (1995). Geologic, Geochemical, and Geographic Controls on NORM in Produced Water from Texas Oil, Gas, and Geothermal Reservoirs. Paper presented at the SPE/EPA Exploration and Production Environmental Conference, Houston, Texas, March 1995. SPE-29709-MS

Gautheron, C., and Moreira, M. (2002). Helium signature of the subcontinental lithospheric mantle. *Earth and Planetary Science Letters* 199, 39–47. doi:10.1016/S0012-821X(02)00563-0

Gautheron, C., Moreira, M., and Allègre, C. (2005). He, Ne and Ar composition of the European lithospheric mantle. *Chemical Geology* 217, 97–112. doi:10.1016/j.chemgeo.2004.12.009

George, P. G., Mace, R. E., and Petrossian, R. (2011). Aquifers of Texas. Texas Water Development Board. 380, pp. 1-182.

Graham, D., Lupton, J., Albaredet, F., and Condominest, M. (1990). Extreme temporal homogeneity of helium isotopes at Piton de Ia Fournaise, Reunion Island. *Nature*. 347, 545-548.

Graham, D. W. (2002). Nobel gas isotope geochemistry of mid-ocean ridge and ocean island basalts: characterization of mantle source reservoirs. *Review in Mineralogy and Geochemistry* 47, 247-318.

Griffin, W. L., O'Reilly, S., and Ryan, C. G. (1999). The composition and origin of sub-continental lithospheric mantle. In *Mantle Petrology: Field Observations and High-Pressure Experimentation: A Tribute to Francis R. (Joe) Boyd* (eds. Y. Fei, C. M. Bertka, B. O. Mysen). The Geochemical Society. Special Publication No.6, 13-44.

Griffin, W. L., O'Reilly, S.Y., Doyle, B. J., Pearson, N. J., Coopersmith, H., Kivi, K., Malkovets V., and Pokhilenko N. (2004). Lithosphere mapping beneath the North American plate. *Lithos* 77, 873–922. doi:10.1016/j.lithos.2004.03.034

Gustavson, T. C., Finley, R. J., and McGillis, K. A. (1980). Regional dissolution of Permian salt in the Anadarko, Dalhart, and Palo Duro basins of the Texas Panhandle: Bureau of Economic Geology Report of Investigations 106, 40 p.

Hall, C. M., Castro, M. C., Lohmann, K. C., and Sun, T. (2012). Testing the noble gas paleothermometer with a yearlong study of groundwater noble gases in an instrumented monitoring well. *Water Resource Research* 48, W04517

Hanson, R. E., Puckett, R. E., Jr., Keller, G. R., Brueseke, M. E., Bulen, C. L., Mertzman, S. A., Finegan, S. A., and McCleery, D. A. (2013). Intraplate magmatism related to opening of the southern Iapetus Ocean: Cambrian Wichita igneous province in the Southern Oklahoma rift zone. *Lithos* 174, 57–70. doi:10.1016/ j.lithos.2012.06.003.

Hester, T. C., Schmoker, J. W., and Sahl, H. L. (1990). Log-derived regional source-rock characteristics of the Woodford Shale, Anadarko basin, Oklahoma. U.S. Geological Survey Bulletin, v. 1866-D, 38 p.

Hills, J. M., and Kottlowski, F. E. (1983). Correlation of stratigraphic units in North America (COSUNA)-southwest/ Mid-continent correlation chart. American Association of Petroleum Geologists, Tulsa.

Hilton, D. R., and Porceli, D. (2003). Noble gases as mantle tracers. In *Treatise on Geochemistry* (eds. H. D. Holland and K. K. Turekian). Elsevier Science. pp. 27-318.

Hilton, D. R., Halldorsson, S. A., Barry, P. H., Fischer, T. P., De Moor, J. M., Ramirez, C. J., and Scarsi, P. (2011). Helium Isotopes at Rungwe Volcanic Province, Tanzania, and the Origin of East African Plateaux, 38, *Chemical Geology* 149, 1–5. doi:10.1029/2011GL049589.

Hiyagon, H., and Kennedy, M. (1992). Noble gases in CH_4-rich gas fields, Alberta, Canada. *Geochimica et Cosmochimica Acta* 56, 1569-1589.

Hoffman, P., Dewey, J. F., and Burke, K. (1974). Aulacogens and their genetic relation to geosynclines, with a Proterozoic example from Great Slave Lake, Canada, in *Modern and Ancient Geosynclinal Sedimentation* (eds., Dott, R.H., Jr., and Shaver, R.H.,) Society of Economic Paleontologists and Mineralogists (SEPM) Special Publication 19, p. 38–55. doi:10.2110/pec.74.19.0038.

Hogan, J. P., Gilbert, M. C., Price, J. D., and Wright, J. E. (1995). Petrogenesis of A-type sheet-granites from an ancient rift, in *The Origin of Granites and Related Rocks: Third Hutton Symposium Abstracts* (eds. Brown, M., and Piccoli, P.M.). U.S. Geological Survey Circular 1129, 68–69.

Hoke, L., Lamb, S., Hilton, D. R., and Poreda, R. J. (2000). Southern limit of mantle-derived geothermal helium emissions in Tibet: implications for lithospheric structure. *Earth and Planetary Science Letters* 180, 297–308. doi:10.1016/S0012-821X(00)00174-6.

Honda, M., McDougall, I., Patterson, D. B., Doulgeris, A., and Clague, D. A. (1991). Possible solar noble-gas component in Hawaiian basalts. *Nature*. 349, 149-151.

Hubert, L. (1995). Pressure regimes, burial history, and source rock maturation of the Pennsylvanian Morrow Formation in the western Anadarko basin and the Hugoton embayment, Kansas, Oklahoma, and Texas: M.S. thesis, University of Wyoming, Laramie, 123 p.

Jacques, J. M., and Clegg, H. (2002). Late Jurassic Source Rock Distribution and Quality in the Gulf of Mexico: Inferences from Plate Tectonic Modelling. *GCAGS Transaction* 52, 429-440.

Johnson, K. S. (1989). Geologic Evolution of the Anadarko Basin. In the *Anadarko Basin Symposium*, *1988*. Oklahoma Geological Survey Circular 90. 3-12.

Johnson, K. S., Amsden, T. W., Denison, R. E., Dutton, S. P., Goldstein, A. G., Rascoe, B., Sutherland, P. K., and Thompson, D. M. (1988a). Southern Midcontinent region, in *Sedimentary Cover—North American Craton* (ed. Sloss, L.L.). Geological Society of America, Boulder, Colorado, pp. 307–359. doi:10.1130/DNAG-GNA-D2.307.

Johnson, K. S., Amsden, T. W., Denison, R. E., Dutton, S. P., Goldstein, A. G., Rascoe, B.R., Sutherland, P. K., and Thompson, D. M. (1988b). Southern Mid-Continent – Geologic Provinces, Basement Rocks, Thickness and Dominant Lithologies of Sedimentary Rocks. In *Sedimentary Cover—North American Craton* (ed. Sloss, L.L.). Geological Society of America. Plate 6.

Jolly, G. D. (1988). Correlation of the Woodford Formation in South-Central Oklahoma Using Gamma-ray Scintillation Measurements of the Natural Background Radiation. Unpublished Masters Thesis, Stephen F. Austin State University, 154 p.

Jordan, L., and Vosburg, D. L. (1963). Permian salt and associated evaporites in the Anadarko basin of the western Oklahoma- Texas panhandle region: Oklahoma Geological Survey Bulletin 102, 76 p.

Jorgensen, D. G., Helgesen, J. O., and Imes, J. L. (1993). Regional aquifers in Kansas, Nebraska, and parts of Arkansas, Colorado, Missouri, New Mexico, Oklahoma, South Dakota, Texas, and Wyoming— Geohydrologic framework. U.S. Geological Survey Professional Paper 1414-B, 72 p.

Kennedy, B. M., Hiyagon, H., and Reynolds, J. H. (1990). Crustal neon: a striking uniformity. *Earth and Planetary Science Letters* 98, 277-286.

Kennedy, B. M., Torgersen, T., and van Soest, M. C. (2002). Multiple atmospheric noble gas components in hydrocarbon reservoirs: a study of the Northwest Shelf, Delaware Basin, SE New Mexico. *Geochimica et Cosmochimica Acta* 66, 2807-2822.

Kennedy, B. M., and van Soest, M. C. (2007). Flow of Mantle Fluids Through the Ductile Lower Crust: Helium Isotope Trends. *Science* 318, 1433-1436.

Kharaka, Y. K., and Daniel J. S. (1988). The solubility of noble gases in crude oil at 25–100°C. *Applied Geochemistry* 3, 137-144.

Kimani, C. N., Kasanzu, C. H., Tyne, R. L., Mtili, K. M., Byrne, D. J., Kazimoto, E. O., Hillegonds, D. J., Ballentine, C. J., and Barry, P. H. (2021). He, Ne, Ar and CO2 systematics of the Rungwe Volcanic Province, Tanzania: Implications for fluid source and dynamics. *Chemical Geology* 586, 120584.

Klemperer, S. L., Kennedy, B. M., Sastry, S. R., Makovsky, Y., Harinarayana, T., and Leech, M. L. (2013). Mantle fluids in the Karakoram fault: Helium isotope evidence. *Earth and Planetary Science Letters* 366, 59–70. doi:10.1016/j.epsl.2013.01.013.

Kreitler, C. W. (1989). Hydrogeology of sedimentary basins. *Journal of Hydrology* 106, 29–53. doi:10.1016/0022-1694(89)90165-0.

Lidiak, E. G., Denison, R. E., and Stern, R. J. (2014). Cambrian (?) Mill Creek diabase dike swarm, eastern Arbuckles: A Glimpse of Cambrian rifting in the Southern Oklahoma Aulacogen. Oklahoma Geological Survey, Guidebook, 38, pp.105-122.

Liu, C., McGovern, G. P., Liu, P., Zhao, H., and Horita, J. (2018). Position-specific carbon and hydrogen isotopic compositions of propane from natural gases with quantitative NMR. *Chemical Geology* 491, 14–26. doi:10.1016/j.chemgeo.2018.05.011.

Ma, L., Castro, M. C., and Hall, C. M. (2009). Atmospheric noble gas signatures in deep Michigan Basin brines as indicators of a past thermal event. *Earth and Planetary Science Letters* 277, 137-147.

Ma, L., Castro, M. C., Hall, C. M., and Walter, L. M. (2005). Cross-formational flow and salinity sources inferred from a combined study of helium concentrations, isotopic ratios, and major elements in the Marshall aquifer, southern Michigan. *Geochemistry Geophysics Geosystems* 6(10), Q10004, doi:10.1029/2005GC001010.

Marty, B., O'Nions, R. K., Oxburgh, E. R., Martel, D., and Lombardi, S. (1992). Helium isotopes in Alpine regions. *Tectonophysics* 206, 1-8.

Meibom, A., Sleep, N. H., Zahnle, K., and Anderson, D. L. (2005). Models for noble gases in mantle geochemistry: Some observations and alternatives. In *Plates, Plumes and Paradigms* (eds. G. R. Foulger, J.H. Natland, D. C. Presnall, and D. L. Anderson). Geological Society of America. doi:10.1130/0-8137-2388-4.347.

Menzies, M. A. (1990). *Continental mantle*. Clarendon Press, Oxford, 184 p.

Mills, J. M., and Kottlowski, F. E. (1983). Correlation of stratigraphic units in North America - Southwest/southwest mid-continent correlation chart. American Association of Petroleum Geologists, Correlation Chart Series.

Moreira, M., and Allegre, C. J. (1998). Helium-neon systematics and the structure of the mantle. *Chemical Geology* 147, 53–59.

Moreira, M., Kunz, J., and Allegre, C. (1998). Rare gas systematics in popping rock: isotopic and elemental compositions in the upper mantle. *Science*. 279, 1178-1181.

Moreira, M., Breddam, K., Curtice, J., and Kurz, M. D. (2001). Solar neon in the Icelandic mantle: new evidence for an undegassed lower mantle. *Earth and Planetary Science Letters* 185, 15–23. doi:10.1016/S0012-821X(00)00351-4.

O'Nions, R. K., and Oxburgh, E. R. (1983). Heat and helium in the Earth. *Nature*. 306, 429-431.

Orr, E. D., and Kreitler, C. W. (1985). Interpretation of pressure-depth data from confined underpressured aquifers exemplified by the Deep-Basin Brine aquifer, Palo Duro Basin, Texas. *Water Resource Research* 21, 533-544.

Oxburgh, E. R., O'Nions, R. K., and Hill, R. I. (1986). Helium isotopes in sedimentary basins. *Nature* 324, 632–635. doi:10.1038/324632a0.

Ozima, M., and Podosek, F. A. (2002) *Noble gas geochemistry*. Cambridge Univ. Press.

Patriarche, D., Castro, M. C., and Goblet, P. (2004). Large-scale hydraulic conductivities inferred from three-dimensional groundwater flow and 4He transport modeling in the Carrizo aquifer, Texas. *Journal of Geophysical Research: Solid Earth* 109, B11202.

Pierce, A. P., Gott, G. B., and Mytton, J. W. (1964). Uranium and helium in the Panhandle gas field, Texas, and adjacent areas. US Geological Survey Professional Paper 454-G, pp.57.

Pinti, D. L., and Marty B. (1995). Noble gases in crude oils from the Paris Basin, France: implications for the origin of fluids and constraints on oil–water–gas interactions. *Geochimica et Cosmochimica Acta*. 59, 3389-3404.

Pinti, D. L., and Marty, B. (1998). The origin of helium in deep sedimentary aquifers and the problem of dating very old groundwaters, in *Dating and Duration of Fluid Flow and Fluid-Rock Interaction* (ed. Parnell, J.). Geological Society, London, pp. 53-68.

Pippin, L. (1970). Panhandle-Hugoton Field, Texas-Oklahoma-Kansas—the First Fifty years, in *Geology of Giant Petroleum Fields*. American Association of Petroleum Geologists. doi:10.1306/M14368C9

Porcelli, D., and Wasserburg, G. J. (1995). Mass transfer of helium, neon, argon, and xenon through a steady-state upper mantle. *Geochimica et Cosmochimica Acta* 59, 4921-4937.

Presley, M. W. (1987). Evolution of Permian evaporite basin in Texas Panhandle: *AAPG Bulletin* 71 2, 167–190.

Prinzhofer, A., Dos Santos Vaz, N. E., and Battani, A. (2010). Coupled use of carbon isotopes and noble gas isotopes in the Potiguar basin (Brazil). Fluids migration and mantle influence. *Marine and Petroleum Geology* 27, 1273–1284.

Rascoe Jr., B. (1968). Permian system in western mid-continent. *The Mountain Geologists* 5, pp. 127–138.

Rice, D. D., Threlkeld, C. N., and Vuletich, A. K. (1988). Character, origin and occurrence of natural gases in the Anadarko basin, southwestern Kansas, western Oklahoma and Texas Panhandle, U.S.A. *Chemical Geology* 71, 149–157. doi:10.1016/0009-2541(88)90111-8.

Rose, P. R. (1986). Hydrocarbon resources of the Palo Duro Basin, Texas Panhandle: technical report. No. BMI/ONWI-590. Telegraph Exploration, Inc., TX, USA.

Rudnick, R., and Nyblade, A. (1999). The thickness and heat production of Archean lithosphere: constraints from xenolith thermobarometry and surface heat flow. *In Mantle Petrology: Field Observations and High Pressure Experimentation: A Tribute to Francis R. (Joe) Boyd* (eds. Fei, Y., Bertka, C. M., Mysen, B. O.). The Geochemical Society. Special Publication No.6, 3-12.

Ruppel, S. C., and Garrett, C. M. (1989). Permian/Pennsylvanian shallow marine carbonate and siliciclastics, Texas Panhandle, in *Atlas of major Texas gas reservoirs* (eds. E. C. Kosters, D. G. Bebout, S. J. Seni, C. M. Garrett Jr., L. F. Brown Jr.,H. S. Hamlin, S. P. Dutton, S. C. Ruppel, R. J. Finley, and N. Tyler). The University of Texas at Austin, Bureau of Economic Geology, 148–151.

Salvador, A. (1991). *The Gulf of Mexico Basin*. Geological Society of America.

Schmoker, J. W. (1986). Oil generation in the Anadarko Basin, Oklahoma and Texas: modeling using Lopatin's method. Oklahoma Geological Survey Special Publication 86-3, 40 p.

Schmoker, J. W. (1989). Thermal maturity of the Anadarko basin, in *Anadarko basin symposium*. Oklahoma Geological Survey Circular 90, pp. 25– 31.

Senger, R. K., and Fogg, G. E. (1987). Regional underpressuring in deep brine aquifers, Palo Duro basin, Texas: 1. Effects of hydrostratigraphy and topography. *Water Resources Research*, 23 8, pp. 1481–1493, doi:10.1029/WR023i008p01481.

Shaw, C. A., and Karlstrom, K. E. (1999). The Yavapai-Mazatzal crustal boundary in the southern Rocky Mountains. *Rocky Mountain Geology* 34, 37–52.

Smith, S. P., Kennedy, B. M. (1983). The solubility of noble gases in water and NaCl brine. *Geochimica et Cosmochimica Acta* 47, 503–515.

Sorenson, R. P. (2005). A dynamic model for the Permian Panhandle and Hugoton fields, western Anadarko basin. *AAPG Bulletin* 89, 921–938. doi:10.1306/03010504045.

Starkey, N. A., Stuart, F. M., Ellam, R. M., Fitton, J. G., Basu, S., and Larsen, L. M. (2009). Helium isotopes in early Iceland plume picrites: Constraints on the composition of high 3He/4He mantle. *Earth and Planetary Science Letters* 277, 91–100. doi:10.1016/j.epsl.2008.10.007

Sun, T., Hall, C. M., and Castro, M. C. (2010). Statistical properties of groundwater noble gas paleoclimate models: Are they robust and unbiased estimators? *Geochemistry, Geophysics, Geosystems* 11, Q02002.

Thomas, W. A., (1991). The Appalachian-Ouachita rifted margin of southeastern North America. *Geological Society of America Bulletin* 103, 415-431.

Thomas, W. A. (2005). Tectonic inheritance at a continental margin. *GSA Today* 16, 4. doi:10.1130/1052-5173(2006)016[4:TIAACM]2.0.CO;2.

Thomas, W. A. (2011). The Iapetan rifted margin of southern Laurentia. *Geosphere* 7, 97–120. doi:10.1130/GES00574.1.

Thomas, W.A. (2014). A mechanism for tectonic inheritance at transform faults of the Iapetan margin of Laurentia. *Geoscience Canada* 41, 321–344. doi:10.12789/geocanj.2014.41.048.

Torgersen, T. (1980). Controls on pore-fluid concentration of ^{4}He and ^{222}Rn and the calculation of $^{4}He/^{222}Rn$ ages. *Journal of Geochemical Exploration* 13, 57-75.

Torgersen, T., Kennedy B. M., Hiyagon H., Chiou K. Y., Reynolds J. H., and Clarke W. B. (1989). Argon accumulation and the crustal degassing flux of 40Ar in the Great Artesian Basin, Australia. *Earth and Planetary Science Letters* 92, 43-56.

Tucker, J. M., and Mukhopadhyay, S. (2014). Evidence for multiple magma ocean outgassing and atmospheric loss episodes from mantle noble gases. *Earth and Planetary Science Letters* 393, 254–265. doi:10.1016/j.epsl.2014.02.050.

Valbracht, P. J., Honda, M., Matsumoto, T., Mattielli, N., McDougall, I., Ragettli, R. and Weis, D. (1996). Helium, neon and argon isotope systematics in Kerguelen ultramafic xenoliths: implications for mantle source signatures. *Earth and Planetary Science Letters* 138, 29-38.

Van Schmus, W. R., Bickford, M. E., and Zietz, I. (1987). Early and Middle Proterozoic provinces in the central United States, in *Proterozoic Lithospheric Evolution*. (ed. Kroner, A.). American Geophysical Union Geodynamics Series 17, 43–68.

Wall, C. J., Hanson, R. E., Schmitz, M., Price, J. D., Donovan, R. N., Boro, J. R., Eschberger, A. M., and Toews, C. E. (2021). Integrating zircon trace-element geochemistry and high-

precision U-Pb zircon geochronology to resolve the timing and petrogenesis of the late Ediacaran–Cambrian Wichita igneous province, Southern Oklahoma Aulacogen, USA. *Geology* 49, 268–272. doi:10.1130/G48140.1.

Warrier, R. B., Castro, M. C., and Hall, C. M. (2012). Recharge and source-water insights from the Galapagos Islands using noble gases and stable isotopes: Recharge and source-water insights from the Galapagos islands. *Water Resource Research* 48, W03508.

Warrier, R. B., Castro, M. C., Hall, C. M., and Lohmann, K. C. (2013). Large atmospheric noble gas excesses in a shallow aquifer in the Michigan Basin as indicators of a past mantle thermal event. *Earth and Planetary Science Letters* 375, 372-382.

Weiss, R. F. (1968). Piggyback sampler for dissolved gas studies on sealed water samples. Deep-Sea Research and Oceanography Abstract 15, 695-699.

Wen, T., Castro, M. C., Ellis, B. R., Hall, C. M., and Lohmann, K. C. (2015a). Assessing compositional variability and migration of natural gas in the Antrim Shale in the Michigan Basin using noble gas geochemistry. *Chemical Geology* 417, 356-370.

Wen, T., Castro, M. C., Hall, C. M., Pinti, D. L., and Lohmann, K. C. (2015b). Constraining groundwater flow in the glacial drift and saginaw aquifers in the Michigan Basin through helium concentrations and isotopic ratios. *Geofluids* 16, 3–25. doi:10.1111/gfl.12133

Wen, T., Castro, M. C., Nicot, J. P., Hall, C. M., Pinti, D. L., Mickler, P., Darvari, R., and Larson T. (2017). Characterizing the noble gas isotopic composition of the Barnett Shale and Strawn Group and constraining the source of stray gas in the trinity aquifer, North-Central Texas. *Environmental Science and Technology* 51, 6533-6541.

Wirojanagud, P., Kreitler, C. W., and Smith, D. A. (1986). Numerical modeling of regional groundwater flow in the Deep-Basin Brine aquifer of the Palo Duro Basin, Texas Panhandle. The University of Texas at Austin, Bureau of Economic Geology Report of Investigations No. 159, 68 pp.

Yatsevich, I., and Honda, M. (1997). Production of nucleogenic neon in the Earth from natural radioactive decay. *Journal of Geophysical Research* 102, 10291–10298.

Young, H. P., and Lee, C.-T. A. (2009). Fluid-metasomatized mantle beneath the Ouachita belt of southern Laurentia: Fate of lithospheric mantle in a continental orogenic belt. *Lithosphere* 1, 370–383. doi:10.1130/L72.1

Zartman, R. E., Wasserburg, G. J., and Reynolds, J. H. (1961). Helium, argon, and carbon in some natural gases. *Journal of Geophysical Research* 66, 277-306.

Zhou, Z., and Ballentine, C.J. (2006). ^{4}He dating of groundwater associated with hydrocarbon reservoirs. *Chemical Geology* 226, 309–327. doi:10.1016/j.chemgeo.2005.09.030

CHAPTER 3

MORB and Solar-OIB like Noble Gas Signatures in the Eagle Ford Shale, Southwest Texas – Implications for the Earth's Geological Evolution and Framework

Abstract

Heterogeneity of oil and gas production in the Eagle Ford Shale, southwest Texas, one of the most prolific shale-oil formations in the world is significant, and an understanding of how fault-fracture networks and deep crustal structures may have affected the Eagle Ford Shale from deposition through maturation is missing. Here, we present the complete set of stable noble gases for gas samples collected in the Eagle Ford Shale. This new dataset, together with that of Byrne et al. [2018] and noble gas information from Harrington et al. [2015] sheds light on the tectonic and magmatic history of the region. These datasets reveal the presence of both crustal and mantle components. Two mantle endmembers are present, a weak one, corresponding to a Mid Ocean Ridge Basalt (MORB) signature, suggesting the presence of an old SW-NE oriented rift, and a more prevalent one, corresponding to a primordial, solar-like signature of which Ocean Island Basalts (OIBs) are also representative. Overall, the noble gas pattern displays an almost pure crustal component in the south, followed by a MORB-type signature in the center, and a solar-like/OIB signature to the west, likely continuing north. The MORB-identified rift follows closely the southern Laurentian lithospheric margin and is parallel to all major known faults in the area. It

is consistent with the palinplastic continentally reconstructed Ouachita Rift (~530 Myrs), if two small clockwise rotations are applied in the area. These rotations can be accommodated through the presence of small transform faults. The latter are consistent with calculated relative ^{40}Ar ages in these gas samples, pointing to a clear spatial variation pattern, with increasingly young ages toward the west, and the presence of discrete blocks within the Eagle Ford Shale. A highly compartmentalized Eagle Ford Shale with the occurrence of distinct noble gas signatures and thus, the likely presence of different hydrocarbon sources, suggests the presence of well-connected fractures and faults across multiple reservoirs that tie to deep fault systems.

The primordial, solar-like component is consistent with an origin in the subcontinental lithospheric mantle, the shallow refractory reservoir beneath the Laurentian craton, an hypothesis consistent with the presence of a heterogeneous mantle. Both, intensive Late Cretaceous volcanic activity in the area as well as reactivation of all major fault systems in the Miocene are consistent with the presence of a recent, prevalent solar-like signature in the Eagle Ford Shale. This solar-like component displays characteristics similar to that identified in the Michigan Basin, also part of the Laurentian craton, supporting the hypothesis by Castro et al. [2009] that primordial noble gas signatures do not necessarily fingerprint the presence of a deep mantle plume.

This work highlights the potential of noble gases to place important constraints in the Earth's geological evolution and framework, while shedding light in poorly understood unconventional hydrocarbon systems in complex tectonic settings.

3.1. Introduction

Hydrocarbons remain the dominant energy source in the USA, accounting for 85% of the country's total needs (https://www.eia.gov/totalenergy/data/monthly/). Since the early 2000's, technological improvements in hydraulic fracturing and horizontal drilling dramatically shifted the focus of oil and gas production from conventional reservoirs to unconventional shale gas and tight oil plays in North America [EIA 2016]. Exploitation of unconventional reservoirs intensified in the last decade and turned the Upper Cretaceous Eagle Ford Shale into one of the most economic and prolific shale-oil formations in the world [Hammes et al., 2016]. However, differences in oil and gas production across the Eagle Ford Shale play remain, highlighting our lack of knowledge and understanding of the key production parameters within unconventional reservoirs [Hammes et al., 2016; Gherabati et al., 2016, 2018]. In particular, in the Eagle Ford Shale (EFS), significant differences in oil and gas production are commonly observed between closely spaced wells [Gherabati et al., 2016], highlighting our current limited knowledge and partial understanding of key attributes that affect oil and gas production in unconventional reservoir systems. An understanding of how fault-fracture networks and deep crustal structures may have affected the Eagle Ford Shale from deposition through maturation is missing.

Noble gas geochemistry has long been used to trace groundwater, and oil and gas in sedimentary systems [Zartman et al, 1961; Bosch and Mazor, 1988; Ballentine et al., 1991; Castro et al., 1998a, b; Castro et al., 2005; Patriarche et al., 2004; Warrier et al., 2012]. Stable noble gases (He, Ne, Ar, Kr, Xe) are chemically inert and are thus transported without being affected by chemical reactions [Ozima and Podosek, 2002]. Noble gases in subsurface fluids are derived from the atmosphere, the crust and the mantle, all of which show distinct isotopic and elemental signatures [Castro et al., 1998a, b; Ozima and Podosek, 2002; Ballentine and Burnard, 2002; Hilton

and Porcelli, 2003]. In most subsurface fluids within sedimentary systems, noble gases are dominated by an atmospheric (Air Saturated Water or ASW) and/or a crustal component derived primarily from radioactive decay of U, Th and ^{40}K [Torgersen et al., 1989; Ballentine and Burnard, 2002; Ma et al., 2009; Sun et al., 2010; Hall et al., 2012; Aeschbach-Hertig and Solomon, 2013]. Noble gases are thus source specific and time dependent rendering them ideal natural tracers for studying the origin and evolution of crustal fluids. Although less common and abundant in sedimentary systems, noble gases originating from the mantle can also be present [Ballentine and O'Nions, 1991; Ma et al., 2009; Warrier et al., 2013]. He and Ne isotopic signatures signal the presence of a mantle component when present [Ballentine, 1997; Castro et al., 2009]. Furthermore, the combined analysis of He and Ne isotopic ratios allows for the distinction between a primordial, solar-like signature commonly found in Ocean Island Basalts (OIBs), traditionally believed to originate deeper in the mantle and that of a Mid-Ocean Ridge Basalt (MORB) type, representative of a degassed upper-mantle [O'Nions and Oxburgh, 1983; Porcelli and Wasserburg, 1995; Moreira and Allegre, 1998; Moreira et al., 2001]. More recently though, Castro et al. [2009] identified a solar-like component in deep brines in the Michigan Basin, a cratonic area where the presence of hotspots was not identified, and suggested that this primordial signature can be accounted for by a shallow refractory reservoir in the Archean subcontinental lithospheric mantle (SCLM).They further concluded that this primordial He and Ne signature does not necessarily reflect the presence of mantle plumes with their associated undegassed lower mantle reservoir.

Noble gas studies conducted in hydrocarbons have largely focused on conventional reservoirs, where it is generally accepted that atmospheric, crustal and mantle noble gases are transported to oil and gas reservoirs by groundwater [Zartman et al., 1961; Bosch and Mazor, 1988; Ballentine et al., 1991; Hiyagon and Kennedy, 1992; Pinti and Marty, 1995; Ballentine et al., 1996].

In these systems, noble gases have been used to constrain the timing of migration and accumulation, as well as to quantify relative volumes of gas and liquid present, in addition to assessing the extent of interactions between hydrocarbons and groundwater [Ballentine et al., 1991, 1996; Barry et al., 2016]. By contrast, noble gas studies in unconventional reservoirs remain scarce. These include studies in the Marcellus and Utica shale in Appalachian Basin [Hunt, et al., 2012], the Antrim Shale in the Michigan Basin [Wen et al., 2015], the Barnett [Wen et al., 2017], the Eagle Ford [Harrington et al., 2015; Byrne et al., 2018] and Haynesville [Byrne et al., 2020] shales in Texas, the East Pennine coalfield in UK [Györe et al., 2018] as well as a study in the Longmaxi Shale in the Sichuan Basin, China [Cao et al., 2018]. Noble gas studies seeking to identify the source of groundwater contamination by methane in the proximity of unconventional shale gas reservoirs have also been carried out [e.g.,Darrah et al., 2014, 2015; Harkness et al., 2017; Wen et al., 2016, 2017; Woda et al., 2018]. However, the study of noble gases in unconventional hydrocarbon systems is in its infancy and it remains unclear whether generally accepted noble gas assumptions with respect to their origin and transport in conventional systems hold true [see, e.g., Byrne et al., 2018]. Indeed, major differences distinguish conventional and unconventional reservoir systems. Conventional hydrocarbon systems are typically characterized by both high porosity and permeability that permit fluid flow, have a caprock that effectively traps hydrocarbons that migrated to the reservoir, and display clear hydrocarbon-water contacts [Spencer, 1989; Schmoker, 1996; Law, 2002]. In conventional systems, hydrocarbons commonly undergo extensive interaction with groundwater, which ultimately affects their noble gas signatures. In most cases, conventional systems act solely as a storage facility. By contrast, unconventional systems consist of organic-matter rich rock units that are typically characterized by low porosity and permeability. Unconventional reservoirs act as hydrocarbon source, reservoir and couverture altogether with the

potential to produce, host and expel multiple oil and/or gas generations over time [Condon and Dyman, 2006] in addition to storage of in-situ derived hydrocarbons. Due to their low permeability, however, hydrocarbon mobility within and between unconventional systems is almost entirely dependent on fluid transport in localized high-permeability zones, which may include fault and fracture systems, and bedding parallel flow high permeability sedimentary layers. The regional tectonic setting, therefore, can play a critical role in the transport of hydrocarbon fluids within and outside of unconventional reservoir systems demonstrating that a deep understanding of the local, regional and sometimes continental tectonic history and features is critical to achieving maximal production and recovery of the hydrocarbon reservoirs in place.

Because of their characteristics and physical properties, noble gases are an excellent tool to complement tectonic studies in complex and poorly understood tectonic settings [e.g., Hoke et al., 2000; Castro et al., 2009; Klemperer et al., 2013]. Noble gases can provide clarification on the tectonic and geological history of a region by identifying and constraining the location of major tectonic structures, including e.g., rifts, faults and fracture networks in addition to identifying past volcanic activity, its nature, as well as preferred hydrocarbon migration paths. Noble gases can also provide clarification on the existence of multiple hydrocarbon sources, and provide a means to quantify formation and migrations times. With such goals in mind, we present here the complete set of stable noble gas data for gas samples collected in the oil zone in the Eagle Ford Shale in southwest Texas. This new noble gas dataset, together with recently published noble gas data primarily from the wet gas zone just south of our study area [Byrne et al., 2018] and noble gas information from the oil zone just north of our sampling location [Harrington et al., 2015] shed new light on the different sources of hydrocarbons present, as well as hydrocarbon generation and migration. It also provides a more comprehensive and, to some extent, unexpected picture of major

tectonic structures present and past volcanic activity in the region. An important observation from this work is the highly dynamic and compartmentalized nature of some unconventional reservoirs and the importance that existing regional tectonic structural fabrics have on such reservoirs. These effects, in turn, might be responsible for the drastic and unexpected behavioral differences observed in neighboring wells [Gherabati et al., 2016]. More importantly, this work provides clarification on the nature of an OIB type signature previously found in the area [Wittke and Mack, 1993; Young and Lee; 2009; Raye et al., 2011] and reinforces the notion that the mantle is highly heterogeneous with the SCLM being a likely reservoir for this primordial signature. This study highlights also the importance of having good spatial coverage of the region being studied, in order to reconstruct the tectonics, geological and geochemical evolution of a region at the local, regional and continental scales.

3.2. Geological Background

The Texas Gulf Coast is a region with a complex tectonic history spanning a period of at least 1.4 Ga. This region was the stage for the breakup and formation of several supercontinents as well as the opening and closure of major oceans through a sequence of orogeny and rifting events. The Llano uplift, in the southern margin of the Laurentian craton (Fig. 3.1), with an age of ~1.4 Ga, is the sole exposed portion of the southern Laurentian craton [Fig. 3.1, Thomas, 1991; Poole et al., 2005; Young and Lee, 2009; Griffin, 2015]. During the Mesoproterozoic (~1.3 – 1.0 Ga), subduction of Laurentia towards the northwest led to partial deformation of the crust (Grenville orogeny) and the formation of Rodinia [Thomas 2005; Chiarenzelli et al., 2010]. In late Proterozoic (~800 - 650 Myrs), Rodinia began to breakup leading to several failed rifts [Salvador, 1991; Adams, 1993; Dehler, 1998]. The Ouachita Rift (~530 Myrs) lead to the final breakup of

Rodinia and the formation of the Iapetus (Proto-Atlantic) Ocean [Fig. 3.1; Thomas 1991, 2005]. Closure of the Iapetus and formation of the Pangea occurred in the Permian (298-254 Myrs) following the collision of the African, South American and North American plates leading to the

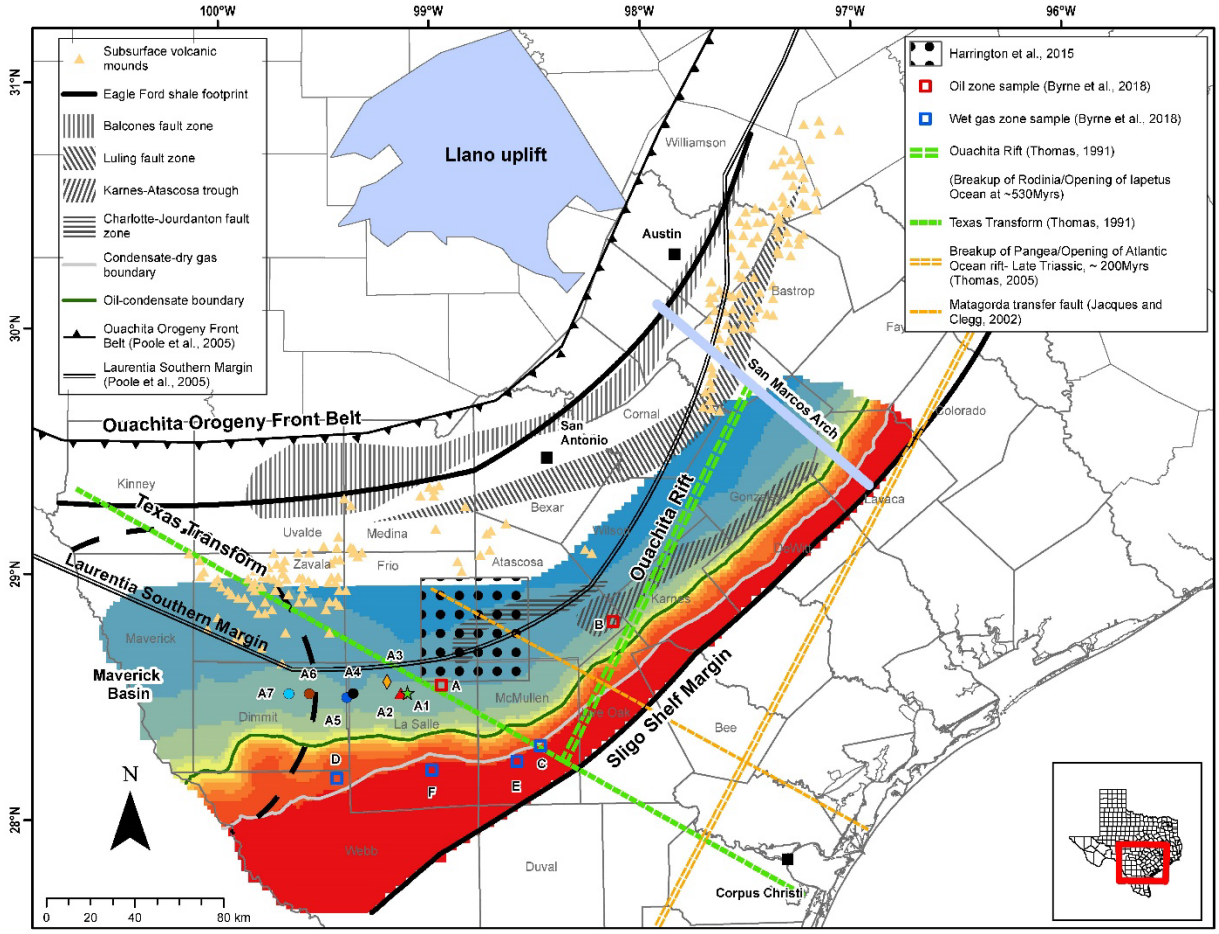

Figure 3.1 Map of the Eagle Ford Shale play within Texas, showing sampled well locations (this study), oil, wet and dry gas windows, subsurface volcanic mounds and major structural features [adapted from Gherabati et al., 2016]. Byrne et al. [2018] well locations (red and blue open squares) and approximate Harrington et al. [2015] sampled area (dotted square area) are also indicated. Location and extent of the Llano uplift and fault zones follow Condon and Dayman [2006].

Ouachita orogenic belt [Thomas, 1991, 2005; Poole et al., 2005; Ewing, 2016]. The Ouachita uplift of Oklahoma and Arkansas and the Marathon Uplift of west Texas formed as a result. A zone of compressed Paleozoic rocks – the Ouachita orogenic front belt - connects these uplifts and curves along the Llano uplift (Fig. 3.1). Pangea began to break up in the Late Triassic (~200 Myrs) when

South America and Africa separated from North America leading to a series of rift basins formed along the North American continental margin and the opening of the Atlantic Ocean [Fig. 3.1; Thomas, 2005; Poole et al., 2005; Ewing, 2016]. The Gulf of Mexico opened subsequently, in Late Jurassic (~150 Myrs), further south [not shown; Salvador, 1987; Jacques and Clegg, 2002].The Eagle Ford Group runs roughly sub-parallel to the Gulf of Mexico shoreline and extends all across south, central and east Texas (Fig. 3.1). Several prominent structural features affected the Eagle Ford Shale deposition. These include the Maverick Basin in the west, the San Marcos Arch and Karnes-Atascosa trough system in south-central Texas, and the relict – Sligo Shelf Margin along the length of the Eagle Ford play [Fig. 3.1; Hentz et al., 2014; Denne and Breyer, 2016; Hammes et al., 2016; Nicot et al., 2018; Loucks, 2018].

The Eagle Ford Group is Late Cretaceous in age (Cenomanian-Turonian) and is divided into a Lower and Upper Eagle Ford Formation in subsurface Texas cores. The Lower Eagle Ford Formation has the highest hydrocarbon-generating potential [Dawson, 2000] and most oil and gas production takes place at this level [Breyer et al., 2013]. The Lower Eagle Ford Formation consists mostly of organic matter-rich carbonate-dominated mudstones and wackestones interlayered with carbonate limestones, along with volcaniclastic layers. The Lower Eagle Ford Formation was deposited during a marine transgressive sequence in poorly-oxygenated, often euxinic bottom water conditions [Loucks, 2018]. The Upper Eagle Ford Formation is also dominated by carbonate-rich mudstones and wackestones, but the more oxygenated bottom waters during this time resulted in lower organic matter content compared to the lower Eagle Ford Formation [Phelps et al., 2015; Loucks, 2018; Hentz et al., 2014; Denne and Breyer, 2016]. The Eagle Ford Group dips toward the southeast and reaches depths over 4.5 km. It exhibits broad parallel zones of roughly equal size that display rapid, natural maturity gradation (Fig. 3.1), from low-gravity oil in

updip Atascosa County [Billingsley et al., 2015; Zhang et al., 2017] to volatile oil, gas condensate, and dry gas further to the south [e.g., Tian et al., 2014; Nicot et al., 2018; Zhang et al., 2017]. Oil transitions to gas condensate and dry gas over short distances, i.e., less than 10 miles in McMullen County [Gherabati et al., 2018; Zhang et al., 2017]. The Eagle Ford Group is part of the Smackover-Eagle Ford-Austin Composite Total Petroleum System [Condon and Dyman, 2006]. The primary source rocks of this system are the carbonate mudstones and marine shales of the Upper Jurassic Smackover Formation, and the Upper Cretaceous Eagle Ford Shale (Fig. 3.2). The main conventional reservoir rocks in the area are the Anacacho Limestone immediately overlying the Austin Chalk Formation, and the San Miguel, Olmos, and Escondido formations of the Upper Cretaceous [Fig. 3.2; Condon and Dyman, 2006]. The Eagle Ford Shale is also a major source rock for conventional hydrocarbon accumulations in the immediately underlying Buda Limestone and overlying Austin Chalk, respectively [Fig. 3.2; Condon and Dyman, 2006]. The Jurassic Smackover Formation is contemporaneous to the opening of the Gulf of Mexico and the formation of a spreading center in the central gulf area [Buffler and Sawyer, 1985; Salvador, 1991]. A series of faults that parallel the Gulf Coast, the Laurentian craton southern margin and the Paleozoic Ouachita orogenic belt are present. These include (Fig. 3.1): 1) the Balcones fault zone to the north, mapped from Williamson County, north of Austin to Uvalde County, west of San Antonio; 2) the Luling fault zone south of the Balcones; the Balcones-Luling fault zones bound a broad down-dropped graben [Condon and Dyman, 2006]; both fault zones extend into the Paleozoic basement; 3) the Charlotte-Jourdanton fault zone, of more limited size, extending from southeast Frio County across Atascosa County to southwestern Wilson County; these are also normal faults, part of a graben; 4) the Karnes-Atascosa through, a fault zone further to the northeast. All these fault

systems are thought to have undergone major movements during the Miocene, a period of regional uplift and extension in the area [Weeks, 1945; Ewing, 1987, 1991].

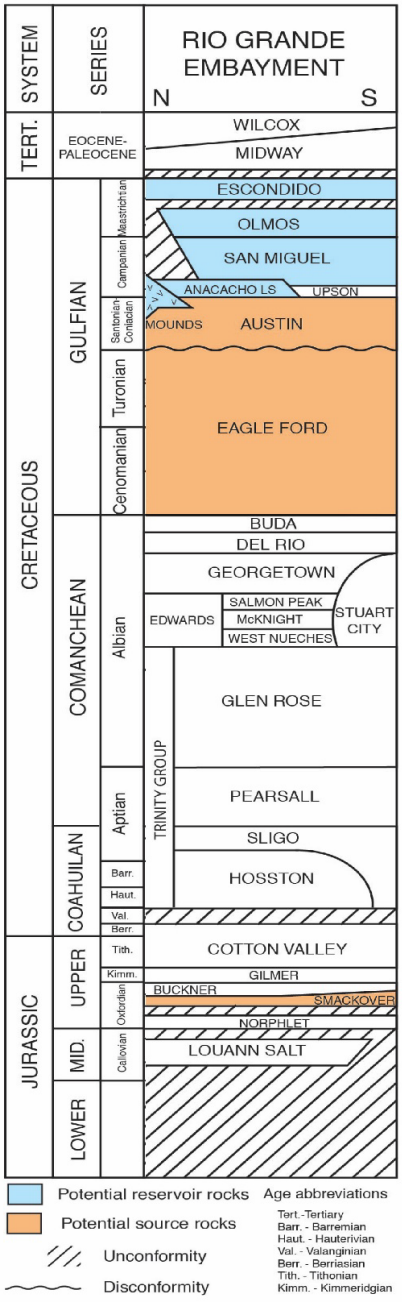

Figure 3.2 Jurassic, Cretaceous and Tertiary geological units in southern Texas [adapted from Condon and Dyman, 2006 and Kosters et al., 1989].

In the late Cretaceous (Santonian to Campanian), a series of submarine volcanoes referred to as the 'Balcones Igneous Province" [BIP; Spencer, 1969] erupted along a 250-mile belt in South-Central Texas forming three groups of seamounts and volcanic islands on the shallow Cretaceous shelf [Fig. 3.1; Welder and Reeves, 1964; Spencer, 1969; Miggins et al., 2004]. These are: 1) the Travis volcanic field along a northeast-trending zone east of Austin; these volcanic mounds are associated with the Luling fault zone and point to the presence of a fault system deeply rooted in the Paleozoic basement; 2) a central group of volcanic unnamed mounds in Wilson, Atascosa, Frio and Medina Counties south of San Antonio, and; 3) the Uvalde volcanic field further southwest, centered in Zavala County and extending into Uvalde, Medina, Frio, Dimmit, Maverick and Kinney Counties (Fig. 3.1). The Uvalde volcanoes do not display a clear orientation along one fault zone. While some individual mounds are elongated along the Balcones fault zone, others are elongated sub-parallel to the axis of the northwest trending Rio Grande embayment and to the Frio River Line (not shown). The Frio River Line is a northwest-southeast structure and was interpreted to be a boundary between two areas with different structural and stratigraphic histories [Ewing, 1987].

3.3. Methods

3.3.1. Sample Collection

Thirteen gas samples were collected for analysis of volume fractions and isotopic ratios of He, Ne, Ar, Kr, and Xe from seven producing wells in the oil zone of the Eagle Ford Shale in La Salle and Dimmit counties, in southwest Texas, south of San Antonio (Fig. 3.1). Except for well A6, two samples were collected from all other wells 30 minutes apart. Samples collected from the A6 and A7 wells, were collected in December of 2018. All other samples were collected in 2017.

Samples for noble gas analysis were collected directly from wellheads in standard refrigeration grade 3/8" copper tubes, which were then sealed by steel pinch-off clamps [Weiss, 1968]. Atmospheric contamination during sampling was minimized by allowing the gas to flush through the system for approximately 5 minutes prior to sample collection. In addition, samples for hydrocarbon gas geochemistry analysis were collected in industry standard 300 cm^3 valve-sealed stainless steel cylinders as well as in Isotubes, also flushed for 5 minutes to avoid air contamination for analysis at the Texas Tech University in Lubbock and at the University of Texas at the Austin Bureau of Economic Geology [Zhao et al., 2020].

3.3.2. Analytical Techniques

Noble gas analyses for the Eagle Ford Shale gas samples were carried out in the Noble Gas Laboratory at the University of Michigan. Extraction, purification, and analysis procedures are described briefly below [see also, e.g., Wen et al., 2017].

Gas samples in Cu tubes are attached to a vacuum extraction and purification system. The copper tube is connected to a vacuum system at a pressure of ~5 x 10^{-7} Torr. Once this pressure is achieved and the system isolated from its turbo-molecular vacuum pump, the lower clamp is opened to release the natural gas into a low He diffusion glass flask. Gas samples were then expanded in a known volume and gas pressure reduced by computer-controlled sequential pumping until reaching a value acceptable for analyses (typically 35 Torr). The gas sample was initially exposed to a Cu-CuO getter at 800°C in order to oxidize the hydrocarbons. The Cu-CuO getter was then allowed to cool to 450°C in order to reabsorb O_2. Subsequently the gas sample was exposed to a 3Å molecular trap to reduce water vapor pressure and reactive gases were removed using three Ti-getters at 600°C for three minutes each.

He, Ne, Ar, Kr, and Xe were quantitatively extracted using a dual chamber computer-controlled cryo-separator at temperatures of 49 K, 84 K, 210 K, 245 K, and 290 K respectively, and sequentially allowed to enter a Thermo Scientific® Helix SFT mass spectrometer for He and Ne isotope analyses, and a Thermo Scientific® ARGUS VI mass spectrometer for the Ar, Kr, and Xe isotope analyses. At the He release temperature, a small percentage of He is introduced into the SFT mass spectrometer and the signal intensity of ^{4}He is determined for use as the He concentration estimate. This estimate is then used by the automated system to optimize the amount of He that should be introduced for measurement of the $^{3}He/^{4}He$ ratio. All noble gas isotopes were measured using a Faraday detector, except for ^{3}He, which was measured using an electron multiplier in ion counting mode. Prior to each analysis, a blank run was conducted using the same procedure as the sample. Typical blanks are 0.3% - 0.9% of the measured sample values. Quantitative analyses were obtained by calibrating the two mass spectrometers with a known aliquot of standard air. Typical standard reproducibility for ^{4}He, ^{20}Ne and ^{36}Ar are 0.4%, 0.9% and 0.3% while for $^{20}Ne/^{22}Ne$ and $^{40}Ar/^{36}Ar$ ratios the reproducibilities are 0.08% and 0.04%, respectively. Calculated standard errors for concentrations range from 1.3 to 2.2% of the measured values.

3.4. Results

3.4.1. Major Gases

Major gas species compositions were determined for all wells (Table 3.1). In all wells, methane (CH_4) is largely dominant over all other components by volume, ranging from 58.54% in well A7, the westernmost well, to 79.87 % in well A4 (Table 3.1). Hydrocarbons with larger molecular mass make up the rest of the gas volume, with ethane (C_2) varying by volume between

11.51% and 18.53%, propane (C_3) between 4.81% and 13.07%, and hydrocarbons with molecular mass equal or heavier than butane (C_{4+}) between 2.87% and 10.82% of the total gas volume (Table 3.1). The dryness of the hydrocarbon samples, defined as $C_1/(C_2+C_3)$ (Bernard et al., 1976), varies between 1.89 and 4.90, with the two wells located on the westernmost side, A6 and A7, being the wettest, with the lowest values (Table 3.1) and thus, displaying the lowest maturity levels. Nitrogen (0.46% - 0.81%), Oxygen (0.11% - 0.27%) and CO_2 (1.1% - 0.73%) are also present although in small amounts. Stable carbon and hydrogen isotopes of the same batch of samples were also analyzed (Zhao et al., 2020). Maturity levels based on $C_1/(C_2+C_3)$ and $\delta^{13}C_{methane}$ point to a thermogenic origin of the Eagle Ford gas samples. Low $\delta\ ^2H$ values of these samples are consistent with the early mature thermogenic nature of these gases and consistent with a dominance of oil-producing wells in our sampled area (Zhao et al., 2020).

Table 3.1 Major gas compositions of the Eagle Ford gas samples.

Well name	Chemical composition （%）							
	Methane (C_1)	Ethane (C_2)	Propane (C_3)	C_{4+}	N_2	O_2	CO_2	$C_1/(C_1+C_2)$
A1	77.91	12.24	5.51	3.26	0.57	0.13	1.08	4.39
A2	77.82	12.24	5.42	3.54	0.41	0.16	0.99	4.40
A3	75.34	12.98	6.37	4.21	0.46	0.22	1.1	3.89
A4	79.87	11.51	4.81	2.87	0.81	0.11	0.95	4.90
A5	76.99	12.66	5.85	3.78	0.60	0.27	0.73	4.16
A6	70.42	15.35	8.83	6.59	-	-	-	2.91
A7	58.54	17.90	13.07	10.82	-	-	-	1.89

3.4.2. Noble Gases

Well names and depths, methane abundances, sample ID, and total ^{4}He, ^{22}Ne, ^{36}Ar, ^{84}Kr and ^{132}Xe volume fractions are provided in Table 3.2. Except for well A6, two samples were collected from all other wells within 30 minutes of each other. The first sample is indicated with the notation "a", the second sample is identified with the notation "b". ^{3}He/^{4}He ratios (R) are normalized to the atmospheric ratio Ra. R/Ra ratios of collected gas samples vary from 0.107 ± 0.0014 to 0.255 ± 0.0030 (Table 3.3), all above the typical crustal R/Ra production values of 0.02-0.05 [Oxburgh et al., 1986]. R/Ra values higher than the crustal production domain suggest the presence of atmospheric or mantle components. If helium is treated as a mixture between a crustal and an atmospheric component, using an atmospheric ^{4}He/^{22}Ne value of 3.12, the crustal He volume fractions can be derived as follows [Ballentine et al., 2002]:

$$^{4}\mathrm{He}^{*} = {}^{4}\mathrm{He}_{\mathrm{measured}} - \left(\frac{^{4}\mathrm{He}}{^{22}\mathrm{Ne}}\right)_{\mathrm{air}} \times {}^{22}\mathrm{Ne}_{\mathrm{measured}} \quad (3.1)$$

where subscripts air and measured refer to the atmosphere and measured values. Crustal ^{4}He volume fractions of all gas samples in this study are listed in Table 3.2.

Similarly, Ne, Ar and Xe are treated as a two-component mixture, with an atmospheric and a crustal endmember. Crustal ^{21}Ne, ^{40}Ar and ^{136}Xe contributions (^{21}Ne*, ^{40}Ar*, ^{136}Xe*) are estimated as follow [Ballentine et al., 2002]:

$$^{21}\mathrm{Ne}^{*} = \left(\left(\frac{^{21}\mathrm{Ne}}{^{22}\mathrm{Ne}}\right)_{\mathrm{measured}} - \left(\frac{^{21}\mathrm{Ne}}{^{22}\mathrm{Ne}}\right)_{\mathrm{air}}\right) \times {}^{22}\mathrm{Ne}_{\mathrm{measured}} \quad (3.2)$$

$$^{40}\mathrm{Ar}^{*} = \left(\left(\frac{^{40}\mathrm{Ar}}{^{36}\mathrm{Ar}}\right)_{\mathrm{measured}} - \left(\frac{^{40}\mathrm{Ar}}{^{36}\mathrm{Ar}}\right)_{\mathrm{air}}\right) \times {}^{36}\mathrm{Ar}_{\mathrm{measured}} \quad (3.3)$$

$$^{136}\mathrm{Xe}^{*} = \left(\left(\frac{^{136}\mathrm{Xe}}{^{130}\mathrm{Xe}}\right)_{\mathrm{measured}} - \left(\frac{^{136}\mathrm{Xe}}{^{130}\mathrm{Xe}}\right)_{\mathrm{air}}\right) \times {}^{130}\mathrm{Xe}_{\mathrm{measured}} \quad (3.4)$$

where $(^{21}Ne/^{22}Ne)_{air}$ = 0.029, $(^{40}Ar/^{36}Ar)_{air}$ = 295.5 and $(^{136}Xe/^{130}Xe)_{air}$ = 2.176 [Ozima and Podosek, 2002]. Calculated $^{21}Ne^*$, $^{40}Ar^*$ and $^{136}Xe^*$ are also listed in Table 3.2.

Total ^4He volume fractions in the Eagle Ford Shale range from 2.90×10^{-5} to 18.50×10^{-5}, with the lowest ^4He value found in the westernmost well A7 (A7-a) and the highest value in well A3, sample A3-b (Fig. 3.3a; Table 3.2). For all samples, the crustal $^4He^*$ component is almost entirely dominant, with over 99.9% of the total ^4He volume in all samples. A direct relationship between crustal $^4He^*$ and methane for most samples is observed and suggests a common origin for these two gases (Fig. 3.3b). Two obvious outliers are samples from well A3 and sample A2-b. They display $^4He^*$ volume fractions significantly higher than expected with respect to the observed trend. Also relevant, is the fact that batches a and b in both wells display significantly different $^4He^*$ volume fraction values, with both batch b samples displaying significantly higher values and pointing to two different hydrocarbon sources being tapped by the same well within short time periods. These, in turn, suggest the presence of well-connected reservoirs either through faults or through a system of fractures. These deviations from the general pattern are discussed below.

R/Ra ratios vary between 0.107±0.001 and 0.255±0.003 (Fig. 3.3c; Table 3.3) and are consistently higher than the typical crustal production values of 0.02-0.05 [shaded area, Fig. 3.3c; Oxburgh et al., 1986; Table 3.3]. No correlation is observed between R/Ra and CH_4 (Fig. 3.3c). These higher values point to the presence of a small mantle He component, either with a MORB-like [R/Ra=8; Moreira et al., 1998; Graham, 2002], OIB-like [R/Ra~50; Starkey et al., 2009] or solar-like [R/Ra~120; Starkey et al., 2009] origin. The origin of this mantle component is discussed below. Assuming a binary mixture between a crustal (R/Ra=0.02) and a MORB-like mantle component (R/Ra=8) endmember, estimated He mantle contributions vary between 1.09% (A7-a)

and 2.94% (A3-a). The presence of a mantle He component in these samples is consistent with our findings based on the Ne isotopic ratios as discussed below.

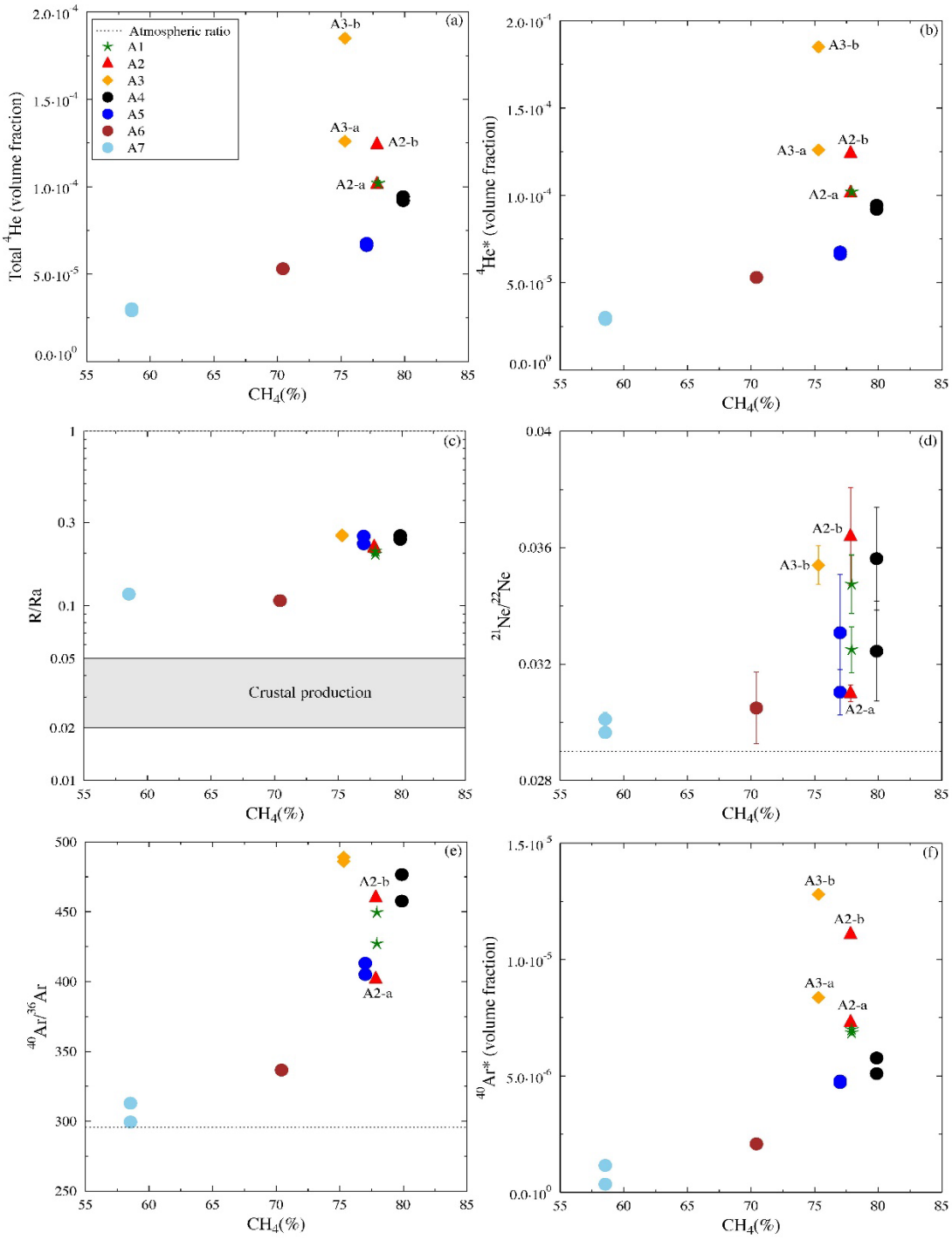

Figure 3.3 (a) Total ^{4}He volume fractions, (b) Crustal ^{4}He* volume fractions, (c) R/Ra ratios, (d) ^{21}Ne/^{22}Ne ratios, (e) ^{40}Ar/^{36}Ar and (f) Crustal ^{40}Ar* volume fractions as a function of methane volume percentages

All $^{21}Ne/^{22}Ne$ ratios are above the atmospheric value of 0.029 [Ozima and Podosek, 2002] and reflect the addition of crustally produced nucleogenic $^{21}Ne^*$, with values varying between 0.0296 ± 0.001 and 0.0364 ± 0.002 (Fig. 3.3d; Table 3.3). Crustal $^{21}Ne^*$ volume fractions for all gas samples are highly variable and range from 0.93×10^{-12} to 5.87×10^{-12}, representing contributions varying between 2.20% and 19.82%, respectively, with respect to the total $^{21}Ne^*$ volume fractions (Table 3.2). The highest crustally produced $^{21}Ne^*$ contribution is found in well A2, sample A2-b (Table 3.2). A generally positive correlation is observed between $^{21}Ne/^{22}Ne$ ratios and methane content suggesting a common origin for both gases (Fig. 3.3d). Unlike ^{4}He, atmospheric ^{21}Ne contributions for all samples are much higher and vary between 67.6% and 87.1% of total ^{21}Ne. Most measured $^{20}Ne/^{22}Ne$ ratios are higher than the atmospheric value of 9.80 [Ozima and Podosek, 2002] and point to the presence of a mantle component. The nature of this mantle component as well as its implications in terms of geological and tectonic evolution, hydrocarbon origin and migration is discussed in detail below.

All samples display $^{40}Ar/^{36}Ar$ ratios above the atmospheric value of 295.5 [Ozima and Podosek, 2002], varying between 299.4 ± 0.4 and 489.4 ± 0.9 (Fig. 3.3e; Table 3.3), reflecting the addition of crustal radiogenic $^{40}Ar^*$. The highest $^{40}Ar/^{36}Ar$ ratio is found in well A3 (A3-b) while the lowest value is found in the A7 well (A7-a) (Fig. 3.3e, Table 3.3). Crustal $^{40}Ar^*$ volume fractions range from 0.35×10^{-6} to 12.80×10^{-6} (Fig. 3.3f, Table 3.2). Like $^{4}He^*$, a positive correlation between crustal $^{40}Ar^*$ and methane is observed, except for the two obvious outliers, samples from well A3 and sample A2-b, which display higher than expected $^{40}Ar^*$ volume fraction values. Also relevant is the fact that batches a and b for both samples display significantly different $^{40}Ar^*$ volume fraction values, with both batch b samples displaying significantly higher values and pointing to two different hydrocarbon sources being tapped by the same well within short time

periods. As previously observed with He, this suggests the presence of well-connected reservoirs either through faults or through a system of fractures. These deviations from the general pattern are discussed below.

$^{86}Kr/^{84}Kr$ ratio values are slightly above the atmospheric value of 0.305 [Table 3.3; Ozima and Podosek, 2002] and likely result from a very small amount of crustally produced $^{86}Kr^*$. Most samples display also $^{136}Xe/^{130}Xe$ ratios above the atmospheric value of 2.176 [Table 3.3; Ozima and Podosek, 2002]. Volume fractions of $^{136}Xe^*$ vary between 0.54×10^{-13} and 16.08×10^{-13} (Table 3.2) corresponding to a minor crustal contribution varying between 0.07% - 1.15%, respectively. No correlations between $^{136}Xe^*$ volume fractions or $^{136}Xe/^{130}Xe$ ratios and methane are observed (not shown).

Table 3.2 Well names, depths, CH_4 contents, noble gas volume fractions (cm^3/cm^3) and crustal noble gas volume fractions for production gas samples from the Eagle Ford Shale.

Well Name	Depth (m)	Sample ID (NGL)	CH_4 (%)	Total ^4He ($x10^{-5}$)	Total ^{22}Ne ($x10^{-9}$)	Total ^{36}Ar ($x10^{-8}$)	Total ^{84}Kr ($x10^{-9}$)	Total ^{132}Xe ($x10^{-10}$)	$^4He^*$ ($x10^{-5}$)	$^{21}Ne^*$ ($x10^{-12}$)	$^{40}Ar^*$ ($x10^{-6}$)	$^{136}Xe^*$ ($x10^{-13}$)
A1	2581	A1-a	77.91	10.2	1.49	5.21	2.30	2.85	10.2±0.2	5.20±1.17	6.85±0.10	4.17±2.30
		A1-b	77.91	10.2	0.66	4.54	2.39	2.95	10.2±0.2	3.78±0.66	6.99±0.10	5.39±1.31
A2	2573	A2-a	77.82	10.1	2.94	6.87	2.31	2.96	10.1±0.2	5.87±0.83	7.30±0.10	5.40±1.41
		A2-b	77.82	12.4	0.66	6.74	1.71	2.78	12.4±0.2	4.89±1.11	11.1±0.16	6.07±2.13
A3	2400	A3-a	75.34	12.6	0.66	4.40	1.98	2.40	12.6±0.2	-*	8.37±0.12	0.54±2.28
		A3-b	75.34	18.5	0.85	6.61	1.48	2.53	18.5±0.3	5.45±0.57	12.8±0.18	7.43±1.36
A4	2316	A4-a	79.87	9.43	0.52	3.15	1.54	2.26	9.43±0.1	1.80±0.90	5.10±0.07	5.44±1.59
		A4-b	79.87	9.20	0.41	3.19	1.67	2.18	9.20±0.1	2.74±0.73	5.77±0.08	5.32±1.82
A5	2302	A5-a	76.99	6.75	1.55	4.36	1.60	2.41	6.75±0.1	3.16±1.22	4.78±0.08	-
		A5-b	76.99	6.62	0.99	4.01	1.65	2.50	6.62±0.1	4.02±1.97	4.72±0.07	3.07±1.73
A6	2133	A6-a	70.42	5.29	0.62	5.05	2.39	3.70	5.29±0.1	0.93±0.77	2.08±0.03	10.66±1.90
A7	2031	A7-a	58.54	2.90	8.58	8.84	2.53	4.19	2.90±0.1	5.58±1.08	0.35±0.03	16.08±2.94
		A7-b	58.54	3.02	3.09	6.63	2.36	4.28	3.02±0.1	3.42±0.74	1.15±0.02	14.88±2.02
Air				0.5	1678.0	3142.0	649.8	233.9				

* $^{21}Ne^*$ of sample A3-a is not included due to its low $^{21}Ne/^{22}Ne$ measurement accuracy.

Table 3.3 Noble gas isotopic ratios for production gas samples from the Eagle Ford Shale

Well Name	Sample ID (NGL)	R/Ra	$^{20}Ne/^{22}Ne$	$^{21}Ne/^{22}Ne$	$^{38}Ar/^{36}Ar$	$^{40}Ar/^{36}Ar$	$^{86}Kr/^{84}Kr$	$^{136}Xe/^{130}Xe$
A1	A1-a	0.197±0.003	10.09± 0.02	0.0325±0.0008	0.1895±0.0013	427.1±1.0	0.3093±0.0005	2.186±0.005
	A1-b	0.206±0.003	9.80± 0.01	0.0347±0.0010	0.1891±0.0012	449.4±0.8	0.3087±0.0005	2.188±0.003
A2	A2-a	0.217±0.004	10.22± 0.01	0.0310±0.0003	0.1877±0.0009	401.8±0.4	0.3090±0.0004	2.188±0.003
	A2-b	0.214±0.002	9.78± 0.02	0.0364±0.0017	0.1880±0.0021	460.0±1.1	0.3085±0.0005	2.190±0.005
A3	A3-a	0.255±0.003	9.89± 0.05	-[b]	0.1908±0.0027	485.5±0.9	0.3091±0.0005	2.177±0.006
	A3-b	0.252±0.002	9.96± 0.01	0.0354±0.0007	0.1893±0.0012	489.4±0.9	0.3096±0.0005	2.196±0.004
A4	A4-a	0.253±0.003	9.79± 0.03	0.0324±0.0017	0.1899±0.0020	457.6±0.6	0.3094±0.0004	2.192±0.005
	A4-b	0.240±0.005	9.82± 0.02	0.0356±0.0018	0.1962±0.0020	476.6±0.9	0.3084±0.0005	2.192±0.006
A5	A5-a	0.251±0.003	10.21± 0.01	0.0310±0.0008	0.1870±0.0016	405.1±1.2	0.3093±0.0006	2.174±0.005
	A5-b	0.227±0.003	10.09± 0.02	0.0331±0.0020	0.1878±0.0022	413.1±0.9	0.3095±0.0006	2.184±0.005
A6	A6-a	0.107±0.001	10.15±0.02	0.0304±0.0012	0.1895±0.0009	336.6±0.5	0.3080±0.0005	2.195±0.003
A7	A7-a	0.116±0.001	10.41±0.01	0.0296±0.0001	0.1846±0.0010	299.4±0.4	0.3074±0.0004	2.201±0.005
	A7-b	0.117±0.001	10.30±0.01	0.0301±0.0001	0.1851±0.0008	312.9±0.3	0.3078±0.0006	2.199±0.003
Air[a]		1	9.80	0.029	0.188	295.5	0.305	2.176

[a] Ozima and Podosek, [2002]

[b] $^{21}Ne/^{22}Ne$ of sample A3-a is not included due to its low measurement accuracy.

3.5. Discussion

As seen in the previous section, a crustal component is present in all noble gases and is entirely dominant for $^{4}He^{*}$ (Table 3.2). These crustal components ($^{4}He^{*}$, $^{21}Ne^{*}$, $^{40}Ar^{*}$) display a positive correlation with CH_4 and suggest that both methane and crustal noble gases are produced and/or transported together. R/Ra and $^{20}Ne/^{22}Ne$ ratios also point to the presence of a mantle He and Ne components of undetermined origin. Below, we provide clarification on the nature of this mantle component using the combined $^{20}Ne/^{22}Ne$ and $^{21}Ne/^{22}Ne$ ratios as well as an in-depth analysis of the different Ne components present and a combined He and Ne isotope analysis.

While our dataset alone, collected from wells in the oil zone of the Eagle Ford Shale, provides critical information, our analysis gains significantly when compared to additional available data in the area that provide extended spatial coverage. Additional data are particularly useful to identify and/or clarify the tectonic features present, hydrocarbon sources and possible geological evolution of the region. Thus, in the analysis presented, when possible, the following data are incorporated (Fig. 3.1): 1) Byrne et al. [2018] dataset comprised of Eagle Ford Shale gas samples collected from four wells in the wet gas zone southeast of our sampling area. In addition, their dataset includes two wells from the oil zone, well A in the immediate vicinity of our samples, to the east, and well B, significantly away of all other oil wells sampled, in the extreme southeast corner of Atascosa County (Fig. 3.1), and; 2) information provided by Harrington et al. [2015] on R/Ra and $^{20}Ne/^{22}Ne$ ratio variations from 27 gas samples collected in the oil zone northeast of our study area, in Frio, Atascosa, LaSalle and McMullen counties (Fig. 3.1).

3.5.1. Resolving He and Ne Mantle Sources

Most of our samples display $^{20}Ne/^{22}Ne$ ratios higher than that of the atmospheric ratio and reach values of up to 10.41±0.01 (Table 3.3). Because nucleogenic ^{20}Ne production as well as the occurrence of mass dependent fractionation were excluded as a potential source of these high $^{20}Ne/^{22}Ne$ values (Appendices B1 and B2, respectively), it is clear that these high $^{20}Ne/^{22}Ne$ ratios largely reflect the addition of mantle ^{20}Ne with contributions of up to over 20% of the total measured ^{20}Ne. These are contributions from either the upper (including the lithosphere) or lower mantle, both enriched in ^{20}Ne, of which the most primordial $^{20}Ne/^{22}Ne$ ratio is represented by the solar endmember value of 13.8 [Benkert et al., 1993; Table 3.4]. By contrast, $^{21}Ne/^{22}Ne$ ratios greater than the atmospheric value of 0.0290 (Table 3.3) up to 0.0364±0.0017 (Table 3.3) reflect the addition of crustally produced nucleogenic ^{21}Ne. $^{20}Ne/^{22}Ne$ ratios versus $^{21}Ne/^{22}Ne$ ratios of our samples are shown in Fig. 3.4. It is apparent that these reflect a three-component mixing between the atmosphere, the crust, and the mantle and provide clarification on the nature of this mantle component, i.e., a MORB, OIB or solar-like source. Specifically, 5 samples (A7-a, A7-b, A6, A5-a, A2-a) plot within the area defined by the Air-MORB-Solar endmembers significantly above the well-established MORB line [Moreira et al., 1998], falling into the domain of multiple OIB lines (e.g., Kerguelen, Reunion, Hawaii, Iceland; Fig. 3.4; Table 3.4), and pointing strongly to the presence of a primordial Ne component. This primordial Ne component can be traced to a solar-like origin as shown by our westernmost sample A7-a which falls on the Solar line (Fig. 3.4; Table 3.4). An in-depth He-Ne combined analysis (below) confirms these findings. On the other hand, 5 samples (A4-a, A4-b, A3-b, A2-b, A1-b) fall within the area defined by the Air-MORB-Crustal endmembers, below the MORB line and thus, into the MORB domain (Fig. 3.4). Two samples (A1-a, A5-b) fall within the boundary between the OIB-Solar-like type and MORB

domains. Significantly, batches a and b samples from well A2 display a different type of mantle source, OIB-Solar-like type for batch a, MORB–type for batch b, an observation consistent with crustal $^{4}He^{*}$ and $^{40}Ar^{*}$ data pointing to two distinct gas sources for these samples (Figs. 3.3b, f; Table 3.2). This, in turn, suggests the presence of a deeper fault system in the area connecting these reservoirs, and facilitating the transport of this deeper OIB-Solar-like type mantle ^{20}Ne component. Unfortunately, due to extremely low levels of ^{21}Ne, no $^{21}Ne/^{22}Ne$ ratio is available for sample A3-a. However, it is apparent that both westernmost wells, A6 and A7, are dominated by an OIB-Solar-like type component, suggesting the possible presence of a spatial, regional differentiation in terms of the mantle component involved. This is discussed below.

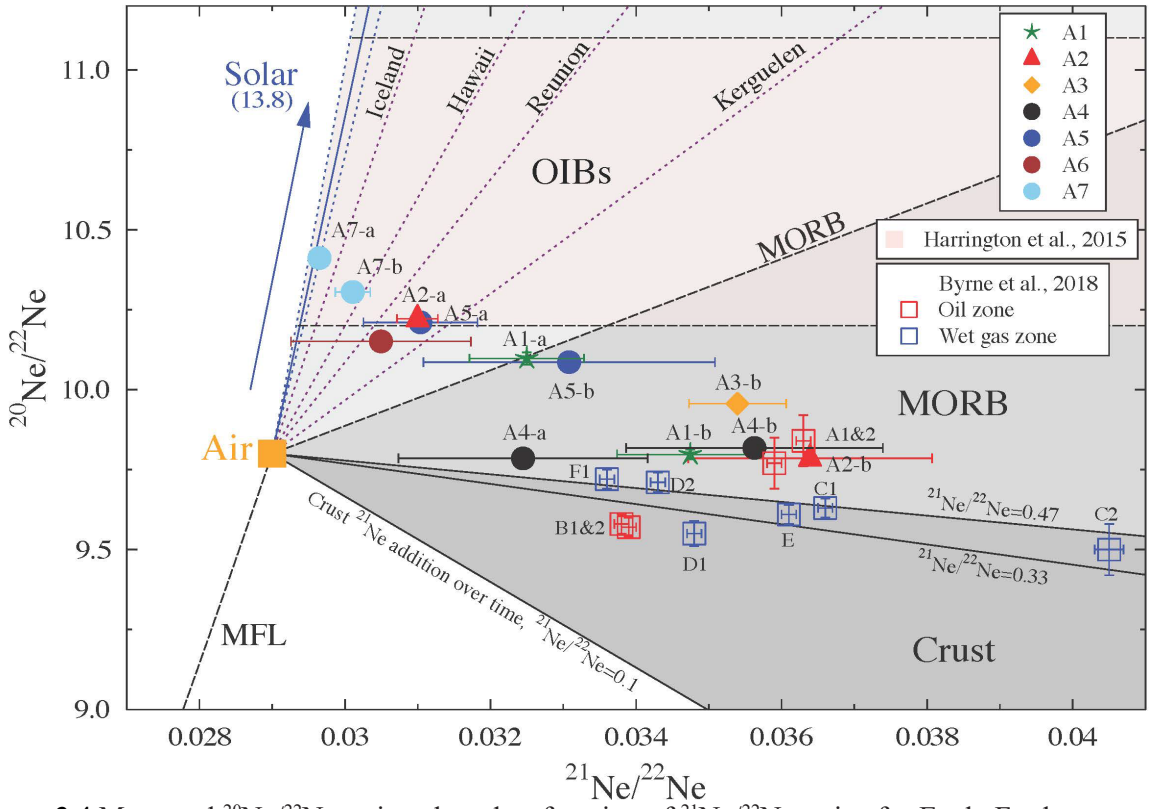

Figure 3.4 Measured $^{20}Ne/^{22}Ne$ ratios plotted as function of $^{21}Ne/^{22}Ne$ ratios for Eagle Ford gas samples. Three components are presented in this diagram: Air, Mantle (MORB, OIBs, Solar), and Crust. Mixing lines between Air–Solar, Air–MORB and Air–OIB endmembers for Iceland, Hawaii, Reunion, and Kerguelen are indicated. Air–Crust mixing lines with $^{21}Ne/^{22}Ne$ ratios of 0.1, 0.47 and 0.33 (Table 3.4) are also shown. Triangular grey areas, from lighter to darker indicate the Air–Solar–MORB, Air–MORB–Crust, and Air Crust domains, respectively. Endmember values are provided in Table 3.4. Blue dashed lines along the Air–Solar line provide uncertainty associated with measurements. Pink area represents the area in which Harrington et al. [2015] fall based on their reported $^{20}Ne/^{22}Ne$ values (10.2 - 11.1).

Byrne et al. [2018] data confirm the presence of spatial variations, not only in terms of a mantle component but also with respect to its absence in certain areas. Interestingly, all samples from the wet gas zone together with sample b from the oil zone in the easternmost corner of Atascosa County [Fig. 3.1; Byrne et al., 2018], appears to display a Ne isotopic signature that is likely devoid of a significant mantle contribution, with Ne isotopic ratios resulting from mixing between Air and two distinct Crustal mixing lines with $^{21}Ne/^{22}Ne$ ratios of 0.47 and 0.1, respectively (Fig. 3.4; Table 3.4). On the other hand, well A, in the oil zone [Byrne et al., 2018], in the vicinity of our sampled wells to the east, falls within the MORB zone, together with five of our Eagle Ford samples (Fig. 3.4). Just northeast of our sampled area, all Harrington et al. [2015] samples fall in a dominated OIB-MORB area, with $^{20}Ne/^{22}Ne$ ratios varying between 10.2 and 11.1 (Fig. 3.4; pink area). It is interesting to note that the lowest $^{20}Ne/^{22}Ne$ ratios reported by Harrington et al. [2015] display values comparable to our sample's highest values, suggesting a potential dominance of an OIB or solar-like source for these oil wells (see below). Thus, a clear spatial pattern on Ne isotopic sources becomes apparent, with what appears to be an almost entirely crustally dominated source in the south and absence of a mantle component, to a mantle MORB-type source in the central area, followed by an OIB-Solar-type mantle source further north and to the west. A tentative representation of this spatial distribution of gradually evolving crustal and mantle sources based on Ne isotopic signatures is illustrated in Fig. 3.6 where the crustal, MORB and OIB-Solar like regions are indicated.

In the Eagle Ford Shale natural gas samples, the existence of a solar-like component for samples lying below the MORB line (Fig. 3.4), if present, can also be traced through the combined analysis of He and Ne isotopic ratios. Here, a primordial component is commonly characterized by directly correlated $^{20}Ne/^{22}Ne$ and inversely correlated $^{21}Ne/^{22}Ne$ with R/Ra ratios, respectively

[Moreira and Allegre, 1998; Graham, 2002]. This combined analysis in our gas samples requires removal of the atmospheric Ne component so that, like R/Ra ratios, Ne isotopic ratios will represent solely a binary mixture between crust and mantle (MORB, OIB, or Solar) endmembers ($^{20}Ne/^{22}Ne_{crust+mantle}$ and $^{21}Ne/^{22}Ne_{crust+mantle}$).

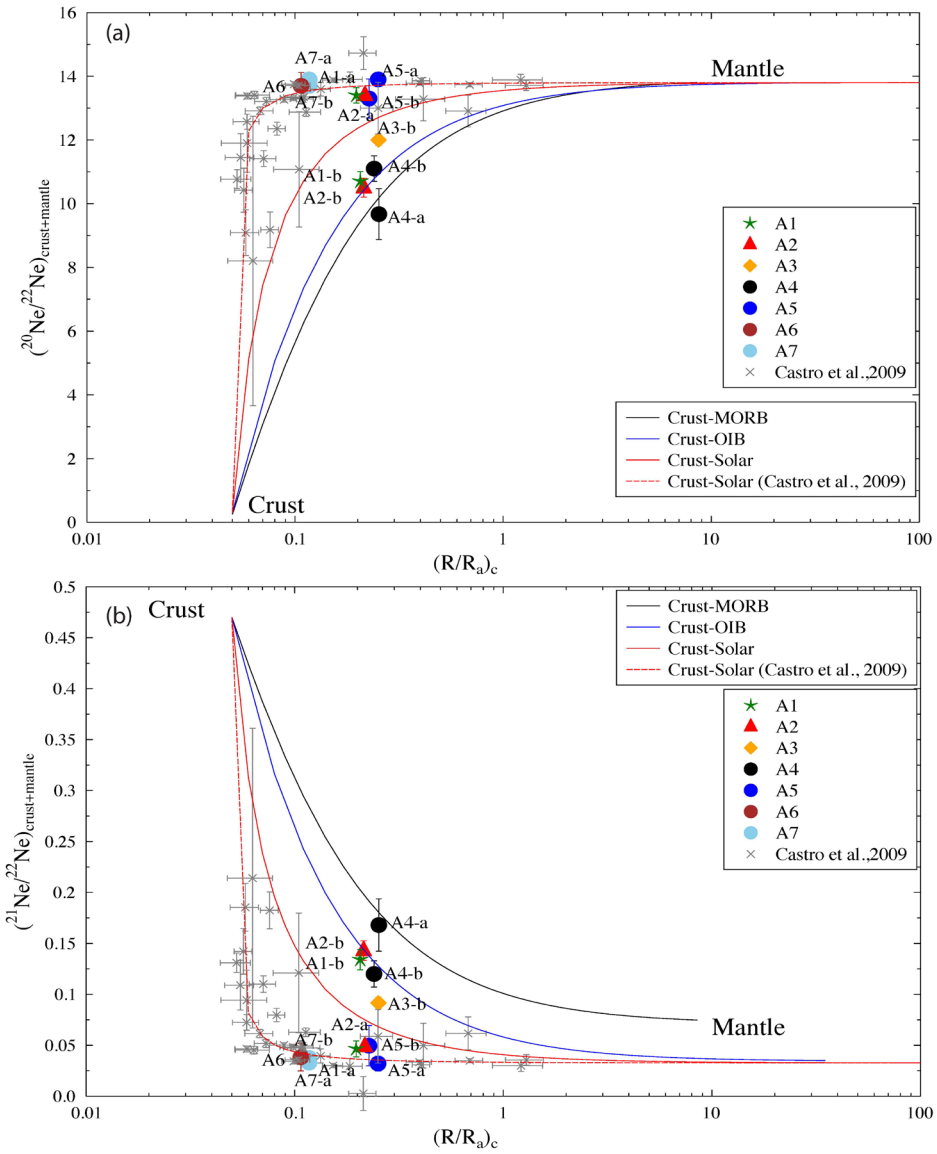

Figure 3.5 Two-component mixing plots for $(R/Ra)_c$ vs. (a) $(^{20}Ne/^{22}Ne)_{crust+mantle}$ and (b) $(^{21}Ne/^{22}Ne)_{crust+mantle}$ for Eagle Ford gas samples in this study and Michigan Basin brines [Castro et al.,2009]. Theoretical crust-MORB, crust-OIB and crust-solar mixing lines are shown. Modified crust-solar [Castro et al., 2009] mixing line is also shown (cf., Appendix B3).

Although as mentioned earlier, atmospheric He contributions are negligible for all samples (Table 3.2, 3.3) and thus, measured R/Ra ratios above the crustal production value represent simply a binary mixture between a crustal and mantle components, removal of the atmospheric He air component was also performed following Craig et al. [1978] (Table 3.5). It is apparent that both measured and air-corrected R/Ra ($(R/Ra)_c$) values are unchanged (Tables 3.3, 3.5). Removal of the atmospheric Ne (Table 3.5) was achieved following previously developed procedures [Appendix B3; Ballentine and O'Nions, 1992; Ballentine, 1997; Castro et al. 2009]. Figures 3.5a, b represent the calculated air-corrected $^{20}Ne/^{22}Ne_{crust+mantle}$ and $^{21}Ne/^{22}Ne_{crust+mantle}$ versus the air-corrected $(R/Ra)_c$, respectively, for the Eagle Ford samples. The same air-corrected values for the Michigan Basin brines [Castro et al., 2009] are also shown, together with theoretical crust-MORB, crust-OIB and crust-solar mixing lines (Table 3.4) as well as the crust-solar mixing line estimated for the Michigan Basin brines [Castro et al., 2009] with a crustal $^{21}Ne/^{22}Ne$ end member value of 0.047. Mixing lines between the crust and mantle (MORB, OIB, and Solar, respectively) in these two-element isotope plots are defined by their respective isotopic ratio endmembers (Table 3.4) as well as by the curvature of each hyperbola defined by $K_{crust\text{-}mantle} = (^4He/^{22}Ne)_{crust}/(^4He/^{22}Ne)_{mantle}$, where $(^4He/^{22}Ne)_{crust}$ and $(^4He/^{22}Ne)_{mantle}$ are the crustal and mantle (MORB, OIB, Solar) $^4He/^{22}Ne$ elemental ratios, respectively (Table 3.4). If no uncertainty were to be associated with the crustal and mantle He and Ne endmembers, and if prior to mixing all endmembers had a spatially constant crustal and mantle $^4He/^{22}Ne$ ratio, all samples would fall along a single mixing line within error. Under these same assumptions, all Eagle Ford natural gas samples would be expected to fall along one of the theoretically defined Crust-MORB, crust-OIB or Crust-Solar line (black, blue and red solid lines, respectively; Figs. 3.5a, b, Table 3.4; see also Appendix B3). This is, however, not observed. Instead, the bulk of samples with the most primordial, stronger mantle signature (A7-a,

A7-b, A6, A5-a, A2-a) falls along one single crust-solar mixing line very similar to that derived for the Michigan Basin brines [Castro et al., 2009] while all other samples fall between this crust-solar mixing line and that of a crust-MORB mixing line. Overall, the combined analysis of He and Ne isotopic ratios points to the presence of two mantle endmembers. One, with a weak Ne mantle signal corresponding to a MORB origin of which sample A4-a (2% mantle ^{20}Ne) is the best representative. The other, significantly stronger, more prevalent, corresponding to a primordial, solar-like mantle component, represented by a cluster of seven samples (A7-a, A7-b, A6, A5-a, A5-b, A1-a, A2-a) of which sample A7-a is the best representative, with over 20% of mantle ^{20}Ne (Figs. 3.5a, b). Samples falling between both endmembers and displaying R/Ra_c values varying within a narrow range, i.e., samples A1-b, A2-b, A3-b and A4-b, are interpreted as resulting from mixing between the MORB and solar-like endmembers. Samples A1-a and A5-b which were located at the boundary of MORB-OIB-Solar-like signature in the Ne component plot (Fig. 3.4) belong unequivocally to the Solar-like domain as revealed by the He-Ne combined analysis (Figs. 3.5a, b). The weak MORB-type mantle signal suggests the presence of an old mantle source, increasingly masked by a crustal signature over time. The stronger, more prevalent solar-like component suggests either a relatively recent addition of that solar-component to this natural gas reservoir directly from its original source, or its storage in a nearby reservoir that has been shielded from crustal contamination. In addition, the similar mixing line shared by both, the Eagle Ford natural gas samples and those of Michigan Basin brines suggests a common source for this primordial solar component. The origin for both the MORB-type and solar-like sources is discussed next.

Table 3.4 Endmember isotopic and elemental ratios of distinct earth reservoirs

	Isotopic ratios			Elemental ratios			$(^4He/^{22}Ne)_{crust} / (^4He/^{22}Ne)_{mantle}$
	R/Ra	$^{20}Ne/^{22}Ne$	$^{21}Ne/^{22}Ne$	$^4He/^{20}Ne$	$^3He/^{22}Ne$	$^4He/^{22}Ne$	
Crust[a]	0.05	0.3	0.47			7.9×10^7	
			0.1				
Mantle							
Primordial (primitive solar nebula)[b]	120	13.8	0.0328	850		1.17×10^4	6735
OIB mantle (Iceland)[c]	35	13.8	0.035		6	1.24×10^5	636
OIB mantle (Hawaii)[c]		13.8	0.039				
OIB mantle (Reunion)[c]		13.8	0.043				
OIB mantle (Kerguelen)[c]		13.8	0.053				
MORB mantle[c]	8	13.8	0.075		8.8	7.50×10^5	105

[a] R/Ra ratio after Oxburgh et al. [1986]; $^{21}Ne/^{22}Ne$ after Kennedy et al. [1990]. $^4He/^{22}Ne$ ratio after Yatsevich and Honda [1997].

[b] R/Ra ratio after Starkey et al. [2009]; $^{20}Ne/^{22}Ne$ and $^{21}Ne/^{22}Ne$ ratios after Benkert et al. [1993]; $^4He/^{20}Ne$ ratio after Anders and Grevesse [1989]; $^4He/^{22}Ne$ ratio calculated from $^4He/^{20}Ne$ and $^{20}Ne/^{22}Ne$ ratios.

[c] Summarized by Graham [2002]; Iceland - Dixon et al. [2000], Hawaii - Honda et al. [1991], Reunion - Hanyu et al. [2001], Kerguelen - Valbracht et al. [1996], MORB - Moreira et al. [1998]. $^4He/^{22}Ne$ ratios calculated from $^3He/^{22}Ne$ and R/Ra ratios.

Table 3.5 He and Ne isotopic compositions after correction of atmospheric component

Well name	Sample ID	$(^3He/^4He)_{crust+mantle}$* / $(R/Ra)_c$	$(^{20}Ne/^{22}Ne)_{crust+mantle}$	$(^{21}Ne/^{22}Ne)_{crust+mantle}$
A1	A1-a	0.1973±0.0025	13.44±0.24	0.0465±0.0078
	A1-b	0.2060±0.0032	10.74±0.31	0.1337±0.0099
A2	A2-a	0.2171±0.0036	13.37±0.07	0.0488±0.0022
	A2-b	0.2136±0.0022	10.45±0.30	0.1429±0.0096
A3	A3-b	0.2522±0.0024	12.04±0.17	0.0916±0.0055
A4	A4-a	0.2527±0.0030	9.67±0.78	0.1680±0.0257
	A4-b	0.2404±0.0046	11.15±0.40	0.1205±0.0129
A5	A5-a	0.2507±0.0026	13.89±0.23	0.0321±0.0073
	A5-b	0.2267±0.0025	13.35±0.61	0.0496±0.0198
A6	A6-a	0.1072±0.0014	13.70±0.42	0.0383±0.0134
A7	A7-a	0.1160±0.0010	13.86±0.03	0.0330±0.0009
	A7-b	0.1166±0.0011	13.72±0.06	0.0376±0.0020

*Estimated after removal of the atmospheric component using the atmosphere-derived ^{22}Ne concentrations following Craig et al. [1978]. $(^3He/^4He)_{crust+mantle}$ ratios are indistinguishable from the measured $^3He/^4He$ ratios (Table 3.3) due to the extremely high measured $^4He/^{22}Ne$ ratios of the Eagle Ford natural gas samples (3384 - 222933), 1084–71453 times the atmospheric value [3.12,Ozima and Podosek, 2002].

3.5.2. Geological and Tectonic Evolution

3.2.5.1. MORB Endmember – Origin and Implications

MORB signatures, as the name suggests, are typically associated with rifts and extensional areas. Thus, the combined He-Ne isotopic MORB-type signature suggests the presence of an old rift system, with a SW-NE orientation as shown in Fig. 3.6. This suggested rift, based on noble gas signatures, is parallel to the multiple fault systems previously identified in the region (Figs. 3.1, 3.6), i.e., the Balcones and Luling, the Karnes-Atascosa Trough, and the Charlotte-Jourdanton, fault zones (Figs. 3.1, 3.6). The transition from a dominant crustal signature almost entirely devoid of a mantle component in the gas zone (samples C, D, E, F; Byrne et al, 2018) and to the northeast, in the oil zone [sample B; Byrne et al., 2018], to one displaying a MORB-type mantle component in the adjacent oil zone appears well defined (Fig. 3.6). This He and Ne crustal-mantle signature transition between the gas and oil zone is the primary support for the chosen rift orientation in this area (Fig. 3.6).

The geological and tectonic history of this region remains poorly understood. This is partly due to the extreme thickness of the sediment cover, up to 14-16 km [Galloway, 2009; Agrawal et al., 2015], rendering access to the formations underneath difficult. Indeed, with the exception of the Llano Uplift, a lack of craton outcrops in the region further complicates the task. However, the occurrence of a MORB-type signature in our wells and our association with the presence of an old rift system in the area is consistent with geological and tectonic reconstructions of breakup and formation of supercontinents as well as the opening and closure of major oceans undertaken at the continental scale [e.g., Thomas, 1991, 2005]. In particular, the approximate location of the Laurentia southern edge was inferred based on geological, seismic and geophysical considerations [Flawn, 1961; Nicholas and Waddel, 1989; North American Magnetic Anomaly Group, 2002;

Thomas, 2005; Poole, et al., 2005] and found to be just north of our sampled wells (Figs. 3.1, 3.6). Palinplastic reconstructions were also carried out to identify the location of the Cambrian-age Ouachita (~530 Myrs) and Triassic (~200 Myrs) rifts at the continental scale, related to the breakup of Rodinia and the opening of the Iapetus Ocean, and to the breakup of Pangea and the opening of the Atlantic Ocean, respectively [Figs. 3.1, 3.6; e.g., Cawood et al., 2001; Thomas, 1991, 2005]. It is apparent that our originally suggested SW-NE rift location based on He and Ne isotopic ratios follows closely the southern Laurentia margin and lies just north of the identified Ouachita Rift [Fig. 3.6; Thomas, 1977, 1991, 2005; Cawood et al., 2001; Poole et al., 2005]. We hypothesize that the continental scale at which these rift reconstructions were carried out do not allow for the capture of detail at the regional and local scales, both in terms of direction and exact location. Indeed, Thomas [1991] cautions that the Appalachian-Ouachita rift system is not defined with sufficient precision to support an interpretation of exact orientations of the various segments. We hypothesize that the actual Ouachita Rift in our specific area has the orientation of our He-Ne MORB-suggested rift, which follows closely that of the Laurentia southern rifted edge (see Fig. 3.6 for comparison between the previously documented Ouachita rift, e.g., Thomas, 1991, 2005 and our proposed direction). This would imply a ~28° clockwise rotation of the currently mapped Ouachita Rift [e.g., Thomas, 2005] in the eastern portion of our study area, which corresponds to the western portion of Karnes County (Fig. 3.6). That rotation would also apply to the Texas transform, a major feature connecting the Ouachita and Marathon rifts, both part of the same rift system along the Appalachian-Ouachita continental margin of southeastern North America. The Marathon Rift is located northwest of the Ouachita Rift section [Thomas, 1991, 2005]. A smaller, ~19° clockwise rotation of the Ouachita Rift may take place near the eastern border of La Salle County, to bring that portion of the Ouachita rift section closer to a WSW-ENE direction and

parallel to our MORB-rift defined direction (Fig. 3.6). These smaller rotations can be accommodated through the presence of smaller transform faults along the rift section. The presence of smaller transform faults dividing narrow (~25 km) crustal zones is also consistent with the characterization by, e.g., Lister et al. [1986] (see also Thomas, 2005) of rifts associated with transitional crust. The presence of smaller transform faults in this area is further supported by our analysis of relative ^{40}Ar ages in our gas samples and the presence of a compartmentalized Eagle Ford Shale (below). We further suggest that the reconstructed Ouachita rift segment extends slightly further to the west than originally mapped [see, e.g., Thomas, 1991, 2005], down to the western portion of La Salle County (Figs. 3.1, 3.6). The modified Texas transform location would move at the proximity of well A4, of which sample A4-a displays the most typical MORB signature among all our samples. To the west of the Texas transform, the impact of a MORB signature, if present, is negligible and undetected. Instead, a solar-like signature is the sole mantle component identified (samples A7 and A6). By contrast, to the east, a MORB-type source influence is present, together with that of a solar-like component. Overall, our suggested He-Ne isotopic Ouachita rift direction follows closely the direction of all the major recognized structures in our study area, in particular, that of the Balcones and Luling fault zones, that of the southern edge of the Laurentia craton as well as that of the Ouachita orogeny [Figs. 3.1, 3.6; Poole et al, 2005]. Thomas [2005], reasoned that each episode of supercontinent assembly and breakup adapt to the tectonic framework of a preexisting continental margin and argued for pervasive continental inheritance. Our noble gas signature findings are consistent with and support the inheritance claims of Thomas [2005] both at the regional and local scales.

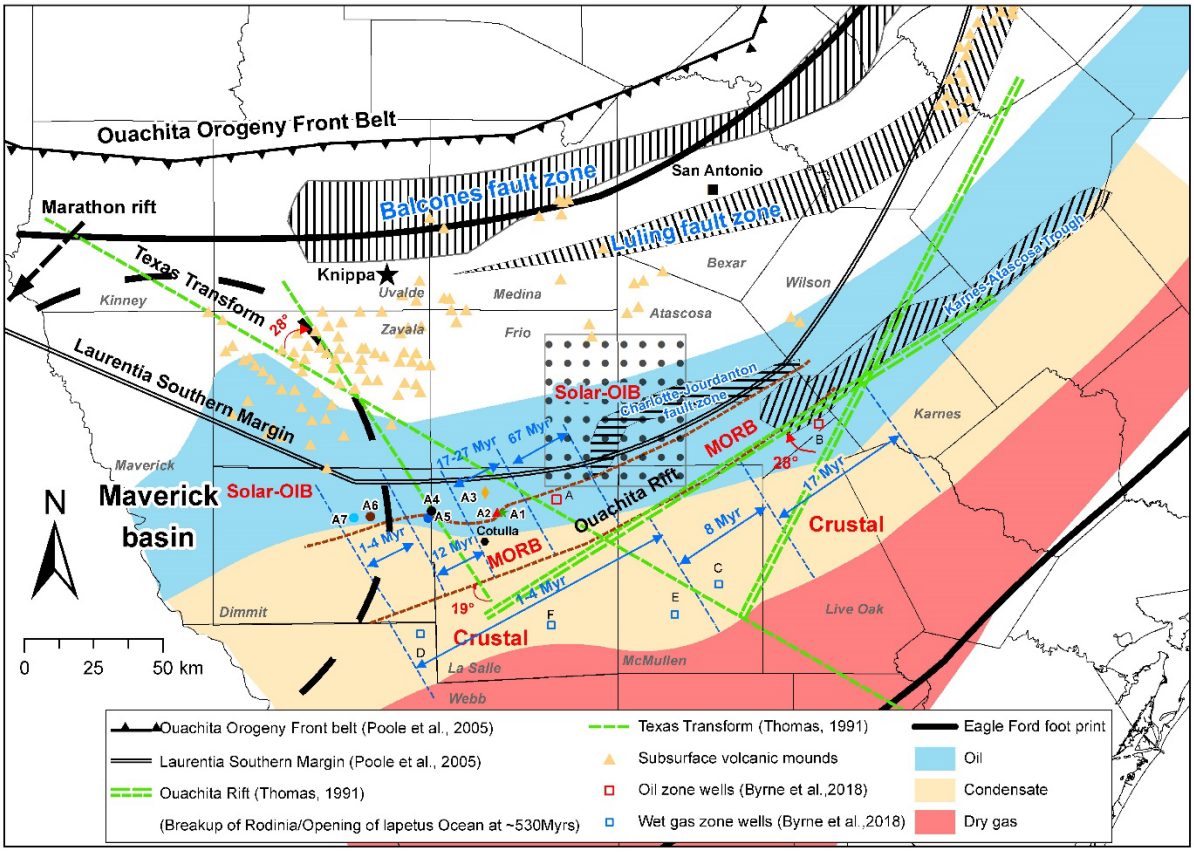

Figure 3.6 Map showing the location of all sampled wells, i.e., this study, Byrne et al. [2018] and Harrington et al. [2015] as well as the oil, wet and dry gas windows and major tectonic features. Boundaries between pure crustal, MORB and solar-like/OIB noble gas signatures are shown (red dashed lines). Suggested rotations of the originally palinplastic reconstructed Ouachita Rift and Texas transform [Thomas, 1991] are shown. The rotated Ouachita rift coincides with the crust-MORB boundary (red dashed line). ^{40}Ar relative age compartments are indicated (see text). Boundaries between compartments are indicated with blue dashed lines, which correspond to possible small transform faults.

3.2.5.2. Solar-Like Endmember – Origin and Implications

The more prevalent presence of a mantle solar-like component in the Eagle Ford natural gas suggests either a relatively recent addition of that solar-like component to this natural gas reservoir directly from its original source, or its storage in a nearby reservoir that has been shielded from crustal contamination. The presence of a primordial He and Ne solar component and, more specifically, that of an OIB-type signature has historically been associated with the presence of a lower, primordial, largely undegassed reservoir from which OIBs would originate via deep mantle plumes [O'Nions and Oxburgh, 1983; Porcelli and Wasserburg, 1995; Moreira et al., 1998]. However, no hotspot or the presence of a hotspot track has been identified in the area. Mickus et al. [2009] suggested that a high-amplitude magnetic anomaly south of the Triassic Rift (Fig. 3.1), pointed to the presence of a large buried mafic igneous complex, probably a volcanic rifted margin and thus, the presence of a mantle plume. However, this is significantly distant from our study area. In addition, their hypothesis was promptly dismissed by Dickinson [2009] and subsequently challenged by others [e.g., Griffin et al., 2010; Speckien, 2012; Agrawal et al., 2015].

Numerous volcanic mounds have been identified in this area, to the northeast, associated with the Balcones and Luling fault zones and to the northwest, where some mounds are aligned along the Frio River Line (not shown), roughly parallel to the Texas transform (Figs. 3.1, 3.6). Some volcanic mounds were also identified in the northern part of Atascosa and Frio counties but have not been associated with tectonic structures (Fig. 3.6). These volcanic mounds, which comprise the "Balcones Igneous Province" [Spencer, 1969] are associated with the discontinuity separating the Mesoproterozoic (Laurentian) cratonic lithosphere and the Jurassic transitional lithosphere, a zone roughly following the southern margin of the Laurentian craton [Griffin, 2008; Griffin et al., 2009, 2010]. Volcanic activity was estimated to have occurred in the Late Cretaceous, between 86 and 63 Myrs [Baldwin and Adams, 1971; Miggins et al., 2004; Griffin et al., 2010].

Volcanic rocks in all three areas consist of nephelinites, basanites, alkali basalts and phonolites [e.g., Spencer, 1969; Griffin et al., 2010]. Primordial, OIB-like mantle sources in nephelinites and basanites of the Uvalde area were first identified by Wittke and Mack [1993]. The strongest evidence for the primitive nature of these mafic magmas is the presence of mantle xenoliths (lherzolites, dunites, harzburgites), pointing to a deep origin of these rocks. Wittke and Mack [1993] concluded that the magmas were likely derived from depths over 80-100 km and may correspond to mantle upwelling from the asthenosphere locally mixed with lithospheric material. Alternatively, it may reflect upwelling of deeper, regionally mixed, mantle sources. Either way, Wittke and Mack [1993] pointed out that most Uvalde rocks displayed no evidence of crustal contamination. More recently, Young and Lee [2009] analyzed mantle xenoliths (spinel lherzolites) collected from the Vulcan open-pit quarry in Knippa, Uvalde County (Fig. 3.6). Their chemistry point to refractory peridotites such as harzburgites and clinopyroxene-poor lherzolite as a source and are thought to represent the residues of previous melt depletion. Whole-rock compositions are also consistent with a refractory origin. A key feature of the whole rock chemistry is the depletion in moderately incompatible trace elements relative to primitive mantle. Association with hot plumes or the asthenosphere was ruled out based on their cool equilibration temperatures (800-1100 °C). Young and Lee [2009] concluded that these xenoliths preserve an arc or subduction signature and likely represent fragments of continental lithospheric mantle formed prior to the Grenville orogeny that has been preserved, despite subsequent orogenic and rifting events. This would indicate that the original continental lithosphere did not undergo wholesale removal or delamination. Raye et al. [2011] subsequently analyzed additional spinel-peridotite xenolith samples collected from the same Vulcan quarry in Knippa and reached similar conclusions.

Although we do not rule out the presence of a mantle plume as the source of our He-Ne solar-like component in the Eagle Ford shale, it is plausible that this primordial component may instead originate in the subcontinental lithospheric mantle (SCLM) as suggested by Young and Lee [2009] and Raye et al. [2011]. This would also be consistent with findings by Castro et al. [2009] who identified the presence of a He-Ne solar-like component in the Michigan Basin, a continental cratonic region also part of the Laurentian craton that has no hotspots or hotspot tracks. Castro et al. [2009] suggested that this solar-like component can be accounted for by a shallow refractory reservoir in the Archean SCLM. Although the nature of the SCLM in southwest Texas is not well known due to the difficulty of access, it is clear that many modified Archean SCLM sections around the world, including that beneath the Michigan Basin and that of the Canadian Shield (Laurentian Plateau) present a number of similar characteristics. They tend to be rich in depleted lherzolites and harzburgites [Griffin et al., 2004] and suggest a highly depleted U-Th-K environment [Anderson, 1998; Rudnick and Nyblade, 1999]. Depleted U-Th environments together with a high concentration of depleted lherzolites and harzburgites suggests the presence of potential He and Ne reservoirs at relatively shallow depths [Graham et al., 1990; Anderson, 1998; Coltice and Ricard, 2002; Meibom et al., 2005]. Typically, Archean SCLM is distinct from younger SCLM both in chemical composition and evolution history [e.g., Dunai and Procelli, 2002; Gautheron and Moreira, 2002, Gautheron et al., 2005], being depleted, refractory, and buoyant relative to the asthenosphere, which greatly limits its potential for recycling, thus enhancing its preservation over time [e.g., Menzies, 1990; Griffin et al., 1999; Young and Lee, 2009]. We suggest that our solar-like noble gas signature found in the Eagle Ford natural gas is likely to originate in a shallow refractory reservoir beneath the Laurentian craton created by one of the mechanisms proposed by Anderson [1998], a hypothesis that is consistent with findings by Young

and Lee [2009] and Raye et al. [2011]. The similarity of the solar-like He-Ne signatures found both in Michigan Basin brines and that of the Eagle Ford natural gas in Texas, suggest a common source for both solar-like components. We expect the Precambrian Basement of the Michigan Basin to share at least one or two of the major structural provinces with the Mesoproterozoic Laurentian cratonic lithosphere underneath our study area in Texas, in particular, the Central Province (1.2-1.5 Ga), also known as the East Granite and Rhyolite Province and the Grenville Province (0.8-1.1 Ga) [e.g., Catacosinos, 1991; Thomas, 2005]. An older, Archean province may have also been present, but it may have been delaminated by subduction.

The presence of mantle fluids in the Eagle Ford shale is apparent not only through noble gas signatures but also through the presence of H_2S. In particular, H_2S was measured in gas samples collected just north of our study area [Harrington et al., 2015; Harrington, 2015]. These authors found that higher noble gas mantle contributions appear to correlate with elevated H_2S, suggesting thermal sulfate reduction induced by magmatic activity. This elevated H_2S is likely related to the Cretaceous volcanism that took place in this area and that appears to be also responsible for the presence of the diverse primordial geochemical signatures found in this region [e.g., Wittke and Mack, 1993; Young and Lee, 2009; Raye et al., 2011; this study]. Of relevance, is the fact that the discontinuity between the Laurentian lithospheric craton and the Jurassic transitional lithosphere and thus, all associated faults in the BIP were reactivated during the Miocene (~25 – 5 Myrs) and major movement recorded, leading, e.g., to the formation of the Balcones escarpment [Weeks, 1945; Ewing, 1991; Galloway et al., 1991; Griffin et al., 2010]. Both, intensive Late Cretaceous volcanic activity in the area and reactivation of all major fault systems in the Miocene are consistent with the presence of a recent, solar-like signature in the Eagle Ford Shale. Indeed, recent fault reactivation has likely facilitated the arrival of this noble

gas primordial component into the Eagle Ford Shale with some of the faults in the BIP extending into the lithosphere [Ewing, 2005]. It is clear that faults associated with volcanic mounds in the Travis field imply deep seated faulting (e.g., 60 ± 15 km) [Barker and Young, 1979].

Recently, Urann et al. [2020] analyzed mantle wedge peridotites dredged from the Mid-Atlantic Ridge and estimated that up to 67% of the mantle above the 660km discontinuity could have been processed through subduction environments and thus, be considered ultra-refractory, over a period of 2.5 Ga. This is also consistent with sampling of ocean island basalt-hosted xenoliths [Simon et al., 2008] where two thirds of samples were considered highly refractory. Urann et al. [2020] concluded that buoyant, highly refractory melt residues are likely ubiquitous in the upper mantle, consistent with earlier views by Anderson [1998] and Albarede [2005]. Findings by Urann et al. [2020] are consistent with and further support our hypothesis that the solar-like He-Ne component present in the Eagle Ford Shale may originate in the SCLM underneath the Laurentian craton.

3.5.3. Hydrocarbon Reservoir Relative Ages and Origin - A compartmentalized Eagle Ford Shale

Several lines of evidence point to the existence of two very distinct zones on opposite sides of the He-Ne rift defined area, which coincides with the southern margin of the Laurentia cratonic lithosphere (Fig. 3.6). In the south is an almost pristine crustal area that is relatively stable compared to that further north. In the north, a far more complex tectonic area, in which the presence of two distinct mantle components, MORB and solar-like is apparent (Fig. 3.6). In this area, a series of faults perpendicular to the remapped Ouachita Rift, with a NW-SE orientation, roughly parallel to the Texas transform appear to be present, leading to an Eagle Ford Shale organized in

a series of blocks, therefore, highly compartmentalized. The presence of these faults is consistent with findings by Lister et al. [1986] (see also Thomas, 2005) in rifts associated with transitional crust as is the case of the Ouachita Rift. Similar faults might also be present in the southern area, but their existence is not as clear as in the north. The main basis for these inferences lies on the relative hydrocarbon reservoir ages. These are discussed below.

Figure 3.7a shows the $^{36}Ar/^{40}Ar$ ratios as a function of the inverse of total ^{40}Ar volume fractions for our gas samples in the oil zone. It is apparent that these gas samples display significantly different ages, and four groups emerge (dashed mixing lines) in this picture, with the westernmost gas samples from the A6 and A7 wells being the youngest by far, and the easternmost wells (A1, A2 and A3) being the oldest (see Appendix B4 for details). Thus, a spatial variation pattern becomes apparent, with ages progressively decreasing from the east toward the west (Fig. 3.7a). As previously pointed out, batches b from wells A2 and A3 are significantly more enriched in crustal components than samples from batch a. The two batch a samples from both wells are thus believed to have a distinct origin, with the more heavily crustally enriched b batches displaying the oldest ^{40}Ar relative ages. Fig. 3.7b shows $^{36}Ar/^{40}Ar$ ratios as a function of the inverse of total ^{40}Ar volume fractions for Byrne et al. [2018] samples from both, the gas and oil zone together with our oil zone samples. From this plot, a more complete picture emerges of the entire system. With respect to samples in the mantle zone, both within the MORB-defined rift zone and in the solar-like region (Fig. 3.6), samples from well A [Byrne et al., 2018] just east of our oil zone samples display by far the oldest ages, thus confirming the decreasing age pattern inferred from east to west previously based solely on our samples.

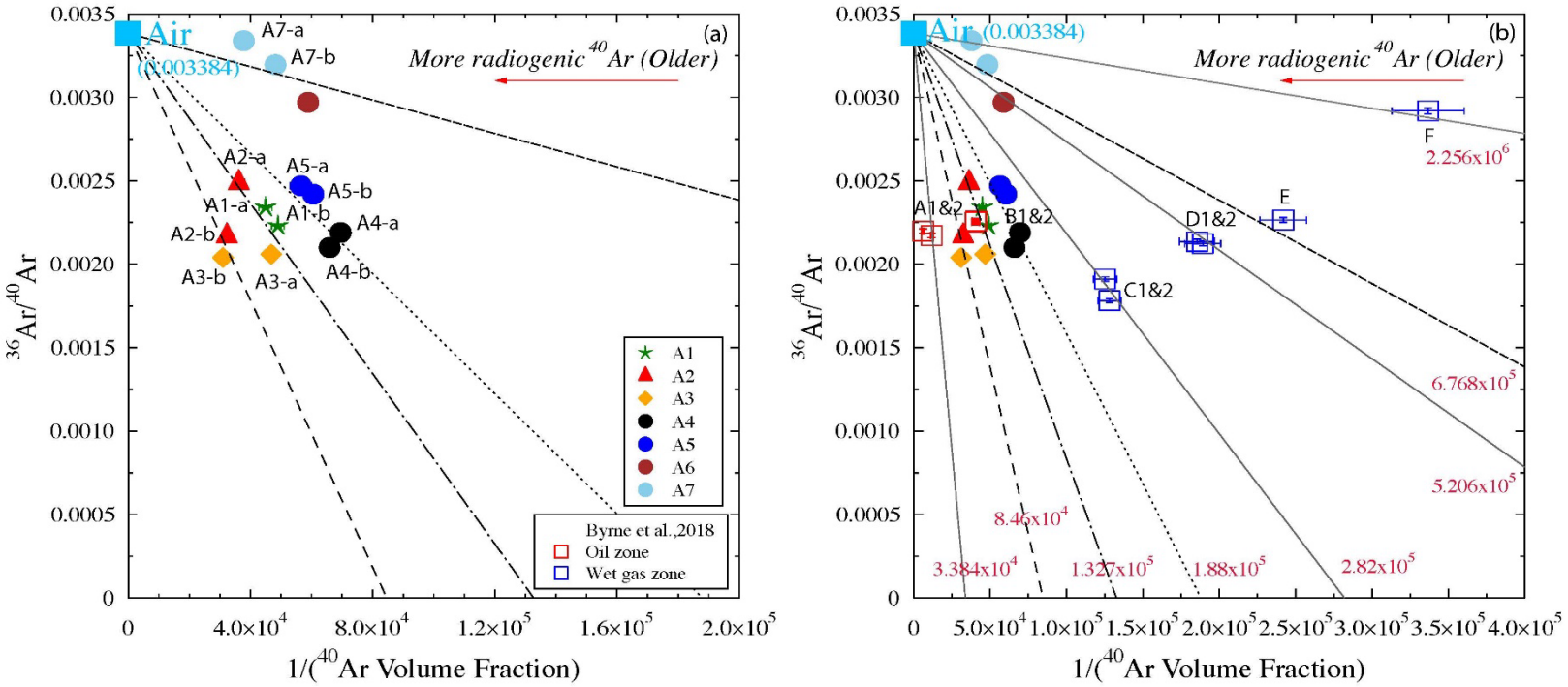

Figure 3.7 (a) ^{36}Ar/^{40}Ar ratios as a function of the reverse of ^{40}Ar volume fractions for all gas samples (this study, Appendix B4). (b) ^{36}Ar/^{40}Ar ratios as a function of the reverse of ^{40}Ar volume fractions for samples in this study and those of Byrne et al. [2018]. Dashed lines represent different age groups. Intercept values of each isochron line on the X-axis are labeled in red

.

South of the MORB-type source zone, where well B and all the gas samples are located, all with an almost pristine crustal noble gas signature, samples also display a decreasing age pattern from east to west (Figs. 3.6, 3.7b). Most gas zone samples are younger than most samples in the oil zone and comparable in age to the younger oil zone gas samples from the A6 and A7 wells. The age range for samples in the zone south of the MORB-defined rift area is significantly narrower than those in the mantle (MORB and solar-like) area. If one takes the youngest samples as a reference, samples A7-a and F (Fig. 3.7b), which fall along the same mixing line with a X-intercept value of 2.256×10^{6} (Fig. 3.7b) and therefore, display a similar ^{40}Ar relative age, and assign this X-intercept value an arbitrary extremely young age of 1 Myrs, that leads to an age range within and north of the rift zone between 1 (A7-a) and 67 Myrs (well A), and between 1 (sample F) and 17 Myrs (well B) south of it. These assume that a particular age is directly proportional to the X-intercept value of each mixing line on which these samples fall (Fig. 3.7b). It also assumes a uniform K content within all formations in the area. Based on the different age groups present, a series of compartments separated by faults can be inferred in the Eagle Ford Shale, particularly, within and north of the rift area. The position of these small transform faults, perpendicular to the rift zone and roughly parallel to the main Texas transform fault connecting the Ouachita and Marathon rifts, and that of the Eagle Ford compartments and age groups, is shown in Fig. 3.6. Within and north of the rift zone, they divide the Eagle Ford into blocks varying between ~19 km and 26 km wide, a range of values consistent with findings by Lister et al. [1986] that provide an average of 25 km between transfer faults in similar areas. Below, we discuss the meaning of these relative ages and their implications in terms of potential reservoir sources and migration.

If we were dealing with a conventional reservoir in which the hydrocarbons are produced in the shale source rock and subsequently migrated to a reservoir rock (e.g., sandstone or

carbonates) which typically has limited in-situ $^{40}Ar^*$ production, it might be fair to assume, if in-situ production was the main $^{40}Ar^*$ source, that the apparent sample age might translate into the timing at which migration from the source into the reservoir rock occurred. In the case of the unconventional Eagle Ford Shale, however, the formation plays both, a role as the source and reservoir rock. Therefore, if one were to assume that all the oil and gas currently in the Eagle Ford was produced in the formation itself, the ages that we have just determined might correspond to the true age at which the gas or oil formed. However, the possibility that at least part of the oil or gas might originate elsewhere, in particular, in underlying formations, should be considered in view of the noble gas isotopic signatures. These, point to the presence of both deep mantle MORB and solar-like sources, in addition to the presence of some significantly older fluids heavily enriched in crustal $^{4}He^*$ and $^{40}Ar^*$, e.g., gas samples A3-b and A2-b.

The main factors impacting the apparent age of these samples are: 1) the ^{40}K content of the source rock if the hydrocarbons remain stored in it – in this case, the ^{40}K content of the Eagle Ford Shale if in-situ production is responsible for a significant amount of $^{40}Ar^*$ in these hydrocarbons, and; 2) an upward ^{40}Ar flux from underlying formations, possibly, the crustal basement [Torgersen et al., 1989; Castro et al., 1998a, b; Castro et al., 2005]. In situ-production assumes that the $^{40}Ar^*$ release temperature from minerals [~250°C; Hall et al., 2000; Parry et al., 2001] was reached. This is a plausible assumption considering that the thermal maturity of the Smackover, Eagle Ford and Austin Groups is thought to have been enhanced by magmatic activity in this area. The geothermal gradient may have also increased in the proximity of magma chambers [Hutchinson, 1994; Condon and Dyman, 2006]. First order in-situ $^{40}Ar^*$ production calculations (Appendix B5) in the Eagle Ford Shale accounts for between ~2.5% of the total $^{40}Ar^*$ in sample A3-b and 92% of the total $^{40}Ar^*$ in A7-a sample. Clearly, these results point to an almost entirely external origin for most of

the natural gas in sample A3-b and at least a partial external origin for the natural gas in the A7-a sample. A7-b points to a significantly lower in-situ contribution of ~28% with respect to total $^{40}Ar^*$ and thus, to a significant external contribution.

The assignment of an arbitrary extremely young age to A7-a and F gas samples of 1 Myrs, corresponding essentially to present time, leads to an age for samples A3-b and A2-b of up to 27 Myrs and, for sample A, just east of these, of 67 Myrs. These ages are likely a lower age bound for these samples. Considering that oil generation in the Eagle Ford Shale is thought to have started between 42 and 26 Myrs ago [Lewan, 2002], that would place the age of sample from well A beyond the expected oil production timing range in the Eagle Ford. Gas production started significantly later, between 22 and 14 Myrs ago [Lewan, 2002]. It is thus plausible that some of the gas in the Eagle Ford Shale might have originated from underlying formations, including the Smackover Formation, the Bexar Shale, a member of the Pearsall Formation, and the Bossier Shale, a member of the Cotton Valley Group (Fig. 3.2). Zhao et al. [2020] found that the position-specific hydrogen data from our samples A1-A5 is generally consistent with a higher maturity level than that expected in the Eagle Ford Shale. Their findings thus support our suggested deeper origin for part of the hydrocarbons currently stored in the Eagle Ford Shale.

The first order age estimation of samples A3-b and A2-b is also likely a lower age bound for these samples and would also potentially place these outsides of the expected oil production timing range in the Eagle Ford. Considering the first order relative age information of these samples together with evidence of a deep mantle noble gas source and extremely enriched crustal ^{4}He and ^{40}Ar components in these samples, a partial origin for the hydrocarbons in underlying formations seems plausible, at least for all the easternmost samples (Fig. 3.6). In wells A2 and A3 two hydrocarbon sources appear to be present and it is also possible that mixing between these two

sources might occur in some wells. The Bossier Shale, part of the Cotton Valley Group (Fig. 3.2) is also a potential candidate for contributing hydrocarbons to the Eagle Ford Shale as is the Bexar Formation. It is unclear, though, when migration may have occurred.

Major movement of all the faults in the region is thought to have occurred recently, during the Miocene (~23-5 Myrs), a period of regional uplift and extension [e.g., Weeks, 1945; Ewing, 1987, 1991]. Assuming an arbitrary age to A7-a and F gas samples of 1 Myrs, leads to ages around or below 10 Myrs for all gas samples south of the MORB source area. It is possible that the gas present in this section of the Eagle Ford might correspond to a second or third gas generation, with limited time to accumulate crustal $^{40}Ar^*$, which would explain the significantly younger ages compared to most gas samples in the oil section.

It is possible that previous generations of hydrocarbons might have been expelled from the Eagle Ford Shale toward shallower levels, e.g., the Navarro and Taylor Group formations. This would be consistent with findings by Byrne et al. [2018] and Zhao et al. [2020] who estimated that about 40% - 60% and that over 50%, respectively, of the methane produced in the Eagle Ford Shale had been expelled. Other studies have suggested methane expulsion levels from shales significantly higher, 50-90% for the Barnett Shale in Texas [Jarvie et al., 2007] with a general range of 60-90% expulsion [Cooles et al., 1986]. Alternatively, it is possible that these younger gas ages in the wet gas zone might reflect a dilution effect with increased maturity as argued by Byrne et al. [2018].

3.6. Conclusions

Thirteen gas samples were collected for analysis of volume fractions and isotopic ratios of He, Ne, Ar, Kr, and Xe from seven producing wells in the oil zone of the Eagle Ford Shale in La

Salle and Dimmit counties, in south Texas. Except for one well, two samples were collected from each well within 30 minutes of each other. All noble gases reveal the presence of a crustal component. This crustal component displays a positive correlation with CH_4 and suggests that both methane and crustal noble gases are produced and/or transported together. Two samples are outliers, and display $^{4}He^{*}$ and $^{40}Ar^{*}$ volume fractions significantly higher than expected with respect to the observed trend, in addition to displaying significantly different $^{4}He^{*}$ and $^{40}Ar^{*}$ volume fraction values in both batches. The latter points to the existence of two different hydrocarbon sources being tapped by the same well within short time periods. This, in turn, suggests the presence of well-connected reservoirs either through faults or through a system of fractures.

An in-depth analysis of the He and Ne isotopic composition reveals the presence of two mantle endmembers. A weak one, corresponding to a MORB-type signature, and a significantly stronger one, corresponding to a primordial, solar-like mantle component. A few samples display different OIB compositions and are interpreted as resulting from mixing between the MORB and solar-like endmembers. The weak MORB-type mantle signal suggests the presence of an old mantle source, increasingly masked by a crustal signature over time. The stronger, more prevalent solar-like component suggests either a relatively recent addition of that solar-component to this natural gas reservoir directly from its original source, or its storage in a nearby reservoir that has been shielded from crustal contamination.

The combined analysis of our dataset from the oil zone together with that of Byrne et al. [2018] both, in the wet gas zone southeast of our sampling area and in the oil zone, to the east of our dataset, together with information provided by Harrington et al. [2015] on R/Ra and $^{20}Ne/^{22}Ne$ ratio variations from gas samples collected in the oil zone northeast of our study area, highlight a

clear spatial pattern in terms of noble gas sources and thus, likely, in terms of gas-phase hydrocarbon sources. From south to north, with a SW-NE orientation, a noble gas signature transition is observed, from an almost pure crustal component in the southern portion of the study area, to a zone with a MORB-type mantle signature in the central portion, to a solar-like component to the west and north.

The weak He-Ne identified MORB-type signature suggests the presence of an old rift system in the area, with a SW-NE orientation. It follows closely the southern Laurentian lithospheric margin, just north of our sampled wells, and is parallel to all the major known structures in the area, including the Ouachita orogeny front belt, the Luling and the Balcones fault zones, the Karnes-Atascosa Trough, as well as the Charlotte-Jourdanton fault system. Our MORB-defined rift area is consistent with palinplastic reconstructions of the Ouachita Rift at the continental scale, a structure that is associated with the breakup of Rodinia and the opening of the Iapetus Ocean at ~530 Myrs (Cambrian). We suggest that the Ouachita Rift in our specific area corresponds to and has the orientation of our MORB-defined rift. This would imply a ~28° clockwise rotation of the currently mapped Ouachita Rift in the eastern portion of our study area (western area of Karnes County). That rotation would also apply to the Texas transform, a major feature connecting the Ouachita and Marathon rifts, both part of the same rift system along the Appalachian-Ouachita continental margin of southeastern North America. We further suggest that the reconstructed Ouachita rift segment extends slightly further to the west than originally mapped, down to the western portion of La Salle County, and that a second, smaller clockwise rotation of the currently reconstructed Ouachita Rift [e.g., Thomas, 2005] may take place near the eastern border of La Salle County. These small rotations can be accommodated through the presence of smaller transform/transfer faults along the rift section. The presence of small transform faults in

this area is supported by our analysis of relative ^{40}Ar ages in the Eagle Ford gas samples. These point to a clear spatial variation pattern, with increasingly young ages toward the west, and the presence of ~20-25 km wide blocks in the Eagle Ford Shale, particularly marked in the MORB-defined rift area and north of it, where the solar-like mantle component is also present.

Although the presence of a mantle plume is not excluded as the source of the observed solar-like mantle component, the hypothesis that this primordial component originates in the subcontinental lithospheric mantle (SCLM) is preferred. We suggest that this solar-like component originates in a shallow refractory reservoir underneath the Laurentian craton, an hypothesis consistent with the presence of a very heterogeneous mantle as advocated earlier by Anderson [1998], Coltice and Ricard [2002], Meibom et al. [2005], Albarede [2005, 2008] and Urann et al. [2020]. This solar-like component, which is similar to that found in the Michigan Basin, another Laurentian cratonic region, is consistent with the hypothesis by Castro et al. [2009] that the presence of a primordial noble gas signature does not necessarily fingerprints the presence of a deep mantle plume. Both, intensive Late Cretaceous volcanic activity in the area as well as reactivation of all major fault systems in the Miocene are consistent with the presence of a recent, strong solar-like signature in the Eagle Ford Shale.

Finally, the presence of a highly compartmentalized Eagle Ford Shale together with the occurrence of distinct noble gas signatures may explain the observed significant differences in oil and gas production between closely spaced wells.

Overall, this work highlights the potential of noble gases to place important constraints in the Earth's geological evolution and framework, while shedding light on poorly understood unconventional hydrocarbon systems located at the boundaries of ancient cratons and younger transitional crust. It also sheds light on the origin of specific mantle noble gas signatures.

3.7. References

Adams, R. L. (1993). Effects of Inherited Pre-Jurassic Tectonics on the U. S. Gulf Coast. *GCAGS Transaction* 43, 1-9.

Aeschbach-Hertig, W., and Solomon, D. K. (2013). Noble Gas Thermometry in Groundwater Hydrology. In *The Noble Gases as Geochemical Tracers* (ed. P. Burnard). Springer Berlin Heidelberg. pp. 81-122.

Agrawal, M., Pulliam, J., Sen, M. K., and Gurrola, H. (2015). Lithospheric structure of the Texas-Gulf of Mexico passive margin from surface wave dispersion and migrated Ps receiver functions, *Geochemistry, Geophysics, Geosystems* 16, 2221–2239.

Albarède, F. (2005). The survival of mantle geochemical heterogeneities. In *Earth's Deep Mantle – Structure, Composition, and Evolution* (eds. R. D. van der Hilst, J. D. Bass, J. Matas, J. Trampert). *AGU Monograph*, 160, 27–46.

Albarède, F. (2008). Rogue Mantle Helium and Neon. *Science* 319, 943–945. https://doi.org/10.1126/science.1150060

Anders, E., and Grevesse, N. (1989). Abundance of the elements: meteoritic and solar. *Geochimica et Cosmochimica Acta* 53, 197–214.

Anderson, D. L. (1998). A model to explain the various paradoxes associated with mantle noble gas geochemistry. *Proceedings of the National Academy of Sciences of the United States of America* 95, 9087–9092. doi:10.1073/pnas.95.16.9087

Aston, F.W. (1933). Mass-spectra and Isotopes. Vol. 40 (London).

Baldwin, O. D., and Adams, J. A. S. (1971). $^{40}K/^{40}Ar$ ages of alkalic igneous rocks of Balcones fault trend of Texas. *Texas Journal of Science* 22. 223-231.

Ballentine, C. J. (1991). He, Ne, and Ar isotopes as tracers in crustal fluids. Ph.D thesis, Univ of Cambridge.

Ballentine, C. J., O'Nions, R. K., Oxburgh, E. R., Horvath, F., and Deak, J. (1991). Rare gas constraints on hydrocarbon accumulation, crustal degassing and groundwater flow in the Pannonian Basin. *Earth and Planetary Science Letters* 105, 229–246.

Ballentine, C. J., and O'Nions, R. K. (1992). The nature of mantle neon contributions to Vienna Basin hydrocarbon reservoirs. *Earth and Planetary Science Letters* 113, 553–567.

Ballentine, C. J., O'Nions, R. K., and Coleman, M. L. (1996). A Magnus opus: Helium, neon, and argon isotopes in a North Sea oilfield. *Geochimica et Cosmochimica Acta* 60, 831-849.

Ballentine, C. J. (1997). Resolving the mantle He/Ne and crustal $^{21}Ne/^{22}Ne$ in well gases *Earth and Planetary Science Letters* 152, 233-249.

Ballentine, C. J., Burgess, R., and Marty, B. (2002). Tracing fluid origin, transport and interaction in the crust. *Review in Mineralogy and Geochemistry* 47, 539-614.

Ballentine, C. J., and Burnard, P. G. (2002). Production, release and transport of noble gases in the continental crust. *Review in Mineralogy and Geochemistry* 47, 481-538.

Barker, D. S., and Young, K. P. (1979). A marine Cretaceous nepheline basanite volcano at Austin, Texas. *Texas Journal of Science* 31, 5-24.

Barry, P. H., Lawson, M., Meurer, W. P., Warr, O., Mabry, J. C., Byrne, D. J., and Ballentine, C. J. (2016). Noble gases solubility models of hydrocarbon charge mechanism in the Sleipner Vest gas field. *Geochimica et Cosmochimica Acta* 194, 291-309.

Benkert, J.-P., Baur, H., Signer P., and Wieler, R. (1993). He, Ne, and Ar from the solar wind and solar energetic particles in Lunar ilmenties and pyroxenes. *Journal of Geophysical Research* 98, 13147-13162.

Bernard, B. B., Brooks, J. M., and Sackett, W. M. (1976). Natural gas seepage in the Gulf of Mexico. *Earth and Planetary Science Letters* 31, 48–54. doi:10.1016/0012-821X(76)90095-9

Billingsley, L., Layton, B., and Finger, L. (2015). Geoscience applications to economic development of a relatively shallow, low gravity, structurally complex Eagle Ford oil development, Atascosa County, Texas. Unconventional Resources Technology Conference, San Antonio, Texas, USA, July 2015. Society of Exploration Geophysicists, American Association of Petroleum Geologists, Society of Petroleum Engineers. doi:10.15530/URTEC-2015-2154871

Bosch, A., and Mazor, E. (1988). Natural gas association with water and oil as depicted by atmospheric noble gases: case studies from the southeastern Mediterranean Coastal Plain. *Earth and Planetary Science Letters* 87, 338-346.

Breyer, J. A., Denne, R., Kosanke, T., Spaw, J. M., Funk, J. E., Christianson, P., Bush, D. A., and Nelson, R. (2013). Facies, Fractures, Pressure and Production in the Eagle Ford Shale (Cretaceous) between the Maverick Basin and the San Marcos Arch, Texas, USA. *SEG Global Meeting Abstracts*. 1556-1576

Buffler, R. T., and Sawyer, D. S. (1985). Distribution of crust and early history, Gulf of Mexico basin. *GCAGS Transaction* 35, 333-344.

Byrne, D. J., Barry, P. H., Lawson, M., and Ballentine, C. J. (2018). Determining gas expulsion vs retention during hydrocarbon generation in the Eagle Ford Shale using noble gases. *Geochimica et Cosmochimica Acta* 241, 240-254.

Byrne, D. J., Barry, P. H., Lawson, M., and Ballentine, C. J. (2020). The use of noble gas isotopes to constrain subsurface fluid flow and hydrocarbon migration in the East Texas Basin. *Geochimica et Cosmochimica Acta* 268, 186-208.

Cao, C., Zhang, M., Tang, Q., Yang, Y., Lv, Z., Zhang, T., Chen, C., Yang, H., and Li, L. (2018). Noble gas isotopic variations and geological implication of Longmaxi shale gas in Sichuan Basin, China. *Marine and Petroleum Geology* 89, 8-46.

Castro, M. C., Jambon, A., Marsily, G. d., and Schlosser, P. (1998a). Noble gases as natural tracers of water circulation in the Paris Basin. 1. Measurements and discussion of their origin and mechanisms of vertical transport in the basin. *Water Resource Research* 34, 2443-2466.

Castro, M. C., Goblet, P., Ledoux, E., Violette, S., and Marsily, G. d. (1998b). Noble gases as natural tracers of water circulation in the Paris Basin. 2. Calibration of a groundwater flow model using noble gas isotope data. *Water Resource Research* 34, 2467-2483.

Castro, M. C., Patriarche, D., and Goblet, P. (2005). 2-D numerical simulations of groundwater flow, heat transfer and ^{4}He transport – implications for the He terrestrial budget and the mantle helium-heat imbalance. *Earth and Planetary Science Letters* 237, 893-910.

Castro, M. C., Ma, L., and Hall, C. M. (2009). A primordial, solar He-Ne signature in crustal fluids of a stable continental region. *Earth and Planetary Science Letters* 279, 174-184.

Catacosinos, P. A., Daniel, Jr. P. A., and Harrison III, W. B. (1991). Structure, stratigraphy, and petroleum geology of the Michigan Basin. In: *Interior cratonic basins* (eds. M.W. Leighton, D.R. Kolata, D.F. Oltz, J.J. Eidel). AAPG Memoir, 51, 561–601.

Cawood, P. A., McCausland, P. J. A., and Dunning, G. R. (2001). Opening Iapetus: Constraints from the Laurentian margin in Newfoundland. *GSA Bulletin.* 113, 443–453.

Chiarenzelli, J., Lupulescu, M., Cousens, B., Thern, E., Coffin, L., and Regan, S. (2010). Enriched Grenvillian lithospheric mantle as a consequence of long-lived subduction beneath Laurentia. *Geology* 38, 151–154. doi:10.1130/G30342.1

Clarke, W. B., Jenkins, W. J., and, Top Z. (1976). Determination of tritium by mass spectrometric measurement of ^{3}He. *The International Journal of Applied Radiation and Isotopes* 27, 515-522.

Coltice, N., and Ricard, Y. (2002). On the origin of noble gases in mantle plumes. *Philosophical Transactions of the Royal Society* 360, 2633–2648. doi:10.1098/rsta.2002.1084

Condon, S. M., and Dyman, T. S. (2006). 2003 Geologic assessment of undiscovered conventional oil and gas resources in the upper Cretaceous Navarro and Taylor groups, Western Gulf Province, Texas. In *Petroleum System and Geological Assessment of Undiscovered Oil and Gas, Navarro and Taylor Groups, Western Gulf Province, Texas.* U.S. Geological Survey.

Cooles, G. P., Mackenzie, A. S., and Quigley, T. M. (1986). Calculation of petroleum masses generated and expelled from source rocks. *Organic Geochemistry* 10, 235–245. doi:10.1016/0146-6380(86)90026-4

Craig, H., and Lupton, J. E. (1976). Primordial neon, helium, and hydrogen in oceanic basalts. *Earth and Planetary Science Letters* 31, 369-385.

Craig, H., Lupton, J. E., and Horibe, Y. (1978). A mantle helium component in circum Pacific volcanic gases: Hakone, the Marianas, and Mt Lassen. In *Terrestrial Rare Gases* (eds. E.C Alexander, M. Ozima),. Japan Sci Societies Press, Tokyo, pp. 3–16.

Darrah, T. H., Vengosh, A., Jackson, R. B., Warner, N. R., and Poreda, R. J. (2014). Noble gases identify the mechanisms of fugitive gas contamination in drinking-water wells overlying the Marcellus and Barnett Shales. *Proceedings of the National Academy of Sciences of the United States of America* 111, 14076-14081.

Darrah, T. H., Jackson, R. B., Vengosh, A., Warner, N. R., Whyte, C. J., Walsh, T. B., Kondash, A. J., and Poreda, R. J. (2015). The evolution of Devonian hydrocarbon gases in shallow aquifers of the northern Appalachian Basin: Insights from integrating noble gas and hydrocarbon geochemistry. *Geochimica et Cosmochimica Acta* 170, 321-355.

Dawson, W. C. (2000). Shale microfacies: Eagle Ford Group (Cenomanian-Turonian) north-central Texas outcrops and subsurface equivalents. *GCAGS Transaction* **L**, 607-621.

Dehler, C. M. (1998). Facies analysis and environmental interpretation of the Middle Chuar Group (Proterozoic)—Implications for the timing of Rodinian breakup. AAPG Annual Convention and Exhibition, Salt Lake City, Utah. #90937 (abstr.)

Denne, R. A., and Breyer, J. A. (2016). Regional Depositional Episodes of the Cenomanian-Turonian Eagle Ford and Woodbine Groups of Texas. Chapter 1: Part 2 In: *The Eagle Ford Shale: A Renaissance in U.S. oil production* (ed. J. A. Breyer). AAPG Memoir, 110, 87-133.

Dickinson, W. R. (2009). The Gulf of Mexico and the southern margin of Laurentia. *Geology* 37, 479–480. doi:10.1130/focus052009.1

Dixon, E. T., Honda, M., McDougall, I., Campbell, I. H., and Sigurdsson, I. (2000). Preservation of near-solar neon isotopic ratios in Icelandic basalts. *Earth and Planetary Science Letters* 180, 309-324.

Dunai, T. J., and Porcelli, D. (2002). Storage and Transport of Noble Gases in the Subcontinental Lithosphere. *Review in Mineralogy and Geochemistry* 47, 371–409.

Ewing, T. E. (1987). The Frio River Line in South Texas--Transition from Cordilleran to Northern Gulf Tectonic Regimes. *GCAGS Transaction* 37, 87-94.

Ewing, T. E. (1991). Structural framework. In *The Gulf of Mexico Basin* (ed. A. Salvador). Boulder, Colorado, Geological Society of America, The Geology of North America, v. J .

Ewing, T.E. (2005). Phanerozoic Development of the Llano Uplift. *STGS Bulletin* 45, 15-25

Ewing, T. E. (2016). *Texas through time: Lone Star geology, landscapes, and resources*. Bureau of economic geology.

Flawn, P.T. (1961), The Ouachita structural belt in Mexico. In *The Ouachita system: Austin, Texas (*eds. P. T. Flawn, A. Goldstein, P. B. King and C. E. Weaver). Univ. of Texas, Bureau of Economic Geology Publication. pp. 99–106.

Galloway, W. E., Bebout, D. G., Fisher, W. L., Dunlap, J. B., Jr., Cabrera-Castro, R., Lugo-Rivera, J. E., and Scott, T. M., (1991). Cenozoic. In *The Gulf of Mexico Basin* (ed. A. Salvador). Boulder, Colorado, Geological Society of America, The Geology of North America, v. J .

Galloway, W. E. (2009). Gulf of Mexico, a mega-province. *Geo ExPro*, 6, 22-26.

Gautheron, C., and Moreira, M. (2002). Helium signature of the subcontinental lithospheric mantle. *Earth and Planetary Science Letters* 199, 39–47. doi:10.1016/S0012-821X(02)00563-0

Gautheron, C., Moreira, M., and Allègre, C. (2005). He, Ne and Ar composition of the European lithospheric mantle. *Chemical Geology* 217, 97–112. doi:10.1016/j.chemgeo.2004.12.009

Gherabati, S. A., Browning, J., Male, F., Ikonnikova, S. A., and McDaid, G. (2016). The impact of pressure and fluid property variation on well performance of liquid-rich Eagle Ford shale. *Journal of Natural Gas Science and Engineering* 33, 1056-1068.

Gherabati, S. A., Hammes, U., Male, F., and Browning, J. (2018). Assessment of hydrocarbon in place and recovery factors in the Eagle Ford shale play, *SPE Reserv. Eval. Eng.* 21, 291-306.

Gonnermann, H. M., and Mukhopadhyay, S. (2007). Non-equilibrium degassing and a primordial source for helium in ocean-island volcanism. *Nature* 449, 1037-1040. doi:10.1038/nature06240.

Graham, D., Lupton, J., Albaredet, F., and Condominest, M. (1990). Extreme temporal homogeneity of helium isotopes at Piton de Ia Fournaise, Reunion Island. *Nature*. 347, 545-548.

Graham, D. W. (2002). Nobel gas isotope geochemistry of mid-ocean ridge and ocean island basalts: characterization of mantle source reservoirs. *Review in Mineralogy and Geochemistry* 47, 247-318.

Griffin, W. L., O'Reilly, S., and Ryan, C. G. (1999). The composition and origin of sub-continental lithospheric mantle. In *Mantle Petrology: Field Observations and High Pressure Experimentation: A Tribute to Francis R. (Joe) Boyd* (eds. Y. Fei, C. M. Bertka, B. O. Mysen). The Geochemical Society. Special Publication No.6, 13-44.

Griffin, W. L., O'Reilly, S.Y., Doyle, B. J., Pearson, N. J., Coopersmith, H., Kivi, K., Malkovets, V. and Pokhilenko, N. (2004). Lithosphere mapping beneath the North American plate. *Lithos* **77**, 873–922. doi:10.1016/j.lithos.2004.03.034

Griffin, W. R. (2008). Decompression Melting of FOZO and FOZO-HIMU Sources by Extensional Focusing, Balcones Igneous Province, Texas. *GSA Abstracts with Programs*, 40, 6, 530.

Griffin, W. L., O'Reilly, S. Y., Afonso, J. C., and Begg, G. (2009). The composition and evolution of lithospheric mantle: A re-evaluation and its tectonic implications: *Journal of Petrology* 50, 1185–1204. doi: 10.1093/petrology/egn033.

Griffin, W. R., Foland, K. A., Stern, R. J., and, Leybourne, M. I. (2010). Geochronology of Bimodal Alkaline Volcanism in the Balcones Igneous Province, Texas: Implications for Cretaceous Intraplate Magmatism in the Northern Gulf of Mexico Magmatic Zone. *Journal of Geolpgy* 118, 1–21. https://doi.org/10.1086/648532

Györe, D., McKavney, R., Gilfillan, S. M. V., and Stuart, F. M. (2018) Fingerprinting coal-derived gases from the UK. *Chemical Geology* 480, 75–85.

Hall, C. M., Kesler, S. E., Simon, G., and Fortuna, J. (2000) Overlapping Cretaceous and Eocene Alteration, Twin Creeks Carlin-Type deposit, Nevada. *Economic geology* 95, 1739-1752.

Hall, C. M., Castro, M. C., Lohmann, K. C., and Sun, T. (2012) Testing the noble gas paleothermometer with a yearlong study of groundwater noble gases in an instrumented monitoring well. *Water Resource Research* 48, W04517

Hammes, U., Eastwood, R., McDaid, G., Vankov, E., Gherabati, S. A., Smye, K., Shultz, J., Potter, E., Ikonnikova, S., and Tinker, S. (2016). Regional assessment of the Eagle Ford Group of South Texas, USA: Insights from lithology, pore volume, water saturation, organic richness, and productivity correlations. *Interpretation* 4, 125-150.

Hanyu, T., Dunai, T. J., Davies, G. R., Kaneoka, I., Nohda, S., and Uto, K. (2001). Noble gas study of the Reunion hotspot: evidence for distinct less-degassed mantle sources. *Earth and Planetary Science Letters* 193, 83-98.

Harkness, J. S., Darrah, T. H., Warner, N. R., Whyte, C. J., Moore, M. T., Millot, R., Kloppmann, W., Jackson, R. B., Vengosh, A. (2017). The geochemistry of naturally occurring methane and saline groundwater in an area of unconventional shale gas development. *Geochimica et Cosmochimica Acta* 208, 302–334. doi:10.1016/j.gca.2017.03.039

Harrington, J. (2015). Using Noble Gas and Hydrocarbon Gas Geochemistry to Source the Origin of Fluids in the Eagle Ford Shale of Texas, USA. Honor Thesis. Ohio State Univ.

Harrington, J., Williams, J. C., and Darrah, T. (2015). Using noble gas geochemistry to characterize sources and migration of fluids in the Eagle Ford shale. AAPG annual convention, Denver. American Association of Petroleum Geologists. #90216 (abstr.).

Hentz, T. F., Ambrose, W. A., and Smith, D. C. (2014). Eaglebine play of the southwestern East Texas basin: Stratigraphic and depositional framework of the Upper Cretaceous (Cenomanian—Turonian) Woodbine and Eagle Ford Groups. *AAPG Bulletin* 98, 2551-2580.

Hilton, D. R., and Porceli, D. (2003). Noble gases as mantle tracers. In *Treatise on Geochemistry* (eds. H. D. Holland and K. K. Turekian). Elsevier Science. pp. 27-318.

Hiyagon, H., and Kennedy, M. (1992). Noble gases in CH_4-rich gas fields, Alberta, Canada. *Geochimica et Cosmochimica Acta* 56, 1569-1589.

Hoke, L., Lamb, S., Hilton, D. R., and Poreda, R. J. (2000). Southern limit of mantle-derived geothermal helium emissions in Tibet: implications for lithospheric structure. *Earth and Planetary Science Letters* 180, 297–308. doi:10.1016/S0012-821X(00)00174-6

Honda, M., McDougall, I., Patterson, D. B., Doulgeris, A., and Clague, D.A. (1991) Possible solar noble-gas component in Hawaiian basalts. *Nature* 349, 149-151.

Hunt, A. G., Darrah, T. H., and Poreda, R. J. (2012). Determining the source and genetic fingerprint of natural gases using noble gas geochemistry: A northern Appalachian Basin case study. *AAPG Bulletin* 96, 1785-1811.

Hutchinson, P. J., (1994). Upper Cretaceous (Austin Group) volcanic deposits as a hydrocarbon trap. GCAGS Transaction 44, 293–303.

Jacques, J. M., and Clegg, H. (2002). Late Jurassic Source Rock Distribution and Quality in the Gulf of Mexico: Inferences from Plate Tectonic Modellin. *GCAGS Transaction* 52, 429-440.

Jarvie, D. M., Hill, R. J., Ruble, T. E., and Pollastro, R. M. (2007). Unconventional shale-gas systems: The Mississippian Barnett Shale of north-central Texas as one model for thermogenic shale-gas assessment. *AAPG Bull*etin 91, 475–499. doi:10.1306/12190606068

Kaneoka, I. (1980) Rare gas isotopes and mass fractionation: An indicator of gas transport into or from a magma. *Earth and Planetary Science Letters* 48, 284–292. doi:10.1016/0012-821X(80)90192-2

Kennedy, B. M., Hiyagon, H., and Reynolds, J. H. (1990). Crustal neon: a striking uniformity. *Earth and Planetary Science Letters* 98, 277-286.

Klemperer, S. L., Kennedy, B. M., Sastry, S. R., Makovsky, Y., Harinarayana, T., and Leech, M. L. (2013). Mantle fluids in the Karakoram fault: Helium isotope evidence. *Earth and Planetary Science Letters* 366, 59–70. https://doi.org/10.1016/j.epsl.2013.01.013

Law, B. E. (2002) Basin-centered gas systems. *AAPG Bulletin* 86, 1891-1919.

Lewan, M. D. (2002). New insights on timing of oil and gas generation in the Central Gulf Coast interior zone based on Hydrous-Pyrolysis kinetic parameters. *GCAGS Transaction* 52, 607-620.

Lister, G. S., Etheridge, M. A., and Symonds, P. A. (1986). Detachment faulting and the evolution of passive continental margins. *Geology* 14, 246-250.

Loucks, R. G. (2018). Eagle Ford–A depositional setting and processes in southwestern Texas: An example of deeper-water, belowstorm-wave-base carbonate sedimentation on a drowned shelf. *GCAGS Transaction* **7**, 59–78,

Ma, L., Castro, M. C., and Hall, C. M. (2009) Atmospheric noble gas signatures in deep Michigan Basin brines as indicators of a past thermal event. *Earth and Planetary Science Letters* 277, 137-147.

Marty, B. (1984). On the Nobles gas isotopic fractionation in naturally occurring gases. *Geochemical Journal* 18, 157-162.

Meibom, A., Sleep, N. H., Zahnle, K., and Anderson, D. L. (2005). Models for noble gases in mantle geochemistry: Some observations and alternatives. In *Plates, Plumes and Paradigms* (eds. G. R. Foulger, J.H. Natland, D. C. Presnall, and D. L. Anderson). Geological Society of America. doi:10.1130/0-8137-2388-4.347

Menzies, M. A. (1990). *Continental mantle*, Clarendon Press, Oxford, pp. 1-184

Mickus, K., Stern, R. J., Keller, G. R., and Anthony, E. Y. (2009). Potential field evidence for a volcanic rifted margin along the Texas Gulf Coast. *Geology* 37, 387–390. doi:10.1130/G25465A.1

Miggins, D. P., Smith, D. V., and Blome, C. D. (2004). Preliminary $^{40}Ar/^{39}Ar$ geochronology of igneous intrusions from Uvalde County, Texas defining a more precise eruption history for the southern Balcones Volcanic Province. U.S. Geological Survey Open-File Report 2004-1031.

Moreira, M., Allegre, C. J. (1998). Helium-neon systematics and the structure of the mantle. *Chemical Geology* 147, 53–59.

Moreira, M., Kunz, J., and Allegre, C. (1998). Rare gas systematics in popping rock: isotopic and elemental compositions in the upper mantle. *Science* 279, 1178-1181.

Moreira, M., Breddam, K., Curtice, J., Kurz, M. D. (2001). Solar neon in the Icelandic mantle: new evidence for an undegassed lower mantle. *Earth and Planetary Science Letters* 185, 15–23. doi:10.1016/S0012-821X(00)00351-4

Nicholas, R.L., and Waddell, D.E. (1989). The Ouachita system in the subsurface of Texas, Arkansas, and Louisiana, in *The Appalachian-Ouachita orogen in the United States* (eds. Hatcher, R.D., Jr., Thomas, W.A., and Viele, G.W.) Boulder, Colorado, Geological Society of America, The Geology of North America, v. F-2, chapter 23, 661–672.

Nicot, J.-P., Gherabati, A., Darvari, R., and Mickler, P. (2018). Salinity reversal and water freshening in the Eagle Ford shale, Texas, USA. *ACS Earth and Space Chemistry* **2**, 1087-1094.

North American Magnetic Anomaly Group (NAMAG) [Geological Survey of Canada, United States Geological Survey, and Consejo de Recursos Minerales de México] (2002) Magnetic Anomaly Map of North America: U.S. Geological Survey Special Map, scale 1:10,000,000, accompanied by 31 p. text.

O'Nions, R. K., and Oxburgh, E. R. (1983). Heat and helium in the Earth. *Nature.* **306**, 429-431.

O'Nions, R. K., and Tolstikhin, I. N. (1994). Behavior and residence times of lithophile and rare gas tracers in the upper mantle. *Earth and Planetary Science Letters* 124, 131–138.

Oxburgh, E. R., O'Nions, R. K., and Hill, R. I. (1986). Helium isotopes in sedimentary basins. *Nature*. 324, 632-635.

Ozima, M., and Podosek, F. A. (2002). *Noble gas geochemistry*. Cambridge Univ. Press.

Parry, W. T., Bunds, M. P., Bruhn, R. L., Hall, C. M., and Murphy, J. M. (2001). Mineralogy, $^{40}Ar/^{39}Ar$ dating and apatite fission track dating of rocks along the Castle Mountain fault, Alaska. *Tectonophysics* 337, 149-172.

Patriarche, D., Castro, M. C., and Goblet, P. (2004). Large-scale hydraulic conductivities inferred from three-dimensional groundwater flow and ^{4}He transport modeling in the Carrizo aquifer, Texas. *Journal of Geophysical Research: Solid Earth* 109, B11202.

Phelps, R. M., Kerans, C., Da-Gama, R. O. B. P., Jeremiah, J., Hull, D., and Loucks, R. G. (2015). Response and recovery of the Comanche carbonate platform surrounding multiple Cretaceous oceanic anoxic events, northern Gulf of Mexico. *Cretaceous research* 54, 117–144. doi:10.1016/j.cretres.2014.09.002

Pinti, D. L., and Marty, B. (1995). Noble gases in crude oils from the Paris Basin, France: implications for the origin of fluids and constraints on oil–water–gas interactions. *Geochimica et Cosmochimica Acta* 59, 3389-3404.

Pinti, D. L., Castro, M. C., Shouakar-Stash, O., Tremblay, A., Garduño, V. H., Hall, C. M., Hélie, J.-F., and Ghaleb, B. (2013). Evolution of the geothermal fluids at Los Azufres, Mexico, as traced by noble gas isotopes, $\delta^{18}O$, δD, $\delta^{13}C$ and $^{87}Sr/^{86}Sr$. *Journal of Volcanology and Geothermal Research* 249, 1–11. doi:10.1016/j.jvolgeores.2012.09.006

Poole, F. G., Perry, W. J., Madrid, R. J., and Amaya-Martínez, R. (2005). Tectonic synthesis of the Ouachita-Marathon-Sonora orogenic margin of southern Laurentia: Stratigraphic and structural implications for timing of deformational events and plate-tectonic model, in: *The Mojave-Sonora Megashear Hypothesis: Development, Assessment, and Alternatives*. Geological Society of America. doi:10.1130/0-8137-2393-0.543

Porcelli, D., and Wasserburg, G. J. (1995). Mass transfer of helium, neon, argon, and xenon through a steady-state upper mantle. *Geochimica et Cosmochimica Acta* 59, 4921-4937.

Porcelli, D., Ballentine, C. J., and Wieler, R. (2002). An Overview of Noble Gas Geochemistry and Cosmochemistry. *Review in Mineralogy and Geochemistry* 47, 1–19. doi:10.2138/rmg.2002.47.1

Raye, U., Anthony, E. Y., Stern, R. J., Kimura, J.-I., Ren, M., Qing, C., and Tani, K. (2011). Composition of the mantle lithosphere beneath south-central Laurentia: Evidence from peridotite xenoliths, Knippa, Texas. *Geosphere* 7, 710–723. doi:10.1130/GES00618.1

Rudnick, R., and Nyblade, A., (1999). The thickness and heat production of Archean lithosphere: constraints from xenolith thermobarometry and surface heat flow. In *Mantle Petrology: Field Observations and High Pressure Experimentation: A Tribute to Francis R. (Joe) Boyd* (eds. Fei, Y., Bertka, C. M., Mysen, B. O.). The Geochemical Society. Special Publication No.6, 3-12.

Salvador, A. (1987). Late Triassic-Jurassic Paleogeography and Origin of Gulf of Mexico Basin. *AAPG Bull*etin 71, 419-451.

Salvador, A. (1991). *The Gulf of Mexico Basin*. Geological Society of America.

Schmoker, J. W. (1996). A Resource evaluation of the Bakken Formation (upper Devonian and lower Mississippian) continuous oil accumulation, Williston Basin, North Dakota and Montana. *The Mountain Geologists*. 33, 1-10.

Schön, J. H. (2015). Density. In *Developments in Petroleum Science*. Elsevier. 65, 109-118.

Simon, N. S., Neumann, E. R., Bonadiman, C., Coltorti, M., Delpech, G., Grégoire, M., and Widom, E., (2008). Ultra-refractory domains in the oceanic mantle lithosphere sampled as mantle xenoliths at ocean islands. *Journal of Petrology* 49,1223-1251.

Speckien, M. (2012). Magnetic investigation of the continental-oceanic crustal boundary; northern Gulf of Mexico. Master thesis. Baylor Univ.

Spencer, A. B. (1969). Alkalic igneous rocks of the Balcones province, Texas. *Journal of Petrology* 10, 272-306.

Spencer, C. W. (1989). Review of characteristics of low-permeability gas reservoirs in western United States. *AAPG Bulletin* 73, 613-629.

Starkey, N. A., Stuart, F. M., Ellam, R. M., Fitton, J. G., Basu, S., and Larsen, L. M. (2009). Helium isotopes in early Iceland plume picrites: Constraints on the composition of high 3He/4He mantle. *Earth and Planetary Science Letters* 277, 91–100. doi:10.1016/j.epsl.2008.10.007

Sun, T., Hall, C. M., and Castro, M. C. (2010). Statistical properties of groundwater noble gas paleoclimate models: Are they robust and unbiased estimators? *Geochemistry, Geophysics, Geosystems* 11, Q02002

Thomas, W. A. (1977). Evolution of Appalachian-Ouachita salients and recesses from reentrants and promontories in the continental margin. *American Journal of Science* 277, 1233–1278.

Thomas, W. A. (1991). The Appalachian-Ouachita rifted margin of southeastern North America. *GSA Bulletin* 103, 415-431.

Thomas, W. A. (2005) Tectonic inheritance at a continental margin. *Gsa Today* **16**, 4. https://doi.org/10.1130/1052-5173(2006)016[4:TIAACM]2.0.CO;2

Tian, Y., Ayers, W. B., and McCain,W. D. (2014). Regional Impacts of Lithologic Cyclicity and Reservoir and Fluid Properties on Eagle Ford Shale Well Performance, in: Day 2 Wed, April 02, 2014. Presented at the SPE Unconventional Resources Conference, SPE, The Woodlands, Texas, USA, D021S004R002.

Torgersen, T. (1980). Controls on pore-fluid concentration of ^{4}He and ^{222}Rn and the calculation of ^{4}He/^{222}Rn ages. *Journal of Geochemical Exploration* 13, 57-75.

Torgersen, T., Kennedy, B. M., Hiyagon, H., Chiou, K. Y., Reynolds, J. H., and Clarke, W. B. (1989). Argon accumulation and the crustal degassing flux of ^{40}Ar in the Great Artesian Basin, Australia. *Earth and Planetary Science Letters* 92, 43-56.

Tucker, J. M., and Mukhopadhyay, S.(2014). Evidence for multiple magma ocean outgassing and atmospheric loss episodes from mantle noble gases. *Earth and Planetary Science Letters* 393, 254–265. doi:10.1016/j.epsl.2014.02.050

U.S. Energy Information Admistration (2016) Annual Energy Outlook 2016 with projections to 2040. Available at: https://www.eia.gov/outlooks/aeo.

Urann, B. M., Dick, H. J. B., Parnell-Turner, R. and Casey, J. F. (2020) Recycled arc mantle recovered from the Mid-Atlantic Ridge. *Nature Communications* 11, 3887. doi:10.1038/s41467-020-17604-8

Valbracht, P. J., Honda, M., Matsumoto, T., Mattielli, N., McDougall, I., Ragettli, R., and Weis, D. (1996). Helium, neon and argon isotope systematics in Kerguelen ultramafic xenoliths: implications for mantle source signatures. *Earth and Planetary Science Letters* 138, 29-38.

Warrier, R. B., Castro, M. C., and Hall, C. M. (2012). Recharge and source-water insights from the Galapagos Islands using noble gases and stable isotopes: Recharge and source-water insights from the Galapagos islands. *Water Resource Research* 48, W03508.

Warrier, R. B., Castro, M. C., Hall, C. M., and Lohmann, K. C. (2013). Large atmospheric noble gas excesses in a shallow aquifer in the Michigan Basin as indicators of a past mantle thermal event. *Earth and Planetary Science Letters* 375, 372-382.

Weeks, A. W. (1945). Balcones, Luling, and Mexia Fault Zones in Texas. *AAPG Bull*etin 29, 1733-1737.

Weiss, R. F. (1968). Piggyback sampler for dissolved gas studies on sealed water samples. *Deep-Sea Res. and Oceanogr. Abstr.* 15, 695-699.

Welder, F. A., and Reeves, R. D. (1964). *Geology and ground-water resources of Uvalde County, Texas* (No. 1584). US Government Printing Office.

Wen, T., Castro, M. C., Ellis, B. R., Hall, C. M., and Lohmann, K. C. (2015). Assessing compositional variability and migration of natural gas in the Antrim Shale in the Michigan Basin using noble gas geochemistry. *Chemical Geology* 417, 356-370.

Wen, T., Castro, M. C., Nicot, J. P., Hall, C. M., Larson, T., Mickler, P., and Darvari, R. (2016). Methane sources and migration mechanisms in shallow groundwaters in Parker and Hood counties, Texas - A Heavy Noble Gas Analysis. *Environmental Science and Technology* 50, 12012-12021.

Wen, T., Castro, M. C., Nicot, J. P., Hall, C. M., Pinti, D. L., Mickler, P., Darvari, R. and Larson, T. (2017). Characterizing the noble gas isotopic composition of the Barnett Shale and Strawn Group and constraining the source of stray gas in the trinity aquifer, North-Central Texas. *Environmental Science and Technology* 51, 6533-6541.

Wetherill, G.W. (1954) Variations in the isotopic abundances of neon and argon extracted from radioactive minerals. *Physical Review* 96, 679-683.

Wittke, J. H., and Mack, L. E. (1993). OIB-like mantle source for continental alkaline rocks of the Balcones province, Texas: trace-element and isotopic evidence. *Journal of Geology* 101, 333-344.

Woda, J., Wen, T., Oakley, D., Yoxtheimer, D., Engelder, T., Castro, M. C., and Brantley, S. L. (2018). Detecting and explaining why aquifers occasionally become degraded near hydraulically fractured shale gas wells. *Proceedings of the National Academy of Sciences* 115, 12349-12358.

Yatsevich, I., and Honda, M. (1997). Production of nucleogenic neon in the Earth from natural radioactive decay. *Journal of Geophysical Research* 102, 10291–10298.

Young, H. P., and Lee, C.-T. A., (2009). Fluid-metasomatized mantle beneath the Ouachita belt of southern Laurentia: Fate of lithospheric mantle in a continental orogenic belt. *Lithosphere* 1, 370–383. doi:10.1130/L72.1

Zartman, R. E., Wasserburg, G. J., and Reynolds, J. H. (1961). Helium, argon, and carbon in some natural gases. *Journal of Geophysical Research* 66, 277-306.

Zhang, T., Sun, X., Milliken, K. L., Ruppel, S. C., and Enriquez, D., (2017). Empirical relationship between gas composition and thermal maturity in Eagle Ford Shale, south Texas. *AAPG Bulletin* 101, 1277–1307. doi:10.1306/09221615209

Zhao, H., Liu, C., Larson, T. E., McGovern, G. P., and Horita, J. (2020). Bulk and position-specific isotope geochemistry of natural gases from the Late Cretaceous Eagle Ford Shale, south Texas. *Marine and Petroleum Geology* 122, 104659.

CHAPTER 4

Heat, Noble Gases and CO_2 Sources in Geothermal Fields of Mexico

Abstract

The Trans-Mexican Volcanic Belt (TMVB) and the Gulf Extensional Province (Baja California) are the regions in Mexico with the highest heat flow and where the main geothermal energy resources are currently exploited. Here, a combined dataset of previously published and newly collected data on heat and volatile species (He, Ar and CO_2) from six geothermal reservoirs is analyzed. This entire dataset set consisting of 132 samples includes samples collected in four TMVB reservoirs (Los Azufres, Los Humeros, Acoculco and Cerritos Colorados) and two in Baja California (Cerro Prieto and Las Tres Vírgenes). The goal is to identify the heat sources, understand how heat is distributed in these geothermal reservoirs, assess the extent of mixing among multiple fluid sources (meteoric, magmatic and crustal), and its impact on heat distribution. We also seek to discriminate volatile components from distinct sources (e.g., crust, mantle and atmosphere) and identify possible heat patterns in these systems. Distinct R/Ra ratios (where R is the measured $^3He/^4He$ ratio and Ra is the atmospheric ratio) are observed throughout the TMVB and Baja California geothermal fields, with those in the TMVB displaying significantly higher R/Ra values (7.14-7.27) than those in Baja California (1.21-6.62), indicating a stronger mantle signal from possibly younger, active magmatic heat sources. Lower R/Ra values in Baja California might reflect local tectonic features, where reservoirs are primarily affected by crustal

contributions from an old, subducted fossil slab related to the Farallon Plate. The analysis of heat to ^{3}He ($Q/^{3}He$) ratios together with information provided by $^{4}He/^{36}Ar$ and $^{4}He/^{3}He$ ratios shows that heat and volatile transfer at the boundary with the hydrothermal system during magma degassing is dominated by convection. The release of He and Ar from magma sources appears to be controlled by their diffusivities. Convection transfers He more rapidly than heat and Ar, fractionating the pristine mantle $Q/^{3}He$ ratios toward lower values and $^{4}He/^{36}Ar$ ratios toward higher values. Boiling and dilution by meteoric water led to further fractionation of heat and volatiles. Distinct sources of heat and volatiles are also reflected in the CO_2 content, the major dry gas component in these geothermal fields. Main sources of CO_2 are limestone (8.93% - 99.80%) and mantle carbon (0.05% - 82.64%), both from local sources and the subducting slab. Contribution of carbon from sediments is generally smaller (0% - 35.55), mainly in Cerro Prieto and Las Tres Virgenes in Baja California, which are affected by the release of volatiles from the subducted Farallon plate. The absence of significant fractionation in $CO_2/^{3}He$ ratios is an indication that helium degassing is controlled by the CO_2 content in parental magma rather than helium diffusivity. Addition of carbon from non-mantle sources can also alter the original fractionation pattern between volatile species and heat.

4.1. Introduction

Geothermal energy is an alternative energy source to fossil fuels, and its relevance is increasing as the world attempts to counteract ongoing global warming [e.g., Prol-Ledesma and Morán-Zenteno, 2019]. Mexico has abundant geothermal energy resources, placing it among the countries with the highest exploited geothermal capacity in the world, reaching around 1005 MWe [e.g., Gutiérrez-Negrín et al., 2020].

Mexican geothermal fields producing electricity can be classified as convection-dominated magmatic geothermal play types, following the schematic classification proposed by Moeck and Beardsmore [2014]. In these plays, heat – produced by shallowly emplaced magma bodies – is transported efficiently from depth to shallower reservoirs by the upward movement of fluid along permeable pathways [Moeck and Beardsmore, 2014]. In Mexico, extended volcanic activity has taken place since the Cenozoic [Ferrari et al., 2012], endowing Mexico with abundant geothermal potential and convective geothermal plays. Most of the geothermal areas of interest in Mexico belong to four regions with intense Quaternary volcanic activity and high heat flow: the Trans-Mexican Volcanic Belt (TMVB), the Sierra Madre Occidental, the Gulf Extensional Province (Baja California) and the Alkaline Volcanism area [Prol-Ledesma et al., 2016, 2019]. The *Comisión Federal de Electricidad* (CFE, the Mexican federal electricity commission) has exploited four major convective geothermal systems at Los Humeros and Los Azufres, within the TMVB, and Cerro Prieto and Las Tres Vírgenes, in the Gulf Extensional Province (Fig. 4.1). Two additional areas of interest in the TMVB characterized by high heat flow are the La Primavera (also known as Cerritos Colorados) and Acoculco. Exploitation of Cerritos Colorados was abandoned in the 1970s due to environmental concerns and public criticism while that of Acoculco, a hot dry rock potential field, is currently under exploration by the CFE (Fig. 4.1).

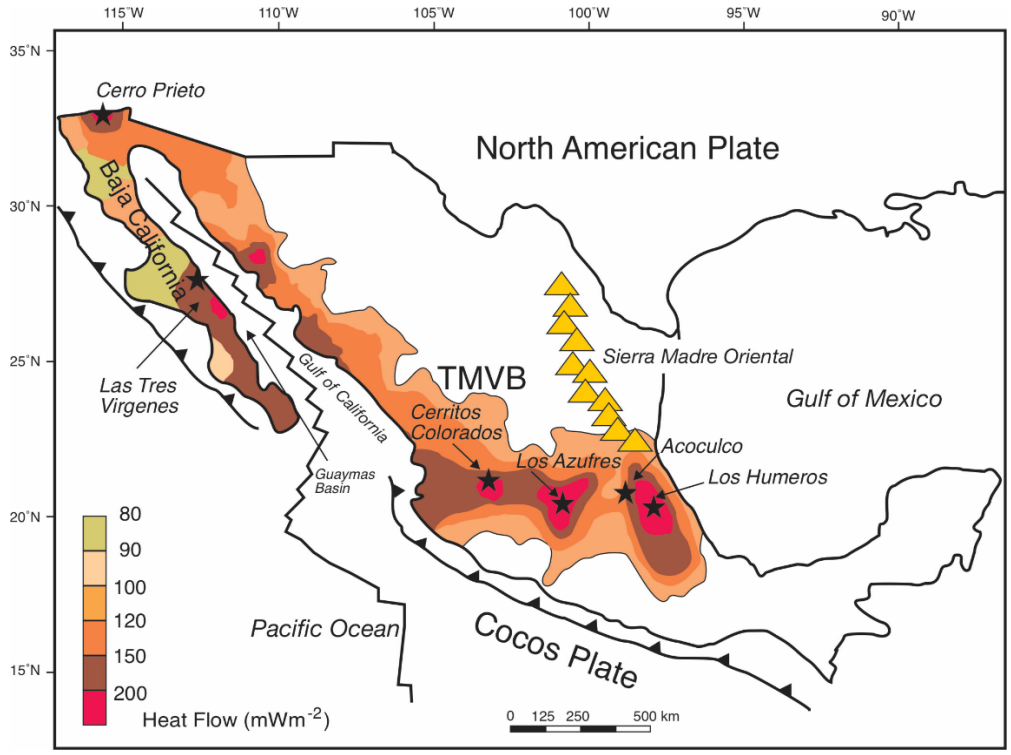

Figure 4.1 Location of Mexican geothermal areas discussed in this study. Major tectonic structures are shown. Heat flow distribution in Mexico is displayed in different colors (simplified and redrawn from Prol-Ledesma, 2019). Batista Cruz et al. [2019] data are from the Baja California Peninsula and the Gulf of California.

Exploitation of these fields began in the last century and since then, extensive studies have been carried out using well production data and water chemistry to assess reservoir conditions and to trace the circulation of geothermal fluids [e.g., Garcia-Estrada et al., 2001; Arellano et al., 2003, 2015; Izquíerdo et al., 2009; Cedillo Rodriguez, 2000; Pro-Ledesma et al., 2016; Cid et al., 2021]. More recently, geochemical studies focused on the use of noble gases (He, Ne, Ar, Kr, Xe) and other isotopic tracers ($^{87}Sr/^{86}Sr$, ^{13}C, ^{2}H, ^{18}O) to unravel fluid sources and assess the potential of the resource at long term [Pinti et al., 2017, 2019a, b, 2021; Wen et al., 2018; Richard et al., 2019; Nūnez-Hernández et al., 2020]. These studies, carried out within the framework of the CeMIEGeo (*Centro Mexicano de Innovación en Energía Geotérmica*) initiative, revealed distinct features in each of the fields, but to this day, with the exception of carbon systematics [Richard et al., 2019], no comprehensive analysis has been conducted across the different fields.

Stable noble gases (He, Ne, Ar, Kr, Xe) are chemically inert and are thus transported without being affected by chemical reactions [Ozima and Podosek, 2002]. Noble gases in subsurface fluids are derived from the atmosphere, the crust, and the mantle, all of which show distinct isotopic and elemental signatures, making them excellent tracers of fluid origin and interactions [Castro et al., 1998a, b; Ballentine and Burnard, 2002; Hilton and Porcelli, 2003]. In geothermal systems, meteoric water, which is air-saturated at solubility equilibrium, provides the atmospheric volatile component. Magmatic heat sources contribute to the mantle component, particularly ^{3}He which is enriched in the mantle compared to ^{4}He, with $^{3}He/^{4}He$ ratios of 8±1Ra for the convective depleted mantle [Allègre et al., 1995]. Crustal fluids generally show lower $^{3}He/^{4}He$ ratios due to the accumulation of radiogenic ^{4}He produced in crustal rocks. The existence of fossil water in geothermal systems has been recently identified based on the distribution of radiogenic ^{4}He [Birkle et al., 2016; Pinti et al., 2019]. The application of noble gas tracers in geothermal systems has traditionally involved the sources and migration pathways of geothermal fluids [e.g., Mazor and Truesdell, 1984; Kennedy and Truesdell, 1996; Kennedy and van Soest, 2006; Birkle et al., 2016; Pinti et al., 2021], the identification of heat sources [e.g., Kennedy et al., 2000; Magro et al., 2003; Wen et al., 2018] and the evaluation of physical processes within the reservoir itself induced by exploitation [e.g., boiling and re-injection; Kennedy and Shuster, 2000; Pinti et al., 2019b; Wen et al., 2018].

As mentioned above, noble gases can be helpful in tracing the heat source, the most important feature of a geothermal area, controlling convective fluid transfer and fluid enthalpy. The current total heat flux from the Earth into space is 44.2±1.0 TW of which 20 TW are derived from the decay of the radioactive isotopes ^{232}Th and ^{238}U in the mantle and the crust [Gando et al., 2011]. These two elements also produce radiogenic ^{4}He. As a result, the presence of a correlation

between heat and helium fluxes into the Earth's surface has traditionally been expected. At mid-ocean ridges, heat and helium are transferred from the mantle to the Earth's surface, and the heat/He ratios are similar to the theoretically predicted values [e.g., Lupton et al., 1999]. However, in most continental settings, including geothermal systems, this correlation between heat and helium has remained elusive [e.g., Polyak et al., 1979; O'Nions and Oxburgh, 1983; Polak et al. 1985; Polyak and Tolstikhin, 1985; Oxburgh and O'Nions, 1987; Polyak et al., 2000; Castro et al., 2005]. Mixing of fluid components from different sources, including meteoric and ancient water, is one of the processes behind the lack of the observed correlation [e.g., Polyak, 2005]. At present, the redistribution of heat and helium in hydrothermal fluids has not been comprehensively assessed.

Here, multi-isotopic datasets from deep fluids sampled in wells from four geothermal fields (Los Azufres, Los Humeros, Cerro Prieto, Las Tres Vírgenes), fluids from hot springs and fumaroles from Cerritos Colorados and Acoculco, together with a large dataset obtained from surface manifestations (cold and hot springs) in Baja California from Batista-Cruz et al. [2019] are combined. The goal is to systematically analyze the sources and mechanisms of transport of geothermal fluids in these systems, and thus, to deconvolute the magmatic, meteoric and crustal contributions in these systems. We also seek to clarify potential fractionation patterns present in magmatic volatiles (e.g., noble gases and CO_2), as well as its dependence on heat transfer and magma degassing.

4.2. Geological Setting

Mexico is located at the convergent boundary along the western North America Plate, with extended magmatic and volcanic activity induced by plate subduction (Fig. 4.1). During the existence of the Pangea supercontinent, the oceanic floor of the Panthalassa super-ocean

surrounding the Pangea was divided into three major plates: the Farallon, the Phoenix and the Izanagi plates, all connected by a triple-junction [e.g., Smith, 2007]. With the formation of the Pacific Plate at the center of the triple junction around 190 Ma ago [Boschman and van Hinsbergen, 2016], the Farallon Plate was pushed underneath the North America Plate. Over half of the Farallon Plate was consumed at the convergent boundary of the southwestern North America Plate before its fragmentation in the early Tertiary [e.g., Lonsdale, 2005]. The northern part of the Farallon Plate was fragmented into the Juan de Fuca, the Explorer and the Gorda Plates, and later into smaller microplates [e.g., Lonsdale, 1989]. The subduction of the remnants of these plates has mostly ceased, but the existence of a fossil slab attached to them has been highlighted by seismic tomography studies [e.g., Wang et al., 2013]. Upwelling mantle in this area may have led to a significant influence from the subducted fossil slab, in Baja California [Wang et al., 2013]. The fragment of the Farallon Plate in Central America is the Cocos Plate, and its subduction beneath central Mexico is ongoing. That has led to the formation of the TMVB at the end of the Cenozoic [Fig. 4.1; Ferrari et al., 2012]. The geothermal areas discussed here are in the Trans-Mexican Volcanic Belt (Los Humeros, Los Azufres, Acoculco and Cerritos Colorados) and in the Baja California (Cerro Prieto and Las Tres Vírgenes).

The Los Humeros field is located on the southern end of the Quaternary TMVB, at the edge of the Sierra Madre Oriental of Miocene age, the latter being the extension of the Basin and Range Province [Ferrari et al., 2012]. The geothermal field is located within a nested caldera system formed during a paroxysmal basalt-andesitic ignimbrite eruption that lasted from 148ka to 69ka. The latter was followed by effusive activity that ended around 2ka [Carrasco-Nūnez et al., 2018]. The heat source of the field is related to the recent Quaternary volcanism, and it is likely located between 5 and 14 km depth. On the other hand, Verma [1985] hypothesized that the heat source

represents a single, voluminous (1500 km^3) stratified magma chamber. Recent petrographic studies suggest a mushroom-like complex network of magma bodies [Lucci et al., 2020]. The low-permeability geothermal reservoir is mainly located in basaltic andesites that overlain a metamorphic carbonate basement. The reservoir is bounded by vertical faults created during the collapse of the internal caldera, which created local enhanced permeability and fluid transfer conduits [De la Cruz, 1983]. The Los Humeros is a high enthalpy (>2400 kJ/kg) steam-dominated field, with liquid fractions as low as 10 to 20% of the total extracted mass [Aragon-Aguilar et al., 2017].

The Acoculco field, part of a Plio-pleistoce volcanic caldera complex, is ~120 km NW of Los Humeros. It underwent two major hydrothermal events that led to reduced permeability of the reservoir rocks. Thermal logs from exploratory wells indicate maximum temperatures exceeding 300◦C at 2000 m depth. Hydrothermal alterations and cold gas discharges are solely observed at the surface [López-Hernández et al., 2009].

The Los Azufres field is located in the central portion of the TMVB (Fig. 4.1), in a Pleistocene silicic volcanic complex [Pérez et al., 2010], within one of the largest intracontinental rift systems of Mexico, the E-W oriented Morelia-Acambay rift. Volcanic activity began in the Miocene with eruption of the Mil Cumbres andesitic ignimbrites, with ages between 27 and 7 Ma, which constitute the main geothermal reservoir. In the Quaternary, a series of rhyodacitic and basaltic units were formed, between 1.22Ma and 0.02Ma [Pérez et al., 2010]. These rhyolitic units act as the cap rock of the reservoir. The heat source is localized beneath the field, at shallow crustal depths. While the origin of this heat source has been associated with the last acidic volcanism, its origin remains unclear. The $^{87}Sr/^{86}Sr$ and $^{3}He/^{4}He$ signatures in these geothermal fluids suggest that basaltic (E-MORB-type) melts are the origin of both the heat and deep volatiles in Los Azufres

[Wen et al., 2018]. Geothermal activity in the Los Azufres field is found in the southern portion of the volcanic structure, which is further divided into two production zones: the Northern Production Zone, which is liquid dominated, and the Southern Production Zone which is vapor-dominated and displays higher enthalpy [Torres- Rodríguez et al., 2005]. Dry gas composition of the fluids exploited at Los Azufres are again dominated by CO_2, which is up to 94% of the total volume [e.g., Richard et al., 2019].

Cerritos Colorados is located close to Guadalajara (Fig. 4.1) and is the westernmost geothermal field operated by the CFE within the TMVB. The geothermal reservoir is located in a rhyolitic volcanic complex, which is associated with a Pleistocene caldera structure [Gutíerrez-Negrín, 1988]. Faults and fractures with NW-SE, N-S and NE-SW orientations are the result of the caldera collapse as well as the uprise of the magma chamber, leading to the formation of fumaroles and hot springs [Vengas et al., 1991]. Existing wells display borehole temperatures of ~284°C at a depth of 1200m [Vengas et al., 1991]. More recent work from Pandarinath and Domínguez-Domínguez [2015] suggests an average reservoir temperature of ~308°C, estimated using multiple geothermometers.

The Cerro Prieto geothermal field is located in Baja California and is not only the largest high-enthalpy liquid-dominated geothermal field in Mexico, but also one of the largest in the world [Gutiérrez-Negrín, 2015]. The field is located in a pull-apart basin created at the transition zone between the Gulf of California spreading center and the San Andreas transform fault system [e.g., Suárez-Vidal et al., 2008]. The heat source is likely a single gabbroic body (MORB-type) associated to crustal extension and thinning, possibly intruded less than 50ky ago, at a depth of ca. 5 km [Elders et al. 1984; Schmitt et al., 2013]. The reservoir is a sequence of Plio-Pleistocene-age sandstones interbedded with grey shales of the Colorado Delta, sitting on a Cretaceous granite

basement. The reservoir is separated in three zones: 1) α reservoir - it is the shallowest (depths of 1000–1500 m), restricted to the western part of the field; 2) β reservoir - it is deeper (depths ranging from 1500 to 2700m), with a temperature of ~300˚C; and 3) γ reservoir - it is currently not exploited and located in the eastern portion of the field. The γ reservoir is also the deepest and hottest reservoir, with temperatures exceeding 350˚C [Lippmann et al., 1991]. Modern recharge into Cerro Prieto is thought to be negligible, based on stable isotope data [Portugal et al., 2005]. Excess radiogenic ^{4}He, relative to in-situ production, point to a (U-Th/^{4}He) age of 2.5 Ma for the Cerro Prieto geothermal fluids, which corresponds to the Pliocene age of the Colorado Delta porewater [Pinti et al., 2019a]. These fluids, of sodium chloride type, are thought to be a mixture of old Colorado River waters and hypersaline marine brines, with only a minor amount of magmatic water [Lippman et al., 1991].

The Las Tres Vírgenes field is located in the Baja California Sur, south of Cerro Prieto (Fig. 4.1), within a Cenozoic rift of NW-SE direction known as the Santa Rosalia Basin [López-Hernández et al., 1995]. This area corresponds to the subduction zone of the Farallon plate during the Miocene [Aguillón-Robles et al., 2001; Bellon et al., 2006; Calmus et al., 2008; Ferrari et al., 2012]. The Las Tres Vírgenes field is associated with a basaltic andesite to dacitic volcanic chain composed of three NNE aligned volcanoes, at the intersection with NW-SE lateral faults [Macías, et al., 2013]. The reservoir is hosted in Cretaceous granodiorite fault zones [Schmitt et al., 2010; Tello- Hinojosa et al., 2005; Macías et al., 2013]. The heat source is the magmatic body underneath [Prol-Ledesma et al., 2016].

4.3. Sampling and Analytic Methods

Fluid samples for noble gases and C stable isotope data ($\delta^{13}C$ in ‰ vs PDB) analysis were collected between 2009 and 2018. The Los Azufres samples were collected in 2009 and 2014 [Pinti et al., 2013; Wen et al., 2018]; the Los Humeros samples were collected in 2015, and again, in 2018 [Pinti et al., 2017, 2021]. Samples from Cerro Prieto and Las Tres Vírgenes were collected in 2016 [Pinti et al., 2019a, b]. Fluid samples for noble gas analysis from the Cerritos Colorados and Acoculco were collected in 2018 and the data are presented here. Fluids for C isotope analysis were not collected from these two fields. A total of 132 fluid samples collected over the years by our research group and analyzed for noble gases are being studied here as a whole. In addition to all the samples collected by our research group, 33 samples of Baja California area taken from Batista-Cruz et al. [2019] are also included in this study for comparison with our data of Cerro Prieto and Las Tres Vírgenes. Among the Batista-Cruz et al. [2019] data, 16 samples are defined as "hydrothermal" gases which correspond to intertidal gases emitted along the eastern and western coasts of Baja California and characterized by low amounts of magmatic gases. In particular, $^3He/^4He$ ratios (R) normalized to that of the atmospheric value [Ra= 1.384×10^{-6}; Clarke et al., 1976] are less than 1.6. The remaining samples are defined by Batista-Cruz et al. [2019] as "magmatic" gases, i.e., gas emissions in areas of Quaternary to Holocene volcanic activity, with $5 \leq R/Ra \leq 7$, indicating a strong presence of magmatic ^3He.

Most fluid samples for both, C isotope and noble gases analysis were collected directly from the steam-water separator at the wellhead in standard refrigeration grade 3/8" copper tubes, which were then sealed by steel pinch-off clamps using an electric drill to minimize atmospheric contamination [e.g., Richard et al., 2019]. When a steam-water separator was not available, gas samples were collected directly from the wellheads using a portable field separator. A more

detailed description of the sampling methods can be found in Pinti et al. [2017, 2019a, 2019b, 2021].

The isotopic analysis of CO_2 was carried out at the GEOTOP research center at the Université du Québec in Montréal. The CO_2 components were first separated from other incondensable gases (e.g., H_2S, CH_4, N_2, He, Ne and Ar), following the methods described in Richard et al. [2019]. The purified CO_2 samples were then analyzed by a 100 Dual Inlet Isotope Ratio Mass Spectrometer (IRMS) and the results were normalized to the V-PDB scale.

Noble gas analyses were carried out in the Noble Gas Laboratory at the University of Michigan, except for samples from Acoculco, which were analyzed at GEOTOP. At the University of Michigan, gas samples in Cu tubes were attached to a stainless-steel vacuum extraction and purification line. The copper tube was connected to a vacuum system at a pressure of ~5 x 10^{-7} Torr. Once this pressure was achieved and the system isolated from its turbo-molecular vacuum pump, the lower clamp was opened to release the natural gas into a low He diffusion glass flask. Gas samples were then expanded in a known volume and gas pressure reduced by computer-controlled sequential pumping until reaching a value acceptable for analyses (typically 35 Torr). The gas sample was initially exposed to a Cu-CuO getter at 800°C to oxidize hydrocarbons. The Cu-CuO getter was then allowed to cool to 450°C to reabsorb O_2. Subsequently, the gas sample was exposed to a 3Å molecular trap to reduce water vapor pressure and reactive gases were removed using three Ti-getters at 600°C for three minutes each. The He, Ne, Ar, Kr, and Xe were quantitatively extracted using a dual chamber computer-controlled cryo-separator at temperatures of 49 K, 84 K, 210 K, 245 K, and 290 K respectively, and sequentially allowed to enter a Thermo® Helix SFT mass spectrometer for He and Ne isotope analyses, and a Thermo® ARGUS VI mass spectrometer for the Ar, Kr, and Xe isotope analyses. At the He release temperature, a small

percentage of He is introduced into the SFT mass spectrometer and the signal intensity of ^{4}He is determined for use as the He concentration estimate. This estimate is then used by the automated system to optimize the amount of He that should be introduced for measurement of the $^{3}He/^{4}He$ ratio. All noble gas isotopes were measured using a Faraday detector, except for ^{3}He, which was measured using an electron multiplier in ion counting mode. Prior to each analysis, a blank run was conducted using the same procedure as the sample. Typical blanks are 0.3% - 0.9% of the measured sample values. Quantitative analyses were obtained by calibrating the two mass spectrometers with a known aliquot of standard air. Typical standard reproducibility for ^{4}He, ^{20}Ne and ^{36}Ar are 0.4%, 0.9% and 0.3% while for $^{20}Ne/^{22}Ne$ and $^{40}Ar/^{36}Ar$ ratios the reproducibility is 0.08% and 0.04%, respectively. Calculated standard errors for concentrations range from 1.3 to 2.2% of the measured values.

At GEOTOP, gases from the copper tubes were collected in a pre-evacuated 12cc stainless-steel finger equipped with a bellow valve. The finger was connected to a stainless-steel extraction line and reactive gases were removed by two Ti-getters at 600˚C for 15 min each and a SAES ST-707 getter at 100˚C for 15 min. Gases were then adsorbed onto an ARS® cryogenic trap containing activated charcoal, and released sequentially at 40K, 110K, 210K, and 280K for He, Ne, Ar, and Kr-Xe respectively. Noble gas isotopes were measured on a Thermo® HELIX-MC Plus. Blanks were routinely measured and were typically on the order of 0.01% for ^{4}He to 0.15% for ^{132}Xe. Quantitative analyses were obtained by calibrating with a known aliquot of standard air. Errors on standard concentrations range from 1 to 3% of the measured values.

4.4. Results

Field name, sample ID, sampling year, and volume fractions of CO_2, ^4He, ^{36}Ar, and ^{40}Ar, $\delta^{13}C$-CO_2 ratios, as well as $^3He/^4He$ ratios and $CO_2/^3He$ ratios are provided for all samples collected by our research group in Table C1 (Appendix C). Radiogenic ^4He ($^4He^*$) and ^{40}Ar ($^{40}Ar^*$), also provided in Table C1, are calculated following [Ballentine et al., 2002]:

$$^4He^* = {}^4He_{measured} - \left(\frac{^4He}{^{20}Ne}\right)_{air} \times {}^{20}Ne_{measured} \quad (4.1)$$

$$^{40}Ar^* = \left(\left(\frac{^{40}Ar}{^{36}Ar}\right)_{measured} - \left(\frac{^{40}Ar}{^{36}Ar}\right)_{air}\right) \times {}^{36}Ar_{measured} \quad (4.2)$$

$Q/^3He$ ratios are calculated as follow [Tuner and Stuart, 1992; Burnard et al., 1999]:

$$\frac{^3He}{Q} = \frac{^3He}{^{36}Ar} \times \frac{^{36}Ar_{ASW}}{(c_p \times \theta)} \quad (4.3)$$

where Q is heat in Joules; C_p is the heat capacity of water [4.4 $JK^{-1}g^{-1}$, Burnard et al., 1999]; θ is the excess of the reservoir temperature with respect to the atmospheric temperature in ℃, and subscript "ASW" represents air-saturated water. The atmospheric temperature used for each field is the local mean annual atmospheric temperature (MAAT). The MAAT is 12℃ in Los Azufres and 22℃ in all other fields. The $^{36}Ar_{ASW}$ concentration in each field is calculated based on the respective MAAT value. The reservoir temperatures of each production well determined by the geothermal gradient and geothermometers are provided by CFE (Table C2, Appendix C). Since the product of C_p and θ is applied as the estimation of enthalpy of the geothermal fluid in equation (4.3), the measured enthalpy value is used to replace the ($C_p \times \theta$) in equation (4.3) when available (Table C2, Appendix C). The fluid enthalpy values of the Los Azufres samples are from Nuñez-Hernández et al. [2020], while the unpublished enthalpy values of the Los Humeros and Las Tres Vírgenes samples are also reported (Table C2, Appendix C). The estimated $Q/^3He$ ratios are also

reported in Table C2, Appendix C. Fluid enthalpy values of Cerro Prieto samples were not measured.

The contribution of atmospheric helium and its influence on the measured R/Ra ratios can be corrected using $^4He/^{20}Ne$ ratios, following Craig et al. [1978]:

$$\left(\frac{R}{Ra}\right)_c = \frac{\left(\frac{R}{Ra} - r\right)}{(1-r)} \tag{4.4}$$

$$\text{with } r = \frac{\left(\frac{^4He}{^{20}Ne}\right)_{ASW}}{\left(\frac{^4He}{^{20}Ne}\right)} \tag{4.5}$$

where subscripts "c" and "ASW" represent the air-corrected value and the value in air-saturated water, respectively. The ASW $^4He/^{20}Ne$ ratio range from 0.265-0.277 and is calculated following solubilities from Smith and Kennedy [1983] assuming local recharge temperatures of 12-22 °C. Measured $^4He/^{20}Ne$ ratios are reported in Table C2 (Appendix C), together with air-corrected R/Ra ratios $(R/Ra)_c$. The $^4He/^{20}Ne$ ratios in the Los Humeros and Los Azufres fields are generally higher than those from the Baja California area, suggesting a lower atmospheric contribution as the $^4He/^{20}Ne$ ASW ratio is very low (< 0.3). The $^4He/^{20}Ne$ ratios are not available for some of the samples due to the extremely low neon level, leading to low measurement accuracy. The atmospheric helium component in these samples was subsequently corrected by replacing the $^4He/^{20}Ne$ ratios in equations (4.4) and (4.5) with $^4He/^{36}Ar$ ratios [Marty et al., 1993]. The $(R/Ra)_c$ errors account for the combined $^3He/^4He$ ratios and ^4He and ^{20}Ne (^{36}Ar) volume fractions errors.

The CO_2 volume fractions vary between 0.14 and 0.98, with the lowest values present in some of the Baja California samples [Batista-Cruz et al., 2019] and the highest ones in Las Tres Vírgenes. The Los Humeros samples have relatively high CO_2 contents, varying from 0.85 to 0.95 (Table C1, Appendix C). Samples from Cerro Prieto display lower CO_2 contents compared to those of Los Humeros and Los Azufres, with values varying between 0.83 and 0.84 (Table C1, Appendix

C). The $\delta^{13}C$ ratios of CO_2 vary between -18.4‰ and -2.24‰ vs. V-PDB, with samples from Baja California displaying the lowest values while some samples from Los Humeros display the highest values (Table C1, Appendix C).

Total ^{4}He volume fractions range from 3.99×10^{-8} to 3.18×10^{-4}, with the highest values found in some of the Baja California samples, and the lowest values in Los Humeros (Table C1, Appendix C). The R/Ra ratio varies between 0.58 and 7.93 (Table C1, Appendix C), with the Baja California hydrothermal samples and some of the Los Azufres samples (e.g., AZ-66D, AZ-2A, and AZ-42) displaying the lowest R/Ra ratios, with values varying between 0.58 and 3.05 (Table C1, Appendix C). Samples from the TMVB, i.e., Los Azufres, Los Humeros, Acoculco and Cerritos Colorados, display generally higher R/Ra ratios than samples from the Baja California, i.e., Las Tres Vírgenes and Cerro Prieto fields. Most air-corrected $(R/Ra)_c$ ratios are similar to measured R/Ra values. Only a few samples (AZ-2A, AZ-42, AZ-90, AA7(SSB), FUM(SSB)) display significant differences between R/Ra and $(R/Ra)_c$, caused by atmospheric contamination. Measured ^{36}Ar volume fractions range between 1.10×10^{-9} and 4.03×10^{-5}, with the lowest values present in the Los Humeros samples, and the highest in the Baja California samples (Table C1, Appendix C). The three Los Azufres samples displaying the lowest R/Ra ratios present relatively high ^{36}Ar contents, varying between 2.62×10^{-5} and 2.89×10^{-5}. Total ^{40}Ar volume fractions among all samples range between 6.56×10^{-7} and 1.22×10^{-2}, with the lowest values present in the Los Humeros samples, and the highest ones in Baja California (Table C1, Appendix C). Radiogenic $^{4}He^{*}$ and $^{40}Ar^{*}$ volume fractions vary between 3.99×10^{-8} and 3.15×10^{-4}, and between 9.21×10^{-8} and 3.02×10^{-4} (Table C1, Appendix C), respectively. The highest values are found in some of the Baja California samples together with low R/Ra (1.07-1.55), indicating a significant crustal contribution.

4.5. Discussion

4.5.1. Heterogeneous Helium Sources

Prior to analyzing the heat and $Q/^3He$ ratio distribution in Mexican geothermal fluids and relevant information it provides, helium sources and those of associated fluids must be identified and discriminated. The $(R/Ra)_c$ ratios range from 1.04 to 7.93 and represent the mixture between crust and mantle helium components. While crustal R/Ra ratios vary within a relatively narrow interval [~0.02-0.05; e.g., Oxburgh et al., 1986], R/Ra ratios in the different hypothetical mantle reservoirs beneath Mexico display significantly distinct values. Therefore, the differentiation among the various sources of mantle helium should be reflected by their distinct R/Ra ratios measured in fluids.

The R/Ra ratio value expected at mid-ocean ridges, which represents the pristine convective depleted MORB-Type mantle (or DMM) is 8±1 [Allègre et al., 1995]. The Gulf of California spreading center (Fig. 4.1) is also expected to have a DMM helium isotopic signature. Lupton [1979], based on helium isotopic measurements from ocean water samples above the Gulf of California spreading center, between the Guaymas and Mazatlan basins (Fig. 4.1), estimated that the R/Ra value of injected mantle helium was 7.84±0.40, which falls within the DMM value range. The R/Ra value of DMM above a subduction plate and beneath a volcanic arc such as the TMVB, i.e., the "mantle wedge", is expected to be lower than a pure DMM reservoir due to release of crustal radiogenic ^4He from the subducting sediments [e.g., Poreda and Craig, 1989; Hilton et al., 2002]. The expected R/Ra value is 5.37±1.87 [Hilton et al., 2002]. The average R/Ra value beneath the central section of the TMVB was constrained by Straub et al. [2011] at 7.3±0.3Ra, based on measurements of olivine separates from basaltic lavas (6.81≤R/Ra ≤to 8.00). This R/Ra value is closer to the DMM than that expected for a mantle wedge, and Straub et al. [2011]

suggested that any crustal He on the slab could have long been driven off during the flat, prolonged slab subduction beneath the Mexican forearc. Another potential reservoir of mantle helium beneath Mexico is the subcontinental lithospheric mantle (SCLM). SCLM shows an average R/Ra value of 6.1±0.9 which is interpreted as reflecting a closed reservoir isolated from the DMM on a 100Ma timescale, and accumulating radiogenically produced ^{4}He [Gautheron and Moreira, 2002]. Sandoval-Velasquez et al. [2021] identified a SCLM reservoir corresponding to that beneath the Basin and Range Province and extending along the Mexican Sierra Madre, with an estimated R/Ra of 7.39±0.14. However, there is not yet evidence that the SCLM extends to the TMVB or that it interferes with the mantle wedge. This is also true for the Los Humeros geothermal field, which is at the boundary between these two mantle regions [Pinti et al., 2021]. However, its occurrence in areas other than the Sierra Madre cannot *a priori* be excluded.

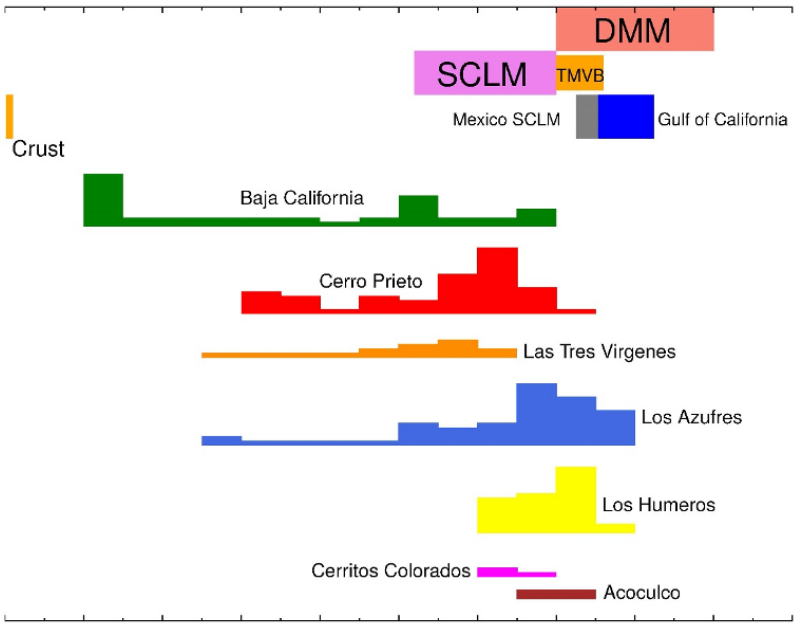

Figure 4.2 $(R/Ra)_c$ of fluids in Mexican geothermal areas. Reference values: depleted mantle or DMM [8±1; Allègre et al., 1995]; DMM under Gulf of California [7.84±0.4; Lupton, 1979]; mantle wedge under the TMVB [7.3±0.3; Straub et al., 2011]; subcontinental lithospheric mantle or SCLM [6.1±0.9; Gautheron and Moreira, 2002]; SCLM beneath Mexico [7.39±0.14; Sandoval-Velasquez et al., 2021]; continental crust [Oxburgh et al., 1986].

Figure 4.2 shows all the expected helium isotopic signatures $(R/Ra)_c$ for the different mantle reservoirs beneath Mexico (DMM, SCLM and TMVB), in the crust and those measured in the fluids of Mexico geothermal reservoirs. Significant variations in $(R/Ra)_c$ ratios are observed among fluids from the different geothermal fields (Table C2, Appendix C; Fig. 4.2). Fluids from the TMVB (Los Azufres, Los Humeros, Cerritos Colorados and Acoculco) generally display higher $(R/Ra)_c$ ratios compared to those from Baja California (Fig. 4.2), an indication that the heat sources in these fields are active, pointing to the presence of young magma chambers with pristine mantle signals. The Los Azufres samples display a wider range of $(R/Ra)_c$ values, with one sample indistinguishable from that of a pure DMM reservoir (7.93±0.09) and a wide range of values down to 2 (Fig. 4.2). A correlation between $^{87}Sr/^{86}Sr$ and $(R/Ra)_c$ values suggests that this lower, more radiogenic-like $(R/Ra)_c$ may be related to a local volcanic source of Miocene age corresponding to the andesitic reservoir of Los Azufres [Wen et al., 2018], while values closer to that of the atmosphere are potentially contaminated by reinjected brines [e.g., Pinti et al., 2013].

Both Los Humeros and Los Azufres display higher $(R/Ra)_c$ values in fluids (7.6 to 7.9), close to those suggested for the DMM [Allègre et al., 1995; Lupton, 1979], the mantle wedge expected in central TMVB [Straub et al., 2011], and the SCLM beneath the Sierra Madre [Sandoval-Velasquez et al., 2021], pointing to a nearly pristine mantle signal. On the other hand, Baja California geothermal fields, i.e., Cerro Prieto and Las Tres Vírgenes, show consistently lower $(R/Ra)_c$ values, between 6.03 and 6.56 compared to the those measured in the TMVB fluids and those helium expected in the DMM beneath the Gulf of California spreading center [Fig. 4.2; Lupton, 1979]. The maximum $(R/Ra)_c$ measured in the Cerro Prieto and Las Tres Vírgenes fluids are close to those of the "magmatic gases" measured in Baja California by Batista-Cruz et al. [2019] (Fig. 4.2). These authors suggested that $(R/Ra)_c$ values in hydrothermal manifestations of Baja

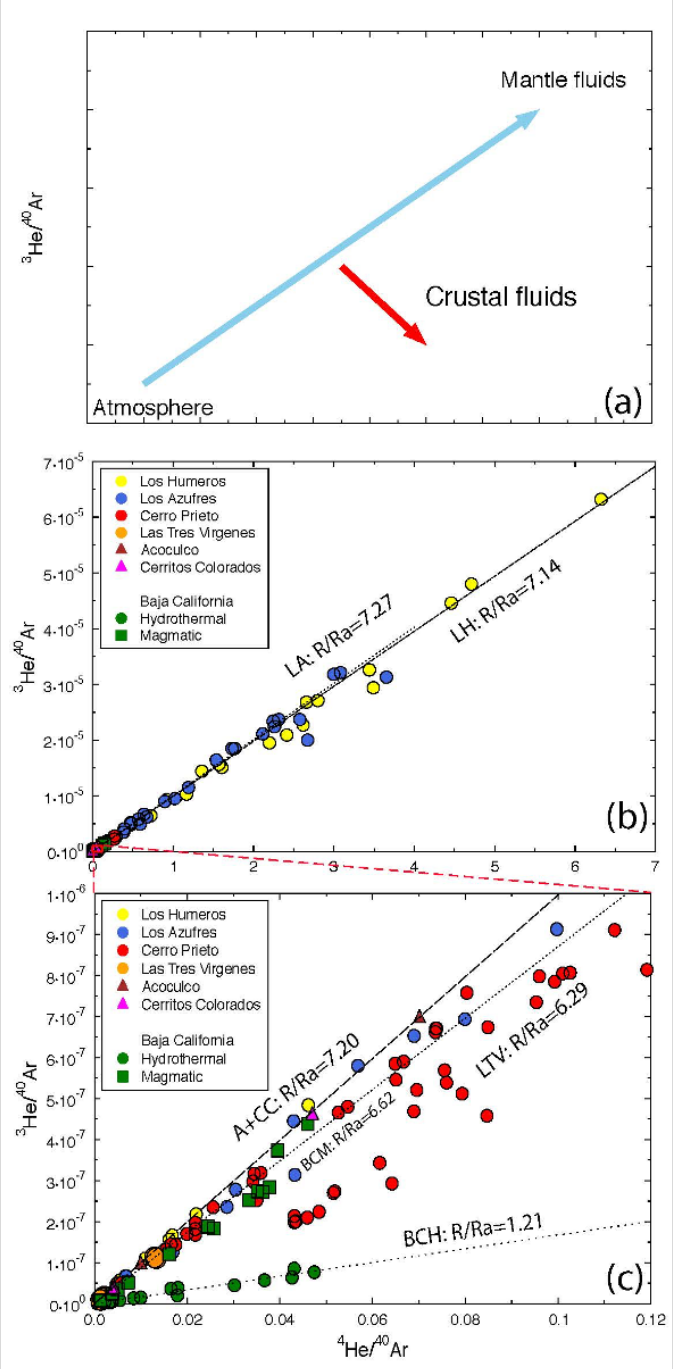

Figure 4.3 (a) Theoretical model of $^3He/^{40}Ar$ vs $^4He/^{40}Ar$; (b) Total $^3He/^{40}Ar$ vs total $^4He/^{40}Ar$ measured in Mexican geothermal fluids; (c) Zoom in of b) with the extent shown as red dashed box. Hydrothermal and magmatic samples from Batista-Cruz et al. [2019] in the Baja California area are shown as green circles and squares, respectively. Regression lines for each geothermal field are shown with their slopes representing the R/Ra ratios of each field. LA: Los Azufres; LH: Los Humeros; A: Acoculco; CC: Cerritos Colorados; LTV: Las Tres Vírgenes; BCH: Baja California magmatic samples

California could be the result of some addition of crustally-produced radiogenic ^{4}He leaking from stacking sections of the Miocene-age subducted Farallon plate. Richard et al. [2019] came to a similar conclusion based on $\delta^{13}C$ of -11.9‰ vs V-PDB measured in Las Tres Vírgenes, which are the lightest values measured in Mexican geothermal fluids and which call for a crustal contribution of carbon from the old, subducted plate. To further discriminate the sources of helium in samples from each of the Mexican geothermal fields, $^{3}He/^{40}Ar$ ratios are plotted as a function of $^{4}He/^{40}Ar$ ratios (Fig. 4.3), where ^{40}Ar is the total argon content. Since both, the x and y-axis have a common denominator (^{40}Ar) and are also on the same scale, mixing between two theoretical endmembers should plot as a straight line, with the slope of the mixing line representing the average R/Ra ratio of the sample cluster (Fig. 4.3a) [Matsuda and Marty, 1995]. One endmember should have low $^{3}He/^{40}Ar$ and $^{4}He/^{40}Ar$ ratios, likely representing a meteoric water component (e.g., $^{3}He/^{40}Ar = 2.21\times10^{-10}$ and $^{4}He/^{40}Ar = 1.58\times10^{-4}$ at 25°C). The other endmember is characterized by significantly higher $^{3}He/^{40}Ar$ and $^{4}He/^{40}Ar$ ratios, likely representative of a mantle-derived component, as the $^{3}He/^{40}Ar$ and $^{4}He/^{40}Ar$ ratios in the mantle are $\sim7\times10^{-5}$ and 10, respectively [Ozima and Podosek, 2002]. Addition of crustal $^{4}He^*$ and $^{40}Ar^*$ should move the data points to the right and below the theoretical mixing line (red arrow; Fig. 4.3a), since the production of ^{3}He in the crustal is usually negligible, while the radiogenic production ratio $^{4}He/^{40}Ar^*$ in the crust is much higher than that in the mantle [e.g., Pinti and Marty, 1998]. In figure 4.3b, samples from Los Azufres and Los Humeros in the TMVB display linear mixing trends between the mantle and the atmospheric components, with little input from the crust (Fig. 4.3b). The other two geothermal fields of interest in the TMVB, Cerritos Colorados and Acoculco, also display a linear trend between the crust and the mantle components (Fig. 4.3c). All four geothermal fields in the TMVB display R/Ra ratios between ~7.1 and ~7.3, which fall within the typical mantle wedge values

beneath central Mexico [Straub et al., 2011], and the SCLM reservoir hypothesized by Sandoval-Velasquez [2021].

Crustal contribution of helium will move the samples toward the lower-right side of the plot, which results in a lower average R/Ra ratio of 6.29 extrapolated for Las Tres Vírgenes geothermal fluids and of 6.62 for the Cerro Prieto geothermal fluids and Baja California magmatic gases (Fig. 4.3c). However, the Cerro Prieto samples display a different distribution pattern compared to the other geothermal fields of Baja California. Specifically, the Cerro Prieto samples fall to the lower-right side of the mixing line while the Las Tres Vírgenes fluids and Baja California magmatic samples are plotted along straight lines. The linear distribution pattern of the Las Tres Vírgenes and Baja California magmatic samples is a direct indication that these samples are a mixture between two components with unique isotopic signatures: an atmospheric endmember with low $^{3}He/^{40}Ar$ and $^{4}He/^{40}Ar$ ratios and a mantle-like one with higher $^{3}He/^{40}Ar$ and $^{4}He/^{40}Ar$ ratios, even though the mantle endmember likely includes a crustal contribution compared to those of the Los Azufres and Los Humeros fields. On the other hand, the distribution pattern of the Cerro Prieto samples suggests the presence of an additional, local crustal component, moving samples to the lower-right of the mixing line (Fig. 4.3c), possibly due to fossil water in the reservoir accumulating radiogenic $^{4}He^{*}$, as previously postulated by Pinti et al. [2019a]. The atmosphere-like R/Ra ratios (Fig. 4.3c) in Baja California hydrothermal samples potentially suggests the presence of an atmospheric component, reaching lower values of $^{3}He/^{40}Ar$ in the plot.

It is apparent that helium isotopic ratios in the Mexican geothermal fields are the reflection of the local geological/tectonic setting, with samples from the TMVB displaying significantly different helium signals compared to those from Baja California. Since helium is usually considered to be associated with heat, the mixing of fluid components from the crust, the mantle

and the atmosphere may also be reflected in the transport and distribution of heat in these geothermal reservoirs. This is discussed below.

4.5.2. Heat Transfer into Mexican Geothermal Systems

During the transport of helium (He), volatiles, and heat (Q) from the magmatic source into the hydrothermal system, fractionation can occur, leading to a change from the original Q/He ratio. $Q/^3He$ ratios in Mexican geothermal fluids were estimated using equation (4.3) and vary between 4.57×10^{10} and 8.67×10^{15} J ccSTP^{-1} (Table C2, Appendix C). In figure 4.4, the estimated $Q/^3He$ ratios are plotted as a function of $^4He/^{36}Ar$ ratios, following Burnard and Polya [2004]. If no mechanism leading to fractionation of the heat - helium pair occurs at the boundary between the magmatic and the hydrothermal systems, the $Q/^3He$ ratios in geothermal fluids should mimic the value of the melt sources. The expected initial $Q/^3He$ ratio in continental hydrothermal systems can vary between two mantle endmembers: the $Q/^3He$ calculated at the mid-ocean ridges ranging from 5×10^{12} to 1×10^{13} J ccSTP^{-1} [labelled DMM in Fig. 4.4; Lupton et al., 1989; Baker and Lupton, 1990, Kennedy et al., 2000; Burnard and Polya, 2004], and that calculated for melts generated beneath continents and corresponding to 2% of partial mantle melting [Martel et al., 1989] which is 1-2 x 10^{12} J ccSTP^{-1} [Burnard and Polya, 2004].

In a plot of $Q/^3He$ vs. $^4He/^{36}Ar$ (Fig. 4.4), hydrothermal fluids usually depart from the DMM or continental melt values along two possible trends: 1) a $^4He/^{36}Ar$ ratio increase accompanied by a decrease of the $Q/^3He$ ratio (labeled “convection/magma degassing”; Fig. 4.4); 2) a $^4He/^{36}Ar$ ratio decrease accompanied by an increase of the $Q/^3He$ ratio (labeled “conduction/ASW dilution/boiling”; Fig. 4.4). Except for most of Los Humeros fluids (yellow dots; Fig. 4.4) and some of the Los Azufres fluids (blue dots and squares; Fig. 4.4), it is apparent that

most Mexican geothermal fluids display $Q/^3He$ values higher than those expected at DMM or those from melts generated beneath continents (high $Q/^3He$ and low $^4He/^{36}Ar$; Fig. 4.4). A trend line (dotted line) based on all Mexican samples represents both trends (Fig. 4.4).

The first trend (high $^4He/^{36}Ar$ and low $Q/^3He$) is interpreted as a convective transfer of heat and volatiles from the cooling magma into the hydrothermal system [Baker and Lupton, 1990; Burnard and Polya, 2004]. Helium will be removed faster from magma than heat and thus, the $Q/^3He$ will decrease with time.

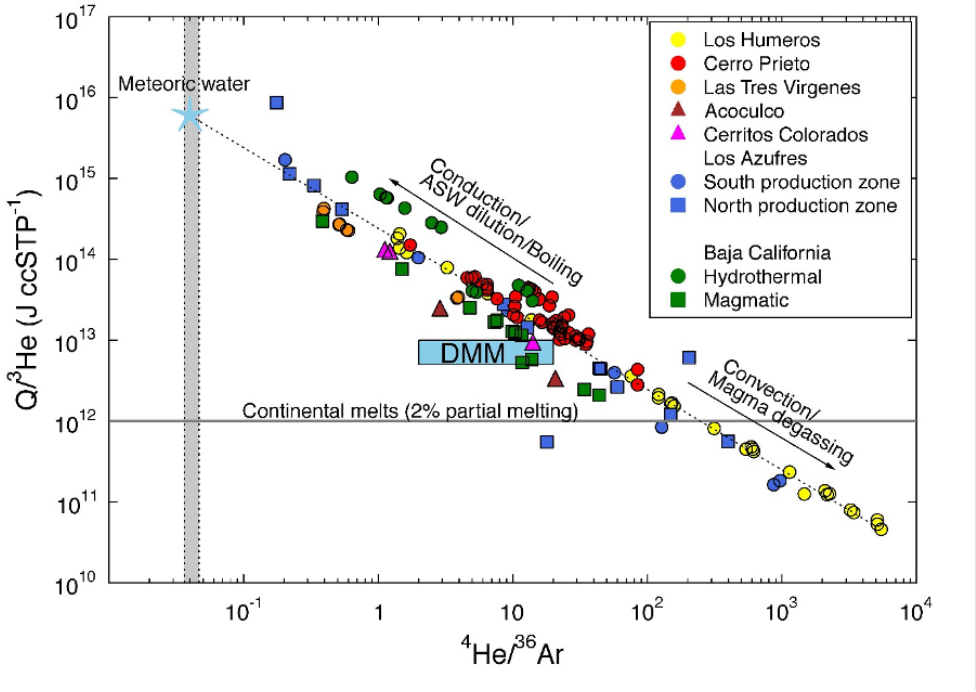

Figure 4.4 The $Q/^3He$ versus $^4He/^{36}Ar$ ratios in the Mexican geothermal fluids. Samples from the southern production zone of Los Azufres are shown as circles, while those from the northern production zone are shown as squares. The $Q/^3He$ values of DMM are from Lupton et al. [1989] and $^4He/^{36}Ar$ values are from Burnard and Polya [2004]. Continental melts $Q/^3He$ value is from Burnard and Polya [2004]. The $^4He/^{36}Ar$ value range of ASW calculated for MAAT of 12-22°C is indicated as a grey surface. The dotted line represents the linear correlation between $Q/^3He$ versus $^4He/^{36}Ar$ ratios among the samples. Symbols as in fig. 4.3.

Besides the fractionation between heat and helium, magma degassing can also fractionate the $^4He/^{36}Ar$ ratios due to the differing solubility and diffusivity values of He compared to Ar. Burnard [2001] concluded that even though solubility-controlled fractionation does exist [Burnard,

1999], variations in He/Ar ratios associated with magma degassing are mostly controlled by their diffusivity differences. During magma degassing, He diffuses faster compared to Ar due to its higher diffusivity [e.g., Matsuda and Marty, 1995], thus resulting in elevated $^{4}He/^{36}Ar$ ratios in the escape phase. More recently, Gonnermann and Mukhopadhyay [2007] proposed that the degassing of noble gases from the original mantle reservoir follows a non-equilibrium model, where helium is degassed without significant limit of its diffusivity (since it's highly diffusive), while those with lower diffusivities (e.g., Ne and Ar) are more likely to be retained in the melt due to diffusion, leading to higher He/Ne and He/Ar ratio values in the escaping phase.

The second trend is interpreted as a conductive cooling of magma which transfers magmatic heat but not magmatic volatiles into a hydrothermal system [Burnard and Polya, 2004]. Following Burnard and Polya [2004], dilution with surface fluids would not affect Q while shifting the $^{4}He/^{36}Ar$ ratio toward ASW values (grey area, Fig. 4.4). Such an interpretation, however, presents some challenges. While dilution by surface fluids leads to a decrease of $^{4}He/^{36}Ar$ ratios toward ASW values, it should also lead to an increase of the $Q/^{3}He$ ratio because atmosphere contain little ^{3}He. Thus, introduction of meteoric water in the system will dilute the ^{3}He content without affecting or adding considerable amount of heat [Kennedy et al., 2000]. Further, it is difficult to conceive of the addition of heat without magmatic volatiles in these geothermal areas. In Acoculco, which is the likely equivalent of a Hot Dry Rock system with few to no fluids at shallow levels while displaying a high heat flux, fumaroles still contain a considerable amount of magmatic helium (Rc/Ra = 7.02-7.41). Since most of the Mexican geothermal fields are classified as convective hydrothermal systems, conduction is unlikely to be the dominating heat transport mechanism. The trend observed in Fig. 4.4 could alternatively represent the progressive dilution of magmatic volatiles added together with heat through the addition of meteoric waters during

convective transfer. The $^{4}He/^{36}Ar$ ratios ranging from 3.72×10^{-2} to 4.42×10^{-2} (grey area, Fig. 4.4), corresponding to ASW at 12-22℃ lead to a $Q/^{3}He$ intercept value within the ASW region of ~6×10^{15} J $ccSTP^{-1}$. While this value is three orders of magnitude higher than the mantle $Q/^{3}He$ ratio, it is consistent with the theoretical value for meteoric waters suggested by Kennedy et al. [2000] (1×10^{15} J $ccSTP^{-1}$). Another mechanism that could lead to elevated $Q/^{3}He$ ratios but lower $^{4}He/^{36}Ar$ ratios is boiling of hydrothermal fluids. During boiling, helium is removed from the residual liquid more efficiently than heat, leading to elevated $Q/^{3}He$ ratios. On the other hand, the higher solubility of argon in water, compared to that of helium, will lead to a lower $^{4}He/^{36}Ar$ ratio in the residual liquid phase after boiling. Therefore, we propose that heat and magmatic volatiles are mainly introduced through convective transfer into the hydrothermal system which is successively diluted by various amounts of meteoric water and partially affected by boiling, as previously noted in a number of Mexican geothermal fields [e.g., Pinti et al., 2013, 2017; Wen et al., 2018]. It is worth noting that only samples from Los Humeros and some samples from Los Azufres show $Q/^{3}He$ ratios below those expected for continental mantle melts (2% partial melting). These fluids are thus less affected by meteoric water. The lower impact of ASW in these two fields is also reflected in the high $^{4}He/^{20}Ne$ ratios [10^{3} -$10^{5;}$ Wen et al., 2018; Pinti et al., 2021] compared to the ASW value (0.273 at 25˚C).

Although the mixing trend between the mantle and the meteoric water components is apparent from Fig. 4.4, identification of the crustal component poses more challenges as the $^{4}He/^{36}Ar$ ratio in the crust is poorly constrained [Turner et al., 1993]. Any crustal addition of radiogenic $^{4}He^{*}$ would shift data points to the right side of the general trend [Fig. 4.4; Burnard and Polya, 2004]. On the other hand, crustal $^{3}He/^{4}He$ ratio is well constrained and distinct from that of the mantle and the atmosphere (i.e., the meteoric water component) [Ballentine et al., 2002] and

thus, a plot of $Q/^3He$ versus $^3He/^4He$ is helpful to discriminate the different fluid sources and their impact on the heat distribution in these hydrothermal systems.

4.5.3. Source of Fluids and Heat Distribution

Figure 4.5 shows the calculated $Q/^3He$ ratios vs. $^4He/^3He$ ratios.

Mixing between DMM and the crust endmembers as well as between the crust and ASW are represented by straight lines [Kennedy et al., 2000]. The DMM endmember has $Q/^3He = 2\times10^{12}$ J ccSTP^{-1} [Lupton et al., 1989] and $^4He/^3He = 90317\pm11289$ [R/Ra=8±1; Allègre et al., 1995], while the ASW endmember has $Q/^3He = 6\times10^{15}$ ccSTPJ^{-1}, as determined from the mixing trend in Fig. 4.4, and $^4He/^3He = 722534$ (R/Ra=1). Radiogenic production of $^4He^*$ and heat will move the ASW value toward the crustal endmember [$Q/^3He = 10^{16}$, R/Ra=0.02; Kennedy et al., 2000; Fig. 4.5b]. This is defined as the "water aging" effect by Kennedy et al. [2000], as it corresponds to meteoric water accumulating radiogenic helium over time as the water flows along a particular flowpath.

Most of the Mexican geothermal fluids plot parallel to the x-axis with some notable exceptions (Fig. 4.5a). It is apparent that magma degassing, boiling and mixing with meteoric water are the three major mechanisms leading to most of the observed fractionations between heat and helium in these fluids. During magma degassing, $Q/^3He$ ratios will decrease as transfer of volatiles, including helium, is more effective than heat [Baker and Lupton, 1990; Lupton et al., 1999]. The $^3He/^4He$ ratios, however, will be not fractionated (data points on the left side of the DMM endmember; Fig. 4.5a). Data points to the right of DMM endmember can be the result of two processes occurring in the reservoir. Fluid samples plotting along a line parallel to the x-axis have $Q/^3He$ ratios higher than those of the DMM but also have an unfractionated DMM $^3He/^4He$

ratio. The only process with the potential to decrease the initial magmatic Q/^{3}He but not the helium isotopic ratio is boiling [e.g., Saby et al., 2020]. During boiling, ^{3}He will be preferentially removed

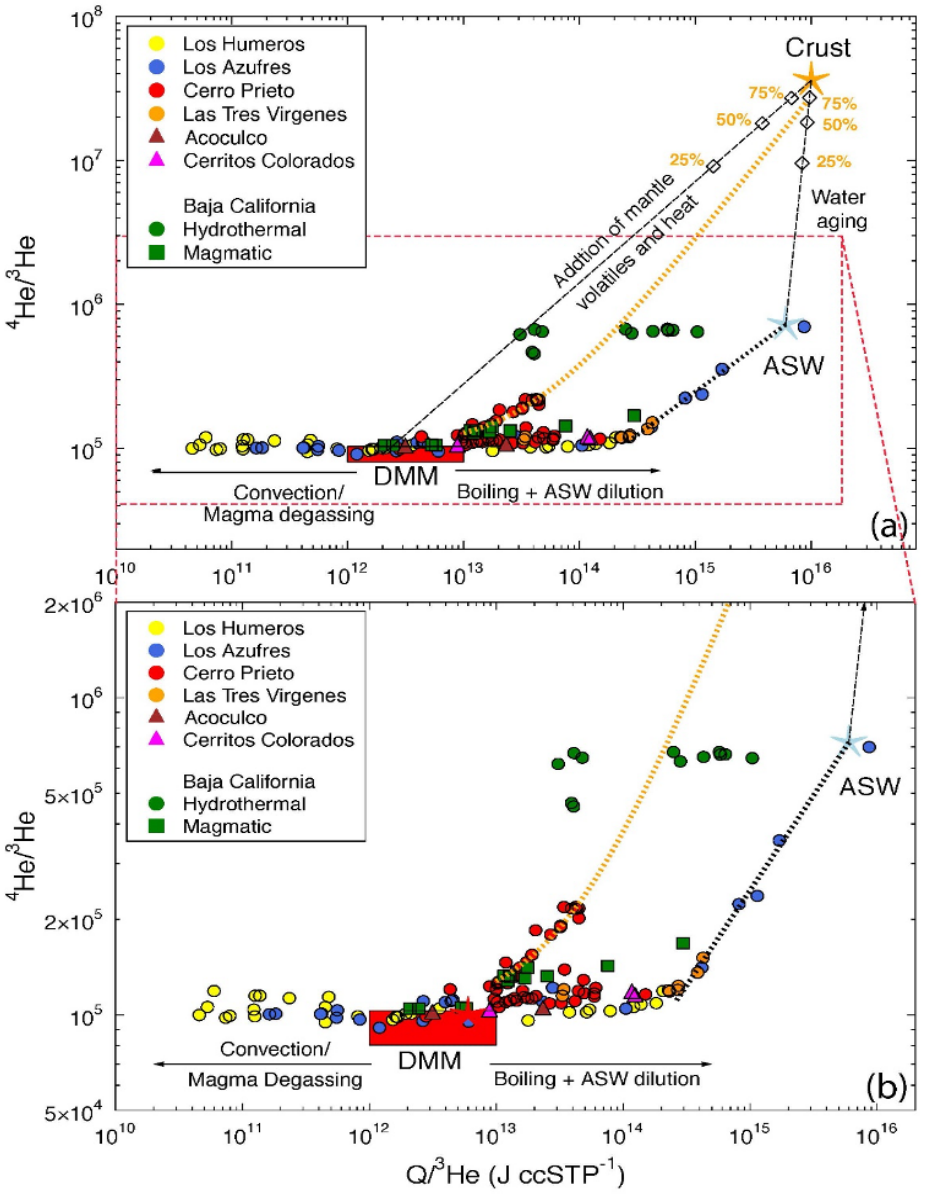

Figure 4.5 (a) The ^{4}He/^{3}He vs Q/^{3}He ratios of the Mexican geothermal fluids. Typical values for the crust, depleted mantle (DMM) and ASW endmembers are shown (see section 4.5.3 for endmember values); (**b**) zoom in to the vicinity of the DMM endmember. Theoretical mixing lines between DMM, the crust and meteoric water are shown as dashed lines, with the percentages of crustal contribution in the mixture indicated in yellow. The orange dotted line represents a binary mixing trend between the DMM and a mixture of ASW and crust with ~75%. crustal contribution. The binary mixing trend between the ASW endmember and the residual liquid phase after boiling is also shown as black dotted line. The extent of b) is indicated by the red dashed box in a). Symbols as in fig. 4.3.

with respect to heat from the boiled phase, leaving the residual liquid with $Q/^3He$ higher than the initial magmatic fluid. Most samples show an increase of the $Q/^3He$ value up to 3-5 x 10^{15} J ccSTP^{-1}, which roughly corresponds to 10-20% of vapor phase removed by boiling [Saby et al., 2020]. A few samples from Los Azufres and Las Tres Vírgenes deviate and seem to follow a mixing trend between a residual boiled phase and an ASW (meteoric water) endmember. Fluid from well AZ-2A in Los Azufres is known to be nearly pure re-injectate brine [Pinti et al., 2013; Nuñez-Hernández et al., 2020]. This is consistent with the ASW-like heat and air-like helium isotopic composition of this sample (Fig. 4.4).

As stated above, there are two notable exceptions to this general trend (Fig. 4.5a). Some of the Cerro Prieto and Baja California magmatic samples display elevated $^4He/^3He$ ratios, possibly due to crustal contributions [Fig. 4.5a, b; Pinti et al., 2019a]. The orange dotted line in figure 4.5a and b represents mixing between the mantle endmember and an ASW component affected by aging. It is apparent that those Cerro Prieto and Baja California magmatic samples with elevated $^4He/^3He$ ratios fall on this mixing line, indicating addition of radiogenic ^4He in these samples (Fig. 4.5b). This is consistent with the presence of fossil water in these reservoirs [cf. Fig. 4.3c, this study and Pinti et al., 2019a]. The hydrothermal samples from Baja California show a significant impact from meteoric water and potentially, also from the crust, as evidenced by their elevated $^4He/^3He$ ratios (Fig. 4.5b).

The presence of a complex mixture of magmatic, crustal and meteoric fluids is also illustrated by the distribution and fractionation between heat and helium (Figs 4.4 and 4.5). This should also be reflected in the content of other gases, such as CO_2, which is the dominant species in most Mexican geothermal systems [e.g., Poreda and Arnorssson, 1992].

4.5.4. Mixing of Geothermal Fluids and Heat as Revealed by CO_2, Noble gases and Heat Data

Figure 4.6 plots the $CO_2/^3He$ ratios as a function of their carbon isotopic ratios in CO_2 ($\delta^{13}C$-CO_2).

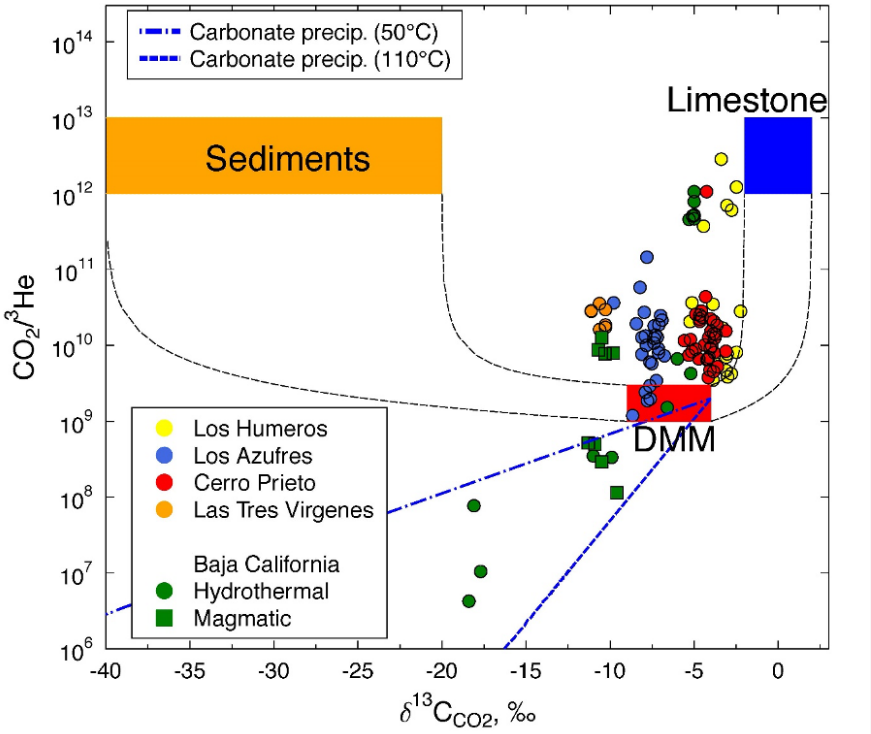

Figure 4.6 The $CO_2/^3He$ ratios of Mexican geothermal fluids vs the $\delta^{13}C$-CO_2. Endmember values of depleted mantle (DMM), the limestone and the organic-rich sediment endmembers from Sano and Marty [1995] are shown in red, blue and orange, respectively. Blue dashed lines represent fractionation caused by carbonate precipitation under 50°C and 110°C following Barry et al. [2020]. Symbols as in fig. 4.3.

Three distinct sources of carbon and helium are shown: a) the mantle (DMM) component with $\delta^{13}C$-CO_2 = -6.5 ± 2.5‰ and $CO_2/^3He$ ratio = $2 \pm 1 \times 10^9$ [Marty and Jambon, 1987; Sano and Marty, 1995; Marty and Tolstikhin, 1998]; b) limestone with $\delta^{13}C$-CO_2 = 0 ± 2‰ and $CO_2/^3He$ ratio = $0.1\text{-}1 \times 10^{13}$ [Sano and Marty, 1995] representing either thermal decomposition of local limestones [e.g., Pinti et al., 2021] or decarbonation of the marine limestones from the subducting slab [Sano and Williams, 1996; Mason et al., 2017]; and c) organic-rich sediments, with $\delta^{13}C$-CO_2 = -30 ± 10‰ and $CO_2/^3He$ ratio = $0.1\text{-}1 \times 10^{13}$ [Sano and Marty, 1995] also representing organic-matter rich subducting sediments along volcanic arcs. Most of the carbon in the Mexican

geothermal fluids appears to be a mixture of these three sources (Fig. 4.6). The fractions of each component in the can be estimated following Sano and Marty [1995]:

$$\delta^{13}C = M \times (\delta^{13}C)_M + S \times (\delta^{13}C)_S + L \times (\delta^{13}C)_L \quad (4.6)$$

$$\frac{^3He}{CO_2} = M \times (\frac{^3He}{CO_2})_M + S \times (\frac{^3He}{CO_2})_S + L \times (\frac{^3He}{CO_2})_L \quad (4.7)$$

$$M + S + L = 1 \quad (4.8)$$

Average compositions of each endmember used in the estimation are: mantle $CO_2/^3He$ = 2×10^9 and $\delta^{13}C\text{-}CO_2$ = -6.5‰; limestone $CO_2/^3He$ = 1×10^{13} and $\delta^{13}C\text{-}CO_2$ = 0‰; and sediments $CO_2/^3He$ = 1×10^{13} and $\delta^{13}C\text{-}CO_2$ = -30‰. The estimated percentages from each C sources are shown in Table C3, Appendix C. Results show that carbon sources in the Los Azufres field are dominated by limestone (8.93-98.86%), followed by the mantle contribution (1.14-82.64%), and finally, organic-rich sediments (0-31.44%). The carbon sources in the Los Humeros field are also dominated by limestone (42.18-95.51%), followed by mantle (0.05-57.30%), with sediments representing the lowest contribution (0-15.91%). Limestone is also the dominant carbon source in Cerro Prieto (44.58-94.58%), while mantle and sediments account for 0.17-53.04% and 0-14.87% of the carbon, respectively. Significant variations in the contribution from limestone (45.73-99.8%), mantle (0.14-47.15%) and sediments (0-34.97%) are found in the Baja California samples. Contributions from sediments are generally higher in Las Tres Vírgenes (31.75-35.55%). However, limestone remains the dominant contributor (54.85-60.44%), with significantly lower mantle carbon (5.61-12.40%). The dominant limestone's source for carbon in these geothermal fields is not surprising, being the subduction of old carbonate platforms, together with mantle carbon, the postulated main sources of carbon in volcanic-arc emissions [Mason et al., 2017]. However, the dominance of a limestone source for carbon in Cerro Prieto, within a spreading

center, is unexpected. This main limestone source for carbon can be resolved if part of the volatiles of these field are supplied by the old subducted Farallon plate [Batista-Cruz et al., 2019].

Some of the Baja California hydrothermal and magmatic samples plot outside of the three-component mixing domain, with both $\delta^{13}C\text{-}CO_2$ and $CO_2/^3He$ ratios lower than DMM (Fig. 4.6). The decrease in $CO_2/^3He$ and in $\delta^{13}C\text{-}CO_2$ values may result from the loss of mantle CO_2 due to the temperature-controlled precipitation of calcite in hydrothermal systems, first proposed by Ray et al. [2009]. In a CO_2-calcite system under relatively low temperature (<192°C), calcite is enriched in ^{13}C compared to CO_2. Thus, the precipitation of calcite in hydrothermal systems can lead to the removal of CO_2 in hydrothermal fluids and to preferential loss of ^{13}C, resulting in lower $\delta^{13}C\text{-}CO_2$ values [Ray et al., 2009; Güleç and Hilton, 2016]. The fractionation lines caused by calcite precipitation under 50 and 110°C are calculated following Barry et al. [2020] and are shown as blue dotted lines (Fig. 4.6). It is apparent that those Baja California samples that fall outside of the three-component domain fall between the two fractionation trends, suggesting calcite precipitation at shallow levels and relatively low temperatures (50-110°C), similar to the scenario suggested by Barry et al. [2020].

Calcite precipitation seems to be a shallower process that does not affect deeper geothermal fluids (Fig. 4.6). Only in Las Tres Vírgenes, calcite precipitate in large amounts in the borehole, but caused by the drop of pressure and not having consequences on the C isotopic ratios [Richard et al., 2019]. Indeed, none of the sampled deep fluids in geothermal wells show C fractionation that resulted from calcite precipitation (Fig. 4.6). This is an important finding that needs further investigation. In a carbon systematics study in deeply sourced springs along the Costa Rica forearc, Barry et al. [2019] showed that about 91% of carbon released from the Cocos plate and mantle is sequestered within the crust by calcite deposition. The total amount of sequestered carbon

corresponds to ~19% of the carbon that does not participate in recycling. In the Mexican section of the Cocos Plate, however, this is not observed and may result from a heterogeneous distribution of balances between C sources and sinks along volcanic arcs. This observation requires further investigation.

Based on Fig. 4.6, identification of potential contributions from ASW is challenging as the $\delta^{13}C$-CO_2 in atmospheric CO_2 [~7.6-7.8‰; Francey et al., 1999] is indistinguishable from the mantle value range (-6.5 ± 2.5‰), and the ASW $CO_2/^3He$ (3.76×10^9 – 7.84×10^9 from 10-25°C) [Smith and Kennedy, 1983] is also close to the mantle endmember value ($2 \pm 1 \times 10^9$).

To investigate the existence of all three components in the Mexican geothermal samples as well as the potential relationship between CO_2 and heat, $CO_2/^3He$ ratios are plotted as a function of the estimated $Q/^3He$ ratios (Fig. 4.7; Table C2). Except for samples from Los Humeros and Los Azufres that fall to the left of the DMM endmember due to magma degassing as previously discussed, it is apparent that most samples fall within the domain constrained by the average compositions of the crust, the DMM and ASW at 17°C (Fig. 4.7). If a $CO_2/^3He$ value range of 1×10^{12} - 1×10^{14} is considered for the crustal endmember as proposed by O'Nions and Oxburgh [1988], most samples to the right of the DMM endmember fall within the mixing area delimited by the magma and upper and lower boundaries of the crustal component (Fig. 4.7, orange shaded area).

The contribution from meteoric water is also apparent for some samples, those falling below the mixing line between the DMM and the lower crustal bound. Samples that display a potential contribution from meteoric water are those from Las Tres Vírgenes in Baja California, in addition to a few samples from the Los Humeros and Los Azufres. By contrast, none of the Cerro Prieto samples fall within this area. The absence of a meteoric water component in Cerro Prieto is

consistent with previous findings by Pinti et al. [2019a] who concluded that Cerro Prieto fluids received limited amounts of modern meteoric water. Lower $CO_2/^3He$ ratios in Baja California samples compared to mantle values are due to carbonate precipitation, as previously discussed.

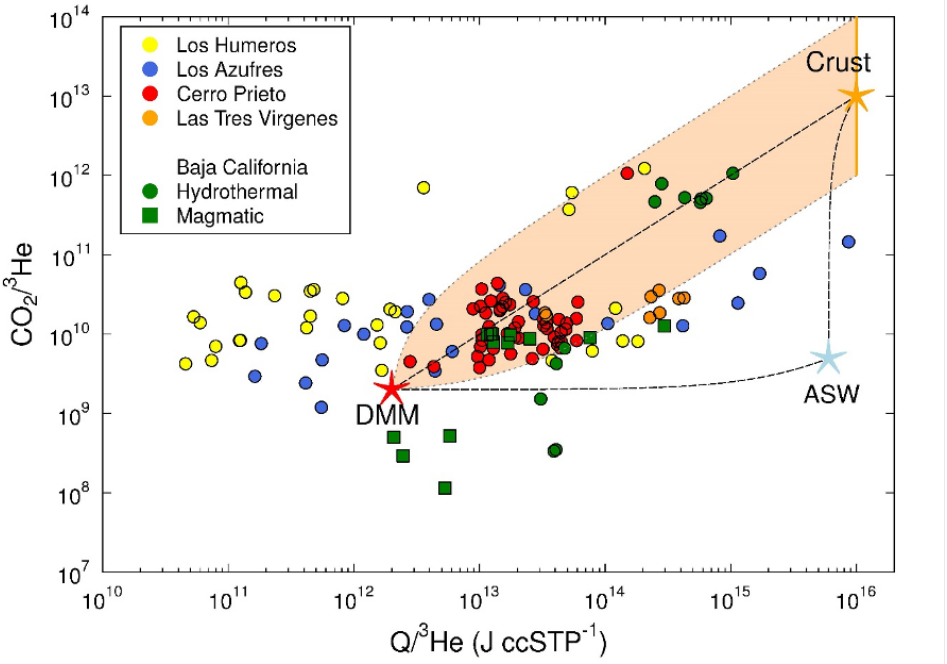

Figure 4.7 The $Q/^3He$ vs $CO_2/^3He$ ratios of Mexican geothermal fluids. The average compositions of depleted mantle (DMM), crust and ASW at 22˚C are shown, while black dashed lines indicate binary mixing between these three endmembers. Orange shaded area indicate the extent of mixing between magma and the upper/lower limits of the crustal component, with $CO_2/^3He$ ratios equal to 1×10^{12} and 1×10^{14} [Sano and Marty, 1995], respectively. Symbols as in fig. 4.3.

To quantitively evaluate the contribution of the mantle, crust and meteoric water components in these samples, measured R/Ra ratios are plotted as a function of: a) $CO_2/^3He$ ratios (Fig. 4.8a); and b) the $CO_2/^4He$ ratios (Fig. 4.8b). It is apparent that most samples fall within the domain constrained by DMM and the upper and lower bounds of the crustal component (orange shaded area; Figs. 4.8a, b). This mixing trend between the crustal and the DMM endmembers was not previously observed in hydrothermal systems [e.g., O'Nions and Oxburgh, 1988; Marty and Jambon, 1987; Poreda et al., 1988]. Sano et al. [1994] suggested that the original binary mixing pattern between the mantle and the crustal components in hydrothermal systems might be altered

by the physical and chemical properties of the hydrothermal fluids (e.g., temperature and pH). However, unlike those hydrothermal samples from hot springs and fumaroles previously analyzed [e.g., O'Nions and Oxburgh, 1988; Marty and Jambon, 1987; Poreda et al., 1988], most samples in this study are magmatic gases from deep production wells. It is thus likely that physical and chemical processes that lead to fractionation of CO_2 and He might occur only in shallow, relatively low temperature environments. Indeed, significant variations in CO_2/He ratios do exist in some samples from Baja California, where significant hydrothermal activity at shallow levels may take place [Batista-Cruz et al., 2019; Barry et al., 2020].

A few samples from the Los Humeros and Cerro Prieto show extremely high $CO_2/^3He$ or $CO_2/^4He$ ratios and fall outside of the DMM-crustal domain (orange shaded area, Fig. 4.8a, b). These are possibly the result of intense limestone decarbonation [e.g., O'Nions and Oxburgh, 1988] or solubility-controlled fractionation between CO_2 and He [Sano et al., 1994]. The fractions of each component in individual samples can be resolved based on simple mass balance equations:

$$\frac{R}{Ra} = M \times \left(\frac{R}{Ra}\right)_M + S \times \left(\frac{R}{Ra}\right)_S + L \times \left(\frac{R}{Ra}\right)_L \quad (4.9)$$

$$\frac{CO_2}{^4He} = M \times \left(\frac{CO_2}{^4He}\right)_M + S \times \left(\frac{CO_2}{^4He}\right)_S + L \times \left(\frac{CO_2}{^4He}\right)_L \quad (4.10)$$

$$M + S + L = 1 \quad (4.11)$$

where M, S, and L refer to the mantle (DMM), sediments, and limestones respectively. The $CO_2/^3He$ endmember value of the crustal component is set to its upper limit (1×10^{14}). The percentages of each component in the Mexican geothermal samples are listed in Table C3, Appendix C. It is apparent that samples from the Los Humeros and Los Azufres fields, in the TMVB, have generally higher fractions of the mantle contribution, averaging 85.8% and 79.1%, respectively. Samples from Baja California, including the Las Tres Vírgenes and the hydrothermal samples from Batista-Cruz et al. [2019], display the highest crustal content, averaging 12.2% and

25.9%, respectively. The highest meteoric water content appears in the Baja California samples. Overall, most of the CO_2 and helium present in the Mexican geothermal reservoirs have a mantle origin. Abundances of crustal and atmospheric components vary significantly and display clear spatial variations among each field.

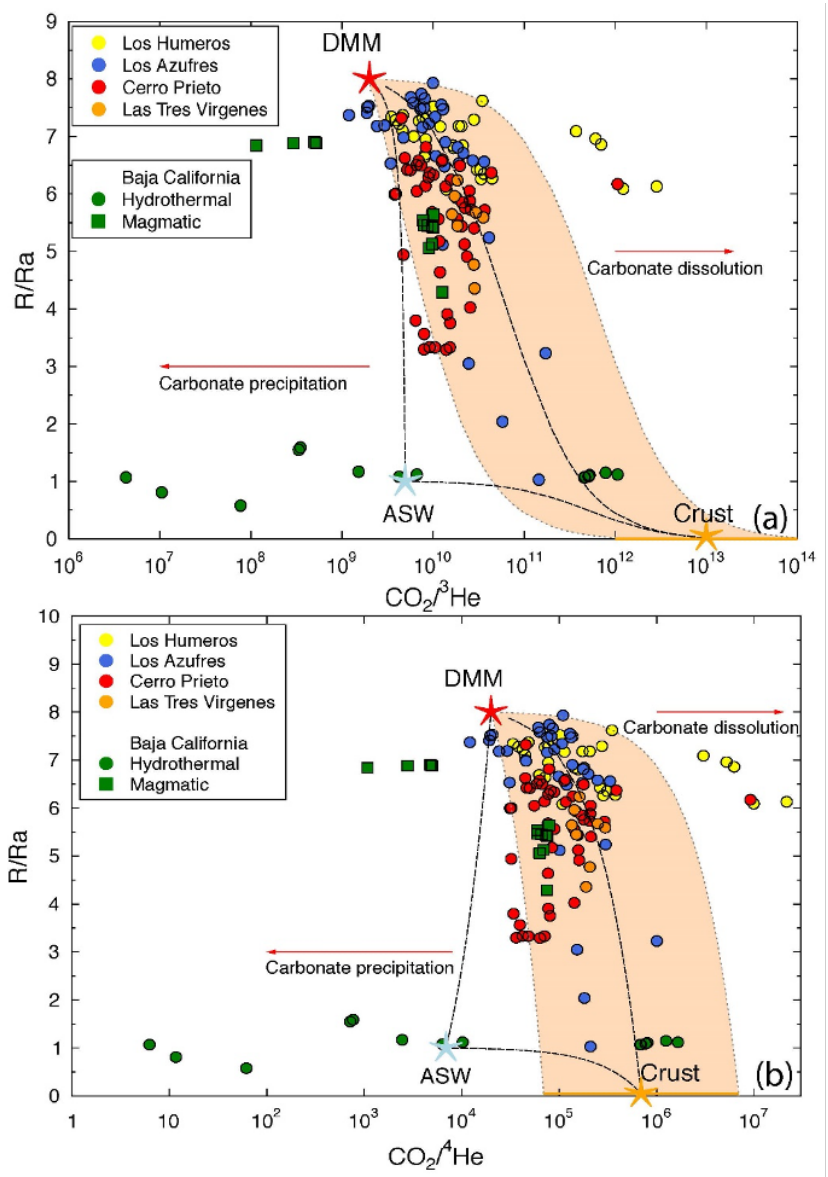

Figure 4.8 (a) $CO_2/^3He$ and (**b**) $CO_2/^4He$ ratios plotted as a function of R/Ra ratios measured in Mexican geothermal fluids. The average compositions of depleted mantle (DMM); crust and meteoric water at 22°C are shown. Black dashed lines indicate binary mixing between these three endmembers. Orange shaded area indicate the extent of mixing between magma and the upper/lower limits of the crustal component. Symbols as in Fig. 4.3.

4.5.5. Fractionation Between Heat and Volatile Species: Dependence on Magma Degassing?

From the discussion above, it is apparent that significant fractionation between heat and helium has occurred as evidenced by the wide range of $Q/^3He$ and noble gas ratios present in the different Mexican geothermal reservoirs (Figs. 4.4, 4.5a, b and 4.7). Samples that display lowered $Q/^3He$ ratios with respect to the mantle value (Fig. 4.4 and 4.5) are possibly the result of magma degassing, which could also lead to elevated He/Ar ratios due to their diffusivity differences as discussed in section 5.2. However, most samples display a relatively narrow $CO_2/^3He$ value range compared to the $Q/^3He$ and noble gas isotope ratios (e.g., $^4He/^{36}Ar$), without an indication of significant fractionation (Fig. 4.7).

Similar results were also reported in high temperature geothermal systems in Iceland, as relatively constant $CO_2/^3He$ ratios were found in both volcanically active and quiescent areas, although several orders of magnitude of difference should be expected based on solubility-controlled degassing models [Poreda and Arnórsson, 1992]. To exclude the potential impact from meteoric water, as discussed in previous sections, $CO_2/^3He$ ratios are plotted as a function of the air-corrected $^{40}Ar^*/^4He^*$ (Fig. 4.9). Crustal $^{40}Ar^*/^4He^*$ is calculated based on the production ratio of ^{40}Ar and ^4He in crustal rocks. These $^{40}Ar^*/^4He^*$ ratios vary between 0.167 and 0.5 [Ballentine et al., 2002], while mantle $^{40}Ar^*/^4He^*$ is determined based on MORB data [Ozima and Zashu, 1983; Sarda and Graham, 1990; Hiyagon et al., 1992] with values varying between 0.208 and 0.714.

It is apparent that most of the samples in the Mexican geothermal systems show a narrow range of $CO_2/^3He$ ratios ($\sim 10^9$ - 5×10^{10}), close to that of the mantle endmember, while displaying a wide range of $^{40}Ar^*/^4He^*$ ratios (~0.02 – 30; Fig. 4.9). In figure 4.9, three groups can be identified: 1) a large group with $CO_2/^3He$ ratios falling between the mantle and crustal endmembers and

$^{40}Ar^*/^4He^*$ ratios close to or lower than DMM values; 2) a group displaying $^{40}Ar^*/^4He^*$ ratios higher than the mantle endmember value, represented by samples from Baja California, Los Humeros and Cerro Prieto (red circle, Fig. 4.9), and; 3) a group displaying $CO_2/^3He$ ratios lower than DMM, represented by some Baja California samples (below the blue dotted line; Fig. 4.9). Among the first group, the Cerro Prieto and Las Tres Vírgenes samples display $^{40}Ar^*/^4He^*$ ratios within DMM values, and $CO_2/^3He$ ratios between the DMM and crustal endmembers, suggesting mixing between these two components (Fig. 4.9). The remainder of the samples, mostly from Los

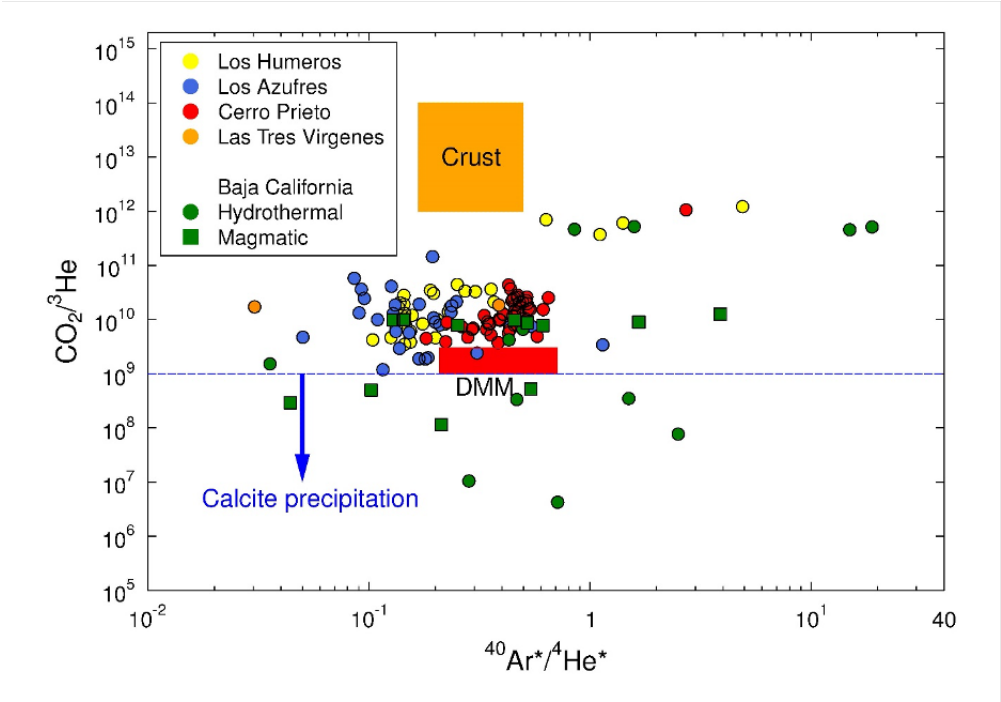

Figure 4.9 $CO_2/^3He$ ratios plotted as a function of air-corrected (terrigenic) $^{40}Ar^*/^4He^*$ ratios of the Mexican geothermal fluids. The depleted mantle endmember (DMM) and crust endmembers are shown. The extent of area affected by calcite precipitation is indicated by the blue arrow.

Humeros and Los Azufres, show $^{40}Ar^*/^4He^*$ ratios close or lower than the suggested DMM value range, but no correlation is observed between $^{40}Ar^*/^4He^*$ and $CO_2/^3He$ ratios (Fig. 4.9). All of the "magma degassing" samples in Fig. 4.7 belong to this group. If the fractionation between all volatile species during magma degassing is controlled by the solubility of each gas in silicate melt, a negative correlation should be expected between $^{40}Ar^*/^4He^*$ and $CO_2/^3He$ ratios as helium is

more soluble than CO_2 but less soluble than Ar [Lux, 1987; Pan et al., 1991]. Similarly, if diffusion is the dominating mechanism, a positive correlation should also be observed between both ratios as helium has higher diffusivity than both, CO_2 and Ar [Lux, 1987; Fisher, 1997]. Therefore, the absence of a correlation between $^{40}Ar^*/^4He^*$ and $CO_2/^3He$ ratios suggests that fractionation between CO_2 and helium is controlled by a different mechanism than that of fractionating He and Ar. Based on the lack of apparent $CO_2/^3He$ ratio variations in high temperature Icelandic hydrothermal fields, Poreda and Arnórsson [1992] suggested that CO_2 and ^3He may have very similar solubilities in basaltic melt. Alternatively, it is possible that the degassing process does not fractionate the two gas species. No conclusive determination could be made. Absence of apparent fractionation between ^3He and CO_2 during hydrothermal circulation was also reported in the East Pacific Rise [Resing et al., 2004]. Subsequently, Gonnermann and Mukhopadhyay [2007] proposed that helium degassing from melt is not limited by its diffusivity as helium is highly diffusive. Rather, the degassing of helium is likely controlled by the CO_2 content in the parental magma, as higher CO_2 abundance can dilute helium in the gas phase, reducing its partial pressure and causing more extensive degassing of mantle helium. Under this scenario, the release of helium and CO_2 is not determined by their respective solubilities or diffusivities, and thus, may not follow the fractionation pattern mentioned above. If the parental magmas have similar amounts of CO_2, then a consistent level of degassing should be expected for the mantle helium and therefore, a fairly uniform $CO_2/^3He$ ratio should be observed in the gas phase. On the other hand, degassing of Ne and Ar is limited by their diffusivities and thus, less efficient compared to helium, resulting in lowered He/Ne and He/Ar ratios. Another possible explanation for the lack of fractionation observed between CO_2 and helium is that, since limestone is the dominating contributor of CO_2 in

most samples, including those affected by magma degassing, the original fractionation pattern between CO_2 and helium may have been masked by the addition of non-mantle carbon dioxide.

As for the second group of samples (including the red circle, Fig. 4.9), their elevated $^{40}Ar^*/^4He^*$ ratios are possibly the result of solubility-controlled degassing and fractionation, since Ar is more soluble than He and exsolves less efficiently than helium [Burnard, 1999]. Most of these samples also display elevated $CO_2/^3He$ compared to the first group, which has been attributed to the decarbonation of limestone (see above). There may be a positive correlation in the remaining three samples from Baja California and Los Azufres, with elevated $^{40}Ar^*/^4He^*$ ratios but with $CO_2/^3He$ ratios close to those of group 1 (Fig. 4.9). However, due to the low number of samples, a definitive conclusion with respect to the presence of a correlation is not possible at this time. The last group of samples displays $CO_2/^3He$ ratios lower than the DMM, a result of calcite precipitation as discussed in the previous section. Their highly variable $^{40}Ar^*/^4He^*$ ratios may reflect the combined impact of solubility or diffusivity-controlled fractionation, as well as the contribution of meteoric water.

4.6. Conclusions

The combined study of six Mexican geothermal fields, from both the TMVB (Los Humeros, Los Azufres, Cerritos Colorados and Acoculco) and Baja California (Cerro Prieto and Las Tres Vírgenes) using published [Pinti et al., 2013, 2017, 2019a, 2019b; Wen et al., 2018; Batista-Cruz et al., 2019] and unpublished (this study) data, reveal the presence of heat and volatile species (noble gases and CO_2) from three distinct sources: the crust, the mantle and the atmosphere, and highlight general fractionation patterns between volatiles and heat. Significant differences are observed in helium isotopic ratios (R/Ra) between TMVB (7.14-7.27) and Baja California samples

(1.21-6.62), with TMVB samples displaying more pristine mantle signals. These differences reflect the presence of distinct tectonic settings, where the TMVB geothermal fields are directly impacted by active magma sources associated with subduction of the Cocos plate, while Baja California reservoirs are primarily affected by crustal contributions from the subducted fossil Farallon Plate, although the latter are currently located within spreading centers. The presence of a meteoric water component is suggested by low R/Ra ratios in Baja California hydrothermal samples (1.21-6.62), while the existence of a local crustal component is suggested in the Cerro Prieto samples as evidenced by the $^{3}He/^{40}Ar$ vs $^{4}He/^{40}Ar$ relationship. The relation between helium and CO_2 ($CO_2/^{3}He$) and carbon isotopic signature ($\delta^{13}C$) allows further identification of volatile sources in these fields. The most prominent feature observed across fields, whether they are located within a volcanic arc (TMVB) or spreading centers (Gulf of California) is the presence of varying amounts of mantle carbon sources (0.05% - 82.64%) as well as carbon originating from limestone (8.93% - 99.80%). Contribution of carbon from sediments is generally significantly smaller (0% - 35.55%). This is consistent with worldwide observations in arc-volcanic settings, where old carbonate platforms are subducted, adding carbonate C to volcanic emissions. Some of the Baja California samples display $CO_2/^{3}He$ ratios below mantle values, likely due to CO_2 loss from calcite precipitation. However, this process appears to solely affect near surface geothermal manifestations.

A combined analysis of the heat/helium ($Q/^{3}He$) relationship with noble gases ($^{4}He/^{36}Ar$) shows that the main mechanisms of transport during magma degassing for heat and magmatic volatiles at the magma/hydrothermal interface is convection. Boiling and dilution by meteoric water led to further fractionation of heat and volatiles. Magma degassing of volatile species (He and Ar) seems to be controlled by their diffusivities in melts, while convection transfers He more

rapidly than heat and Ar, fractionating the original mantle $Q/^3He$ ratios toward lower values and $^4He/^{36}Ar$ ratios toward higher values. The simultaneous presence of mantle, crust and meteoric water components is evidenced by the correlation between $Q/^3He$ and R/Ra ratios in fluids. A significant influence from the meteoric water endmember is observed in some of the Las Tres Vírgenes, Los Azufres and the Baja California hydrothermal samples, while a clear crustal contribution is found in Cerro Prieto and Baja California magmatic samples.

Systematic analysis of heat, noble gases and CO_2 in geothermal samples show how crust, mantle and meteoric water components affect heat and redistribute it within geothermal reservoirs. Although magma degassing and successive convective transport fractionate heat and noble gases (He and Ar), this seems not be the case for $CO_2/^3He$, as most fluids display a relatively narrow range of $CO_2/^3He$ ratios that display no correlation with $^{40}Ar^*/^4He^*$. The absence of significant fractionation in $CO_2/^3He$ ratios is an indication that helium degassing is controlled by the CO_2 content in parental magma, as higher CO_2 abundances can dilute helium in the gas phase, reducing its partial pressure and causing more extensive degassing of mantle helium. If the parental magmas have similar amounts of CO_2, a consistent level of degassing should be expected for mantle helium, and therefore, a fairly uniform $CO_2/^3He$ ratio should be in the gas phase. On the other hand, release of noble gases heavier than He is dependent on their diffusivities, leading to less extensive degassing of these noble gases, and therefore, lowered elemental ratios, including He/Ar ratios. It is also possible that the observed fractionation pattern between CO_2 and helium was modified by the addition of non-mantle carbon. However, further in-depth work is needed to better understand the mechanisms of degassing-related fractionation in geothermal systems. Overall, heat from magmatic sources is convectively transferred into the Mexican geothermal systems, while mixing

with multiple fluid components, boiling and chemical processes (e.g., calcite precipitation) lead to the redistribution and fractionation between heat and volatile species.

4.7. Acknowledgments

The staff of the Gerencia de Proyectos Geotermoeléctricos of the CFE is thanked for facilitating sample collection in the four geothermal fields within the years. This work was supported by CeMIEGeo (Centro Mexicano de Innovacion en Energia Geotermica), Grant No. 207032 SENER-CONACyT, Project 20. Work of DLP is supported with a Natural Sciences and Engineering Research Council of Canada (NSERC) Discovery Grant (RGPIN-2015-05378) and by Chinese Academy of Sciences President's International Fellowship Initiative (Grant No. 2020VMA0011). Financial support by the NSF Instrumentation & Facilities award EAR-1049822 to MCC, a Canadian Foundation for Innovation award 10621 to DLP was greatly appreciated.

4.8. References

Aguillón-Robles, A., Calmus, T., Benoit, M., Bellon, H., Maury, R.C., Cotten, J., Bourgois, J., and Michaud, F. (2001). Late Miocene adakites and Nb-enriched basalts from Vizcaino Peninsula, Mexico: indicators of east pacific rise subduction below southern Baja California? *Geology* 29, 531–534.

Allègre, C.J., Moreira, M., and Staudacher, T. (1995). $^{4}He/^{3}He$ dispersion and mantle convection. *Geophysical Research Letters* 22, 2325-2328.

Aragón-Aguilar, A., Izquíerdo-Montalvo, G., López-Blanco, S., and Arellano-Gómez, V. (2017). Analysis of heterogeneous characteristics in a geothermal area with low permeability and high temperature. *Geoscience Frontiers* 8, 1039–1050.

Arellano, V., García, A., Barragán, R., Izquíerdo, G., Aragón, A., and Nieva, D. (2003). An updated conceptual model of the Los Humeros geothermal reservoir (Mexico). *Journal of Volcanology and Geothermal Research* 124, 67–88.

Arellano, V.M., Barragán, R.M., Ramírez, M., López, S., Aragón, A., Paredes, A., Casimiro, E., and Reyes, L. (2015). Reservoir processes related to exploitation in Los Azufres (Mexico) geothermal field indicated by geochemical and production monitoring data. *International Journal of Geosciences* 6, 1048–1059.

Baker, E.T., and Lupton, J.E. (1990). Changes in submarine hydrothermal ^{3}He/heat ratios as an indicator of magmatic/tectonic activity. *Nature* 346, 556–558.

Ballentine, C. J., and Burnard, P.G. (2002). Production, release and transport of noble gases in the continental crust. *Review in Mineralogy and Geochemistry* 47, 481-538.

Ballentine, C. J., Burgess, R., and Marty, B. (2002). Tracing fluid origin, transport and interaction in the crust. *Review in Mineralogy and Geochemistry* 47, 539-614.

Barry, P.H., de Moor, J.M., Giovannelli, D. and 33 others (2019). Forearc carbon sink reduces long-term volatile recycling into the mantle. *Nature* 568, 487-492.

Barry, P.H., Negrete-Aranda, R., Spelz, R.M., Seltzer, A.M., Bekaert, D.V., Virrueta, C., and Kulongoski, J.T. (2020). Volatile sources, sinks and pathways: A helium-carbon isotope study of Baja California fluids and gases. *Chemical Geology* 550, 119722.

Batista, Cruz, R.Y., Rizzo, A.L., Grassa, F., Bernard, Romero, R., González, Fernández, A., Kretzschmar, T.G., and Gómez-Arias, E. (2019). Mantle degassing through continental crust triggered by active faults: The case of the Baja California Peninsula, Mexico. *Geochemistry, Geophysics, Geosystems* 20, 1912–1936.

Bellon, H., Aguillón-Robles, A., Calmus, T., Maury, R.C., Bourgois, J., and Cotten, J. (2006). La Purísima volcanic field, Baja California Sur (Mexico): Miocene to Quaternary volcanism related to subduction and opening of an asthenospheric window. *Journal of Volcanology and Geothermal Research* 152, 253–272.

Birkle, P., Portugal Marín, E., Pinti, D.L., and Castro, M.C. (2016). Origin and evolution of geothermal fluids from Las Tres Vírgenes and Cerro Prieto fields, Mexico - Co-genetic volcanic activity and paleoclimatic constraints. *Applied Geochemistry* 65, 36–53.

Boschman, L.M., and van Hinsbergen, D.J.J. (2016). On the enigmatic birth of the Pacific Plate within the Panthalassa Ocean. *Science Advance*s 2, e1600022.

Burnard, P. (2001). Correction for volatile fractionation in ascending magmas: noble gas abundances in primary mantle melts. *Geochimica et Cosmochimica Acta* 65, 2605–2614.

Burnard, P.G., Hu, R.Z., Turner, G., and Bi, X.W. (1999). Mantle, crustal and atmospheric noble gases in Ailaoshan gold deposits, Yunnan Province, China. *Geochimica et Cosmochimica Acta* 63, 1595–1604.

Burnard, P.G., and Polya, D.A. (2004). Importance of mantle derived fluids during granite associated hydrothermal circulation: He and Ar isotopes of ore minerals from Panasqueira. *Geochimica et Cosmochimica Acta* 68, 1607–1615.

Calmus, T., Pallares, C., Maury, R.C., Bellon, H., Pérez-Segura, E., Aguillón-Robles, A., Carreño, A.-L., Bourgois, J., Cotten, J., and Benoit, M. (2008). Petrologic diversity of Plio-Quaternary post-subduction volcanism in northwestern Mexico: an example from Isla San Esteban, Gulf of California. *Bulletin de la Société géologique de France* 179, 465–481.

Carrasco-Nūnez, G., Bernal, J.P., Dávila, P., Jicha, B., Giordano, G., and Hernández, J. (2018). Reappraisal of Los Humeros Volcanic complex by New U/Th Zircon and $^{40}Ar/^{39}Ar$ Dating: implications for Greater Geothermal potential. *Geochemistry, Geophysics, Geosystems* 19, 132–149.

Castro, M.C., Jambon, A., de Marsily, G., and Schlosser, P. (1998a). Noble gases as natural tracers of water circulation in the Paris Basin. 1. Measurements and discussion of their origin and mechanisms of vertical transport in the basin. *Water Resource Research* 34, 2443-2466.

Castro, M.C., Goblet, P., Ledoux, E., Violette, S., and de Marsily, G. (1998b). Noble gases as natural tracers of water circulation in the Paris Basin. 2. Calibration of a groundwater flow model using noble gas isotope data. *Water Resource Research* 34, 2467-2483.

Castro, M.C., Patriarche, D., and Goblet, P. (2005). 2-D numerical simulations of groundwater flow, heat transfer and 4He transport — implications for the He terrestrial budget and the mantle helium–heat imbalance. *Earth and Planetary Science Letters* 237, 893–910.

Cedillo Rodríguez, F. (2000). Hydrogeologic model of the geothermal reservoirs from Los Humeros, Puebla, Mexico. Proc. World Geothermal Congress 2000, Kyushu - Tohoku, Japan, May 28–June 10, p. 6.

Cid, H.E., Carrasco-Nuñez, G., Manea, V.C., Vega, S., and Castaño, V. (2021). The role of microporosity on the permeability of volcanic-hosted geothermal reservoirs: a case study from Los Humeros, Mexico. *Geothermics* 90, 102020.

Clarke, W. B., Jenkins, W. J., Top, Z. (1976). Determination of tritium by mass spectrometric measurement of ^{3}He. *The International Journal of Applied Radiation and Isotopes* 27, 515-522.

De la Cruz, M.V. (1983). Estudio geológico a detalles de la zona geotérmica de Los Humeros, Pue. CFE Internal Report 10/83.

Elders, W.A., Bird, D.K., Williams, A.E., and Schiffman, P. (1984). Hydrothermal flow regime and magmatic heat source of the Cerro Prieto geothermal system, Baja California, Mexico. *Geothermics* 13, 27-47.

Ferrari, L., Orozco-Esquivel, T., Manea, V., and Manea, M. (2012). The dynamic history of the Trans-Mexican Volcanic Belt and the Mexico subduction zone. *Tectonophysics* 522–523, 122–149.

Fisher, D.E. (1997). Helium, argon, and xenon in crushed and melted MORB. *Geochimica et Cosmochimica Acta* 61, 3003–3012.

Francey, R.J., Allison, C.E., Etheridge, D.M., Trudinger, C.M., Enting, I.G., Leuenberger, M., Langenfelds, R.L., Michel, E., and Steele, L.P. (1999). A 1000-year high precision record of $\delta^{13}C$ in atmospheric CO_2. *Tellus* 51B, 170-193.

Gando, A., Gando, Y., Ichimura, K., and 64 others (2011). Partial radiogenic heat model for Earth revealed by geoneutrino measurements. *Nature Geoscience* 4, 647-651.

Garcia-Estrada, G., López-Hernandez, A., and Prol-Ledesma, R.M. (2001). Temperature–depth relationships based on log data from the Los Azufres geothermal field, Mexico. *Geothermics* 30, 111–132.

Gautheron, C., and Moreira, M. (2002). Helium signature of the subcontinental lithospheric mantle. *Earth and Planetary Science Letters* 199, 39-47.

Gonnermann, H.M., and Mukhopadhyay, S. (2007). Non-equilibrium degassing and a primordial source for helium in ocean-island volcanism. *Nature* 449, 1037-1040.

Güleç, N., and Hilton, D.R. (2016). Turkish geothermal fields as natural analogues of CO_2 storage sites: Gas geochemistry and implications for CO_2 trapping mechanisms. *Geothermics* 64, 96–110.

Gutiérrez-Negrín, L.C.A. (1988). The La Primavera, Jalisco, Mexico, geothermal field. *GRC Transaction* 12, 161-165.

Gutiérrez-Negrín, L.C.A. (2015). Cerro Prieto, Mexico - A convective extensional geothermal play. *GRC Transaction* 39, 711–716.

Gutiérrez-Negrín, L.C.A., Canchola Félix, I., Romo-Jones, J.M., and Quijano-León, J.L. (2020). Geothermal energy in Mexico: update and perspectives. Proceeding World Geothermal Congress 2020, Reykjavik, Iceland, April-October 2020.

Hilton D.R., and Porcelli D. (2003). Noble gases as mantle tracers. In *Treatise on Geochemistry* (eds. H.D. Holland and K.K. Turekian). Pergamon Press, Vol. 2, 277-318.

Hilton, D.R., Fischer, T.P., and Marty, B. (2002). Noble gases and volatile recycling at subduction zones. *Review in Mineralogy and Geochemistry* 47, 319–370.

Hiyagon, H., Ozima, M., Marty, B., Zashu, S., and Sasaki, H. (1992). Noble gases in submarine glasses from mid-oceanic ridges and Loihi seamount: Constraints on the early history of the Earth. *Geochimica et Cosmochimica Acta* 56, 1301–1316.

Izquíerdo, G., Gutiérrez-Negrín, L.C.A., and Aragón, A. (2009). Considerations on the origin of acid fluids in Los Humeros geothermal field, Pue., Mexico. *GRC Transaction* 33, 59–62.

Kennedy, B.M., and Shuster, D.L. (2000). Noble Gases: sensitive natural tracers for detection and monitoring injectate returns to geothermal reservoirs. *GCR Transaction* 24, 247-252.

Kennedy, B.M., Fischer, T.P., and Schuster, D.L. (2000). Heat and helium in geothermal systems. Twenty-Fifth Workshop on Geothermal Reservoir Engineering. SGP-TR-165. Stanford University, Stanford, California, p. 5.

Kennedy, B.M., and Truesdell, A.H. (1996). The northwest geysers high-temperature reservoir: evidence for active magmatic degassing and implications for the origin of the Geysers geothermal field. *Geothermics* 25, 365–387.

Kennedy, B.M., and van Soest, M.C. (2006). A helium isotope perspective on the Dixie Valley, Nevada, hydrothermal system. *Geothermics* 35, 26–43.

Lippmann, M.J., Truesdell, A.H., Halfman-Dooley, S.E., and Mañon M, A. (1991). A review of the hydrogeologic-geochemical model for Cerro Prieto. *Geothermics* 20, 39-52.

Lonsdale, P. (1989). Segmentation of the Pacific–Nazca spreading center 1°N–20°S. *Journal of Geophysical Research* 94, 12197– 12225.

Lonsdale, P. (2005). Creation of the Cocos and Nazca plates by fission of the Farallon plate. *Tectonophysics* 404, 237–264.

López-Hernández, A., Garcia-Estrada, G.H., Arellano Guadarrama, J.F. (1995). Geothermal exploration at Las Tres Vírgenes, B.C.S. Mexico. Proc. World Geothermal Congress, Florence, Italy, pp. 707–712.

López-Hernández, A., Garcia-Estrada, G., Aguirre-Díaz, G., González-Partida, E., Palma-Guzmán, H., and Quijano-León, J.L. (2009). Hydrothermal activity in the Tulancingo–Acoculco Caldera Complex, central Mexico: Exploratory studies. *Geothermics* 38, 179-293.

Lucci, F., Carrasco-Núñez, G., Rossetti, F., Theye, T., White, J.C., Urbani, S., Azizi, H., Asahara, Y., and Giordano, G. (2020). Anatomy of the magmatic plumbing system of Los Humeros Caldera (Mexico): implications for geothermal systems. *Solid Earth* 11, 125–159.

Lupton, J.E. (1979). Helium-3 in the Guaymas Basin: Evidence for injection of mantle volatiles in the Gulf of California. *Journal of Geophysical Research* 84, 7446-7456.

Lupton, J.E., Baker, E.T., and Massoth, G.J. (1989). Variable ^{3}He/heat ratios in submarine hydrothermal systems: evidence from two plumes over the Juan de Fuca ridge. *Nature* 337, 161–164.

Lupton, J.E., Baker, E.T., and Massoth, G.J. (1999). Helium, heat, and the generation of hydrothermal event plumes at mid-ocean ridges. *Earth and Planetary Science Letters* 171, 343–350.

Lux, G. (1987). The behavior of noble gases in silicate liquids: Solution, diffusion, bubbles and surface effects, with applications to natural samples. *Geochimica et Cosmochimica Acta* 51, 1549–1560.

Macías, J. L., and Jiménez-Salgado, E. (2013). Estudio de estratigrafía y geología del Complejo Volcánico Tres Vírgenes. BCS. *Geotermia* 26, 14-23.

Magro, G., Ruggieri, G., Gianelli, G., Bellani, S., and Scandiffio, G. (2003). Helium isotopes in paleofluids and present-day fluids of the Larderello geothermal field: Constraints on the heat source. *Journal of Geophysical Research* 108, ECV 3-1 – 3-12.

Martel, D.J., Déak, J., Dövenyi, P., Horvàth, F., O'Nions, R.K., Oxburgh, E.R., Stegena, L., and Stute, M. (1989). Leakage of helium from the Pannonian basin. *Nature* 342, 908-912.

Marty, B., and Jambon, A. (1987). C/He-3 in volatile fluxes from the solid earth – implications for carbon geodynamics. *Earth and Planetary Science Letters* 83, 16–26.

Marty, B., and Tolstikhin, I.N. (1998). CO_2 fluxes from mid-ocean ridges, arcs and plumes. *Chemical Geology* 145, 233–248.

Marty, B., Torgersen, T., Meynier, V., O'Nions, R.K., and de Marsily, G. (1993). Helium isotope fluxes and groundwater ages in the Dogger aquifer, Paris Basin. *Water Resource Research* 29, 1025–1036.

Mason, E., Edmonds, M., and Turchyn, A.V. (2017). Remobilization of crustal carbon may dominate volcanic arc emissions. *Science* 357, 290-294.

Matsuda, J., and Marty, B. (1995). The ^{40}Ar/^{36}Ar ratio in the undepleted mantle: a reevaluation. *Geophysical Research Letters* 22, 1937–1940.

Mazor, E., and Truesdell, A. (1984). Dynamics of a geothermal field traced by noble gases: Cerro Prieto, Mexico. *Geothermics* 13, 91–102.

Moeck, I., and Beardsmore, G. (2014). A new 'geothermal play type' catalog: Streamlining exploration decision making. Proc. Thirty-Ninth Workshop on Geothermal Reservoir Engineering Stanford University, Stanford, California, February 24-26. SGP-TR-202.

Nuñez-Hernández, S., Pinti, D.L., López-Hernández, A., Shouakar-Stash, O., Martínez-Cinco, M.A., Abuharara, A., Eissa, M.A., Castro, M.C., and Ramírez-Montes, M. (2020). Phase

segregation, boiling, and reinjection at the Los Azufres Geothermal Field, Mexico, monitored by water stable isotopes, chloride, and enthalpy. *Journal of Volcanology and Geothermal Research* 390, 106751.

O'Nions, R.K., and Oxburgh, E.R. (1983). Heat and helium in the Earth. *Nature* 306, 429-431.

Oxburgh, E.R., and O'Nions, R.K. (1987). Helium loss, tectonics, and terrestrial heat budget. *Science* 237, 1583-1588.

O'Nions, R.K., and Oxburgh, E.R. (1988). Helium, volatile fluxes and the development of continental crust. *Earth and Planetary Science Letters* 90, 331–347.

Oxburgh, E.R., O'Nions, R.K., and Hill, R.I. (1986). Helium isotopes in sedimentary basins. *Nature* 324, 632–635.

Ozima, M., and Zashu, S. (1983). Noble gases in submarine pillow volcanic glasses. *Earth and Planetary Science Letters* 62, 24–40.

Ozima, M., and Podosek, F.A. (2002). Noble gas geochemistry (2nd ed). Cambridge Univ. Press.

Pandarinath, K., and Domínguez-Domínguez, H. (2015). Evaluation of the solute geothermometry of thermal springs and drilled wells of La Primavera (Cerritos Colorados) geothermal field, Mexico: A geochemometrics approach. *Journal of South American Earth Sciences* 62, 109-124.

Pan, V., Holloway, J.R., and Hervig, R.L. (1991). The pressure and temperature dependence of carbon dioxide solubility in tholeiitic basalt melts. *Geochimica et Cosmochimica Acta* 55, 1587–1595.

Pérez, H., Macías, J.L., Garduño, V.H., Arce, J.L., García, F., Castro, R., Layer, P., Saucedo, R., Martínez, C., Jiménez, A., Valdes, G., Meriggi, L., and Hernández, R. (2010). Estudio vulcanológico y structural de la secuencia estratigráfica Mil Cumbres y del campo geotérmico de Los Azufres, Mich. *Geotermia* 23, 51-63.

Pinti, D.L., and Marty, B. (1998). The origin of helium in deep sedimentary aquifers and the problem of dating very old groundwaters. *Geological Society, London Specical Publication* 144, 53–68.

Pinti, D.L., Castro, M.C., Shouakar-Stash, O., Tremblay, A., Garduño, V.H., Hall, C.M., Hélie, J.-F., and Ghaleb, B. (2013). Evolution of the geothermal fluids at Los Azufres, Mexico, as traced by noble gas isotopes, $\delta^{18}O$, δD, $\delta^{13}C$ and $^{87}Sr/^{86}Sr$. *Journal of Volcanology and Geothermal Research* 249, 1–11.

Pinti, D.L., Castro, M.C., López-Hernandez, A., Han, G., Shouakar- Stash, O., Hall, C.M., and Ramírez-Montes, M. (2017). Fluid circulation and reservoir conditions of the Los Humeros Geothermal Field (LHGF), Mexico, as revealed by a noble gas survey *Journal of Volcanology and Geothermal Research* 333–334, 104–115.

Pinti, D.L., Castro, M.C., López-Hernández, A., Hernández Hernández, M.A., Richard, L., Hall, C.M., Shouakar-Stash, O., Flores-Armenta, M., Rodríguez-Rodríguez, M.H. (2019a).

Cerro Prieto Geothermal Field (Baja California, Mexico) – A fossil system? Insights from a noble gas study. *Journal of Volcanology and Geothermal Research* 371, 32–45.

Pinti, D.L., Castro, M.C., López-Hernández, A., Hernández Hernández, M.A., Shouakar-Stash, O., Richard, L., Nuñez-Hernández, S., Hall, C.M., and Ramírez-Montes, M. (2019b). Signature of ongoing brine reinjection on noble gas isotopes and fluid chemistry at Las Tres Vírgenes geothermal field, Mexico. *Journal of Volcanology and Geothermal Research* 377, 33–42.

Pinti, D.L., Castro, M.C., López-Hernández, A., Hernández-Hernández, M.A., Shouakar-Stash, O., Hall, C.M., Bahena-Romero, J., and Ramírez-Montes, M. (2021). Origin of volatile species and aqueous fluids in the Los Humeros Geothermal Field, Mexico. Chemical Geology 584, 120539.

Polak, B.G., Kononov, V.I., Prasolov, E.M., I.V., S., Prol-Ledesma, R.M., González, A., Razo, A. and Molina-Berbeller, R. (1985). First estimations of terrestrial heat flow in the TMVB and adjacent areas based on isotopic composition of natural helium. *Geofisica Internacional* 24, 465-476.

Polyak, B.G. (2005). Heat and mass transfer from the mantle: heat flow and He-isotope constraints. Annales Geophysicae 48, 9-17.

Polyak, B.G., and Tolstikhin, I.N. (1985). Isotopic composition of the Earth's helium and the motive forces of tectogenesis. *Chemical Geology* 52, 9-33.

Polyak, B.G., Tolstikhin, I.N., and Yakutseni, V.P. (1979). Helium isotope composition and heat flow as geochemical and geophysical aspects of tectogenesis, *Geotektonika*, 5, 3-23 (in Russian).

Polyak, B.G., Tolstikhin, I.N., Kamenskii, I.N., Yakovlev, L.E., Marty, B., and Cheshko, A.L. (2000). Helium isotopes, tectonics and heat flow in the Northern Caucasus. *Geochimica et Cosmochimica Acta* 64, 1925-1944.

Poreda, R., and Craig, H. (1989). Helium isotope ratios in circum-Pacific volcanic arcs. *Nature* 338, 473-478.

Poreda, R.J., and Arnórsson, S. (1992). Helium isotopes in Icelandic geothermal systems: II. Helium-heat relationships. *Geochimica et Cosmochimica Acta* 56, 4229–4235.

Poreda, R.J., Jeffrey, A.W. A., Kaplan I.R., and Craig, H. (1988). Magmatic helium in subduction-zone natural gases. *Chemical Geology* 71,199-210.

Portugal, E., Izquíerdo, G., Truesdell, A.H., and Alvarez, J. (2005). The geochemistry and isotope hydrology of the southern Mexicali Valley in the area of the Cerro Prieto, Baja California, Mexico, geothermal field. *Journal of Hydrology* 313, 132–148.

Prol-Ledesma, R.M., and Morán-Zenteno, D.J. (2019). Heat flow and geothermal provinces in Mexico. *Geothermics* 78, 183–200.

Prol-Ledesma, R.M., Arango-Galván, C., and Torres-Vera, M.-A. (2016). Rigorous analysis of available data from Cerro Prieto and Las Tres Vírgenes geothermal fields with calculations for expanded electricity generation. *Natural Resources Research* 25, 445-458.

Ray, M.C., Hilton, D.R., Muñoz, J., Fischer, T.P., and Shaw, A.M. (2009). The effects of volatile recycling, degassing and crustal contamination on the helium and carbon geochemistry of hydrothermal fluids from the Southern Volcanic Zone of Chile. Chemical Geology 266, 38–49.

Resing, J.A, Lupton, J.E., Feely, R.A., and Lilley, M.D. (2004). CO_2 and ^3He in hydrothermal plumes: implications for mid-ocean ridge CO_2 flux. *Earth and Planetary Science Letters* 226, 449– 464

Richard, L., Pinti, D.L., Hélie, J.-F., Hernández, A.L., Shibata, T., Castro, M.C., Sano, Y., Shouakar-Stash, O., and Sandoval-Medina, F. (2019). Variability of deep carbon sources in Mexican geothermal fluids. *Journal of Volcanology and Geothermal Research* 370, 1–12.

Saby, M., Pinti, D.L., van Hinsberg, V., Gautason, B., Sigurðardóttir, Á., Castro, C., Hall, C., Óskarsson, F., Rocher, O., Hélie, J.-F., and Méjean, P. (2020). Sources and transport of fluid and heat at the newly-developed Theistareykir Geothermal Field, Iceland. *Journal of Volcanology and Geothermal Research* 405, 107062.

Sandoval-Velasquez, A., Rizzo, A.L., Frezzotti, M.L., Saucedo, R., and Aiuppa, A. (2021). The composition of fluids stored in the central Mexican lithospheric mantle: Inferences from noble gases and CO_2 in mantle xenoliths. *Chemical Geology* 576, 120270.

Sano, Y., and Marty, B. (1995). Origin of carbon in fumarolic gas from island arcs. *Geology* 119, 265-274.

Sano, Y., and Williams S.N. (1996). Fluxes of mantle and subducted carbon along convergent plate boundaries. *Geophysical Research Letters* 23, 2749-2752.

Sano, Y., Hirabayashi, J.-I., Oba, T., and Gamo, T. (1994). Carbon and helium isotopic ratios at Kusatsu-Shirane Volcano, Japan. *Applied Geochemistry* 9, 371–377.

Sano, Y., Takahata, N., and Seno, T. (2006). Geographical distribution of $^3He/^4He$ ratios in the Chugoku district Southwestern Japan. *Pure and Applied Geophysics* 163, 745–757.

Sarda, P., and Graham, D. (1990). Mid-ocean ridge popping rocks: Implications for degassing at ridge crests. *Earth and Planetary Science Letters* 97, 268–89.

Schmitt, A.K., Martín, A., Weber, B., Stockli, D.F., Zou, H., and Shen, C.-C. (2013). Oceanic magmatism in sedimentary basins of the northern Gulf of California rift. *GSA Bulletin* 125, 1833–1850.

Schmitt, A.K., Stockli, D.F., Niedermann, S., Lovera, O.M., and Hausback, B.P. (2010). Eruption ages of Las Tres Vírgenes volcano (Baja California): a tale of two helium isotopes. Quarter. *Geochronology* 5, 503–511.

Smith, A.D. (2007). A plate model for Jurassic to recent intraplate volcanism in the Pacific ocean basin, in plates, plumes and planetary processes (eds., G.R. Foulger, D.M. Jurdy). GSA Special Paper 430, 471–495.

Smith, S.P., and Kennedy, B.M. (1983). The solubility of noble gases in water and NaCl brine. *Geochimica et Cosmochimica Acta* 47, 503–515.

Straub, S.M., Gomez-Tuena, A., Stuart, F.M., Zellmer, G.F., Espinasa-Perena, R., Cai, Y., and Iizuka, Y. (2011). Formation of hybrid arc andesites beneath thick continental crust. *Geochimica et Cosmochimica Acta* 303, 337–347.

Suárez-Vidal, F., Mendoza-Borunda, R., Nafarrete-Zamarripa, L.M., Rámirez, J., and Glowacka, E. (2008). shape and dimensions of the Cerro Prieto pull-apart basin, Mexicali, Baja California, Mexico, based on the regional seismic record and surface structures. *International Geology Review* 50, 636–649.

Tello-Hinojosa E, Verma MP, and González-Partida E., (2005). Geochemical characteristics of reservoir fluids in the Las Tres Vírgenes, BCS, México. Proc. World Geothermal Congress 2005. Antalya, Turkey, 24-29 April 2005.

Torres-Rodríguez, M.A., Mendoza-Covarrubias, A., and Medina-Martínez, M. (2005). An update of the Los Azufres geothermal field, after 21 years of exploitation. Proc. World Geothermal Congress 2005. Antalya, Turkey, 24-29 April 2005

Turner, G., Burnard, P., Ford, J.L., Gilmour, J.D., Lyon, I.C., and Stuart, F.M. (1993). Tracing fluid sources and interactions. Phil. Trans. Royal Soc. London A 344, 127-140

Vengas, S., Ramírez, G., Romero, C., Reyes, P., Razo, A., and Arellano, F. (1991). La Primavera geothermal field, Jalisco, in The Geology of North America Vol. P-3, Economic Geology, Mexico (ed., Salas, G.P.).

Verma, S.P. (1985). On the magma chamber characteristics as inferred from surface geology and geochemistry: examples from Mexican geothermal areas. *Physics of the Earth and Planetary Interiors* 41, 207–214.

Wang, Y., Forsyth, D.W., Rau, C.J., Carriero, N., Schmandt, B., Gaherty, J.B., and Savage, B. (2013). Fossil slabs attached to unsubducted fragments of the Farallon plate. *Proceedings of the National Academy of Sciences* 110, 5342–5346.

Wen, T., Pinti, D.L., Castro, M.C., López-Hernández, A., Hall, C.M., Shouakar-Stash, O., and Sandoval-Medina, F. (2018). A noble gas and $^{87}Sr/^{86}Sr$ study in fluids of the Los Azufres geothermal field, Mexico – Assessing impact of exploitation and constraining heat sources. *Chemical Geology* 483, 426–441.

CHAPTER 5

Summary and Conclusions

This final chapter summarizes the major findings of previous chapters, in addition to providing an overall conclusion of this dissertation.

5.1. Summary of Major Results

Chapter 2: This chapter presents a noble gas study of natural gas samples from the Panhandle and Hugoton Fields (PHF), to investigate the composition, sources and migration of both hydrocarbons and noble gases in the PHF. PHF samples are generally enriched in terrigenic noble gases (^{4}He*, ^{21}Ne* and ^{40}Ar*). A positive correlation between terrigenic noble gases (^{4}He* and ^{21}Ne*) and methane is observed in the west Panhandle Field, suggesting that both are produced and/or transported together from adjacent basins in the west, e.g., Palo Duro and Dalhart basins. By contrast, east Panhandle samples display no correlation between methane and terrigenic noble gases. Instead, a positive correlation between terrigenic noble gases and depth is apparent, suggesting a dominant upward flux from underlying strata and basement rocks. A combined analysis of the He and Ne isotopic compositions reveal the presence of a primordial, OIB-type mantle component in the east Panhandle Field, likely originating in the mantle plume associated with the Wichita Igneous Province. However, an origin in the SCLM cannot be ruled out. The west Panhandle samples display both mantle helium and CO_2 contents higher than those in east

Panhandle, suggesting contributions originating in the Bravo Dome field. The observed correlations between $^{4}He^{*}/^{40}Ar^{*}$ and $^{21}Ne^{*}/^{40}Ar^{*}$ in the PHF samples shows that all samples have solubility-controlled fractionation patterns similar to the crustal components, suggesting an external input from crustal sources. A first-order estimation of $^{4}He^{*}$ and $^{40}Ar^{*}$ production shows that in the west Panhandle and Hugoton Fields, in-situ contributions of $^{4}He^{*}$ vary from 5.11% to 21.76%, and from 9.15% to 26.46% for $^{40}Ar^{*}$. In the east Panhandle Field, the contributions vary from 28.53% to 65.46% for $^{4}He^{*}$, and from 21.22% to 78.79% for $^{40}Ar^{*}$. ^{40}Ar relative ages are increasingly older from east Panhandle to Kansas Hugoton to west Panhandle, Texas and Oklahoma Hugoton. More interaction with groundwater in West Panhandle, Texas and Oklahoma Hugoton gas results in higher Vw/Vg ratios and higher concentrations of terrigenic noble gases, likely being collected by groundwater from adjacent basins. The relatively low Vw/Vg ratios and terrigenic noble gas contents in east Panhandle samples are consistent with the shortest migration distance, youngest migration ages and absence of significant groundwater flow in this area. These findings confirm that noble gases are excellent tracers in fingerprinting the sources and migration of subsurface fluids in conventional hydrocarbon systems.

Chapter 3: This chapter presents a comprehensive noble gas study of shale gas samples from the unconventional Eagle Ford Shale play in southwest Texas, to explore the tectonic and magmatic history of the region, as well as how fault-fracture networks and deep crustal structures may have affected the formation and evolution of its hydrocarbon reservoirs. All noble gases reveal the presence of a crustal component, and a positive correlation between methane and crustal noble gases, suggesting a common origin for both. Two outliers fall above the observed trend with significantly higher crustal noble gas contents compared to those collected from the same wells, suggesting the existence of different hydrocarbon sources, and interconnectivity between

reservoirs either through faults or fracture systems. A combined in-depth analysis of He and Ne isotopic compositions reveals the presence of two distinct mantle endmembers in most samples. A primordial, solar-like mantle component is observed in the north and west portions of the shale play in southwest Texas, likely originating in a shallow refractory reservoir in the SCLM underneath the Laurentian craton. A solar-like signature possibly entered the shale reservoir during late Cretaceous volcanic activity or during reactivation of major fault systems in the Miocene. On the other hand, a mantle signature corresponding to a MORB component is observed in the center of the study area, suggesting the presence of an old rift system, with a SW-NE orientation. This MORB-defined rift likely corresponds to the Ouachita Rift during the breakup of Rodinia, after a ~28° clockwise rotation. Relative ^{40}Ar ages of the Eagle Ford gas samples become increasingly younger from east to west, pointing to the presence of ~20-25 km wide age blocks. The clear spatial variation pattern in relative ages supports the presence of small transform faults with a NW-SE orientation, and also a highly developed compartmentalization in the shale reservoir. This study highlights the application of noble gas geochemistry in tracing hydrocarbon sources, identifying tectonic implications, and characterizing reservoir properties in unconventional hydrocarbon systems.

Chapter 4: This chapter focuses on noble gases, CO_2 and stable carbon isotope ($\delta^{13}C$-CO_2) data in six Mexican geothermal fields. It reveals the presence of heat and volatile species from three distinct sources, the crust, the mantle and the atmosphere, while highlighting general fractionation patterns between volatiles and heat. Significant differences in helium isotopic ratios (R/Ra) are observed between the Trans-Mexico Volcanic Belt (TMVB) (7.14-7.27) and Baja California samples (1.21-6.62), with TMVB samples displaying more pristine mantle signals. These differences reflect the presence of distinct tectonic settings, where the TMVB geothermal

fields are impacted by active magma sources associated with subduction of the Cocos plate, while Baja California reservoirs are primarily affected by crustal contributions from the subducted fossil Farallon Plate. The presence of varying amounts of mantle carbon sources (0.05% - 82.64%) as well as carbon originating from limestone (8.93% - 99.80%) are observed through $CO_2/^3He$ ratios and carbon isotopic signatures ($\delta^{13}C\text{-}CO_2$). Contribution of carbon from sediments is generally smaller (0% - 35.55%). These findings are consistent with worldwide observations in arc-volcanic settings, where old carbonate platforms are subducted, adding carbon to volcanic emissions. Some of the Baja California samples collected from near surface geothermal manifestations display $CO_2/^3He$ ratios below typical mantle values, likely due to CO_2 loss from calcite precipitation. A combined analysis of heat/helium ratios ($Q/^3He$) with $^4He/^{36}Ar$ ratios shows that convection is the main mechanism controlling the transport of heat and magmatic volatiles during magma degassing. Further fractionation between heat and volatiles is caused by boiling and meteoric water dilution. The presence of mantle, crust and meteoric water components is evidenced by the correlation between $Q/^3He$ and R/Ra ratios. A significant influence from the meteoric water endmember is observed in some of the Las Tres Vírgenes, Los Azufres and the Baja California hydrothermal samples, while a clear crustal contribution is found in Cerro Prieto and Baja California magmatic samples. The absence of significant fractionation in $CO_2/^3He$ ratios is an indication that helium degassing is controlled by the CO_2 content in parental magma rather than helium diffusivity.

5.2. Overall Conclusions

This dissertation focuses on stable noble gases (He, Ne, Ar, Kr, Xe), major gases (e.g., CH_4, CO_2), and stable isotopes ($\delta^{13}C\text{-}CO_2$) in subsurface fluids within hydrocarbon (conventional and unconventional) systems, as well as noble gases, volatiles (e.g., CO_2) and heat in geothermal

systems. This dissertation investigates 12 natural gas samples from 12 production wells in the Panhandle Field, and published noble gas dataset from Ballentine and Lollar [2002] in the Hugoton Field; 13 shale gas samples from 7 production wells, as well as published noble gas data from Byrne et al. [2018] and Harington et al [2015] in the Eagle Ford Shale play; and 132 geothermal fluid samples from production wells, fumaroles and hot springs in Mexico, together with published dataset from Batista-Cruz et al., [2019] in the Baja California area. It explores the information that noble gases can provide in conventional and unconventional natural gas systems in terms of hydrocarbon sources, fluid migration, reservoir interconnectivity and compartmentalization, and tectonic implications. In geothermal systems, noble gases reveal heat and volatile sources, and fractionation mechanisms between heat and volatile species. Noble gas geochemistry is a powerful tool to fingerprint subsurface fluids in various types of energy systems. This dissertation has societal relevance in both hydrocarbon (conventional and unconventional) production and geothermal energy exploitation, to cope with the soaring demand for clean energy and the challenge to address global climate change. Findings in this dissertation are an important complement to our current understanding of subsurface energy systems, and can facilitate the advancement in exploration and management strategies in natural gas and geothermal energy production. This dissertation has important implications to the fields of petroleum geology, hydrology, and geothermal research.

APPENDICES

Additional text, tables and figures that support the results and discussions in Chapter 2-4 are provided in Appendices A, B and C, respectively.

Appendix A includes additional text and two figures (Figs. A1-A2) that support the results in chapter 2.

Appendix B includes additional text and one figure (Fig B1) that support the results in chapter 3.

Appendix C includes three additional tables (Tables C1-C3) that support the results in chapter 4.

Appendix A

Supplementary Materials for Chapter 2

Appendix A1. Mass Fractionation

Mass fractionation is calculated after Kaneoka [1980] [see also Aston, 1933], whose model is defined as an isotopic separation by diffusion through porous material. The modeled fractionation results in two gas reservoirs, the residual gas and the diffused gas. Since isotopes with lighter mass will diffuse faster than heavier isotopes, heavier isotopes should be enriched in the residual gas while light isotopes should be enriched in the diffused gas. Marty [1984] [see also Matsumoto et al., 2004] reviews the gaseous diffusion processes that create elemental and isotopic fractionation in natural gases and distinguishes three mechanisms that may affect noble gases: a) free-molecule diffusion; b) mutual diffusion, and c) thermal diffusion. Molecular diffusion has the greatest potential to create fractionation between different isotopes. The mass fractionation lines (MFL) derived both following Kaneoka [1980] and Marty [1984] for molecular diffusion are shown in Fig. A1 where $^{20}Ne/^{22}Ne$ ratios are plotted as a function of $^{38}Ar/^{36}Ar$. It is apparent that mass dependent fractionation can be ruled out as the source of higher measured $^{20}Ne/^{22}Ne$ ratios in most of the eastern side samples, except for sample Johnson-5 (Fig. A1). Indeed, most of the eastern side samples with high $^{20}Ne/^{22}Ne$ ratios are plotted directly above the MDF lines (solid black and red dashed lines), ruling out the possibility of single or multiple (not shown) MDF stages from an atmospheric component. In contrast, nearly all samples from the western side fall on the MDF lines within their 1-sigma error, suggesting potential impact from MDF (Fig. A1).

Thermal diffusion, as described by Marty [1984], do not apply to our eastern Panhandle samples. Indeed, extreme temperature differences are required to generate significant fractionation

between isotopes through thermal diffusion. Marty [1984] demonstrated that a temperature difference of 340℃, which is about 10 times higher than the reservoir temperature (~30℃, inferred from gas-water contact temperature estimated in Brown, 2019), can only result in ~2.5% enrichment of ^{20}Ne over ^{22}Ne. Therefore, thermal diffusion cannot be responsible for the observed high ^{20}Ne/^{22}Ne ratios in the eastern Panhandle samples. Mutual diffusion [not shown; Marty, 1984] also cannot account for the high measured ^{20}Ne/^{22}Ne ratios.

Besides MDF, mixing with crustal component can also account for the alteration of the original isotopic ratios. In Fig. A2, measured ^{21}Ne/^{22}Ne ratios are plotted as a function of ^{38}Ar/^{36}Ar to compare the impact of MDF and crustal component. It is apparent that all of the Panhandle samples fall above the MDF lines, indicating a negligible influence from MDF compared to crustal input, and the elevated ^{21}Ne/^{22}Ne ratios reflect significant contribution from crust.

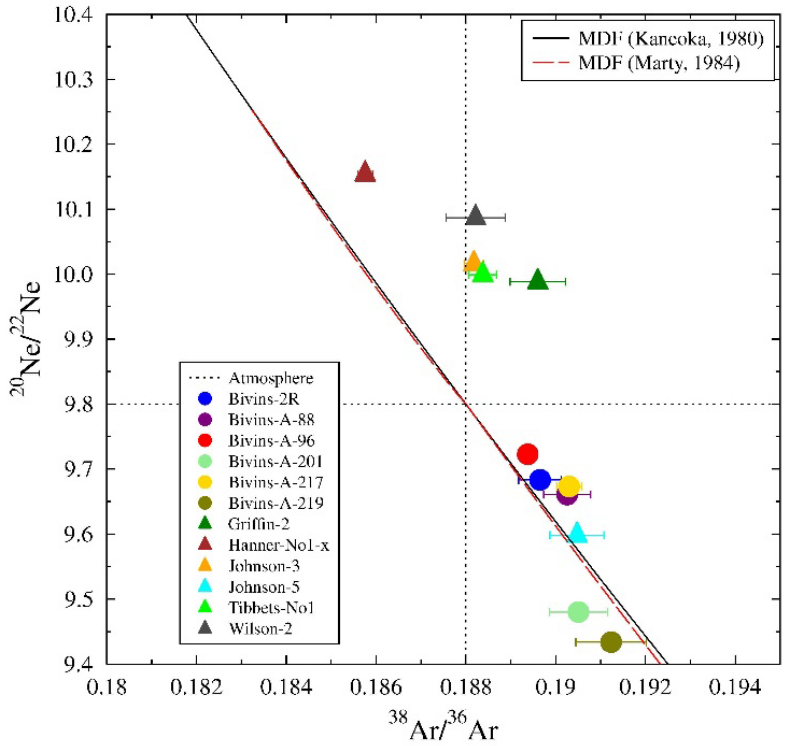

Figure A1 Measured ^{20}Ne/^{22}Ne ratios plotted as a function of ^{38}Ar/^{36}Ar ratios. Mass-dependent fraction lines from an atmospheric component following Kaneoka [1980] and Marty [1984] are shown.

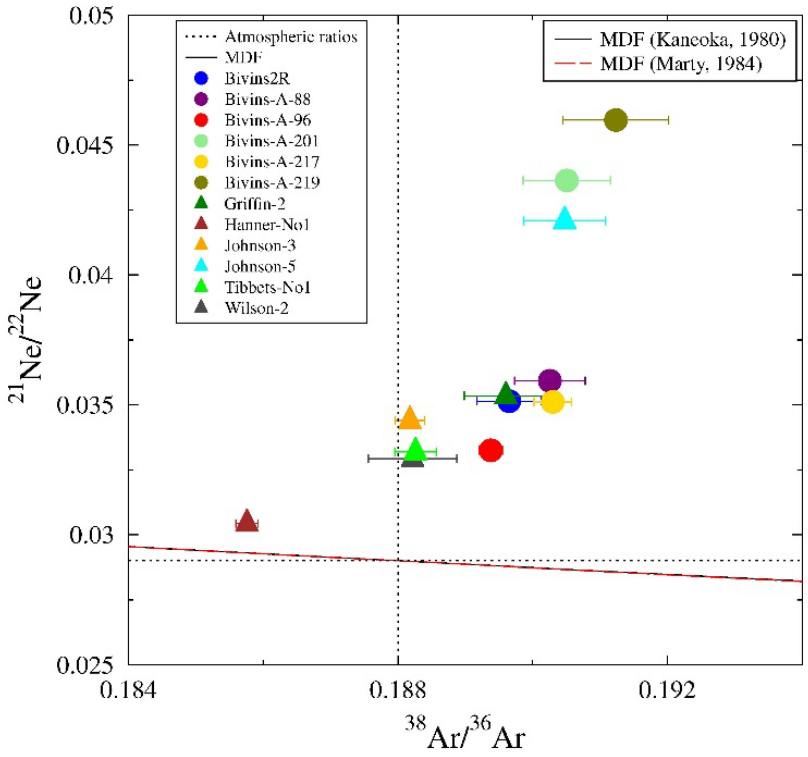

Figure A2 Measured $^{21}Ne/^{22}Ne$ ratios plotted as a function of $^{38}Ar/^{36}Ar$ ratios. Mass-dependent fraction lines from an atmospheric component following Kaneoka [1980] and Marty [1984] are shown

Appendix A2. Atmospheric Ne Removal and Optimized Crust-Solar Mixing Line

The procedure followed for separation of the atmospheric Ne component was that described in detail by Ballentine and O'Nions [1992] and Ballentine [1997], in addition to some modifications subsequently implemented by Castro et al. [2009]. In these studies, two variables needed to be determined for the separation of different Ne components: the $K_{(crust+mantle)}$ value which controls the curvature of the He-Ne hyperbolic mixing line, and the crustal $^{21}Ne/^{22}Ne$ ratio. $K_{crust-mantle} = (^4He/^{22}Ne)_{crust}/(^4He/^{22}Ne)_{mantle}$, where $(^4He/^{22}Ne)_{crust}$ and $(^4He/^{22}Ne)_{mantle}$ are the crustal and mantle (MORB, OIB, Solar) $^4He/^{22}Ne$ elemental ratios, respectively (Table 2.4). In Castro et al. [2009], optimal values for $K_{(crust+mantle)}$ and crustal $^{21}Ne/^{22}Ne_{crust}$ were obtained using a χ^2 minimization procedure developed based on Ballentine [1997]. In that study, the sum of

squared error-weighted misfits of air corrected Ne ratios to a He-Ne mixing curve was plotted as a function of $K_{(crust+mantle)}$ and the crustal $^{21}Ne/^{22}Ne$ ratio. An optimal set of values was determined at the point where the resulting χ^2 statistic was a minimum. However, for the eastern Panhandle samples, the χ^2 minimization procedure does not yield a reasonable estimate of the needed value and without a minimum χ^2 value, it is not possible to obtain an optimized $K_{(crust+mantle)}$ and corresponding crustal $^{21}Ne/^{22}Ne$ ratio. The difficulty to apply a χ^2 analysis on the eastern Panhandle samples relates to the limited number of samples (6 in total, with Johnson-5 being potentially fractionated) and the narrow range of air-corrected R/Ra ($(R/Ra)_c$) ratios in these samples (0.1 – 0.26), since a set of closely scattered data points are not ideal for the curve fitting procedure. In comparison, the air-corrected R/Ra ratios in Ballentine [1997] and Castro et al. [2009] range from 0.1 to 5 and from 0.05 to 1.3, respectively. Therefore, in this study, the separation of different Ne components was done following Ballentine and O'Nions [1992], with fixed endmember values of $^{20}Ne/^{22}Ne_{air}$ = 9.8, $^{21}Ne/^{22}Ne_{air}$= 0.029, $^{20}Ne/^{22}Ne_{crust}$ = 0.3, $^{21}Ne/^{22}Ne_{crust}$ =0.47, $^{20}Ne/^{22}Ne_{mantle}$=13.8 and $^{21}Ne/^{22}Ne_{mantle}$=0.035 (Table 2.4). Instead of being determined from the χ^2 minimization procedure, an average crustal value of 0.47 was used as $^{21}Ne/^{22}Ne_{crust}$ (Table 2.4). The calculated air-corrected $(^{20}Ne/^{22}Ne)_{crust+mantle}$ and $(^{21}Ne/^{22}Ne)_{crust+mantle\ values}$ are listed in Table 2.5. An analysis of the air-corrected He and Ne isotopic ratios reveals that most of the eastern samples with a solar-like component (Griffin-2, Hanner-No1-x, Johnson-3, Tibbets-No1, Wilson-2) falls on a similar mixing trend to that estimated for the Michigan Basin samples, with a slightly different $(^{21}Ne/^{22}Ne)_{crust+mantle}$ of 0.47 as opposed to that estimated for the Michigan Basin samples of 0.33. The similar crust-Solar mixing trend exhibited for both the eastern Panhandle gas samples and that of Michigan Basin brines suggests that this primordial component has a similar source at both locations.

It has been argued that MORB and OIBs might have similar $^{3}He/^{22}Ne$ values [e.g., O'Nions and Tolstikhin, 1994; Gonnermann and Mukhopadhyay, 2007]. Recent studies, however, suggest an obvious heterogeneity of $^{3}He/^{22}Ne$ values in different mantle sources [e.g., Tucker and Mukhopadhyay, 2014]. We have performed calculations using these values. It is apparent that changes in these mixing curves using different$^{3}He/^{22}Ne$ values are minor and have no impact on our conclusions.

References

Aston, F.W. (1933) *Mass-spectra and Isotopes.* Vol. 40 (London).

Ballentine, C. J. (1997). Resolving the mantle He/Ne and crustal $^{21}Ne/^{22}Ne$ in well gases. *Earth and Planetary Science Letters* 152, 233-249.

Ballentine, C. J., and O'Nions, R. K. (1992). The nature of mantle neon contributions to Vienna Basin hydrocarbon reservoirs. *Earth and Planetary Science Letters* 113, 553–567.

Brown, A. (2019). Origin of helium and nitrogen in the Panhandle–Hugoton field of Texas, Oklahoma, and Kansas, United States. *AAPG Bulletin* 103, 369–403. doi:10.1306/07111817343.

Castro, M. C., Ma, L., and Hall, C. M. (2009). A primordial, solar He-Ne signature in crustal fluids of a stable continental region. *Earth and Planetary Science Letters* 279, 174-184.

Gonnermann, H. M., and Mukhopadhyay S. (2007). Non-equilibrium degassing and a primordial source for helium in ocean-island volcanism. *Nature* 449, 1037-1040. doi:10.1038/nature06240

Kaneoka, I. (1980). Rare gas isotopes and mass fractionation: An indicator of gas transport into or from a magma. *Earth and Planetary Science Letters* 48, 284–292. doi:10.1016/0012-821X(80)90192-2.

Marty, B. (1984). On the Nobles gas isotopic fractionation in naturally occurring gases. *Geochemical Journal* 18, 157-162.

Matsumoto, T., Honda M., McDougall I., Yatsevich I., and O' Reilly S.Y. (2004). Isotope fractionation of neon during stepheating extraction?: a comment on 'reinterpretation of the existence of a primitive plume under Australia based on neon isotope fractionation during step heating' by Gautheron and Moreira (2003). *Terra Nova* 16, 23–26.

O'Nions, R. K., and Tolstikhin, I. N. (1994) Behavior and residence times of lithophile and rare gas tracers in the upper mantle. *Earth and Planetary Science Letters* 124, 131–138.

.

Appendix B

Supplementary Materials for Chapter 3

Appendix B1. Nucleogenic Production of ^{20}Ne

Production of ^{20}Ne in the crust is dominated by nuclear reactions $^{17}O(\alpha,n)^{20}Ne$ and $^{23}Na(n,\alpha)^{20}Ne$ [Wetherill, 1954]. ^{20}Ne production rates can be estimated for variable U, Th, O and Na compositions in the host rock following Ballentine and Burnard [2002]. For the composition of the average lower Eagle Ford shale (U=4 ppm and Th=6 ppm, O=28.7 wt% and Na=0.43 wt%) [Tinnin and Darmaoen, 2016], the ^{20}Ne production rate is $1.96\times10^{-21}cm^3STP/g$. Consider an average porosity of 8% [Gherabati et al., 2016], complete release of Ne from host minerals and assumptions similar to those used in the in-situ production estimation of $^{4}He^*$ and $^{40}Ar^*$[Appendix B5], it takes at least 2 Ga to produce the amounts of non-atmospheric ^{20}Ne observed in these samples. This age is significantly older than the formation age of the Eagle Ford shale (~96 Ma). Alternatively, if we consider the production of ^{20}Ne in the upper crust (U=2.8 ppm, Th=10.7 ppm, O=47.8 wt% and Na=2.89 wt%) [Rudnick and Fountain, 1995], 1.6 Ga would still be required to produce the observed excess ^{20}Ne in the Eagle Ford samples.

Of greater significance is the fact that the ^{22}Ne nuclear production rate is far more pronounced in the crust than that of ^{20}Ne [Wetherill,1954; Ballentine and Burnard, 2002], thus leading to an extremely small $^{20}Ne/^{22}Ne$ crustal production ratio of ~0.3 (Table 3.4). Consequently, in the event that the excess ^{20}Ne is solely the result of crustal production, the expected $^{20}Ne/^{22}Ne$ ratios in the samples should vary between 1.3-5.7, much lower than the atmospheric ratio of ~9.8, as opposed to our observed values above the atmospheric $^{20}Ne/^{22}Ne$ ratio. Crustal nuclear reactions

can therefore be ruled out to explain the observed ^{20}Ne excesses in the Eagle Ford samples and corresponding high $^{20}Ne/^{22}Ne$ values.

Appendix B2. Mass Fractionation

Mass fractionation is calculated after Kaneoka [1980] [see also Aston, 1933], and Marty [1984] (see also Matsumoto et al., 2004). Details are described in Appendix A1. The mass fractionation lines (MFL) derived both following Kaneoka [1980] and Marty [1984] for molecular diffusion are shown in Fig. B1 where $^{20}Ne/^{22}Ne$ ratios are plotted as a function of $^{38}Ar/^{36}Ar$. It is apparent that mass dependent fractionation can be ruled out as the source of higher measured $^{20}Ne/^{22}Ne$ ratios in most of the Eagle Ford gas samples and particularly in samples with the highest $^{20}Ne/^{22}Ne$ values (Fig. B1). Indeed, most samples with high $^{20}Ne/^{22}Ne$ ratios have their $^{38}Ar/^{36}Ar$ ratios similar to or lower than the atmospheric value (0.188) and plot directly above the MDF line (solid black and red dashed lines), ruling out the possibility of single or multiple (not shown) MDF stages from an atmospheric component.

Thermal diffusion, as described by Marty [1984], do not apply to our Eagle Ford samples. Indeed, extreme temperature differences are required to generate significant fractionation between isotopes through thermal diffusion. Marty [1984] demonstrated that a temperature difference of 340℃, which is about 4 times higher than the reservoir temperature in the sampled oil production zone [~90°C; Gherabati et al., 2018], can only result in ~2.5% enrichment of ^{20}Ne over ^{22}Ne. Therefore, thermal diffusion cannot be responsible for the observed high $^{20}Ne/^{22}Ne$ ratios in the Eagle Ford samples.

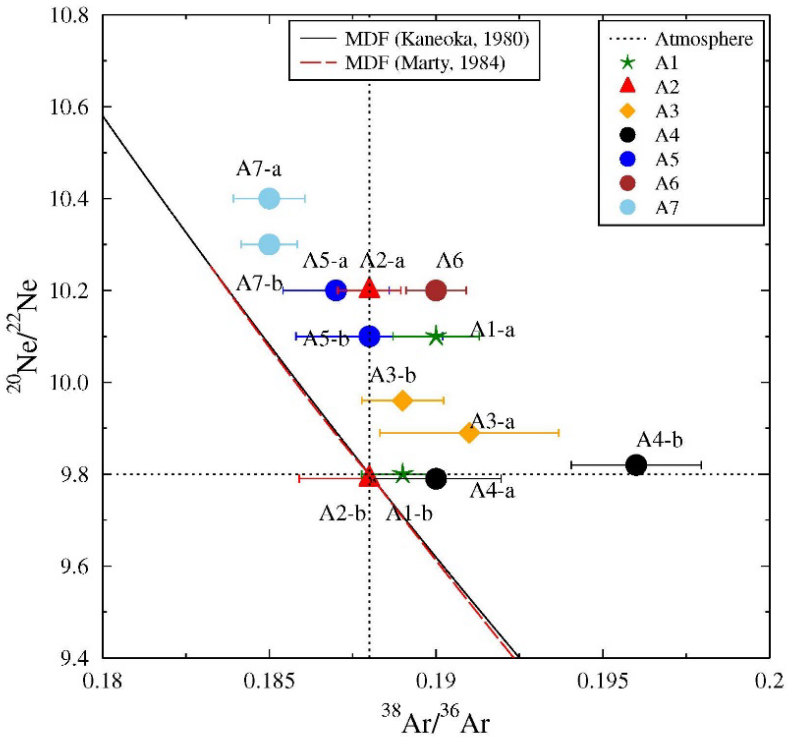

Figure B1 Measured $^{20}Ne/^{22}Ne$ ratios plotted as a function of $^{38}Ar/^{36}Ar$ ratios. Mass-dependent fraction lines from an atmospheric component following Kaneoka [1980] and Marty [1984] are shown.

Appendix B3. Atmospheric Ne Removal and Optimized Crust-Solar Mixing Line

The procedure followed for separation of the atmospheric He and Ne components are described in detail in Appendix A2. The calculated air-corrected $(^{20}Ne/^{22}Ne)_{crust+mantle}$ and $(^{21}Ne/^{22}Ne)_{crust+mantle}$ values are listed in Table 3.5. Calculated $(^{20}Ne/^{22}Ne)_{crust+mantle}$ and $(^{21}Ne/^{22}Ne)_{crust+mantle}$ ratios of sample A3-a are associated with very large estimated errors. For clarity purposes, sample A3-a is not included in the table and the figures. An analysis of the air-corrected He and Ne isotopic ratios reveals that the bulk of the Eagle Ford samples with a solar-like component (A7-a, A7-b, A6, A5-a, A5-b, A1-a, A2-a) falls on a similar mixing trend to that estimated for the Michigan Basin samples, with a slightly different $(^{21}Ne/^{22}Ne)_{crust+mantle}$ of 0.47 as opposed to that estimated for the Michigan Basin samples of 0.33. The similar crust-Solar mixing

trend exhibited for both the Eagle Ford natural gas samples displaying a primordial component and that of Michigan Basin brines suggests that this primordial component has a similar source at both locations.

Appendix B4. Ar Isochrons and ^{40}Ar Relative Ages

In Ar-Ar dating, argon isotope ratios are frequently plotted as $^{36}Ar/^{40}Ar$ versus $^{39}Ar/^{40}Ar$, where ^{39}Ar is an artificially produced proxy for potassium [McDougall and Harrison, 1999]. This so-called "isochron" diagram can illustrate mixing between a pure initial argon component (i.e., non-zero ^{36}Ar) versus a pure crustal (radiogenic) component (i.e., zero ^{36}Ar). Because ^{40}Ar appears in the denominator of both the x and y values of such a plot, any mixture between two fixed end members, i.e., a single initial $^{36}Ar/^{40}Ar$ and a single $^{39}Ar/^{40}Ar$ ratio will plot along a line. Since the apparent age of a rock sample is a function of the $^{39}Ar/^{40}Ar^{*}$ ratio, where $^{40}Ar^{*}$ is the pure crustal (radiogenic) component, the x-intercept of an isochron line defines the argon age of the rock sample [McDougall and Harrison, 1999].

By analogy to the Ar-Ar dating isochron procedure applied to date rocks, a similar graphical analysis can be used to provide a relative gas sample age. Indeed, in lieu of plotting $^{39}Ar/^{40}Ar$ values along the x-axis, in our analysis of gas samples we will plot $1/^{40}Ar$. This style of plot has many of the properties of the traditional Ar-Ar isochron diagram. A gas sample will consist of a mixture of the atmospheric (air) $^{36}Ar/^{40}Ar$ ratio (y-intercept) and a fixed crustal volume fraction (x-intercept). Because the reciprocal of the ^{40}Ar volume fraction is being plotted, samples that result from mixing between an air component and a highly enriched crustal ^{40}Ar* endmember will plot closer to the origin in the x-axis, while mixing between an Air component and a poorly enriched crustal ^{40}Ar* endmember will plot further to the right in the x-axis. Thus, in this plot,

ages will increase from right to left. A special case is when there is no crustal (radiogenic) $^{40}Ar^*$ component at all, which would lead to gas samples plotting along a horizontal line through the air value at the y-axis, i.e., the radiogenic intercept would plot at infinity along the x-direction. Samples that share the same K-content in their source and the same transport history should plot along a mixing line between air and a fixed x-axis value of $1/^{40}Ar$.

Appendix B5. Calculation of Noble Gases in-Situ Production

In-situ production of both $^4He^*$ and $^{40}Ar^*$ are estimated following the same methods in section 2.5.3. Under the pressure of ~6500 psi (440 atm) and a temperature of ~90 ℃ in the oil zone reservoir [Gherabati et al., 2018], methane in the pore space of the shale should be in its supercritical phase, and the expansion coefficient R can be expressed as:

$$R = \frac{\rho_{STP}}{\rho_{Rev}} \tag{B1}$$

where ρ_{STP} stands for the density of methane under standard temperature and pressure, and ρ_{Rev} represents the density of methane under reservoir conditions.

Given a production time of 96 Myrs which corresponds to the deposition age of the lower Eagle Ford Shale, an average U and Th concentrations in the lower Eagle Ford shale of 4 ppm and 6 ppm, respectively [Tinnin and Darmaoen, 2016], a shale density of 2.36 g/cm^3, an average porosity of 0.08, a saturation rate of 0%, and ρ_{STP} and ρ_{Rev} of 0.00065g/cm^3 and 0.22g/ cm^3 [Schon, 2015] respectively, and a release efficiency Λ =1, one can calculate the volume fraction of in-situ produced radiogenic ^4He. The expected in-situ ^4He volume fraction is about 5.14×10^{-6}, which accounts for 2.78%-17.71% of the total radiogenic ^4He in our samples. A similar estimation was also made by Byrne et al. [2018]. Their estimated in-situ production value is lower than that of our study. This is not surprising, since Byrne et al. [2018] used the ideal gas law (PV=RT) to

account for the volume change of pressurized methane. When applying the temperature and pressure in the condensate zone instead of the oil zone, the expansion coefficient derived from the ideal gas law decreases significantly, leading to a significantly lower expected ^{4}He concentration. In both cases, the expected in-situ ^{4}He volume fraction is insufficient to account for the measured concentrations, pointing to an external origin of a significant amount of the total crustal $^{4}He^{*}$[O'Nions and Ballentine, 1993].

Using again the production time period of 96 Myr, a rock density of 2.36 g/cm3, an average porosity of 0.08, a water saturation rate of 0%, ρ_{STP} and ρ_{Rev} of 0.00065g/cm3 and 0.22g/ cm3, and an average potassium concentration of 10748 ppm in the lower Eagle Ford shale [Tinnin and Darmaoen, 2016], the expected volume fraction of radiogenic ^{40}Ar is 3.21×10^{-7}, which accounts for 2.51% - 91.59% of the total measured radiogenic $^{40}Ar^{*}$ in our gas samples.

References

Schön, J.H. (2015). Density, in *Developments in Petroleum Science*. Elsevier, pp. 109–118. doi:10.1016/B978-0-08-100404-3.00004-4

Byrne, D. J., Barry, P. H., Lawson, M., and Ballentine, C. J. (2018). Determining gas expulsion vs retention during hydrocarbon generation in the Eagle Ford Shale using noble gases. *Geochimica et Cosmochimica Acta* 241, 240-254.

O'Nions, R. K. and Ballentine, C. J. (1993). Rare gas studies of basin scale fluid movement Philos. *Trans. R. Soc. London*. *Series A: Physical and Engineering Sciences* 344, 141–156

McDougall, I., and Harrison, T. M. (1999). *Geochronology and Thermochronology by the $^{40}Ar/^{39}Ar$ Method*. Oxford University Press.

Ballentine, C. J., and Burnard, P. G. (2002). Production, release and transport of noble gases in the continental crust. *Reviews in Mineralogy and Geochemistry* 47, 481-538.

Gherabati, S. A., Browning, J., Male, F., Ikonnikova, S. A., and McDaid, G. (2016). The impact of pressure and fluid property variation on well performance of liquid-rich Eagle Ford shale. *Journal of Natural Gas Science and Engineering* 33, 1056-1068.

Rudnick, R. L., and Fountain, D. M. (1995). Nature and composition of the continental crust: A lower crustal perspective. *Reviews of Geophysics* 33, 267. doi:10.1029/95RG01302

Wetherill, G.W. (1954). Variations in the isotopic abundances of neon and argon extracted from radioactive minerals. *Physical Review* 96, 679-683.

Tinnin, B. M., and Darmaoen, S. T. R. (2016). Chemostratigraphic variability of the Eagle Ford shale, south Texas: Insights into Paleoredox and sedimentary facies changes. In *The Eagle Ford Shale* (ed. J. Breyer). American Association of Petroleum Geologists. pp. 259-283.

Appendix C

Supplementary Materials for Chapter 4

Table C1 Geothermal fields, sample ID, sampling year, CO_2 volume fractions, the $\delta^{13}C$ ratios of CO_2, R/Ra ratios, noble gas volume fractions (cm^3/cm^3) and crustal noble gas volume fractions in Mexican geothermal samples.

Field	ID	Sampling year	CO_2	$\delta^{13}C$-CO_2	±	R/Ra	±	^4He	±	^{36}Ar	±	^{40}Ar	±	^4He*	±	^{40}Ar*	±
Cerro Prieto																	
Cerro Prieto	CP-109	2016	0.83	-4.72	0.01	6.05	0.09	1.50E-05	2.25E-07	2.32E-06	3.02E-08	6.91E-04	2.32E-05	1.49E-05	2.95E-07	5.10E-06	2.66E-07
Cerro Prieto	CP-112	2016	0.84	-5.59	0.01	5.56	0.099	9.40E-06	1.41E-07	1.45E-06	1.89E-08	4.33E-04	1.45E-05	9.31E-06	1.85E-07	4.20E-06	2.20E-07
Cerro Prieto	CP-114	2016	0.83			6.13	0.071	7.13E-06	1.07E-07	1.20E-06	1.56E-08	3.58E-04	1.20E-05	7.06E-06	1.40E-07	3.36E-06	1.75E-07
Cerro Prieto	CP-301	2016	0.84	-4.91	0.01	6.29	0.051	1.08E-05	1.62E-07	1.06E-06	1.38E-08	3.16E-04	1.06E-05	1.07E-05	2.13E-07	2.44E-06	1.27E-07
Cerro Prieto	CP-302	2016	0.84	-4.05	0.01	6.37	0.072	1.03E-05	1.55E-07	9.59E-07	1.25E-08	2.87E-04	9.63E-06	1.02E-05	2.03E-07	3.55E-06	1.85E-07
Cerro Prieto	CP-207D	2016	0.84	-3.64	0.09	5.56	0.057	5.89E-06	8.84E-08	2.00E-07	2.60E-09	6.18E-05	2.07E-06	5.88E-06	1.17E-07	2.70E-06	1.41E-07
Cerro Prieto	CP-218	2016	0.83			5.18	0.06	9.90E-06	1.49E-07	9.42E-07	1.23E-08	2.83E-04	9.49E-06	9.84E-06	1.96E-07	4.52E-06	2.36E-07
Cerro Prieto	CP-220D	2016	0.84	-4	0.01	3.33	0.028	1.18E-05	1.77E-07	8.95E-07	1.16E-08	2.72E-04	9.11E-06	1.18E-05	2.34E-07	7.25E-06	3.78E-07
Cerro Prieto	CP-230D	2016	0.83	-4.18	0.01	6.50	0.069	1.41E-05	2.12E-07	6.35E-07	8.26E-09	1.92E-04	6.44E-06	1.41E-05	2.80E-07	4.13E-06	2.16E-07
Cerro Prieto	CP-232	2016	0.84	-4.03	0.01	5.76	0.072	4.69E-06	7.03E-08	1.49E-07	1.94E-09	4.64E-05	1.56E-06	4.68E-06	9.29E-08	2.41E-06	1.26E-07
Cerro Prieto	CP-233	2016	0.84	-5.32	0.01	6.49	0.079	1.25E-05	1.87E-07	1.93E-06	2.51E-08	5.74E-04	1.92E-05	1.24E-05	2.45E-07	3.28E-06	1.71E-07

Cerro Prieto	CP-234D	2016	0.84			5.72	0.067	4.04E-06	6.06E-08	1.54E-07	2.01E-09	4.76E-05	1.60E-06	4.03E-06	8.00E-08	2.09E-06	1.09E-07
Cerro Prieto	CP-247	2016	0.84			6.00	0.08	2.59E-05	3.88E-07	3.05E-07	3.97E-09	9.59E-05	3.22E-06	2.59E-05	5.13E-07	5.76E-06	3.01E-07
Cerro Prieto	CP-248	2016	0.84	-3.83	0.01	3.91	0.034	1.08E-05	1.62E-07	4.15E-07	5.40E-09	1.28E-04	4.28E-06	1.08E-05	2.14E-07	4.94E-06	2.58E-07
Cerro Prieto	CP-500	2016	0.83			3.33	0.036	1.72E-05	2.57E-07	1.32E-06	1.71E-08	3.99E-04	1.34E-05	1.71E-05	3.39E-07	8.71E-06	4.55E-07
Cerro Prieto	CP-500	2016	0.83			3.30	0.038	2.30E-05	3.45E-07	1.66E-06	2.16E-08	5.01E-04	1.68E-05	2.29E-05	4.55E-07	1.05E-05	5.46E-07
Cerro Prieto	CP-501	2016	0.84	-4.04	0.01	3.34	0.036	1.98E-05	2.96E-07	1.35E-06	1.76E-08	4.09E-04	1.37E-05	1.97E-05	3.91E-07	9.86E-06	5.14E-07
Cerro Prieto	CP-505	2016	0.84	-4.53	0.01	4.91	0.057	5.23E-06	7.85E-08	2.49E-07	3.24E-09	7.59E-05	2.55E-06	5.21E-06	1.03E-07	2.34E-06	1.22E-07
Cerro Prieto	CP-512	2016	0.84	-4.67	0.01	5.13	0.038	5.34E-06	8.01E-08	2.30E-07	2.99E-09	7.03E-05	2.36E-06	5.33E-06	1.06E-07	2.37E-06	1.24E-07
Cerro Prieto	CP-512	2016	0.83	-4.67	0.01	5.44	0.059	5.37E-06	8.06E-08	2.32E-07	3.01E-09	7.11E-05	2.39E-06	5.36E-06	1.06E-07	2.58E-06	1.34E-07
Cerro Prieto	CP-513	2016	0.84	-4.24	0.01	3.80	0.039	2.46E-05	3.70E-07	1.57E-06	2.04E-08	4.75E-04	1.59E-05	2.45E-05	4.87E-07	1.07E-05	5.57E-07
Cerro Prieto	CP-522D	2016	0.84	-4.66	0.01	6.05	0.056	3.98E-06	5.98E-08	2.01E-07	2.62E-09	6.12E-05	2.05E-06	3.97E-06	7.88E-08	1.81E-06	9.44E-08
Cerro Prieto	CP-531D	2016	0.84	-4.9	0.01	4.03	0.045	5.86E-06	8.78E-08	3.13E-07	4.07E-09	9.52E-05	3.19E-06	5.84E-06	1.16E-07	2.75E-06	1.44E-07
Cerro Prieto	CP-533D	2016	0.84	-3.8	0.01	3.56	0.059	2.12E-05	3.18E-07	1.63E-06	2.12E-08	4.92E-04	1.65E-05	2.11E-05	4.19E-07	9.94E-06	5.19E-07
Cerro Prieto	CP-538D	2016	0.83	-4.06	0.01	4.94	0.052	2.59E-05	3.89E-07	7.11E-07	9.24E-09	2.17E-04	7.29E-06	2.59E-05	5.14E-07	7.25E-06	3.79E-07
Cerro Prieto	CP-542	2016	0.84	-3.71	0.01	3.29	0.026	1.32E-05	1.98E-07	6.75E-07	8.78E-09	2.06E-04	6.90E-06	1.32E-05	2.61E-07	6.21E-06	3.24E-07
Cerro Prieto	CP-545D	2016	0.84	-5.22	0.01	4.64	0.045	1.09E-05	1.64E-07	4.53E-07	5.89E-09	1.37E-04	4.61E-06	1.09E-05	2.16E-07	3.62E-06	1.89E-07
Cerro Prieto	CP-E24	2016	0.84	-4.13	0.01	6.59	0.053	7.18E-06	1.08E-07	9.39E-07	1.22E-08	2.80E-04	9.41E-06	7.13E-06	1.41E-07	2.91E-06	1.52E-07
Cerro Prieto	CP-E50	2016	0.83	-5.14	0.01	6.14	0.063	1.18E-05	1.77E-07	2.57E-06	3.34E-08	7.64E-04	2.56E-05	1.16E-05	2.31E-07	4.11E-06	2.15E-07
Cerro Prieto	CP-E56	2016	0.84	-3.84	0.01	5.85	0.061	4.95E-06	7.43E-08	1.41E-07	1.83E-09	4.41E-05	1.48E-06	4.94E-06	9.82E-08	2.45E-06	1.28E-07

Cerro Prieto	CP-M126	2016	0.84	-3.11	0.01	3.75	0.036	1.04E-05	1.57E-07	6.64E-07	8.63E-09	2.02E-04	6.78E-06	1.04E-05	2.06E-07	5.58E-06	2.91E-07
Cerro Prieto	CP-M148A	2016	0.84			5.88	0.065	4.03E-06	6.04E-08	7.69E-07	1.00E-08	2.30E-04	7.71E-06	3.98E-06	7.90E-08	2.61E-06	1.36E-07
Cerro Prieto	CP-M160	2016	0.84	-4.26	0.01	6.17	0.08	9.20E-08	1.38E-09	5.32E-08	6.91E-10	1.60E-05	5.36E-07	9.10E-08	1.81E-09	2.50E-07	1.31E-08
Cerro Prieto	CP-308	2016	0.84	-4.16	0.01	5.99	0.097	2.67E-05	4.01E-07	9.07E-07	1.18E-08	2.78E-04	9.34E-06	2.66E-05	5.29E-07	1.02E-05	5.35E-07
Cerro Prieto	CP-309	2016	0.84			6.49	0.06	4.70E-06	7.06E-08	2.37E-07	3.08E-09	7.25E-05	2.43E-06	4.69E-06	9.31E-08	2.44E-06	1.27E-07
Cerro Prieto	CP-311	2016	0.83	-4.38	0.01	6.33	0.068	9.40E-06	1.41E-07	5.70E-07	7.41E-09	1.72E-04	5.77E-06	9.37E-06	1.86E-07	3.65E-06	1.90E-07
Cerro Prieto	CP-318	2016	0.83	-3.11	0.01	6.81	0.084	1.06E-05	1.59E-07	4.34E-07	5.64E-09	1.32E-04	4.43E-06	1.06E-05	2.10E-07	3.73E-06	1.95E-07
Cerro Prieto	CP-345	2016	0.84	-3.95	0.01	5.68	0.046	1.09E-05	1.63E-07	3.45E-07	4.49E-09	1.06E-04	3.56E-06	1.09E-05	2.15E-07	4.28E-06	2.23E-07
Cerro Prieto	CP-346	2016	0.84	-3.61	0.01	6.42	0.074	1.81E-05	2.71E-07	5.08E-07	6.61E-09	1.57E-04	5.25E-06	1.81E-05	3.58E-07	6.45E-06	3.37E-07
Cerro Prieto	CP-E35A	2016	0.83			6.41	0.066	1.67E-05	2.50E-07	1.05E-06	1.37E-08	3.17E-04	1.06E-05	1.66E-05	3.30E-07	7.14E-06	3.73E-07
Cerro Prieto	CP-E37A	2016	0.84			6.25	0.072	6.08E-06	9.11E-08	1.23E-06	1.59E-08	3.67E-04	1.23E-05	5.97E-06	1.19E-07	3.20E-06	1.67E-07
Cerro Prieto	CP-M110	2016	0.83	-4.12	0.01	6.58	0.051	1.32E-05	1.98E-07	5.92E-07	7.69E-09	1.79E-04	6.00E-06	1.32E-05	2.61E-07	3.91E-06	2.04E-07
Cerro Prieto	CP-404	2016	0.83	-4.56	0.01	5.40	0.061	3.95E-06	5.93E-08	1.86E-07	2.41E-09	5.68E-05	1.91E-06	3.94E-06	7.82E-08	1.86E-06	9.71E-08
Cerro Prieto	CP-414	2016	0.84			5.72	0.048	2.87E-06	4.31E-08	9.36E-08	1.22E-09	2.89E-05	9.70E-07	2.86E-06	5.69E-08	1.25E-06	6.55E-08
Cerro Prieto	CP-423	2016	0.84	-3.84	0.01	7.32	0.067	1.84E-05	2.76E-07	2.17E-07	2.82E-09	6.75E-05	2.26E-06	1.84E-05	3.65E-07	3.34E-06	1.74E-07
Cerro Prieto	CP-424	2016	0.84			6.63	0.059	1.86E-05	2.79E-07	1.79E-06	2.33E-08	5.40E-04	1.81E-05	1.85E-05	3.67E-07	1.07E-05	5.61E-07
Cerro Prieto	CP-431D	2016	0.84	-4.32	0.01	6.37	0.086	2.17E-06	3.26E-08	1.07E-07	1.39E-09	3.25E-05	1.09E-06	2.16E-06	4.30E-08	9.31E-07	4.86E-08
Cerro Prieto	CP-509	2016	0.84	-3.78	0.01	6.57	0.088	7.40E-06	1.11E-07	3.30E-07	4.29E-09	1.01E-04	3.37E-06	7.38E-06	1.47E-07	3.00E-06	1.57E-07
Los Azufres																	

Los Azufres	AZ-2A	2014	0.97	-8.22	0.01	2.04	0.02	5.33E-06	7.99E-08	2.62E-05	5.24E-07	7.71E-03	4.02E-04	5.33E-06	1.07E-07	2.77E-07	5.56E-09
Los Azufres	AZ-4	2014	0.97			5.24	0.04	3.23E-06	4.85E-08	2.52E-07	5.04E-09	7.47E-05	3.90E-06	3.21E-06	6.38E-08	1.63E-06	3.26E-08
Los Azufres	AZ-5	2014	0.97	-6.77	0.01	7.48	0.07	1.29E-05	1.93E-07	8.54E-08	1.71E-09	2.69E-05	1.40E-06	1.29E-05	2.56E-07	2.38E-06	4.75E-08
Los Azufres	AZ-6	2014	0.97	-7.1	0.02	6.81	0.06	5.48E-06	8.22E-08	2.61E-07	5.22E-09	7.95E-05	4.15E-06	5.43E-06	1.08E-07	1.16E-06	2.33E-08
Los Azufres	AZ-9A	2014	0.97	-7.84	0.06	7.93	0.09	8.85E-06	1.33E-07	5.93E-08	1.19E-09	1.87E-05	9.76E-07	8.84E-06	1.76E-07	1.34E-06	2.76E-08
Los Azufres	AZ-9AD	2014	0.97			7.74	0.06	1.22E-05	1.82E-07	1.93E-08	3.86E-10	7.04E-06	3.68E-07	1.22E-05	2.49E-07	1.59E-06	3.18E-08
Los Azufres	AZ-12D	2014	0.97	-9.79	0.02	6.56	0.08	2.91E-06	4.36E-08	3.18E-07	6.36E-09	9.56E-05	4.99E-06	2.88E-06	5.73E-08	1.47E-06	2.96E-08
Los Azufres	AZ-13	2014	0.97	-7.52	0.01	7.68	0.08	1.59E-05	2.39E-07	3.00E-08	6.00E-10	1.03E-05	5.40E-07	1.59E-05	3.16E-07	7.47E-06	2.54E-07
Los Azufres	AZ-18	2014	0.97			7.51	0.06	4.91E-05	7.37E-07	2.86E-08	5.72E-10	1.59E-05	8.31E-07	4.91E-05	9.82E-07	1.90E-06	4.01E-08
Los Azufres	AZ-18	2014	0.97			7.66	0.08	1.13E-05	1.69E-07	6.31E-09	1.26E-10	3.77E-06	1.97E-07	1.13E-05	2.26E-07	2.81E-06	5.62E-08
Los Azufres	AZ-19	2014	0.97	-7.38	0.01	5.93	0.06	6.49E-06	9.74E-08	7.59E-07	1.52E-08	2.27E-04	1.19E-05	6.42E-06	1.28E-07	1.32E-06	2.65E-08
Los Azufres	AZ-25	2014	0.97	-8.44	0.01	6.53	0.05	5.57E-06	8.35E-08	9.37E-08	1.87E-09	2.90E-05	1.51E-06	5.56E-06	1.11E-07	1.66E-06	4.10E-08
Los Azufres	AZ-26	2014	0.97	-7.39	0.01	6.66	0.05	9.82E-06	1.47E-07	7.28E-09	1.46E-10	3.81E-06	1.99E-07	9.82E-06	1.96E-07	1.58E-06	3.17E-08
Los Azufres	AZ-28	2014	0.96	-7.9	0.04	6.48	0.05	8.07E-06	1.21E-07	1.84E-07	3.68E-09	5.60E-05	2.92E-06	8.06E-06	1.60E-07	4.25E-06	9.84E-08
Los Azufres	AZ-32	2014	0.97	-7.61	0.01	7.53	0.05	4.70E-05	7.06E-07	7.56E-08	1.51E-09	2.66E-05	1.39E-06	4.70E-05	9.33E-07	9.32E-06	2.88E-07
Los Azufres	AZ-34a	2014	0.97	-7.78	0.01	7.41	0.06	5.04E-05	7.56E-07	4.22E-08	8.44E-10	2.18E-05	1.14E-06	5.04E-05	1.01E-06	2.11E-06	4.41E-08
Los Azufres	AZ-34b	2014	0.97	-7.12	0.01	7.5	0.08	1.17E-05	1.76E-07	1.05E-08	2.10E-10	5.21E-06	2.72E-07	1.17E-05	2.34E-07	2.26E-06	4.53E-08
Los Azufres	AZ-36	2014	0.97	-7.12	0.01	7.22	0.06	1.08E-05	1.62E-07	3.30E-08	6.60E-10	1.20E-05	6.27E-07	1.08E-05	2.14E-07	1.81E-06	3.62E-08
Los Azufres	AZ-38	2014	0.96			7.34	0.05	9.03E-06	1.36E-07	4.72E-08	9.44E-10	1.58E-05	8.23E-07	9.02E-06	1.80E-07		

Los Azufres	AZ-42	2014	0.97	-7	0.01	3.05	0.03	6.36E-06	9.53E-08	2.89E-05	5.78E-07	8.51E-03	4.44E-04	3.11E-06	6.16E-08	2.02E-06	4.05E-08
Los Azufres	AZ-43	2014	0.97			6.98	0.06	2.12E-05	3.18E-07	5.33E-08	1.07E-09	1.78E-05	9.28E-07	2.12E-05	4.21E-07	3.57E-07	7.14E-09
Los Azufres	AZ-46	2014	0.97	-7.3	0.01	6.9	0.08	7.10E-06	1.06E-07	3.57E-06	7.14E-08	1.06E-03	5.51E-05	6.61E-06	1.31E-07	1.72E-06	3.46E-08
Los Azufres	AZ-47D	2014	0.97	-7.19	0.01	7.47	0.1	7.31E-06	1.10E-07	5.71E-08	1.14E-09	1.86E-05	9.72E-07	7.30E-06	1.45E-07	4.02E-06	8.07E-08
Los Azufres	AZ-48	2014	0.97	-7.25	0.01	6.53	0.05	3.12E-05	4.68E-07	6.93E-07	1.39E-08	2.09E-04	1.09E-05	3.11E-05	6.18E-07	9.12E-05	1.83E-06
Los Azufres	AZ-51	2014	0.97	-8.66	0.01	7.37	0.04	7.99E-05	1.20E-06	4.45E-06	8.90E-08	1.41E-03	7.34E-05	7.99E-05	1.59E-06	1.77E-06	3.57E-08
Los Azufres	AZ-51	2014	0.96	-7.64	0.03	7.58	0.07	1.53E-05	2.29E-07	7.50E-08	1.50E-09	2.39E-05	1.25E-06	1.53E-05	3.03E-07	4.40E-06	1.35E-07
Los Azufres	AZ-62a	2014	0.97	-7.64	0.03	7.19	0.05	3.32E-05	4.98E-07	3.82E-08	7.64E-10	1.57E-05	8.19E-07	3.32E-05	6.58E-07	1.76E-06	3.68E-08
Los Azufres	AZ-62b	2014	0.96	-8.11	0.01	7.16	0.08	1.28E-05	1.93E-07	1.32E-08	2.64E-10	5.66E-06	2.96E-07	1.28E-05	2.55E-07		
Los Azufres	AZ-65	2014	0.97	-8.11	0.01	5.12	0.05	9.63E-06	1.45E-07	1.79E-05	3.58E-07	5.28E-03	2.76E-04	8.09E-06	1.61E-07		
Los Azufres	AZ-66D	2014	0.97	-7.81	0.01	1.03	0.01	4.62E-06	6.92E-08	2.63E-05	5.26E-07	7.76E-03	4.05E-04	4.62E-06	9.24E-08	1.46E-06	2.92E-08
Los Azufres	AZ-67	2014	0.97	-7.38	0.01	7.55	0.08	7.53E-06	1.13E-07	1.26E-07	2.52E-09	3.87E-05	2.02E-06	7.52E-06	1.49E-07		
Los Azufres	AZ-83a	2014	0.97	-7.9	0.01	7.18	0.04	4.02E-05	6.04E-07					4.02E-05	8.04E-07	1.50E-06	4.06E-08
Los Azufres	AZ-83b	2014	0.97	-6.92	0.01	6.71	0.07	4.86E-06	7.29E-08	1.10E-08	2.20E-10	4.75E-06	2.48E-07	4.86E-06	9.72E-08	9.71E-07	1.95E-08
Los Azufres	AZ-89	2014	0.97	-7.97	0.01	6.58	0.07	3.90E-06	5.85E-08	6.84E-08	1.37E-09	2.12E-05	1.11E-06	3.90E-06	7.80E-08		
Los Azufres	AZ-90	2014	0.96			3.23	0.03	9.63E-07	1.44E-08	2.89E-06	5.78E-08	8.51E-04	4.44E-05	5.97E-07	1.18E-08	2.77E-07	5.56E-09
Los Humeros																	
Los Humeros	H-03D	2015	0.93	-5.13	0.01	6.35	0.05	3.01E-06	4.52E-08	5.08E-09	1.27E-10	2.58E-06	9.08E-08	3.01E-06	5.99E-08	1.08E-06	2.15E-08
Los Humeros	H-06	2015	0.91	-3.88	0.02	7.62	0.07	2.62E-06	3.93E-08	4.84E-09	1.74E-10	1.93E-06	9.93E-08	2.62E-06	#DIV/0!	4.97E-07	9.94E-09

Los Humeros	H-06	2015	0.91	-3.88	0.02	7.34	0.06	2.71E-05	4.06E-07	1.78E-07	2.32E-09	5.65E-05	7.38E-07	2.71E-05	5.37E-07	3.93E-06	7.87E-08
Los Humeros	H-06	2018	0.91			7.17	0.07	8.03E-06	1.20E-07	1.30E-08	1.69E-10	5.11E-06	7.00E-08	8.03E-06	1.59E-07	1.26E-06	2.53E-08
Los Humeros	H-07	2015	0.94	-3.03	0.01	7.32	0.08	1.23E-05	1.84E-07	8.23E-08	1.07E-09	2.61E-05	3.41E-07	1.23E-05	2.43E-07	1.80E-06	3.60E-08
Los Humeros	H-07	2018	0.94			7.1	0.1	2.09E-05	3.13E-07	3.21E-06	4.17E-08	9.53E-04	1.24E-05	2.06E-05	4.08E-07	4.17E-06	8.35E-08
Los Humeros	H-09	2015	0.90	-3.05	0.01	6.86	0.05	1.45E-07	2.17E-09	1.91E-09	6.86E-11	6.56E-07	3.34E-08	1.45E-07	6.34E-09	9.21E-08	1.84E-09
Los Humeros	H-11D	2015	0.96	-3.43	0.01	7.13	0.13							0.00E+00	#DIV/0!		
Los Humeros	H-12	2015	0.93	-5.01	0.01	6.95	0.07	1.20E-05	1.81E-07	5.53E-09	7.19E-11	4.28E-06	7.58E-08	1.20E-05	5.81E-07	2.65E-06	5.30E-08
Los Humeros	H-15D	2015	0.85	-2.77	0.01	6.96	0.06	1.63E-07	2.45E-09	3.34E-08	4.34E-10	1.01E-05	1.38E-07	0.00E+00	#DIV/0!	2.30E-07	4.61E-09
Los Humeros	H-17D	2015	0.90	-2.48	0.01	6.09	0.08	9.09E-08	1.36E-09	6.29E-08	8.18E-10	1.90E-05	2.67E-07	1.62E-07	3.21E-09	4.47E-07	8.93E-09
Los Humeros	H-19D	2015	0.97	-3.09	0.01	7.27	0.07	1.37E-05	2.05E-07	4.23E-09	1.01E-10	3.07E-06	1.04E-07	8.76E-08	1.74E-09	1.82E-06	3.64E-08
Los Humeros	H-19D	2015	0.97	-3.09	0.01	7.37	0.06	2.02E-05	3.03E-07	5.90E-09	7.66E-11	4.29E-06	7.30E-08	1.37E-05	2.72E-07	2.55E-06	5.09E-08
Los Humeros	H-20	2015	0.93	-2.24	0.02	7.29	0.05	3.39E-06	5.08E-08	1.08E-08	1.41E-10	3.68E-06	5.68E-08	2.02E-05	4.00E-07	4.87E-07	9.74E-09
Los Humeros	H-30	2015	0.71	-3.86	0.01	7.00	0.05	1.57E-05	2.35E-07	4.82E-06	6.26E-08	1.43E-03	1.85E-05	1.50E-05	2.97E-07	2.41E-06	4.82E-08
Los Humeros	H-31	2015	0.88	-3.85	0.01	7.18	0.06	5.07E-06	7.60E-08	4.17E-08	5.42E-10	1.31E-05	1.76E-07	5.07E-06	1.00E-07	7.30E-07	1.46E-08
Los Humeros	H-32	2018	0.92			7.52	0.1	9.03E-06	1.36E-07	6.56E-07	8.52E-09	1.96E-04	2.54E-06	8.95E-06	1.78E-07	1.84E-06	3.67E-08
Los Humeros	H-33	2015	0.72			6.69	0.06	1.16E-05	1.74E-07	8.05E-06	1.05E-07	2.37E-03	3.10E-05	1.03E-05	2.03E-07		
Los Humeros	H-34	2015	0.97	-5.25	0.01	7.18	0.06	4.72E-06	7.08E-08	3.90E-08	5.07E-10	1.22E-05	1.64E-07	4.72E-06	9.37E-08	6.51E-07	1.30E-08
Los Humeros	H-35	2015	0.79	-4.44	0.01	7.09	0.05	2.62E-07	3.93E-09	5.18E-08	6.73E-10	1.56E-05	2.05E-07	2.60E-07	5.16E-09	2.90E-07	5.80E-09
Los Humeros	H-39a	2018	0.94			6.27	0.06	2.49E-06	3.73E-08	1.10E-09	8.38E-11	9.51E-07	1.03E-07	2.49E-06	1.20E-07	6.26E-07	1.25E-08

Los Humeros	H-39b	2018	0.94			6.26	0.05	3.30E-06	4.95E-08	1.58E-09	3.79E-11	1.37E-06	4.69E-08	3.30E-06	7.00E-08	9.00E-07	1.80E-08
Los Humeros	H-41	2015	0.86	-3.39	0.01	6.13	0.07	3.99E-08	5.98E-10					3.99E-08	7.98E-10		
Los Humeros	H-42	2015	0.93			6.42	0.06	3.56E-06	5.33E-08	3.12E-09	6.23E-11	1.62E-06	4.54E-08	3.56E-06	7.54E-08	6.96E-07	1.39E-08
Los Humeros	H-44D	2015	0.86	-2.48	0.01	6.64	0.08	1.20E-05	1.79E-07	8.65E-06	1.12E-07	2.56E-03	3.31E-05	1.08E-05	2.14E-07		
Los Humeros	H-45D	2015	0.96	-2.79	0.01	7.22	0.06	2.27E-05	3.41E-07	4.15E-09	7.46E-11	3.59E-06	9.14E-08	2.27E-05	5.68E-07	2.36E-06	4.73E-08
Los Humeros	H-48D	2015	0.95	-3.29	0.01	6.8	0.07	6.07E-06	9.11E-08	9.99E-09	1.30E-10	3.78E-06	6.94E-08	6.07E-06	1.20E-07	8.26E-07	1.65E-08
Los Humeros	H-49D	2015	0.95	-3.01	0.01	7.28	0.06	2.47E-05	3.70E-07	4.32E-07	5.62E-09	1.31E-04	1.71E-06	2.46E-05	4.88E-07	3.80E-06	7.60E-08
Los Humeros	H50a	2018	0.88			6.84	0.04	6.15E-06	9.22E-08	1.20E-09	4.79E-11	1.79E-06	1.02E-07	6.15E-06	2.40E-07	1.43E-06	2.87E-08
Los Humeros	H50b	2018	0.88			6.08	0.06	8.19E-06	1.23E-07	1.60E-09	3.35E-11	2.35E-06	6.90E-08	8.19E-06	1.63E-07	1.87E-06	3.75E-08
Los Humeros	H55	2018	0.98			7.49	0.05	7.11E-06	1.07E-07	4.49E-08	5.84E-10	1.43E-05	1.87E-07	7.11E-06	1.41E-07	1.03E-06	2.06E-08
Los Humeros	H56	2018	0.90			7.3	0.07	1.14E-05	1.71E-07	7.76E-09	1.01E-10	4.29E-06	6.05E-08	1.14E-05	2.26E-07	2.00E-06	3.99E-08
Los Humeros	H59	2018	0.80			6.84	0.05	4.42E-06	6.63E-08	2.71E-06	3.52E-08	8.02E-04	1.04E-05	3.93E-06	7.80E-08	1.63E-06	3.25E-08
Los Humeros	H65	2018	0.93			6.42	0.09	3.29E-06	4.93E-08	1.20E-08	1.56E-10	4.54E-06	6.38E-08	3.29E-06	6.53E-08	9.98E-07	2.00E-08
Las Tres Virgenes																	
Las Tres Virgenes	LV-6	2016	0.98	-10.28	0.01	5.45	0.10	6.54E-06	9.81E-08	1.26E-05	1.64E-07	3.71E-03	1.24E-04	5.01E-06	9.95E-08		
Las Tres Virgenes	LV-6	2016	0.98	-10.28	0.01	5.68	0.06	3.95E-06	5.92E-08	6.76E-06	8.79E-08	1.99E-03	6.68E-05	3.07E-06	6.09E-08		
Las Tres Virgenes	LV-6/ inhibitor	2016	0.98	-10.63	0.01	5.59	0.08	3.31E-06	4.97E-08	6.49E-06	8.44E-08	1.92E-03	6.43E-05	2.52E-06	5.00E-08		
Las Tres Virgenes	LV-6/ inhibitor	2016	0.98	-10.63	0.01	5.65	0.07	7.28E-06	1.09E-07	1.21E-05	1.58E-07	3.56E-03	1.19E-04	5.70E-06	1.13E-07		
Las Tres Virgenes	LV-11	2016	0.98	-11.12	0.01	4.36	0.05	5.21E-06	7.81E-08	1.32E-05	1.72E-07	3.88E-03	1.30E-04	3.48E-06	6.90E-08		

Las Tres Virgenes	LV-11	2016	0.98	-11.12	0.01	4.77	0.06	4.76E-06	7.14E-08	1.22E-05	1.59E-07	3.59E-03	1.21E-04	3.16E-06	6.28E-08		
Las Tres Virgenes	LV-13	2016	0.98	-10.28	0.01	5.96	0.10	6.87E-06	1.03E-07	1.74E-06	2.26E-08	5.14E-04	1.73E-05	6.67E-06	1.32E-07	2.09E-07	2.71E-09
Las Tres Virgenes	LV-13	2016	0.98	-10.28	0.01	6.24	0.08	6.08E-06	9.13E-08	1.58E-06	2.05E-08	4.69E-04	1.57E-05	5.90E-06	1.17E-07	2.35E-06	3.06E-08
Cerritos Colorados																	
Cerritos Colorados	Rio Caliente					6.33	0.05	6.26E-06	9.40E-08	5.58E-06	7.26E-08	1.65E-03	3.30E-05	5.35E-06	1.06E-07	9.19E-07	1.20E-08
Cerritos Colorados	Los Volcanes					6.18	0.05	1.26E-05	1.89E-07	1.03E-05	1.34E-07	3.03E-03	6.05E-05	1.09E-05	2.16E-07		
Cerritos Colorados	Las Tinajas					7.07	0.05	1.20E-05	1.80E-07	8.50E-07	1.11E-08	2.55E-04	5.11E-06	1.19E-05	2.35E-07	4.10E-06	5.35E-08
Acoculco																	
Acoculco	ACP02					6.93	0.13	1.21E-04	2.99E-08					1.02E-04	7.11E-08		
Acoculco	ACP03-1					7.17	0.17	7.01E-05	9.69E-08	3.38E-06	1.96E-08	1.00E-03	8.22E-06	6.39E-05	1.00E-07	1.22E-06	1.00E-08
Acoculco	ACP03-2					7.14	0.17	7.52E-05	2.07E-08								
Acoculco	LB-01					6.96	0.20	2.65E-07	9.58E-11	9.20E-08	2.25E-10	2.65E-05	9.41E-08	8.33E-08	4.86E-11		
Baja California																	
Baja California	SF-1	2016		-5.00	0.10	1.09	0.02	1.26E-06	2.52E-08	1.22E-06	2.44E-08	3.87E-04	7.74E-06	1.09E-06	2.19E-08	2.38E-05	4.76E-07
Baja California	SF-2	2016	0.98	-5.30	0.11	1.07	0.02	1.45E-06	2.90E-08	1.24E-06	2.48E-08	3.89E-04	7.78E-06	1.28E-06	2.57E-08	2.17E-05	4.34E-07
Baja California	SF-3	2016	0.98	-5.10	0.10	1.09	0.02	1.27E-06	2.54E-08	1.11E-06	2.22E-08	3.29E-04	6.59E-06	1.08E-06	2.15E-08		
Baja California	SF-4	2016	0.97	-5.00	0.10	1.11	0.02	1.23E-06	2.46E-08	7.80E-07	1.56E-08	2.26E-04	4.52E-06	1.11E-06	2.22E-08	1.95E-06	3.90E-08
Baja California	SF-5	2016	0.99	-5.00	0.10	1.07	0.02	1.41E-06	2.82E-08	4.80E-07	9.60E-09	1.41E-04	2.81E-06	1.37E-06	2.75E-08	1.20E-06	2.40E-08
Baja California	SF1 (SSB)	2017	0.97	-5.00	0.10	1.12	0.02	6.00E-07	1.20E-08	9.40E-07	1.88E-08	2.74E-04	5.48E-06	5.30E-07	1.06E-08		

Baja California	SF2 (SSB)	2017	0.99	-5.00	0.10	1.15	0.02	8.00E-07	1.60E-08	3.20E-07	6.40E-09	9.47E-05	1.89E-06	7.62E-07	1.52E-08		
Baja California	PE-1	2016	1.00	-6.60	0.13	1.17	0.02	1.71E-04	3.41E-06	1.22E-05	2.44E-07	3.61E-03	7.21E-05	1.70E-04	3.40E-06	6.10E-06	1.22E-07
Baja California	PE-2	2016	0.42	-5.20	0.10	1.08	0.02	9.17E-05	1.83E-06	7.17E-06	1.43E-07	2.15E-03	4.31E-05	9.14E-05	1.83E-06	3.94E-05	7.89E-07
Baja California	PE1 (SSB)	2017	0.58	-6.00	0.12	1.12	0.02	6.79E-05	1.36E-06	6.14E-06	1.23E-07	1.85E-03	3.70E-05	6.77E-05	1.35E-06	3.38E-05	6.75E-07
Baja California	CO1y	2016	0.70	-17.70	0.35	0.81	0.02	1.70E-04	3.41E-06	3.22E-05	6.44E-07	9.54E-03	1.91E-04	1.67E-04	3.35E-06	4.83E-05	9.67E-07
Baja California	CO2	2016		-18.40	0.37	1.07	0.02	3.18E-04	6.36E-06	3.49E-05	6.99E-07	1.05E-02	2.11E-04	3.15E-04	6.30E-06	2.27E-04	4.54E-06
Baja California	CO3	2016		-18.10	0.36	0.58	0.01	3.23E-05	6.47E-07	3.24E-05	6.48E-07	9.68E-03	1.94E-04	2.73E-05	5.45E-07	8.11E-05	1.62E-06
Baja California	PU	2016		-11.70	0.23	1.43	0.03	1.46E-04	2.91E-06	1.14E-05	2.27E-07	3.38E-03	6.76E-05	1.41E-04	2.83E-06	2.84E-05	5.69E-07
Baja California	PU1	2016		-11.00	0.22	1.59	0.03	2.02E-04	4.03E-06	4.03E-05	8.06E-07	1.22E-02	2.44E-04	1.98E-04	3.97E-06	3.02E-04	6.04E-06
Baja California	PU1 new	2017	0.16	-9.90	0.20	1.55	0.03	2.10E-04	4.20E-06	3.92E-05	7.85E-07	1.17E-02	2.34E-04	2.06E-04	4.13E-06	9.81E-05	1.96E-06
Baja California	SLG1	2017	0.15	-10.50	0.21	6.88	0.14	1.90E-04	3.79E-06	5.57E-06	1.11E-07	1.65E-03	3.30E-05	1.89E-04	3.78E-06	8.36E-06	1.67E-07
Baja California	SLG2	2017	0.53	-10.90	0.22	6.9	0.14	1.03E-04	2.07E-06	2.35E-06	4.70E-08	7.00E-04	1.40E-05	1.03E-04	2.06E-06	1.06E-05	2.12E-07
Baja California	SLG1(SSB)	2017	0.49	-9.60	0.19	6.84	0.14	1.32E-04	2.64E-06	1.12E-05	2.25E-07	3.34E-03	6.68E-05	1.32E-04	2.64E-06	2.81E-05	5.62E-07
Baja California	SLG2 (SSB)	2017	0.14	-11.30	0.23	6.88	0.14	7.28E-05	1.46E-06	5.25E-06	1.05E-07	1.58E-03	3.17E-05	7.26E-05	1.45E-06	3.94E-05	7.88E-07
Baja California	AA1	2016	0.36	-10.70	0.21	5.45	0.11	1.43E-05	2.86E-07	2.98E-06	5.96E-08	8.89E-04	1.78E-05	1.39E-05	2.78E-07	7.45E-06	1.49E-07
Baja California	AA2	2016	0.94	-11.10	0.22	5.1	0.1	1.41E-05	2.81E-07	6.36E-06	1.27E-07	1.94E-03	3.87E-05	1.26E-05	2.51E-07	5.41E-05	1.08E-06
Baja California	AA3	2016		-10.60	0.21	4.71	0.09	1.35E-05	2.70E-07	1.19E-05	2.38E-07	3.58E-03	7.16E-05	1.18E-05	2.35E-07	6.54E-05	1.31E-06
Baja California	AA4	2016		-10.30	0.21	5.54	0.11	1.59E-05	3.18E-07	2.17E-06	4.34E-08	6.50E-04	1.30E-05	1.57E-05	3.13E-07	9.77E-06	1.95E-07
Baja California	AA5	2016	0.95	-9.80	0.20	5.46	0.11	1.40E-05	2.80E-07	1.41E-06	2.82E-08	4.20E-04	8.40E-06	1.38E-05	2.76E-07	3.53E-06	7.05E-08

Baja California	AA6	2016	0.84	-10.20	0.20	4.63	0.09	1.26E-05	2.52E-07	1.08E-05	2.15E-07	3.23E-03	6.46E-05	1.10E-05	2.19E-07	4.84E-05	9.68E-07
Baja California	AA7	2016				5.13	0.1	1.38E-05	2.77E-07	1.80E-06	3.60E-08	5.38E-04	1.08E-05	1.36E-05	2.72E-07	6.30E-06	1.26E-07
Baja California	AA4 (SSB)	2017	0.96			5.64	0.11	1.22E-05	2.43E-07	1.17E-06	2.34E-08	3.46E-04	6.92E-06	1.20E-05	2.40E-07	1.76E-06	3.51E-08
Baja California	AA5 (SSB)	2017	0.96			5.41	0.11	1.26E-05	2.52E-07	1.20E-06	2.40E-08	3.46E-04	6.92E-06	1.24E-05	2.47E-07	1.80E-06	3.60E-08
Baja California	AA5* (SSB)	2017	0.94			5.43	0.11	1.28E-05	2.56E-07	1.10E-06	2.20E-08	3.38E-04	6.76E-06	1.26E-05	2.52E-07	1.65E-06	3.30E-08
Baja California	AA7 (SSB)	2017	0.94			5.06	0.1	1.19E-05	2.38E-07	7.90E-06	1.58E-07	2.36E-03	4.72E-05	1.01E-05	2.02E-07	1.98E-05	3.95E-07
Baja California	FUM (SSB)	2017	0.75	-10.50	0.21	4.29	0.09	7.09E-06	1.42E-07	1.84E-05	3.68E-07	5.46E-03	1.09E-04	3.85E-06	7.70E-08	2.76E-05	5.52E-07

Table C2 Temperature, enthalpy, measured $^{4}He/^{20}Ne$ ratios, air-corrected R/Ra ratios and estimated heat/^{3}He ratios in the Mexican geothermal samples

ID	Temperature (°C)	Enthalpy (kJ/kg)	$^{4}He/^{20}Ne$	±	(R/Ra)c	±	$Q/^{3}He$	±	ID	Temperature (°C)	Enthalpy (kJ/kg)	$^{4}He/^{20}Ne$	±	(R/Ra)c	±	$Q/^{3}He$	±
Cerro Prieto									**Los Humeros**								
CP-109	311.5		38.84	0.77	6.08	0.09	4.44E+13	8.88E+11	H-03D	331.2	2660	1833.09	36.39	6.35	0.05	4.79E+11	9.58E+09
CP-112	316.9		31.79	0.63	5.60	0.10	4.87E+13	9.74E+11	H-06	308.9	2660			7.62	0.07	4.50E+11	9.00E+09
CP-114	332.3		31.69	0.63	6.17	0.07	4.94E+13	9.88E+11	H-06	308.9	2660	332.56	6.60	7.34	0.06	1.67E+12	3.34E+10
CP-301	171.2		50.03	0.99	6.32	0.05	2.05E+13	4.10E+11	H-06	308.9	2525	2743.29	54.45	7.17	0.07	4.20E+11	8.40E+09
CP-302	174.4		56.64	1.12	6.39	0.07	1.91E+13	3.82E+11	H-07	291.7	2525	336.68	6.68	7.33	0.08	1.62E+12	3.24E+10
CP-207D	343.7		155.17	3.08	5.57	0.06	1.12E+13	2.24E+11	H-07	291.7	2660	19.51	0.39	7.19	0.10	3.77E+13	7.54E+11
CP-218	357.0		55.76	1.11	5.20	0.06	3.45E+13	6.90E+11	H-09	337.8	2660	1067.37	46.60	6.86	0.05	3.59E+12	7.18E+10
CP-220D	359.6		76.55	1.52	3.34	0.03	4.28E+13	8.56E+11	H-11D	293.5	2660	598.12	14.95	7.13	0.13		
CP-230D	354.5		125.54	2.49	6.51	0.07	1.29E+13	2.58E+11	H-12	361.1	2660	22076.47	1068.15	6.95	0.07	1.23E+11	2.46E+09
CP-232	348.3		170.90	3.39	5.77	0.07	1.02E+13	2.04E+11	H-15D	315.0	2660	39.42	0.78	7.00	0.06	5.44E+13	1.09E+12
CP-233	316.3		32.03	0.64	6.54	0.08	4.17E+13	8.34E+11	H-17D	302.07	2660	8.84	0.18	6.25	0.10	2.06E+14	4.12E+12
CP-234D	346.3		136.23	2.70	5.73	0.07	1.23E+13	2.46E+11	H-19D	290.1	2660	8569.10	170.09	7.27	0.07	7.94E+10	1.59E+09
CP-247	461.9		426.28	8.46	6.01	0.08	4.33E+12	8.66E+10	H-19D	290.1	2660	15342.50	304.54	7.37	0.06	7.37E+10	1.47E+09
CP-248	418.9		140.78	2.79	3.91	0.03	2.04E+13	4.08E+11	H-20	319.8	2660	1945.38	38.61	7.29	0.05	8.12E+11	1.62E+10
CP-500	376.1		75.56	1.50	3.34	0.04	4.46E+13	8.92E+11	H-30	306.0	2660	6.88	0.14	7.25	0.13	7.90E+13	1.58E+12
CP-500	376.1		77.43	1.54	3.31	0.04	4.24E+13	8.48E+11	H-31	328.3	2660	453.80	9.01	7.18	0.06	2.13E+12	4.26E+10
CP-501	370.6		84.68	1.68	3.34	0.04	3.93E+13	7.86E+11	H-32	299.5	2660	34.07	0.68	7.57	0.10	1.78E+13	3.56E+11
CP-505	333.0		110.73	2.20	4.92	0.06	1.74E+13	3.48E+11	H-33	303.4	2660	2.74	0.05	7.32	0.34	1.38E+14	2.76E+12
CP-512	338.3		123.84	2.46	5.13	0.04	1.53E+13	3.06E+11	H-34	311.0	2068	456.51	9.06	7.18	0.06	1.94E+12	3.88E+10
CP-512	338.3		121.02	2.40	5.45	0.06	1.45E+13	2.90E+11	H-35	251.9	2408	33.47	0.66	7.14	0.05	5.15E+13	1.03E+12
CP-513	365.2		82.25	1.63	3.81	0.04	3.20E+13	6.40E+11	H-39a	362.0	2559	7516.89	363.70	6.27	0.06	1.26E+11	2.52E+09
CP-522D	373.1		102.17	2.03	6.06	0.06	1.61E+13	3.22E+11	H-39b	362.0	2559	8197.52	173.90	6.26	0.05	1.37E+11	2.74E+09
CP-531D	402.5		100.80	2.00	4.03	0.05	2.68E+13	5.36E+11	H-41	312.2	2660			6.13	0.07		
CP-533D	419.0		73.91	1.47	3.57	0.06	4.47E+13	8.94E+11	H-42	317.2	2454	4587.12	97.31	6.42	0.06	2.34E+11	4.68E+09
CP-538D	440.4		186.25	3.70	4.95	0.05	1.19E+13	2.38E+11	H-44D	285.7	2584	3.17	0.06	7.17	0.29	1.82E+14	3.64E+12
CP-542	461.9		110.89	2.20	3.30	0.03	3.41E+13	6.82E+11	H-45D	306.2	2583	32546.65	813.67	7.22	0.06	4.57E+10	9.14E+08

CP-545D	440.4		121.88	2.42	4.65	0.05	1.91E+13	3.82E+11	H-48D	280.4	2660	1566.36	31.09	6.80	0.07	4.50E+11	9.00E+09
CP-E24	279.3		44.17	0.88	6.63	0.05	3.25E+13	6.50E+11	H-49D	264.7		97.23	1.93	7.30	0.06		
CP-E50	290.0		22.09	0.44	6.20	0.06	5.93E+13	1.19E+12	H50a	324.4	2660	14593.99	569.17	6.84	0.04	5.30E+10	1.06E+09
CP-E56	338.9		183.98	3.65	5.86	0.06	8.88E+12	1.78E+11	H50b	324.4	2660	14657.99	290.95	6.08	0.06	5.97E+10	1.19E+09
CP-M126	365.2		91.62	1.82	3.76	0.04	3.22E+13	6.44E+11	H55	329.8	2603	787.61	15.63	7.49	0.05	1.53E+12	3.06E+10
CP-M148A	353.8		26.33	0.52	5.93	0.07	6.07E+13	1.21E+12	H56	295.7	1913	4283.90	85.03	7.30	0.07	1.25E+11	2.50E+09
CP-M160	268.0		28.76	0.57	6.22	0.08	1.50E+14	3.00E+12	H59	305.1	2098	2.85	0.06	7.45	0.05	1.21E+14	2.42E+12
CP-308	322.2		144.47	2.87	6.00	0.10	1.00E+13	2.00E+11	H65			559.59	11.11	6.42	0.09		
CP-309	353.8		103.88	2.06	6.51	0.06	1.45E+13	2.90E+11	**Las Tres Virgenes**								
CP-311	311.5		90.15	1.79	6.35	0.07	1.66E+13	3.32E+11	LV-6		1176.13	1.36	0.03	5.84	0.13	2.72E+14	5.44E+12
CP-318	316.9		127.11	2.52	6.83	0.08	1.05E+13	2.10E+11	LV-6		1176.13	1.43	0.03	6.09	0.10	2.32E+14	4.64E+12
CP-345	354.5		139.78	2.77	5.69	0.05	1.04E+13	2.08E+11	LV-6/ inhibitor		1176.13	1.34	0.03	6.03	0.12	2.69E+14	5.37E+12
CP-346	461.9		155.33	3.08	6.43	0.07	9.64E+12	1.93E+11	LV-6/ inhibitor		1176.13	1.47	0.03	6.03	0.11	2.27E+14	4.54E+12
CP-E35A	332.2		81.36	1.62	6.43	0.07	1.77E+13	3.54E+11	LV-11		1141.24	0.96	0.02	4.77	0.12	4.25E+14	8.50E+12
CP-E37A	343.2		18.25	0.36	6.33	0.07	5.92E+13	1.18E+12	LV-11		1141.24	0.95	0.02	5.32	0.14	3.86E+14	7.72E+12
CP-M110	231.6		112.88	2.24	6.59	0.05	1.02E+13	2.04E+11	LV-13		1146.27	10.86	0.22	6.00	0.10	3.40E+13	6.79E+11
CP-404	316.9		112.87	2.24	5.41	0.06	1.53E+13	3.06E+11	LV-13		1146.27	10.74	0.21	6.28	0.08	3.32E+13	6.65E+11
CP-414	340.0		169.61	3.37	5.73	0.05	1.04E+13	2.08E+11	**Cerritos Colorados**								
CP-423	311.5		434.29	8.62	7.32	0.07	2.80E+12	5.60E+10	Rio Caliente	308		2.18	0.04	7.24	0.06	1.24E+14	2.49E+12
CP-424	332.3		59.43	1.18	6.65	0.06	2.63E+13	5.26E+11	Los Volcanes	308		2.36	0.05	6.99	0.06	1.17E+14	2.34E+12
CP-431D	336.1		111.25	2.21	6.38	0.09	1.39E+13	2.78E+11	Las Tinajas	308		27.79	0.55	7.14	0.05	8.84E+12	1.77E+11
CP-509	316.9		129.35	2.57	6.58	0.09	1.19E+13	2.38E+11	**Acoculco**								
Los Azufres									ACP02	302		20.15	0.40	7.02	0.13		
AZ-2A	240.6	1208			2.27	0.02	1.70E+15	3.40E+13	ACP03-1	302		35.11	0.70	7.23	0.17	3.14E+12	6.27E+10

AZ-4	274.6	1669	56.04	1.11	5.26	0.04	1.44E+13	2.88E+11	ACP03-2	302	37.63	0.75	7.20	0.17		
AZ-5	252.2		771.68	15.32	7.48	0.07			LB-01	302	4.55	0.09	7.41	0.17	2.33E+13	4.65E+11
AZ-6	276.7		36.43	0.72	6.85	0.06			**Baja California**							
AZ-9A	268.3	2444	533.26	10.58	7.93	0.09	1.20E+12	2.40E+10	SF-1	254.44	2.42	0.07	1.11	0.01	6.38E+14	1.28E+13
AZ-9AD	267.9		3609.64	73.96	7.74	0.06		0.00E+00	SF-2	254.42	2.79	0.08	1.08	0.01	5.73E+14	1.15E+13
AZ-12D	286.6	2388	28.10	0.56	6.61	0.08	2.32E+13	4.64E+11	SF-3	257.82	2.08	0.06	1.10	0.01	5.82E+14	1.16E+13
AZ-13	235.2		2343.19	46.51	7.68	0.08			SF-4	266.05	3.32	0.09	1.12	0.01	4.30E+14	8.60E+12
AZ-18	242.3				7.51	0.06			SF-5	275.63	12.82	0.36	1.08	0.01	2.49E+14	4.98E+12
AZ-18	242.3				7.66	0.08			SF1 (SSB)	262.08	2.73	0.08	1.14	0.01	1.04E+15	2.08E+13
AZ-19	261.4	2420	28.45	0.56	5.98	0.06	2.78E+13	5.56E+11	SF2 (SSB)	284.35	6.67	0.19	1.16	0.01	2.82E+14	5.64E+12
AZ-25	279.8		296.98	5.89	6.54	0.05	2.66E+12	5.32E+10	PE-1	184.88	115.35	3.26	1.17	0.01	3.07E+13	6.14E+11
AZ-26	236.7				6.66	0.05			PE-2	204.89	90.78	2.57	1.08	0.01	4.09E+13	8.18E+11
AZ-28	262.1	2218	191.08	3.79	6.48	0.05	4.54E+12	9.08E+10	PE1 (SSB)	212.46	78.99	2.23	1.12	0.01	4.76E+13	9.52E+11
AZ-32	255.8		2377.98	47.20	7.53	0.05			CO1y		17.29	0.49	0.81	0.01		
AZ-34a	238.8				7.41	0.06			CO2		35.76	1.01	1.08	0.01		
AZ-34b	238.8				7.5	0.08			CO3		2.03	0.06	0.50	0.02		
AZ-36	222.6		972.05	19.29	7.23	0.06			PU		10.86	0.31	1.44	0.02		
AZ-38	194.6		506.26	10.05	7.34	0.05			PU1	126.71	19.37	0.55	1.60	0.02	4.06E+13	8.12E+11
AZ-42	268.5	1307	0.63	0.01	4.47	0.03	1.14E+15	2.28E+13	PU1 new	127.25	17.74	0.50	1.56	0.02	3.91E+13	7.82E+11
AZ-43	267.8	2664	1887.33	37.46	6.98	0.06	5.59E+11	1.12E+10	SLG1	208.81	86.97	2.46	6.90	0.06	2.46E+12	4.92E+10
AZ-46	276.7	2470	4.65	0.09	7.24	0.08	1.05E+14	2.10E+12	SLG2	226.65	103.34	2.92	6.92	0.06	2.08E+12	4.16E+10
AZ-47D	253.7	1379	413.82	8.21	7.47	0.1	8.40E+11	1.68E+10	SLG1(SSB)	159.99	171.49	4.85	6.86	0.06	5.30E+12	1.06E+11
AZ-48	301.7	2235	198.68	3.94	6.54	0.12	4.42E+12	8.84E+10	SLG2 (SSB)	200.88	125.53	3.55	6.89	0.06	5.79E+12	1.16E+11
AZ-51	269.8	1421	1048.15	20.81	7.37	0.04	5.51E+11	1.10E+10	AA1	235.68	11.73	0.33	5.57	0.05	2.52E+13	5.04E+11
AZ-51	269.8	1421	1143.73	22.70	7.58	0.07	6.07E+12	1.21E+11	AA2		2.97	0.08	5.59	0.05		
AZ-62a	255.3	1955	2103.52	41.75	7.19	0.05	1.63E+11	3.26E+09	AA3		2.47	0.07	5.26	0.04		
AZ-62b	255.3	1955	4168.08	82.73	7.16	0.08	1.83E+11	3.66E+09	AA4	242.61	19.89	0.56	5.62	0.04		
AZ-65	268.3	1971	2.00	0.04	5.73	0.05	4.16E+14	8.32E+12	AA5	249.42	24.54	0.69	5.52	0.04	1.68E+13	3.36E+11
AZ-66D	266.6	2701			1.04	0.01	8.67E+15	1.73E+14	AA6		2.48	0.07	5.17	0.04	1.29E+13	2.58E+11

AZ-67	272.8	2041	252.91	5.02	7.55	0.08	2.64E+12	5.28E+10	AA7	246.98	18.44	0.52	5.20	0.04		
AZ-83a	269.1	2256			7.18	0.04	4.13E+11	8.26E+09	AA4 (SSB)	256.51	21.35	0.60	5.71	0.04	1.76E+13	3.52E+11
AZ-83b	269.1	2256			6.71	0.07			AA5 (SSB)	256.06	18.50	0.52	5.49	0.05	1.23E+13	2.46E+11
AZ-89	271.3	2549			6.59	0.07	3.96E+12	7.92E+10	AA5* (SSB)	256.61	21.68	0.61	5.50	0.05	1.27E+13	2.54E+11
AZ-90	285.8	1510	0.84	0.02	4.21	0.03	8.18E+14	1.64E+13	AA7 (SSB)	208.58	2.14	0.06	5.77	0.04	1.15E+13	2.30E+11
									FUM (SSB)	180.54	0.70	0.02	7.04	0.05	7.57E+13	1.51E+12

Table C3 Estimated percentages of various carbon sources in Mexican geothermal samples

ID	Mantle[a] (%)	Limestone[a] (%)	Sediments[a] (%)	Mantle[b] (%)	Crust[b] (%)	Meteoric water[b] (%)	ID	Mantle[a] (%)	Limestone[a] (%)	Sediments[a] (%)	Mantle[b] (%)	Crust[b] (%)	Meteoric water[b] (%)
Cerro Prieto							**Los Humeros**						
CP-109	30.24	60.58	9.18	72.52	2.97	24.51	H-03D	5.49	78.60	15.91	78.48	14.67	6.84
CP-112	17.37	67.76	14.87	65.85	4.74	29.41	H-06	5.74	82.57	11.69	83.55	16.45	0.00
CP-114	14.58	85.42	0.00	74.06	5.61	20.33	H-06	57.30	42.18	0.52	90.68	0.74	8.58
CP-301	22.48	66.02	11.50	76.10	4.09	19.81	H-06	16.65	83.35	0.00	88.81	4.76	6.43
CP-302	21.87	69.37	8.76	77.27	4.20	18.53	H-07	25.89	69.62	4.49	90.69	2.88	6.43
CP-207D	10.85	79.37	9.78	26.59	7.20	26.59	H-07	43.28	56.72	0.00	87.33	1.33	11.34
CP-218	17.08	82.92	0.00	35.82	3.97	35.82	H-09	0.27	89.62	10.11			
CP-220D	13.05	76.44	10.50	62.53	3.67	62.53	H-11D						
CP-230D	30.43	62.23	7.34	17.86	3.11	17.86	H-12	24.14	64.39	11.47	85.42	2.97	11.61
CP-232	8.91	79.59	11.50	21.68	9.08	21.68	H-15D	0.31	90.52	9.17			
CP-233	27.01	61.11	11.88	17.40	3.60	17.40	H-17D	0.14	91.62	8.24			
CP-234D	7.64	92.36	0.00	20.95	10.14	20.95	H-19D	28.60	67.30	4.10	89.94	2.63	7.43
CP-247	51.40	48.60	0.00	26.98	1.37	26.98	H-19D	43.00	56.02	0.98	91.21	1.48	7.32
CP-248	13.97	76.29	9.74	53.92	3.98	53.92	H-20	7.10	86.97	5.93	87.22	12.78	0.00
CP-500	19.03	80.97	0.00	64.22	2.17	64.22	H-30	32.72	61.50	5.78	85.90	1.36	12.74
CP-500	25.14	74.86	0.00	65.40	1.57	65.40	H-31	10.45	78.98	10.57	89.37	7.75	2.88
CP-501	21.84	69.42	8.73	64.08	2.24	64.08	H-32	19.79	80.21	0.00	93.73	4.17	2.11
CP-505	8.49	78.25	13.26	34.79	8.19	34.79	H-33	24.40	75.60	0.00	81.60	2.24	16.16
CP-512	9.03	77.36	13.61	31.90	8.05	31.90	H-34	9.74	74.87	15.39	89.60	9.41	0.99
CP-512	9.69	76.84	13.47	27.52	7.97	27.52	H-35	0.52	84.79	14.69			
CP-513	31.04	61.55	7.41	57.92	1.85	57.92	H-39a	4.49	95.51	0.00	77.80	17.98	4.21
CP-522D	7.98	78.21	13.80	15.64	10.70	15.64	H-39b	5.93	94.07	0.00	77.01	13.36	9.62
CP-531D	7.79	77.56	14.64	48.39	7.37	48.39	H-41	0.05	88.66	11.29	79.15	12.31	8.54
CP-533D	25.08	67.69	7.23	61.00	2.08	61.00	H-42	6.56	93.44	0.00	80.95	2.72	16.33
CP-538D	42.45	53.21	4.34	41.71	1.74	41.71	H-44D	24.74	72.36	2.91	89.02	1.19	9.78
CP-542	14.37	76.38	9.25	63.55	3.28	63.55	H-45D	47.38	52.62	0.00	83.84	6.99	9.17
CP-545D	16.79	69.45	13.76	43.37	4.09	43.37	H-48D	11.89	79.72	8.39	89.85	0.98	9.16

CP-E24	15.73	73.91	10.36	13.27	5.98	13.27
CP-E50	24.20	63.91	11.89	22.30	3.77	22.30
CP-E56	9.60	79.68	10.72	20.91	8.58	20.91
CP-M126	12.97	79.47	7.56	56.02	4.08	56.02
CP-M148A	7.89	92.11	0.00	18.70	10.16	18.70
CP-M160	0.17	85.67	14.16			
CP-308	53.04	44.58	2.37	71.55	1.71	26.74
CP-309	10.13	89.87	0.00	26.74	8.66	11.70
CP-311	19.79	69.90	10.31	11.70	4.61	18.56
CP-318	23.97	70.86	5.17	18.56	3.98	12.40
CP-345	20.48	70.79	8.73	12.40	3.97	28.59
CP-346	38.45	57.85	3.70	28.59	2.41	19.82
CP-E35A	35.51	64.49	0.00	19.82	2.25	20.11
CP-E37A	12.72	87.28	0.00	20.11	6.63	17.49
CP-M110	28.80	63.70	7.49	17.49	3.30	16.57
CP-404	7.07	79.26	13.67	16.57	10.77	24.82
CP-414	5.42	94.58	0.00	24.82	14.34	16.25
CP-423	44.53	52.32	3.15	16.25	2.38	7.03
CP-424	40.89	59.11	0.00	7.03	2.00	17.36
CP-431D	4.57	82.02	13.41	17.36	19.49	1.09
CP-509	16.11	74.78	9.11	1.09	0.00	20.49
Los Azufres						
AZ-2A	3.43	69.91	26.66	16.07	8.65	75.28
AZ-4	4.85	95.15	0.00	62.57	14.25	23.19
AZ-5	27.61	55.81	16.58	92.97	2.82	4.22
AZ-6	10.73	67.92	21.34	84.11	7.94	7.95
AZ-9A	20.06	58.15	21.79	95.52	4.48	0.00
AZ-9AD	26.90	73.10	0.00	96.70	2.99	0.31
AZ-12D	5.49	63.07	31.44	81.64	15.77	2.60
AZ-13	35.01	47.51	17.48	95.72	2.09	2.19

H-49D	51.94	48.06	0.00	84.31	6.31	9.38
H50a	12.10	87.90	0.00	73.21	4.59	22.20
H50b	14.37	85.63	0.00	93.54	5.93	0.53
H55	15.37	84.63	0.00	90.42	3.01	6.56
H56	24.02	75.98	0.00	84.57	8.13	7.30
H59	9.46	90.54	0.00	85.82	6.26	7.91
H65	6.06	93.94	0.00	79.15	12.31	8.54
Las Tres Virgenes						
LV-6	10.79	57.28	31.93	64.65	8.21	27.14
LV-6	6.76	60.44	32.80	68.63	13.18	18.19
LV-6/ inhibitor	5.61	60.17	34.22	67.77	15.58	16.65
LV-6/ inhibitor	12.40	54.85	32.75	67.41	7.49	25.11
LV-11	7.00	57.45	35.55	49.39	10.22	40.39
LV-11	7.12	57.35	35.52	55.43	11.11	33.46
LV-13	11.61	56.64	31.75	71.97	7.87	20.16
LV-13	10.79	57.28	31.93	76.04	8.78	15.18
Cerritos Colorados						
Rio Caliente				308		2.18
Los Volcanes				308		2.36
Las Tinajas				308		27.79
Acoculco						
ACP02				302		20.15
ACP03-1				302		35.11
ACP03-2				302		37.63
LB-01				302		4.55
Baja California						
SF-1	0.37	83.04	16.59	6.75	39.01	54.25
SF-2	0.42	82.01	17.58	5.78	34.12	60.10
SF-3	0.37	82.71	16.92	6.69	38.63	54.68
SF-4	0.36	83.05	16.59	7.23	40.40	52.37

AZ-18				93.00	0.03	6.97	SF-5	0.41	83.01	16.58	5.86	34.70	59.44
AZ-18	24.74	75.26	0.00	95.61	3.33	1.06	SF1 (SSB)	0.17	83.20	16.63	13.31	82.84	3.84
AZ-19	11.09	66.71	22.20	71.36	6.66	21.98	SF2 (SSB)	0.24	83.15	16.62	10.91	62.63	26.46
AZ-25	10.40	63.72	25.88	80.10	7.84	12.06	PE-1				2.50	0.49	97.01
AZ-26	18.68	60.74	20.59	81.43	4.07	14.51	PE-2	47.15	45.73	7.12	1.22	0.55	98.23
AZ-28	15.02	61.90	23.08	79.00	5.12	15.88	PE1 (SSB)	30.20	56.34	13.46	1.83	0.82	97.35
AZ-32				93.30	0.07	6.63	CO1y						
AZ-34a				91.57	0.01	8.41	CO2				1.21	1.47	97.32
AZ-34b	25.11	56.60	18.29	93.31	3.20	3.49	CO3						
AZ-36	22.33	58.77	18.89	89.36	3.56	7.09	PU						
AZ-38	19.03	80.97	0.00	91.19	4.41	4.40	PU1				8.54	0.82	90.64
AZ-42	8.11	70.31	21.58	30.28	7.10	62.62	PU1 new				7.96	0.71	91.33
AZ-43	42.36	57.64	0.00	85.62	1.38	13.00	SLG1	22.91	50.05	27.04	84.12	0.87	15.01
AZ-46	14.69	64.16	21.15	85.12	5.93	8.96	SLG2				84.43	1.01	14.56
AZ-47D	15.61	63.81	20.58	93.22	5.68	1.09	SLG1(SSB)				83.53	0.70	15.77
AZ-48	58.47	30.03	11.50	79.10	0.69	20.21	SLG2 (SSB)				84.15	1.06	14.80
AZ-51				91.00	0.00	9.00	AA1				64.14	4.05	31.81
AZ-51	33.15	48.56	18.28	94.31	2.20	3.49	AA2						
AZ-62a	68.25	21.07	10.68	88.50	0.54	10.96	AA3						
AZ-62b	26.34	52.34	21.33	88.40	2.85	8.75	AA4				65.37	3.69	30.93
AZ-65	15.73	60.64	23.62	59.46	4.32	36.22	AA5	20.51	51.27	28.22	64.23	3.67	32.10
AZ-66D	1.36	72.90	25.74	1.85	10.14	88.01	AA6	19.73	50.54	29.72			
AZ-67	16.24	62.68	21.08	94.34	5.48	0.18	AA7	19.98	80.02	0.00	59.45	3.22	37.33
AZ-83a	82.64	8.93	8.43	88.33	0.28	11.39	AA4 (SSB)	20.34	79.66	0.00	66.81	3.71	29.48
AZ-83b	9.33	69.63	21.05	82.84	9.07	8.09	AA5 (SSB)	22.23	77.77	0.00	63.49	3.50	33.01
AZ-89	7.33	67.69	24.98	81.33	11.54	7.13	AA5* (SSB)	15.87	84.13	0.00	63.77	3.45	32.78
AZ-90	1.14	98.86	0.00	38.81	49.67	11.52	AA7 (SSB)	0.20	99.80	0.00	58.41	2.90	38.69
							FUM (SSB)	0.14	64.89	34.97	47.63	4.48	47.89

[a] Estimated from the $CO_2/^3He$ and $\delta^{13}C$-CO_2 ratios.

[b] Estimated from the $CO_2/^4He$ and R/Ra ratios.